MASSACHUSETTS INSTITUTE OF TECHNOLOGY

THE ENERGY LABORATORY

IMPROVEMENT OF THE ENVIRONMENTAL AND ECONOMIC
CHARACTERISTICS OF THE ROTARY COOLING TOWER
by

Javier Valenzuela
John Dong
Je-Chin Han
Bruce R. Andeen
Leon R. Glicksman
Warren M. Rohsenow

IMPROVEMENT OF THE

ENVIRONMENTAL AND ECONOMIC CHARACTERISTICS

OF THE ROTARY COOLING TOWER

by

Javier Valenzuela
John Dong
Je-Chin Han
Bruce R. Andeen
Leon R. Glicksman
Warren M. Rohsenow

ENERGY LABORATORY

In Association With

HEAT TRANSFER LABORATORY

DEPARTMENT OF MECHANICAL ENGINEERING

MASSACHUSETTS INSTITUTE OF TECHNOLOGY

Executive Summary

This report describes research for the past year on methods to enchance the environmental and economic performance of dry cooling towers.

The work has concentrated on dry cooling towers utilizing periodic water to air heat exchangers. Periodic towers have sheet metal discs partially submerged in hot, power plant condenser effluent. As the discs rotate, the discs alternately absorb heat from the effluent and discharge heat to the air. The means of heat transfer on the air side can be either evaporative and/or convective, depending upon the amount of eff- luent carried into the air side on the surface of the plates. An oil layer, floated on the water's surface, has been shown to be effective in eliminating water carry-over to the air side.

The advantages of the periodic tower lie in the low cost of the discs and the ability to operate dry. A periodic tower should be signi- ficantly less expensive than a conventional dry tower fabricated with finned tubes. Further, since the periodic tower can also operate wet, by removing the oil film, the high capacity losses incurred during warm months by conventional dry towers can be eliminated.

In the past year, the five foot diameter rotor matrix fabricated during the previous year was parametrically tested and evaluated in the full scale test facility. The rotor's performance deviated from the prior, simplified analysis, necessitating a more complex analytic system model. Such a model was developed, and agrees with the data, within the data's experimental accuracy.

Oil studies were performed to identify (1) the prevalent mechanisms

in the periodic tower of generating oil/water emulsions, (2) desirable oil properties, and (3) the impact oil properties have on disc performance, rotational speeds and disc geometry.

The enhancement of the air side film coefficient by roughening the disc surface with ribs was experimentally determined and economically evaluated using the previously developed optimization routine. This optimization study projected a 13% reduction in the capital cost of a periodic cooling tower with the use of rib roughners.

Minor studies were also made in three additional areas. The first two studies showed that cross linking rotor systems in parallel and series combinations could increase the system effectiveness by up to 50%; and that at normal operating velcoities no identifiable fouling of condensers would occur due to possible contamination of the circulating water with oil. Finally, a preliminary annular matrix was evaluated. Although the matrix generated oil dripping, the dripping was linked to the specific fabrication technique employed, rather than a problem inherent to the annular concept.

Acknowledgements

TABLE OF CONTENTS

LIST OF FIGURES

LIST OF TABLES

15.

NOMENCLATURE

A   -   area

C   -   heat capacity

c_p -   specific heat

D   -   dilution

D_h -   hydraulic diameter

D_i -   inner diameter of disc

D_o -   outer diameter of disc

e   -   rib height

e^+ -   non-dimensional rib height

f   -   friction factor

g   -   gravitional constant

H   -   water level

h   -   heat transfer coefficient

h   -   oil thickness (Section 3)

k   -   thermal conductivity

L   -   flow length

ℓ -   characteristic length for conducter

$\dot{m}$ -   mass flow rate

N   -   number of revolution

N_{TU} -   number of transfer units

P   -   pressure

p   -   pitch

Pr   -   Prandtl number

Q   -   volume/flow

Q   -   rate of heat rejection per disc

q   —   rate of heat transfer

R   —   radius

R_o —   outer radius of disc

R_w —   radius of disc at water level

Re   —   Reynolds number

RH   —   relative humidity

S   —   disc spacing

St   —   Stanton number

T   —   temperature

t   —   time

U   —   overall heat transfer coefficient

V   —   velocity

V   —   volume

V_A —   air velocity

u,v,w   —   velocity component in X,Y,Z direction, respectively

X,Y,Z   —   coordinate axis

x,y,z   —   distance in coordinate direction

Greek symbols

α —   flow angle of attack

δ —   thickness

ε —   heat exchanger effectiveness

ε

μ —   absolute viscosity

ν —   kinematic viscosity

ρ -   density

σ -   surface tension

τ -   shear stress

ϕ -   rib shape

ϕ · -

ω, Ω -   angular velocity, RPM

Subscripts

a   -   air

avg   -   average

c   -   critical

d   -   disc

eff   -   effective

exp   -   experimental

f   -   frontal

m,net -   metal

m   -   model

max   -   maximum

min   -   minimum

o   -   oil

o/A   -   at oil-air interface

rot   -   induced by disc rotation

tot   -   total

w   -   water

x,y,z -   in coordinate direction

air
in

discs

air
out

oil

water
out

water
in
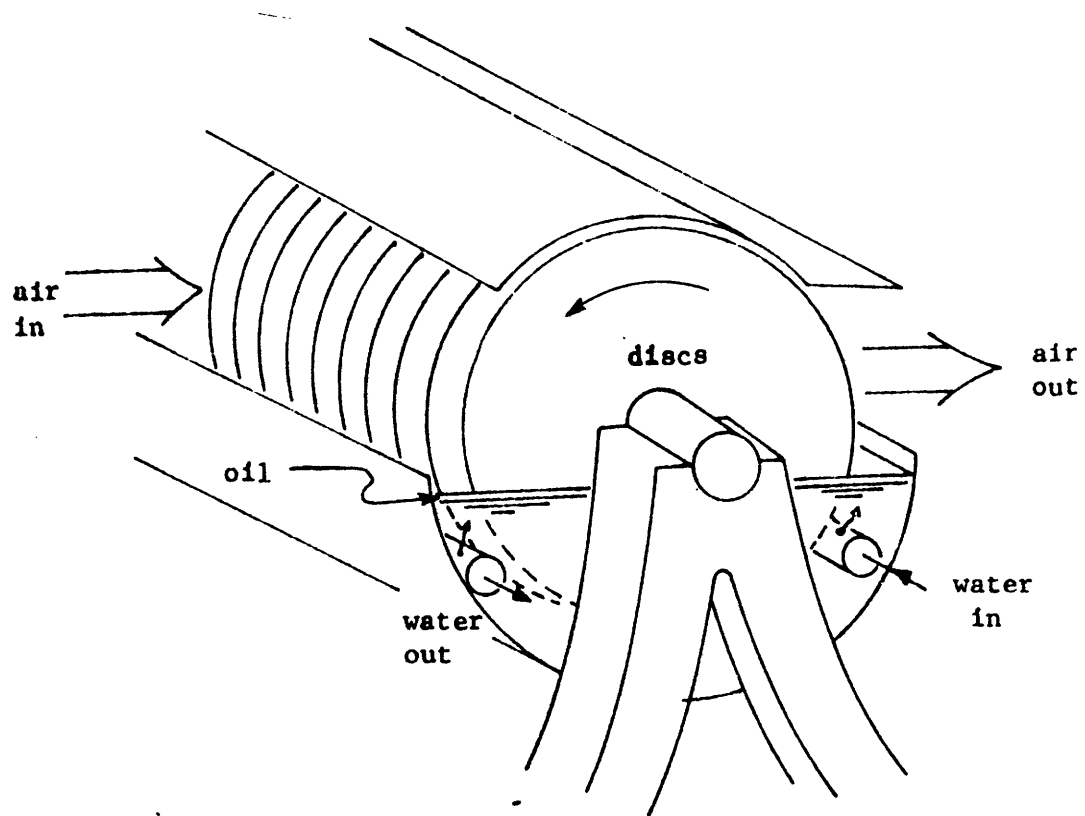
Conceptual design of periodic heat exchanger

Figure 1

I. <u>INTRODUCTION</u>

This report summarizes the results of the 4th year of investigation on the improvement of the environmental and economic characteristics of cooling towers.

Steam-turbine electric power plants operate with a thermal efficiency of about 40%. Thus, for every 4 units of energy generated as electricity, 6 units of energy have to be rejected as waste heat. In the past, this waste heat was rejected to the environment by circulating large quantities of water to cool the condenser. The water after cooling the condenser is simply discarded. This is the so-called once-through cooling system. An electric power plant with a once-through cooling system has to be located near a river or a lake where a large quantity of water is available.

There are occasions when an electric power plant has to be built in a location where the water supply is not abundant, or the protection of the ecology of water bodies such as rivers and lakes from thermal pollution prevents the use of the once-through cooling system. Evaporative cooling can sometimes provide a cheap alternative to once-through cooling. However, evaporative cooling also has its drawbacks. In evaporative cooling, the tower circulating water is heated up as it cools the condenser. This hot circulating water is heated up as it cools the condenser. This hot circulating water is cooled by splashing it down through a wet cooling tower. The water evaporated to the air in the process carries with it the waste heat to the atmosphere. The cooled water collected at the basin of the wet cooling tower is then circulated

back to cool the condenser again. Usually about 1.5% of the circulating

water in the wet cooling tower is lost to the atmosphere in the form

of water vapor, and drift adds another 0.2% loss [1]. Evaporative cool-

ing makes a significant improvement towards reducing the requirement of

water supply. However, for a large electric power plant, the consump-

tion of 1.7% of the circulating water is still a significant amount.*

Let us consider as an example of an electric power plant of, say 1000

megawatts. Assuming the most efficient heat transfer performance now in

practice, it requires 0.38 GPM of circulating water to generate 1 kilo-

watt of electricity [2]. For an electric power plant of 1000 megawatts,

the amount of water lost to the atmosphere in evaporative cooling can

be as much as 9.3 million gallons per day. In addition to the availability

of an adequate water supply, the possible impact on the environment of the

rejection of such a large quantity of water vapor to the atmosphere must

be considered. With cold ambient air and a high relative humidity, the

water vapor rejected by the wet cooling tower may form a fog plume. The

fog plume, besides being aesthetically unpleasing, may also impair the

visibility on highways and in airports.

A dry cooling tower can handle the waste heat rejection without any

one of the aforementioned problems. But unfortunately, in many circum-

stances the dry cooling tower costs three or four times more than a con-

ventional wet cooling tower [3]. This high cost of dry cooling is a di-

rect result of the relatively poor heat transport properties of air.

Rejecting a given heat rate to air rather than water requires more surface

---

*The rate of water loss is approximately equal to the water flow rate
  through the boiler.

area, and dry surface costs   more per unit area than wet fill does. To minimize the cost of a dry tower, one must find a surface with a low ratio of cost to performance and optimize the interaction of the cooling tower with the power plant. One surface which has such a low ratio is the periodic cooling tower developed during this program.

1.1. The Periodic Concept

The periodic cooling tower (PCT) consists of a number of properly

spaced steel discs which are mounted on a rotating shaft. The lower

half of the discs is immersed in a trough of hot water. On the upper

half of the discs, air is drawn through the spacings between the discs.

Therefore as the discs rotate, heat is transferred from the hot water

in the trough to the air by means of the periodic convective cooling

and heating of the steel discs on the air side and on the water side

respectively. The water after cooling the condenser is circulated through

the trough. Hot water enters the trough at an inlet and, after being

cooled by the rotating discs, it leaves the trough through an outlet. On

the top of the hot water in the trough floats a thin layer of oil. The

oil, by covering the water in the trough and by coating the rotating discs,

has the function of eliminating any water evaporation. The cooled water

leaving the trough is circulated to cool the condenser again. Figure

[1.1] shows a conceptual design of the periodic cooling tower.

The periodic cooling tower has the following advantages:

1. The cooling system of the periodic cooling tower is a closed

    system. It has a very low water consumption rate and hence it

    does not require a continuous supply of a large quantity of water.

2. The periodic cooling tower has no significant impact on

    the environment   because there is no rejection of hot water into

    the rivers or lakes.

3. The periodic cooling tower has the advantages of a dry cooling

    tower. But the cost of construction of a periodic cooling tower

    should be much cheaper than that of a conventional dry cooling

tower of finned-surface with the same heat transfer performance.

4. During the occasional summer peaks in ambient air temperature, when conventional dry towers loose much of their performance capability, the PCT has the potential of increasing its capacity by removing oil from some of the disc modules and operating those modules temporarily as wet towers.

1.2 Brief Summary of the First Three Years of Study

During the first year of study on the periodic tower, the initial assessment of the concept was made. A model with 12 inch discs rotating through heated, but stagnant, water was constructed and tested. Its performance was within 10% of theoretical predictions. A slow leak through the shaft support bearings prevented an accurate assessment of the model's ability to operate totally dry. However, ignoring the leak and assuming all water losses were due to evaporation, less than .4% of the heat load was borne by evaporation. This compares to a figure of about 80% for conventional wet towers.

The oil used for the separation of water and air in these tests was a parafinic hydrocarbon oil, but initial calculations based upon pro- jected operating temperatures, surface areas, and available information on vapor pressures indicated that hydrocarbons would have a significant depletion due to evaporation. It was therefore recommended that silicon oils be used to reduce evaporation losses of the oil.

An economic optimization was also performed on the periodic tower during the first year. Results indicated that with five foot diameter discs the periodic tower held a significant cost advantage over dry towers using conventional finned surfaces.

During the second year, work progressed on three fronts:

1. Scale model tests. A larger scale, 20" model was constructed. This model included a water circulation system to study circu- lation patterns in the disc trough and determine the most de- sirable locations of water input and drain ports in the trough.

Further, the 20 inch model was used to show that the churning effect of the discs on a layer of silicone oil was well within acceptable limits for the proposed 5 foot full sized disc.

2. Surface roughening. The greatest resistance to heat transfer is on the air side of the discs. A means of decreasing this resistance (and thereby increasing the disc performance) by roughening the surface with ribs was analytically examined. Using existing correlations for the surface roughening effect and a modification of the optimization program, a parametric study of characteristic rib dimensions was performed. Results indicated that under optimum conditions, the resistance to heat transfer is 20% less than that of a smooth plate.

3. Full scale test facility. Construction was begun on a test facility large enough to test a one foot module of the full sized 5 foot discs. The test facility required the design and construction of: a contraction cone to deliver air with a uniform velocity profile to the test section, a test section to contain the discs and both air and water systems, a fan to drive air through the test section, and a hot water supply system to simulate hot power plant effulent.

The third year of study was again centered in three main efforts:

1. Small scale testing. The 20 inch model was employed to make heat transfer tests, and further study on oil chruning caused by various disc designs.

2. Full scale testing. The full scale test facility was completed and fully instrumented. A module of 5 foot discs was constructed

and tests run on it to determine the thickness of the oil layer
on the discs.

3. Disc performance enhancement by surface roughening with ribs.
   Previous correlations on heat transfer augmentation by use
   of ribs are based upon high Reynolds' number flows and square
   rib profiles. Under actual operating conditions, the rib shape
   will be altered by the presence of an oil film, and will ex-
   perience lower Reynolds' number flows. A test facility has been
   built and calibrated to evaluate the effect of rib shape in
   Reynolds' numbers representative of the periodic tower.

For more details regarding the first three years of study, see
references 4, 5 and 6.

1.3 Areas of study covered in the Fourth Year

This report covers the fourth year of the PCT study. The main effort of the program was in three main areas, with minor efforts in three additional areas:

1. Large Scale Testing and Computer Simulation. An initial matrix, fabricated during the third year was experimentally evaluated in the full scale test facility. Its performance was parametrically evaluated both with and without the floating oil layer. Its dry performance was mathematically simulated, and the model was compared to experimental results.

2. The Oil System. A study was undertaken to understand and evaluate the interaction between the floating oil layer and the other systems (disc, air stream and water stream). The study was both experimental and analytical in nature.

3. Disc Performance Enhancement by Surface Roughening with Ribs. The test facility constructed and calibrated during the third year was used to parametrically evaluate the effect of surface rougheners on the film coefficient and flow resistance as a function of the Reynolds' number, rib height, rib spacing, rib shape and flow attack angle. The results are presented in the form of a generalized correlation.

The generalized correlation has been used in conjunction with the optimized design program (7,8) to evaluate the economic advantages of surface roughening.

4. Improvement of Rotor Performance by cross coupling rotor Systems. The PCT simulation model developed in effort 1 above was employed to analytically evaluate the potential benefits of coupling rotor systems in series/parallel combinations.

5. Oil fouling of the condensor. With oil floating on the circulating water, there exists a possibility of oil entering the condensor. Initial tests were made to evaluate the impact of oil in the condensor tubes on the condensor performance.

6. Preliminary evaluation of a new matrix. A new, full scale annular matrix, fabricated by C-E Air Preheater, was put through preliminary tests in the full scale facility. This matrix was constructed quickly, with the specific intent of testing a fabrication technique of generating an annular matrix from rectangular sheet steel. Complete testing was not done because of problems with the matrix, but sufficient full scale and small scale testing was done to verify that the problems were not with the annular concept, but with some specific fabrication techniques employed.

The following sections describe in detail the investigations of this last year.

2. Solid Discs: Full Scale Testing and Computer Modeling

Parametric performance testing of the first, full scale, prototype matrix has been completed. Further, in order to facilitate future parametric testing and evaluation, a mathematical model of the periodic tower has been developed. The experimental results, the model development and a comparison between the experimental results and the model are included in the following subsections.

2.1 Modes of Operation

Three distinct modes of operation have been identified for the periodic cooling tower (PCT): the dry, the starved and the wet modes. These differ in the quanties of oil used, and the fraction of heat load borne by evaporation.

In the dry mode of operation, a relatively thick oil layer is floated on the water. The thick layer prevents the oil layer from being depleted on the side where the discs rotate into the water. This depletion is due to two contributing factors. First, the water level is below the center of the discs. This causes the rotating discs to exert a horizontal drag on the oil layer proportional to the horizontal component of the disc rotational velocity. Second, when the disc is under the water the oil layer is several times thicker than when the disc is in the air. As the disc leaves the water and enters the air, the excess oil drains from the disc and is left on the water. Thus there is a net transport of oil from the interface where the disc enters the water to the interface where the disc leaves the water.

The difference in oil level between the two sides drives the oil back to the depleted side and is balanced by the drag and thickness factors moving oil to the other side.

If the oil layer floating on the water is thick enough, the low side will always have enough oil to cover it and prevent water evaporation from that surface. Typically, operation in the dry mode for the full-sized solid disc matrix with a one inch spacing between plates required about 1 gallon of oil per disc.

In the dry mode of operation there is no water evaporation at all. The previous two studies (4,6) dealt with this dry mode. Even with the water completely covered with a layer of oil evaporation can occur if water beads on the surface of the discs. Water beading occurs when water penetrates the floating oil layer and forms water drops which cling to the air side of the disc surface. This beading mechanism is discussed in more detail in Section 3.

The oil layer thickness and hence amount of oil can be reduced and the cooling tower can still operate in the dry mode by pumping oil from one side of the discs to the other. This was not done on the full scale model of the periodic cooling tower. In an actual tower, there will have to be some pumping of oil to filter out the dirt which accumulates in the oil. An alternative procedure would be to periodically drain and filter the oil.

If the oil layer thickness is reduced and no oil pumping is employed, one side of the trough will be pumped free of oil and only a thin mono-layer of oil will cover it. This is the 'starved' mode of operation, since one side is starved of oil to cover the water surface. In the starved condition, evaporation can occur from the free water surface. The amount of water evaporation can be varied by increasing or decreasing the quantity of oil. This varies the amount of water surface covered by an oil layer. As in the dry mode, additional water evaporation can occur if there is water beading on the discs. From a performance point of view, since the P.C.T. is supposed to replace dry towers, it is desirable to have the smallest amount of evaporation at the lowest cost. The optimum case probably occurs when there is sufficient oil to prevent

the formation of water beads on the disc surface. If there is no bead-ing, the only evaporation is through the monolayer of oil on the de-pleted side of the water surface. The runs made in the starved mode had no evidence of water beading with about a third of the oil required for dry operation. Evaporation accounted for about 8% of the total heat transfer in the starved mode.

To handle high ambient air temperatures, which degrade dry cooling tower performance, the P.C.T. has the option of operating in a wet mode. The wet mode has no oil layer floating on the water surface, thus allowing a large amount of evaporation. In the wet mode, not only is there evaporation from the water surface, but there is also evaporation from the disc surface, since the disc carries water up into the air stream. Water on the disc is usually in the form of beads, since there is still a thin oil layer on the disc, preventing the water from wetting the disc surface. In due time, the oil layer adhering to the disc sur-face will wash off and the water will then cover the disc surface in a film. The water evaporation will then be much larger than with a beaded water disc surface.

A complete description of the dry and starved modes, water beading, oil pumping and oil film thickness is made in Section 3.

2.2 FULL SCALE EXPERIMENTAL APPARATUS

The layout of the full scale model is shown in Figure 2.2.1. The schematic of the water flow system is shown in Figure 2.2.2. There are eight 5-foot diameter discs spaced one inch apart in the test section. Each disc has a dish shape which makes the disc more rigid, so that it is able to support itself on the rotating shaft. The disc is horizontally displaced three inches in the center as shown in Figure 2.2.3. Small notches are placed on the edge of the disc to relieve the stress and prevent disc buckling. For more information on the shape, see reference (6).

The disc temperatures were measured by eight thermocouples located on disc number four in the test section. They were spaced evenly over a 90° angle of the disc and space three inches apart on different radii, starting from 1-1/2 inches from the rim (see Figure 2.2.4). The thermocouples were made of .005 inch copper-constantan wire, which had a response time of .04 seconds. The thermocouples were connected to a switch and read out on slip rings. The output from the slip rings was put into an operational amplifier circuit which amplified the signal about ten times. This was then fed to a Hewlett-Packard chart recorder which measured the temperature profile vs. time of each thermocouple. The thermocouples were calibrated by heating up the water in the tank, until the water was a constant temperature across the trough. The temperature of the water was determined by thermometers placed at the inlet and outlet of the water trough.

The outlet air temperature profile was determined by using a thermocouple grid across the exit. The thermocouple grid is composed of six
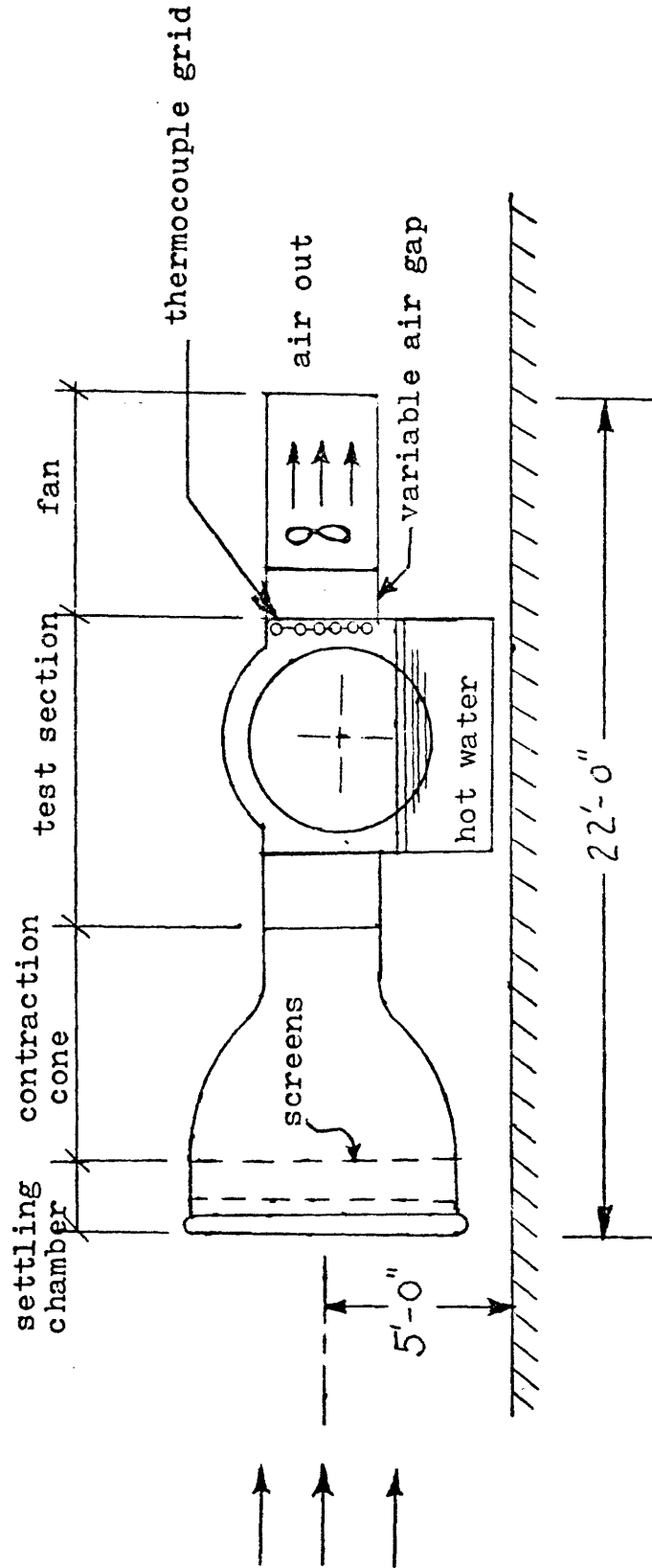
FULL SCALE MODEL OF THE PERIODIC COOLING TOWER

FIGURE 2.2.1
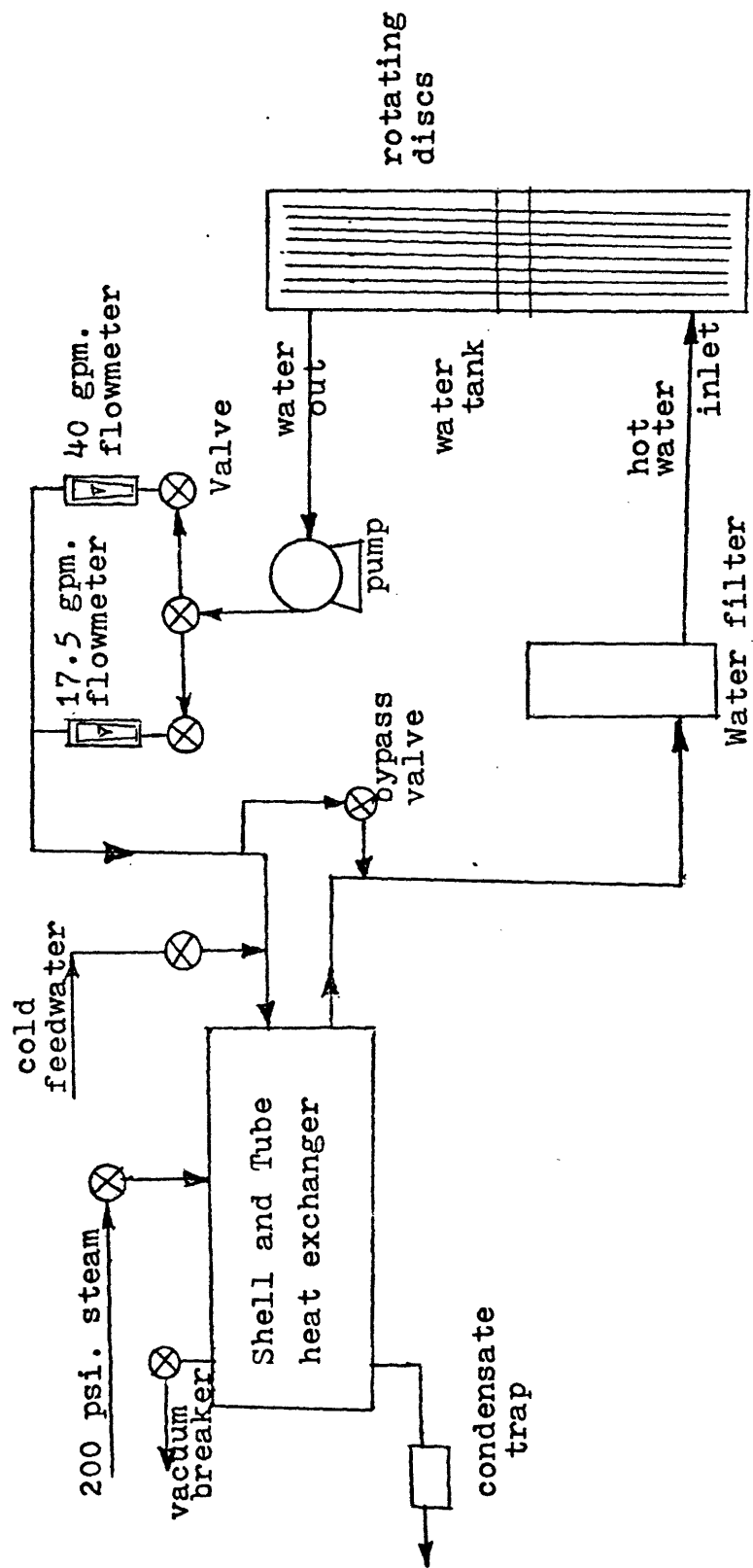
WATER FLOW DIAGRAM

FIGURE 2.2.2
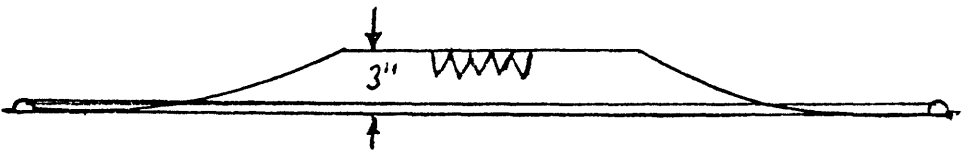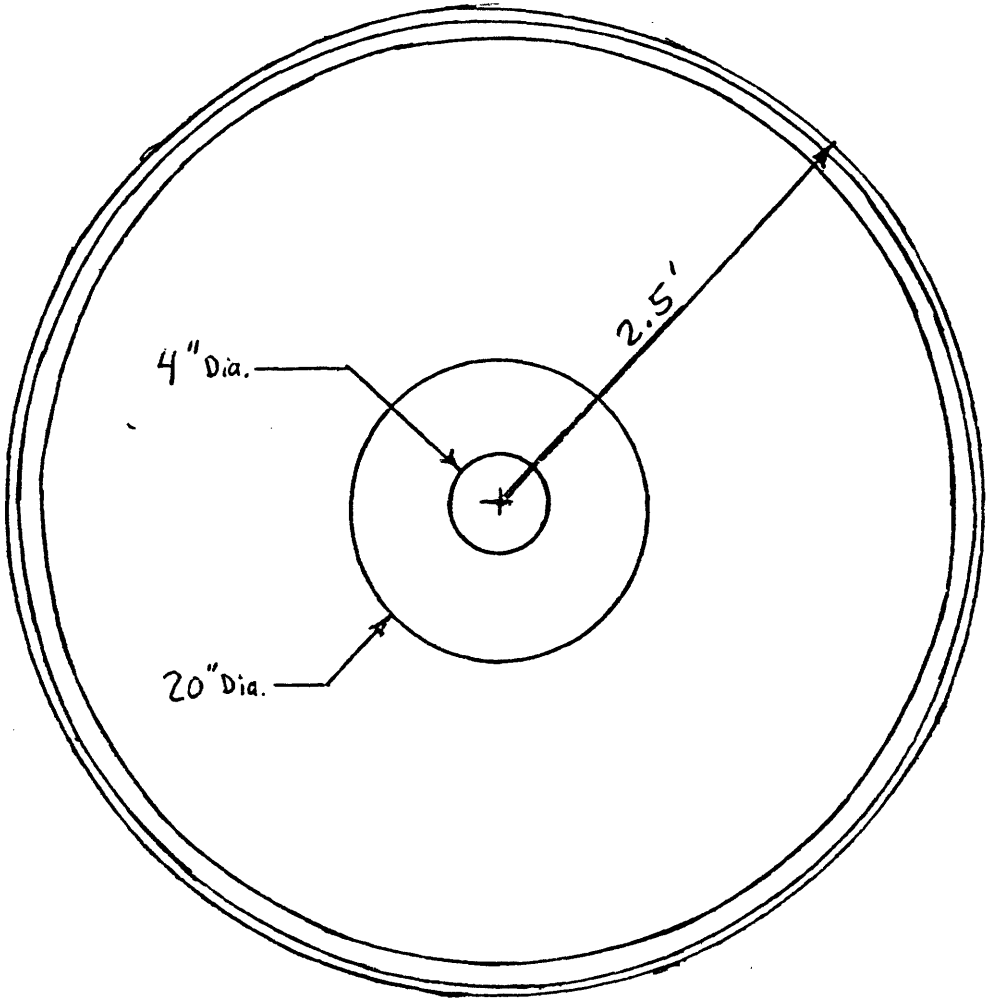
SHAPE of the DISHED DISC

Figure 2.2.3
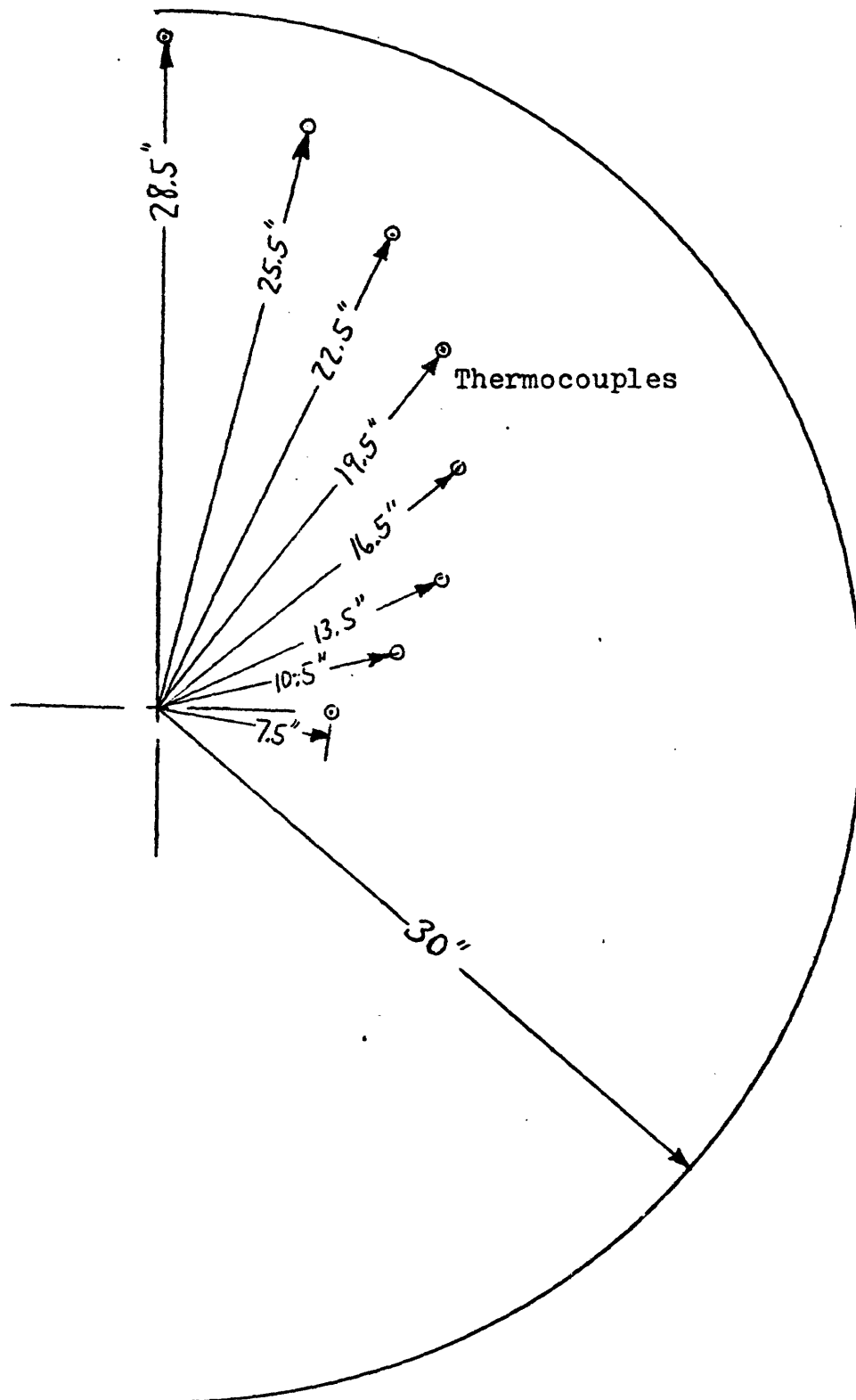
THERMOCOUPLES ON THE DISC

FIGURE 2.2.4

rakes with five thermocouples on each rake for a total of thirty thermo-couples (see Figure 2.2.5). The thermocouples on the rakes were read using a digital voltmeter or a potentiometer.

The evaporation rates were measured in two different ways. The first was the direct way: the entire system was made leak-proof and water-tight, so no water was lost other than through evaporation. Over a sufficient period of time, the water level drop in the tank was measured and from that the latent heat transfer was calculated. A typical starved mode heat transfer test lasted from two to three hours, during which the water level dropped less than one centimeter. For the wet mode tests the amount of time was much less, since much more water was lost and could be detected in a shorter time. A typical wet test lasted one to two hours with the water level dropping two to three centi-meters. If the latent heat transfer was significant, such as in the wet mode, this method of directly measuring evaporative losses was sufficiently accurate. When evaporative losses were small, as in the starved mode, the process took an excessively long time, and was less accu-rate because of the small changes in water level.

The second method involved using an EG&G Model 880 thermoelectric dew point hygrometer to measure the dew point of the air. The dew point of the incoming air as well as the dew point at each of the thirty thermocouple points on the exhaust side were measured. The majority of evaporation was occuring from this oil depleted free water surface of the trough and resulted in nonuniform moisture profile at the exhaust. It was this nonuniform profile which necessitated the extensive sampling of the exhaust side.
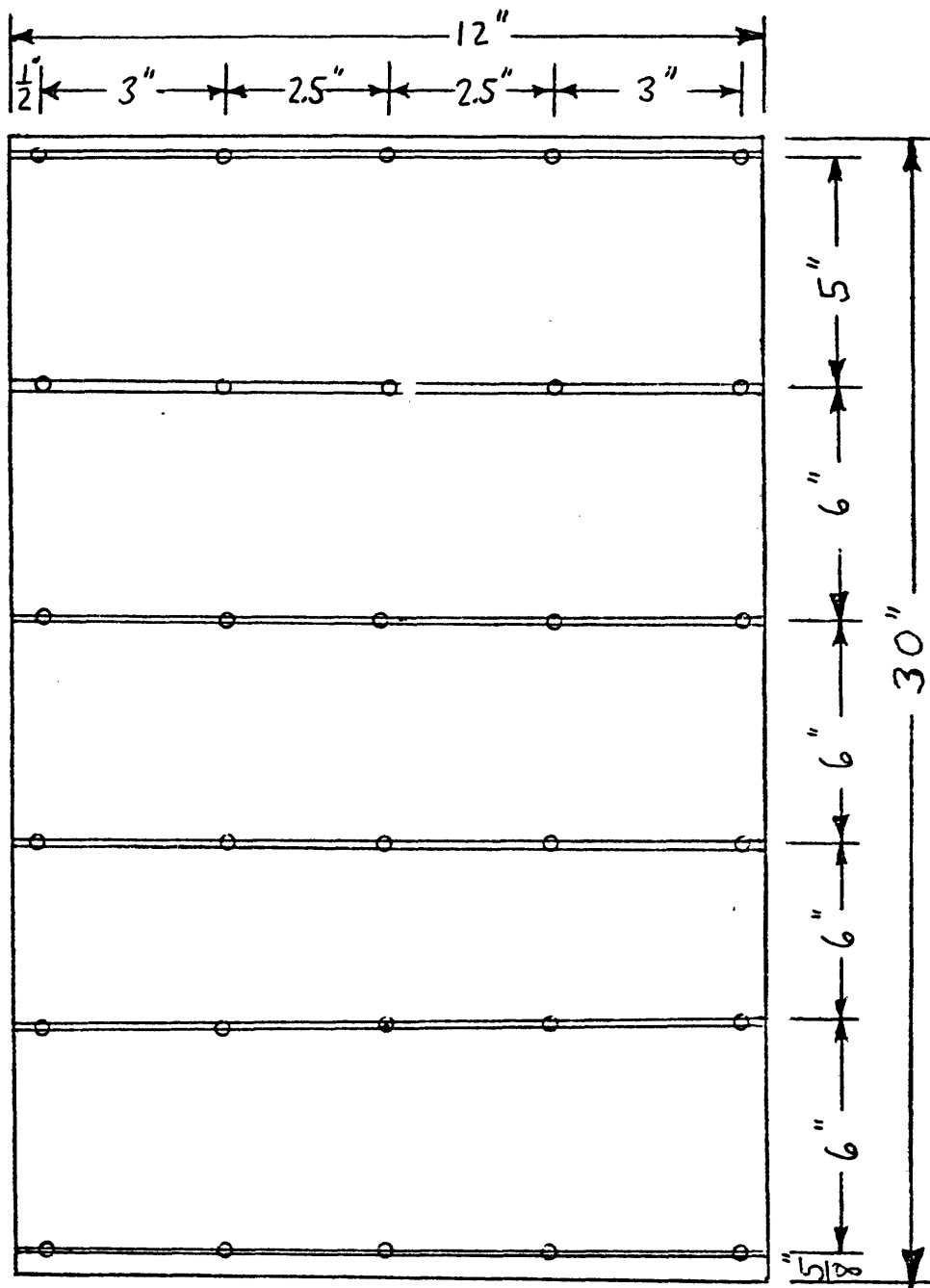
AIR OUTLET THERMOCOUPLE GRID

FIGURE   2.2.5

From the dew point, the moisture gained by the air in passing through the P.C.T. can be determined from the psychrometric charts. The evaporation rate and hence the latent heat transfer can then be determined.

The inlet air velocity through the contraction cone was measured by a calibrated inclined manometer accurate to ±.001 inches of water. The exit air velocity pattern was very non-uniform due to the spacing and shape of the discs. A typical exit velocity profile is shown in Figure 2.2.6. The outlet velocity at each point of the thermocouple grid was taken for a certain inlet velocity. The ratio between local velocities as obtained was then assumed to be applicable to other runs, as long as the inlet air velocities were close to the value of the inlet velocity for which the grid was obtained. Two such outlet grids were obtained. One covered runs with inlet velocities from 10 ft/sec to 13 ft/sec, and the other from 13 ft/sec to 15 ft/sec. The flow pattern was then used to determine the average exit air temperature and average dew point. This was then used in the heat balance. The exit velocities at each point were measured using the inclined manometer and a pitot tube.

To measure the water side temperature profile of the trough, when the discs were running, three thermocouple probes were built. They consisted of hollow metal tubes through which were run thermocouples. They were then sealed to prevent water from coming into the tube and the electrical contacts were also checked to insure that there was no short circuiting or interference with the signal. These thermocouples were then read out with either a digital voltmeter or a potentiometer.

The water inlet and outlet temperatures are measured by using the

5.1	7.4	11.5	12.5	10.19
5.1	10.4	14.2	14.2	14.6
13.3	14.4	16.2	15.1	14.4
14.2	14.9	15.1	14.6	16.2
12.7	12.2	12.5	14.2	15.7
8.7	11.8	12.2	12.9	12.5

in feet per second

↑ top
← front
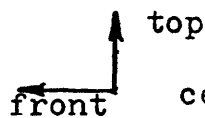
for $V_{A_1} = 11.2 \frac{ft}{sec}$.
center of discs
pushed out towards front

TYPICAL AIR EXIT VELOCITY PROFILE

Figure 2.2.6

thermometers placed in the inlet and outlet plumbing to the trough. The

water flow rate was measured by either of the two rotometers, depending

on the water flow rate of the test.

2.3 EXPERIMENTAL PROCEDURE

To run a heat transfer test, the water temperature was first brought up to about the operating temperature. The fan was then turned on and the discs were started rotating at the desired velocities. The steam valve and the water flow rates are then set. The system is then run until steady state is nearly achieved. Steady state was difficult to achieve because of changing air inlet temperatures. It usually takes an hour to two hours to achieve a condition where the water inlet and outlet temperatures do not vary by more than 0.1°C every 15 minutes. This was defined as steady state. Once steady state was achieved, the disc temperatures, air exit temperature, air exit dew points, and water side temperature profile were measured. Air (inlet) and water (inlet and outlet) temperatures were measured several times during a run to obtain an average value.

This data was taken to determine the heat transfered between the water and air streams, and to perform a heat balance for each test. The heat lost by the water should be gained by the air stream. If there is a disagreement in the heat balance larger than the experimental un- certainty, the heat transfer test results were not used. The experi- mental uncertainty is discussed in a later section.

The water side heat transfer is straightforward. The product of the temperature drop and the water heat capacity flow rate gives the total heat transfer. The air side is more complex. The inlet air velo- city is taken with the inclined manometer. The inlet air velocity is varied by adjusting the variable air gap shown in Figure 2.2.1. There was some air leakage in the system which was not significant, so that

the mass flow of air coming in was equal to the mass flow going out.
The inlet air temperatures and dew points are easily measured, because
of the uniform velocity at the entrance. The air exit, however, is
non-uniform. To get an average value for the exit dew point and temper-
ature, temperature, velocity and humidity measurements were made at 30
locations across the exhaust duct. These locally measured values for
temperature and humidity were weighted by the local mass flows to deter-
mine an average exhaust temperature and humidity.

At each point of this matrix, the percent of area that the location
on the grid represents and the air velocity are multiplied together to
form the thirty-element matrix. To get the average temperature, for
example, the temperature measured at each point on the grid is multiplied
by the volume flow rate of the corresponding matrix element. These are
all summed up and then divided by the total exhaust volume flow, yielding
the average temperature. The same is done for the dew point. This pro-
cedure associates a certain mass flow rate with each grid point, and can
be expressed mathematically as:

$$T_{avg} = \frac{\sum\limits_{i=1}^{30} M_i T_i}{\sum\limits_{i=1}^{30} M_i} \tag{31}$$

where $M_i = A_i V_i$;

A_i = area of each point;

V_i = air velocity at each point.

When the inlet air velocity is very low ($V \lesssim 7$ ft/sec), the boundary layer at the wall is large and covers the 18 outer thermocouples close to the wall. In this case, the regular average of the twelve inner temperatures are taken.

It was found later that an average of twelve dew points on the grid could be taken which would give the same results as the thirty-element matrix method would. It gave the same average outlet dew point and saved a great deal of time in the measurements. Once the average exit temperature and dew point temperature are known, the energy gain of the air stream can be calculated and compared to the energy loss of the water stream.

The overall dry effectiveness, which is used to compare the analytical results to the experimental results in the starved mode, is obtained as follows. Only the experimental sensible heat transfer for the air is used. The dry bulb temperature rise of the air is divided by the temperature difference between the air inlet temperature and the water inlet temperature. The expression for the dry effectiveness is shown below.

$$\epsilon_{dry} = \frac{T_{a2} - T_{a1}}{T_{h1} - T_{a1}} \qquad (32)$$

In one test, the water heat capacity was smaller than the air heat capacity.

In that case, the equation below was used.

$$\varepsilon_{dry} = \frac{C_a (T_{a2} - T_{a1})}{C_w (T_{h1} - T_{a1})} \quad . \tag{33}$$

2.4 Experimental Results

Tests were run on the full scale model of the periodic cooling tower at different air and water flow rates, different disc rotational velocities and different water nozzle inlet positions. Two different oils were used in the tests.

The first oil, Rubrex 100 made by Mobil Oil, was used before in the smaller model tests. This oil was used for the dry mode tests and some of the starved mode tests. In the starved mode, the discs were able to be run up to 4 r.p.m., without water breaking through the oil layer and beading on the disc surface. The one problem with this oil was that if the discs were left motionless in the water for several hours, the oil would come off the discs and permit the water to wet the discs. This caused oxidation of the zinc coating steel discs.

Another oil with better wetting properties was found. This oil, specially blended by Texaco and designated TL-10150, could only let the discs run at 2 r.p.m. without water beading. It did not let the water wet the discs when the discs were left still in the water. The properties and performance of these oils are more fully discussed in Section 3.

2.4.1 Dry Mode Results

The P.C.T. was run in the dry mode under several different operation conditions. The results are shown in Table 2.4.1. For these operating conditions, one gallon of oil per disc was required and used to keep the P.C.T. in the dry mode. The oil used was Rubrex 100.

TABLE 2.4.1

DRY MODE RESULTS

Run	T_{w_1}	V_A	C_W	T_{A_1}	C_A	C_D	$\dfrac{Q_{tot}}{DISC}$	ω	ε_{exp}
1	130.3	10.5	82.5	86	27.2	90	2330	3.5	.26
2	130.5	11.4	82.5	85.5	29.9	93	2440	3.6	.25
3	127.4	12.75	82.5	83	33.4	93	2440	3.6	.224
4	134.9	10.1	82.5	83.5	26.5	77	2490	3.0	.25

T_{w_1} - hot inlet water, °F

T_{A_1} - inlet ambient air temperature, °F

V_A - inlet air velocity, ft/sec

C_W - heat capacity of water, BTU/min°F

C_A - heat capacity of air, BTU/min°F

C_D - heat capacity of the disc and oil, BTU/min°F

ω - disc rotational speed, revoluations per minute

ε_{exp} - experimentally measured effectiveness

$\dfrac{Q_{tot}}{disc}$ - total heat transfer per disc BTU/hr

2.4.2 Starved Mode Results

There were many more tests run in the starved mode than the dry mode, because it is a better operating condition for an actual operating cooling tower. The starved mode for a given operating condition has a better sensible heat transfer than the dry mode. This is because the water side overall heat transfer coefficient in the starved mode is roughly 2 1/2 times that of the dry mode, due to the much thicker oil layer in the dry mode. This difference can be seen when run 11 in Table 2.4.2 is compared to run 4 in Table 2.4.1. Approximately each case experienced the same operating conditions, but the dry effectiveness of run 11 is 12% higher than the effectiveness of run 4. The water side heat transfer coefficient has a relatively small effect, because the air side heat transfer coefficient is an order of magnitude lower than the water side coefficient. The air side is thus the major resistance to heat transfer in the P.C.T.

The operating conditions which were run in the starved mode were varied more than in the dry mode. The results are shown in Table 2.4.2. The amount of oil used was the same in all tests. There was roughtly 1/2 gallon used per disc. Rubrex 100 was used in runs 6, 11 and 12. Tl-10150 was used in the rest of the runs.

2.4.3 Wet Mode Results

Four tests were run in the wet mode and the results are shown in Table 2.4.3. The wet mode increases the heat transfer substantially as was expected. The tests were all run with a water beaded disc surface. None were run with the water film surface.

TABLE 2.4.2

STARVED MODE RESULTS

Run	T_{w_1}	C_W	T_{A_1}	C_A	V_A	C_D	ω	$\dfrac{Q_{tot}}{DISC}$	ε_{Dry}	$\dfrac{Q_{evap}}{DISC}$	$\dfrac{Q_{tot}-Q_{evap}}{DISC}$
1	136.2	33.16	73	19.0	7.3	49	2	2560	.26	180	2380
2	135.1	33.16	78	28.0	10.8	49	2	3100	.22	155	2945
3	134.8	33.16	84	38.6	14.9	49	2	3280	.24	262	3018
4	134.1	33.16	74	29.0	11.1	49	2	3150	.23	189	2961
5	134.2	33.16	75	28.9	11.1	49	2	3230	.23	162	3068
6	135.5	33.16	73	33.8	13.0	107.5	4	3890	.23	312	3578
7	134.6	49.5	89.5	37.9	14.6	49	2	3010	.21	241	2769
8	134.2	66.0	73	18.7	7.2	49	2	2940	.31	147	2793
9	134.2	66.0	88.3	37.9	14.6	49	2	3120	.23	125	2995
10	132.5	82.5	72.6	18.7	7.2	49	2	2890	.31	116	2774
11	131.5	82.5	83	26.0	10.0	77.3	2	2910	.29	146	2764
12	130.5	82.5	80.5	26.0	10.0	107.5	4	2910	.28	146	2764
13	132.0	99.5	83	18.4	7.1	49	2	2610	.34	209	2401
14	130.2	99.5	84.3	38.5	14.8	49	2	3530	.24	282	3248
15	132.0	115.5	74	28.3	10.9	49	2	3590	.26	251	3339

ε_{DRY} = Dry effectiveness, i.e. without evaporation heat transfer = $\dfrac{T_{c2}-T_{cl}}{T_{hl}-T_{cl}}$

$\dfrac{Q_{evap}}{DISC}$ = Measured latent heat transfer per disc, BTU/hr

Units: T: °F
        C: BTI/min°F
        V: ft/sec
        w: RPM
        Q: BTU/hr

TABLE 2.4.3

WET MODE RESULTS

Run	C_W	C_A	C_D	V_A	ω	$\dfrac{Q_{tot}}{DISC}$	T_{A_1}	RH%
1	82.5	26	82	10	4	8125	79	30
2	82.5	26	41	10	2	5650	79	70
3	82.5	26	82	10	4	6100	80	67
4	82.5	26	41	10	2	5100	77	67

C_W, C_A, C_D - the heat capacity of the air, water and discs with oil, respectively, BTU/min°F

$\dfrac{Q_{tot}}{DISC}$ - Total heat transfer measured per disc, BTU/hr

T_{A_1} - Inlet air temperature, °F

RH% - percent relative humidity at the inlet

V_A - inlet velocity of air, ft./sec.
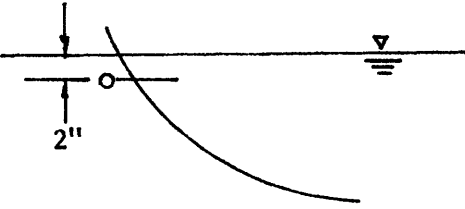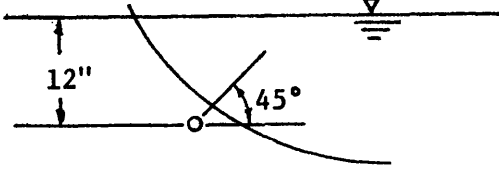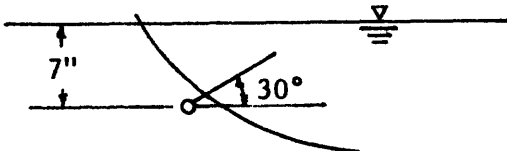
2.4.4 Water Side Configuration Results

In the starved mode, three tests were run at almost the same
air, water and disc heat capacity. Only the location of the inlet water
nozzle was varied. The temperature profile of the water tank was also
taken. Thw water nozzle had eight   1/4 inch holes spaced one inch apart.
Table 2.4.4 shows the position and angle at which the nozzle injected
water into the bank.

In these tests, the tip speed of the rotating discs was less than
the exit velocity of the water jets coming from the nozzle. Whenever
the exit velocity of the water jets became greater than 5 feet per
second, oil was blown off the discs by the water jet and filled the
water in the tank with little oil drops. In tests where the flow rate
was 6 gallons per minute or greater, nozzles with larger holes or two
nozzles were used to prevent oil from being blown off the discs.

The heat transfer data for these tests are in Table 2.4.2. The
positions and the results are shown in Table 2.4.4. Run 4 illustrates
the better positioning based upon the highest water side effectiveness
as determined by the disc thermocouple temperatures. Although the water
side effecitveness is increased 22%, the effect on the overall effectiveness
is within the experimental uncertainty of the data and hence is not
detected by that parameter. The approximate water tank temperature profiles
are shown in Figure 2.4.1. The water flow circulation profiles observed
visually are shown in Figures 2.4.2.

TABLE 2.4.4

EFFECT OF WATER INLET
POSITION

RUN	POSITION	ε_W

2	2"	.62
5	12" 45°	.54
4	7" 30°	.66

ε_W - measured effectiveness on the water side,

$$\varepsilon_W = \frac{T_{W1} - T_{W2}}{T_{W1} - T_{Dc}}$$

T_{W_1}, T_{W_2} - temperature of the inlet and outlet water respectively, °F

T_{Dc} - Measured area averaged lowest disc temperature , °F

The water circulation induced by the discs was measured very roughly by visual flow studies. It was found that the volume flow rate induced by the discs at 4 r.p.m. was around 25 gallons per minute. This means that the disc induced water circulation dominates the water flow circulation in the tank, unless very high water inlet flow rates are used.

2.4.5 Experimental Uncertainty

The maximum uncertainty for the water side heat transfer is 6.2%. The uncertainty for most of the runs is 5% for the water side heat transfer.

For the air side heat transfer, which includes both latent and sensible heat transfer, the maximum uncertainty was 9%. The rest of the runs had an air side uncertainty of 7.4%.

The heat balance between the air and water heat transfers had a maximum uncertainty of 10.8%. The heat balance in most of the tests had an uncertainty of around 8.9%.

The maximum uncertainty in the measurement of the effectiveness is 8.1%. For most cases the effectiveness uncertainty is 6.6%.

2.5 Computer Simulation of Rotor Performance

An accurate simulation of the periodic tower will allow easy assessment of modified designs and will allow the prediction of the overall performance of the cooling tower-power plant system.

The use of a simulation will permit the characterization of a new design with a limited number of experimental tests. The long time

RUN 2

125°F   123.5   123
2"   123
inlet
nozzle   122°F   outlet
                     122.5   123-
                              123.5

RUN 4

123.   122.5   122   122 °F
7"   123.5
         121.5°F
30°   121.5
inlet   outlet
                 121 °F

RUN 5

122 °F   120.5
12" 122.5   121
inlet 45°   120 °F   outlet
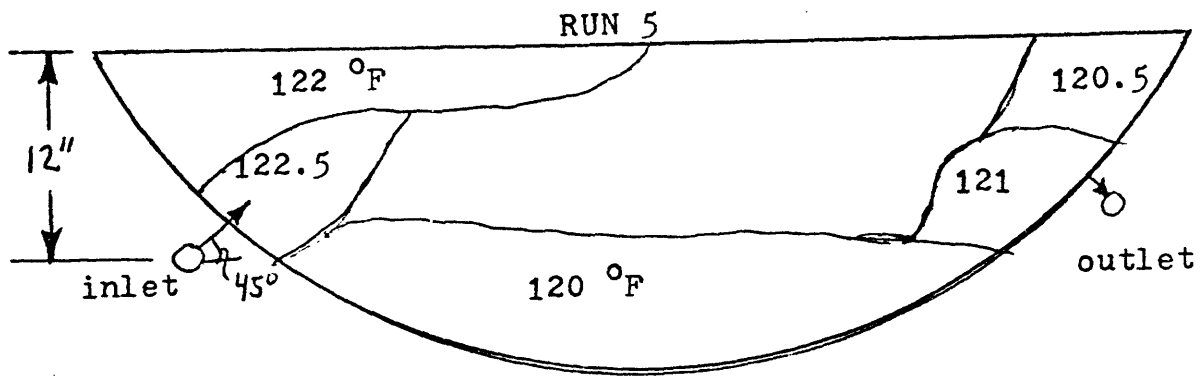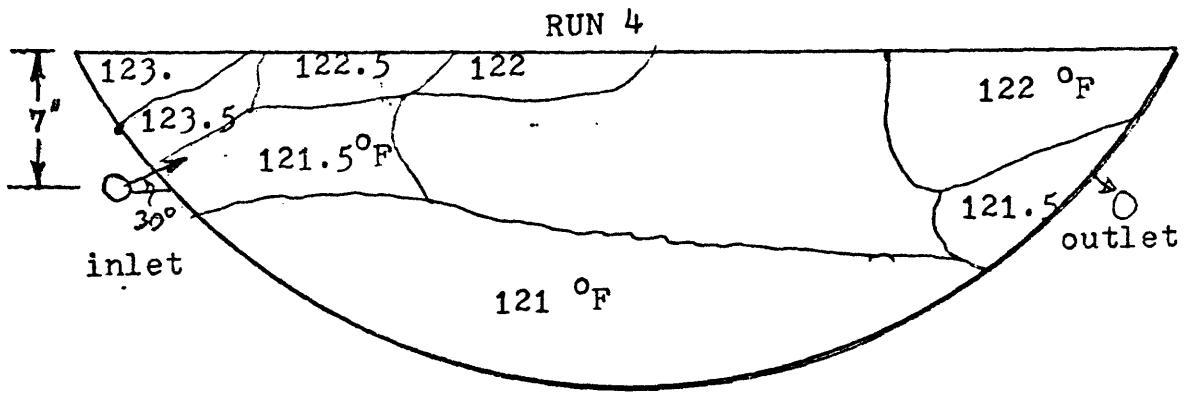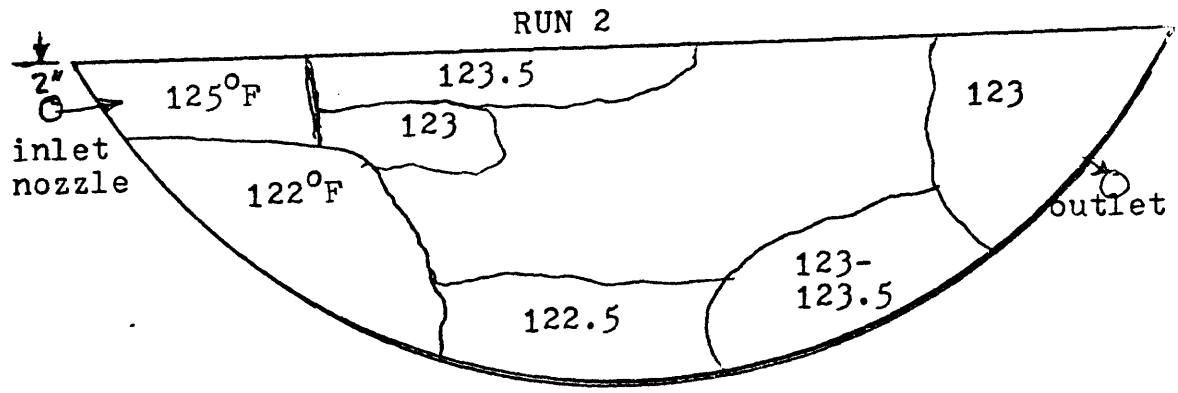
WATER TEMPERATURE PROFILE
Figure 2.4.1

RUN 2

inlet
water
nozzle

outlet
water
nozzle

RUN 5

7"

inlet
nozzle

30°

outlet
nozzle

RUN 4

12"

inlet
nozzle

45°

outlet
nozzle
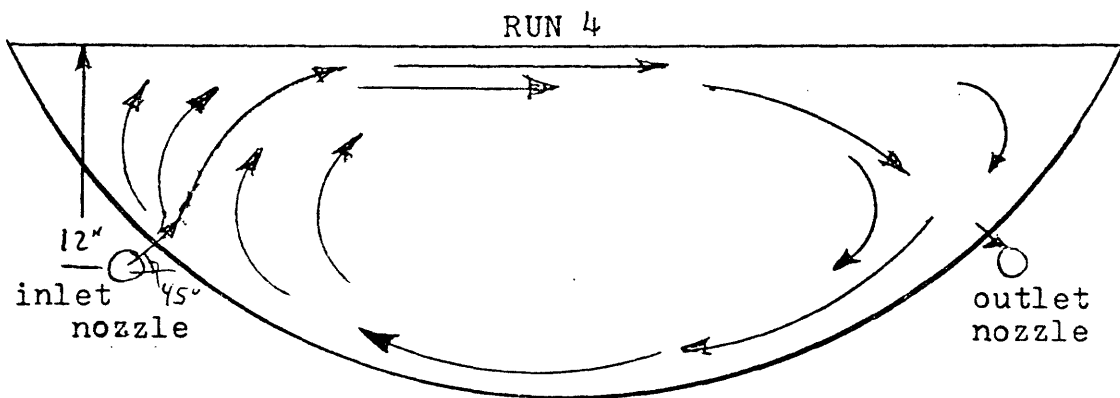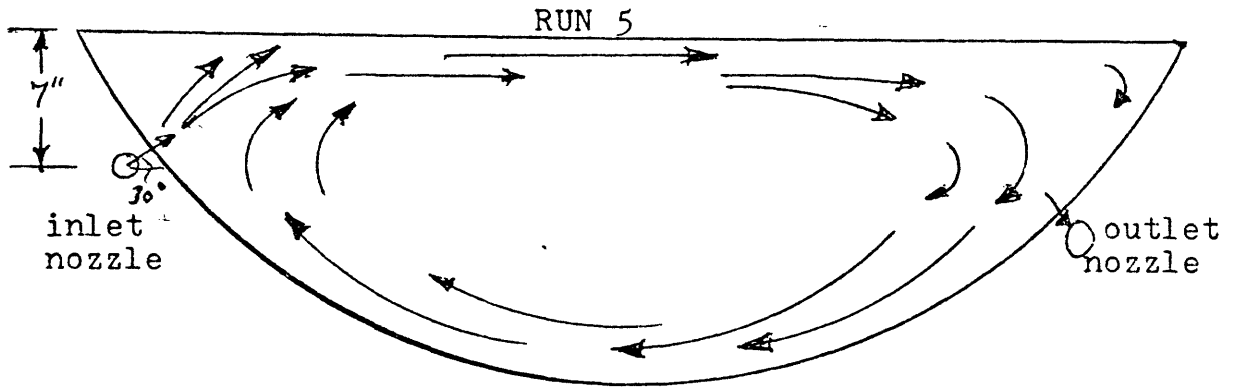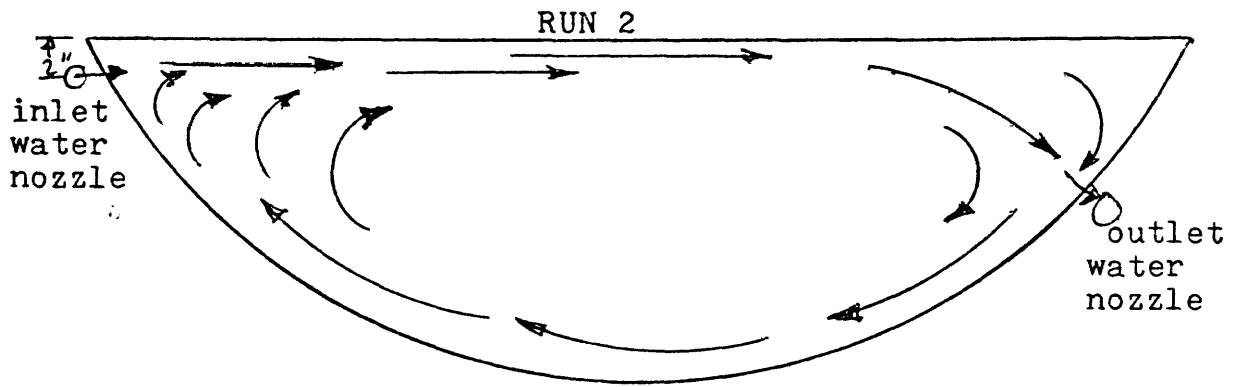
WATER FLOW CIRCULATION
(based on approximate visual observations)

Figure 2.4.2

required for a complete test to be run (set up, realization of steady
state, data taking and data reduction) for one set of flow conditions
makes complete parametric testing untenable. The following sections
describe the development of a model, its inherent assumptions, and a
comparison of the model with the experimental results.

2.5.1 Model Formulation

For modeling, the periodic cooling tower system is divided into
four subsystems, each modeled as a separate heat exchanger. The actual
disc system and the four subsystems are portrayed in Figure 2.5.1. Note
that the central region of the disc (labeled 'inactive' in Figure 2.5.1),
is essentially an adiabatic region since it never becomes wetted by
the hot water.

The disc rotation induces flows within the water bath. By experimental
measurement, these individual flows are sufficiently great to mix almost
the entire bath to one temperature. The sole anomaly is a small region
of slightly higher temperature in the vicinity of the water inlet port.
Consequently, the water side is modeled as two 'well mixed' regions. The
air side is modeled as two cross flow heat exchangers. The subsections
are connected as illustrated in Figure 2.5.1b.

2.5.2 Model Assumptions

2.5.2.1 Heat Capacities

Disc: The oil being carried by the metal disc heats and cools
as it passes between fluid streams. Consequently, part of the heat load
of the disc system is borne by the oil on the disc. It is therefore
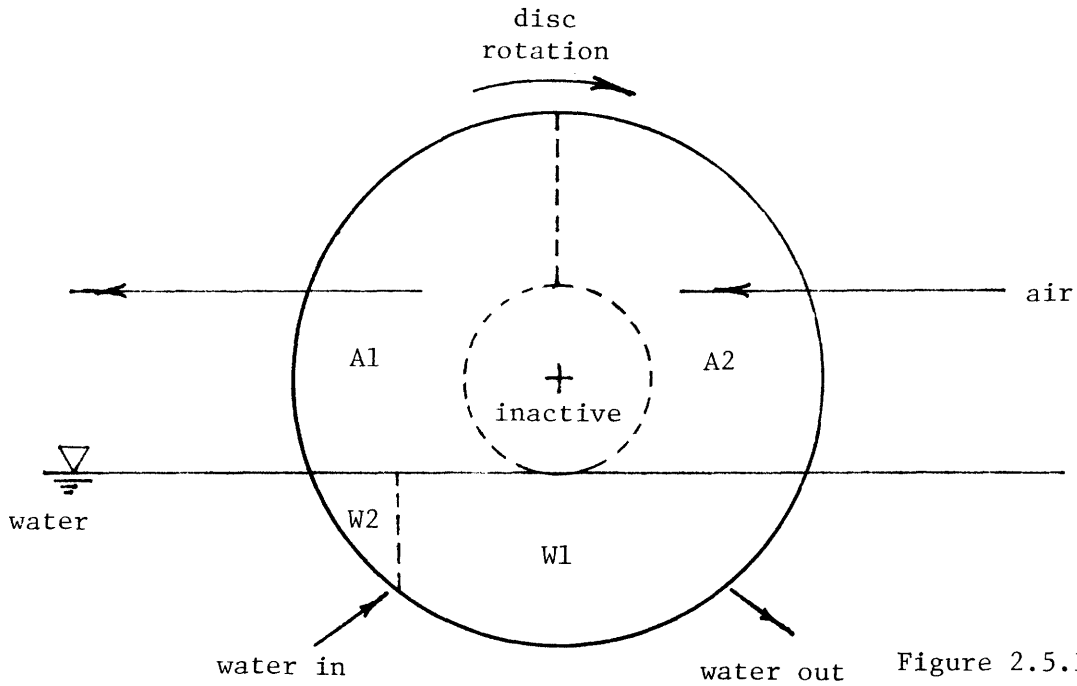
Figure 2.5.1a
ACTUAL DISC
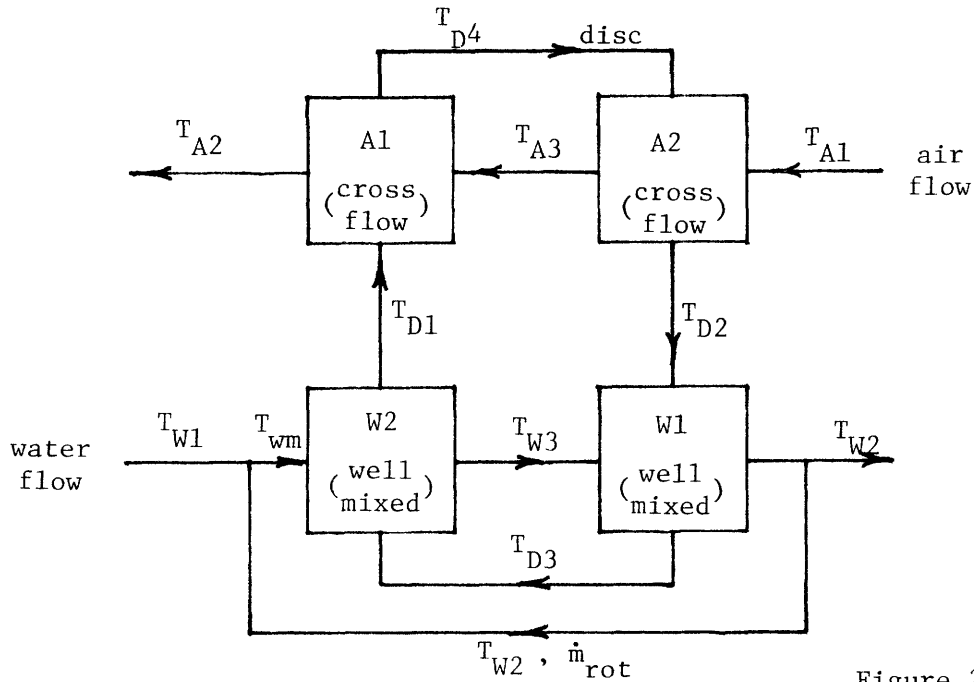
Figure 2.5.1b

DISC MODELED
AS FOUR HEAT
EXCHANGERS

DISC MODELING

Figure 2.5.1b

assumed that the total heat capacity of the metal disc/oil system is the sum of the heat capacity of the metal and the oil deposited on the metal. Or,

$$C_{disc} = C_{metal} + C_{oil}$$

C_{metal} is determined using the thermophysical properties of the disc, geometry and rotational speed. These considerations yield:

$$C_{metal} = \pi \, \omega \, c_{P_D} \, \rho_D \, \delta_D \, (R_o^2 - R_w^2) \quad (BTU/min\,°F)$$

C_{oil} is approximated by evaluating the oil thickness at $[R = (R_w + R_o)/2]$ using Levich's relation modified by Fink's experimental results [6]. It is then assumed that this calculated oil thickness is representative of the oil which is always on the disc. Using this effective oil thickness, the heat capacity of the oil can be expressed as:

$$C_{oil} = 2\pi \, \omega \, C_{P_o} \, \rho_o \, \delta_o (R_o^2 - R_w^2) \quad (BTU/min\,°F)$$

The form of this relation is identical to that of the disc -- the coefficient has been increased   by 2   as there are two oil films per disc (one per disc side).

Fluids: Air heat capacity is directly calculated from air thermal physical properties, the typical frontal area, and the air velocity.

$$C_{air} = C_{P_A} \, \rho_A \, V_A \, A_f = C_{P_A} \, \rho_A \, V_A S(R_o + R_w) \quad (BTU/sec\,°F)$$

The heat capacity of the water entering the trough is simply expressed as:

$$C_{water} = C_{P_w} \dot{M}_{w_{in}}$$

Since the analysis is based upon one disc, $\dot{M}_{w_{in}}$ is the mass flow per disc.

2.5.2.2 Disc Induced Flows

As noted in Section 2.5.1 on model formulation, flows in the trough are induced by the disc rotation. In Figure 2.5.2 are drawn streamlines indicating the approximate flow conditions. These compare favorably with actual streamlines observed in prior dry studies (5). Experimental observations described in Section 2.4.4 report the presence of a region of higher temperature in the vicinity of the inlet water port. The magnitude of this hot temperature is a function of the inlet stream flow rate and temperature, the temperature of the recirculating water, and the mass of recirculating water (the number of recirculation streamlines the inlet water crosses). Considering only shear forces in the horizontal direction, an analysis (Appendix 2A) yields the induced flow as a function of ω, R_o and R_w. The induced flow decreases with increasing horizontal distance from the disc centerline. For the purposes of quantifying a representative induced flow with which the inlet flow mixes, it is assumed that the inlet flow mixes with that portion of the induced flow which passes the horizontal location of the inlet port (see Figure 2.5.2).

disc
rotation

water
inlet

streamlines of induced flow
assumed to mix with inlet flow
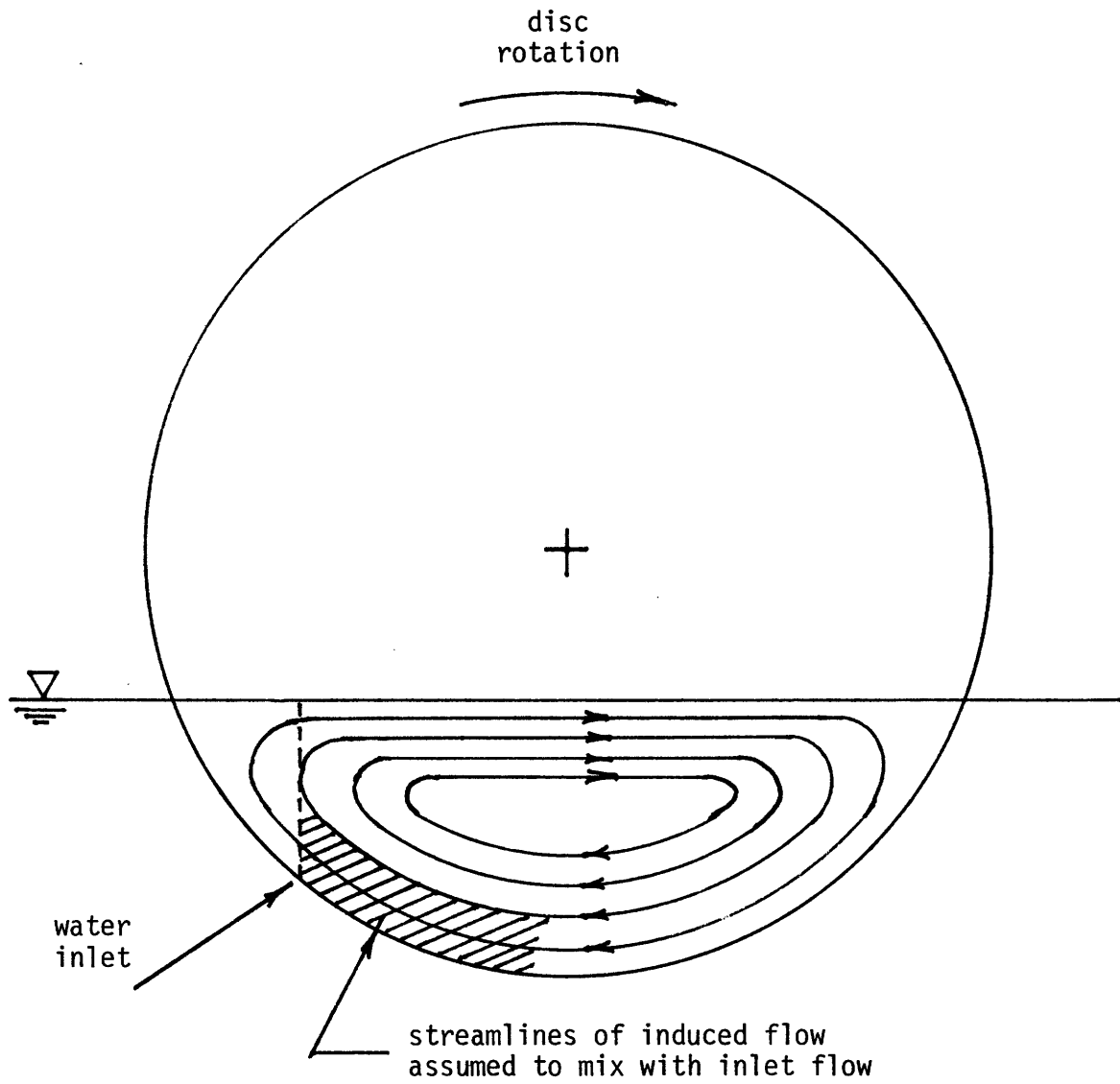
DISC INDUCED FLOW
Figure 2.5.2

The area of the 'hot zone' is assumed to be equal to the water

wetted area to the left of the inlet port in Figure 2.5.2. As formu-

lated by this model, as the inlet port moves farther from the axial

centerline (to the left in Figure 2.5.2), the hot region in the proxi-

mity of the inlet port increases in temperature (the inlet flow is diluted

less by the induced flow) but the area of influence decreases.

2.5.2.3 Film Coefficients

Air side film coefficients on the smooth disc are approximated using

relative disc and air velocities and the McAdams correlation.

However, the sub-heat exchanger exposed to the inlet air stream

is experiencing a developing boundary layer, and therefore has an average

film coefficient in excess of that predicted by the McAdams relation.

The average coefficient for this sub-heat exchanger is predicted by (9)

$$h_{avg} = h_{McAdams} \ (1.0 + 6 \ D_h/L).$$

On the water side, the complexity of the flow conditions precluded the

use of a generalized correlation to approximate the film coefficient.

Hence, a value of 60 $BTU/hr-F^2 \,^\circ F$ was used. This was a typical value as

back calculated by the experimental measurements.

2.5.2.4 Internal Temperature Gradients in the Disc/Oil System

While the disc is in the air stream, there is a negligible thermal

gradient across the thickness of the disc and oil system. This can be

seen by comparing typical values for the film coefficient between the

air and oil (h $\simeq$ 10), and the effective resistance across the oil layer

(k/1 $\simeq$ (.076)(12)/(.0118) $\simeq$ 77) and the disc (k/1 $\simeq$ (25)(12)/(.016) $\simeq$

18000). The resistance to heat transfer across the oiled disc is much

smaller than from the oil surface to the air: consequently, the
temperature of the oil surface varies insignificantly from the tempera-
ture at the center of the disc.

An approximate means of judging when internal temperature gradients
can be ignored is when the ratio of k/lh exceeds 6 [10].

When internal temperature gradients can be ignored, the analysis
of the system is simplified. The temperature of the body in air is
now an exponential decay with time and can be expressed as:

$$\frac{T_s - T_f}{T_o - T_f} = \exp\left[\frac{-ht}{\rho cV/_A}\right] \qquad (2.5.1)$$

Since, at a given time, the temperature across the system is uniform,
$\frac{\rho CV}{A}$ can be evaluated by 'lumping', or combining, disc and oil systems
together such that $\frac{\rho CV}{A} = \rho_D C_D \frac{\delta_D}{2} + \rho_o C_o \delta_o$

When the disc/oil system is heated by the water, with film co-
efficients of about 60 BTU/hr-ft^2-^{o}F, the ratio of k/lh is less than
6. Thermal gradients now exist across the oil in the disc/oil system,
and the simple 'lumped' analysis no longer applies. Rather than
laboriously solving the exact solution for the internal temperature
gradient (and hence the rate of heat transfer) an approximate solution
was used.

The exact solution for the disc/oil system is presented in graphi-
cal form in the Handbook of Heat Transfer [11]. Using these graphs,
and given the properties and dimensions of the disc, oil properties,
and the time of exposure, one can determine the temperature of both
the disc/oil interface and the oil/water interface.

Assuming a linear temperature profile across the oil film, and recognizing that the disc itself still has negligible thermal gradients across it, the average temperature of the disc/oil system can be defined by:

$$T_{avg} = \frac{C_{oil} \dfrac{T_{0/A} + T_D}{2} + C_{MET} T_D}{C_{oil} + C_{MET}} \qquad (2.5.2)$$

T_{avg} is the temperature the disc/oil system would achieve if allowed to equilibrate.

If it were possible to lump the disc/oil system in the water, this equilibrium temperature of the system could be expressed by using equation (2.5.1). The approximate solution employed was to use equation (2.5.1) in the form of:

$$\frac{T_w - T_{avg}}{T_w - T_o} = \exp[- \frac{htA}{\rho CV}] \qquad (2.5.3)$$

T_{avg} can be determined using the exact graphical solution (11) and equation (2.5.2). $\rho CV/_A$ of the system is determined from physical parameters.

Ignoring the heat capacity of the oil film, the resistance to heat transfer from the disc to the water includes the film coefficient between the oil and water plus the resistance across the oil film. The film coefficient would then be:

$$h = \frac{1}{\dfrac{1}{h_{o/_w}} + \dfrac{\delta_o}{k_o}}$$

However, since the oil does have a finite heat capacity and all of the heat does not have to be transferred to the disc, the effective film coefficient is somewhat higher. This can be approximated by assuming that the effective coefficient can be expressed as:

$$h_{eff} = \frac{1}{\dfrac{1}{h_{w/o}} + \dfrac{K\delta_0}{k_0}}$$

<div align="right">(2.5.4)</div>

where $h_{w/o}$ can be determined using McAdams relation.

A value of K can be determined such that T_{avg} evaluated by equations 2.5.3 and 2.5.4 is identical to T_{avg} evaluated by the exact graphical solution and equation 2.5.2. For the range of our operating parameters ($0.01" < \delta < 0.03"$, $5/3 \sec < t < 5 \sec$), K can be treated as a constant ($K \simeq .75$) with only a nominal effect on the accuracy of equation 2.5.4.

Essentially the approximate solution is achieved by forcing the lumped solution to follow the exact solution.

2.5.3 Formulations of Energy Equations and Heat Transfer Relations

The temperature of the disc/oil system, the air, and the water at various locations are defined in Figure 2.5.1. Of these temperatures, two are assumed known (the inlet air and water temperature), leaving nine unknown temperatures. Applying the conservation of energy to the system provides five equations; the remaining required for are supplied by heat transfer effectiveness equations applied to each sub-heat exchanger. These nine equations are developed in Appendix 2-B.

These energy balance and heat exchanger relations are dependent upon the heat capacities of the water, air, and disc (C_w, C_a, C_d); the flow induced in the trough by the rotating discs; and the effectiveness of each of the four sub-heat exchangers. The heat capacities and the induced flow have been quantified in section 2.5.2. As each air side heat exchanger is assumed to be a cross flow heat exchanger with both streams unmixed, their effectiveness can be expressed by the analytical approximation [12]:

$$\varepsilon = 1 - \exp\left\{[\exp(-Ntu^{.73} \frac{C_{min}}{C_{max}}) - 1] \frac{C_{max}}{C_{min}} Ntu^{.22}\right\}$$

On the water side, as mentioned in section 2.5.1, the heat exchanger is modeled as being 'well mixed'. The effectiveness of a well mixed heat exchanger is derived in Appendix 2C, and can be expressed as:

$$\varepsilon = K \frac{1 - e^{-Ntu}}{\frac{C_d}{C_w}(1 - e^{-Ntu})}$$

where

$$K = 1 \text{ if } C_d < C_w, \quad K = \frac{C_d}{C_w} \text{ if } C_d > C_w$$

Note that the effectiveness of each heat exchanger is a function of

Ntu, or the number of transfer units, where Ntu is defined by:

$$Ntu = \frac{U\ A}{C_{min}}$$

Here U is the film coefficient operating over the area of the heat

exchanger (A). Means of evaluating these values of U have been

described in section 2.5.2.3.

2.6 Comparison of Model to Experimental Results

The formulated equation, derived in Appendix 2.B were solved

simultaneously using matrix operations.

The input parameters were changed to represent the operating

conditions of the actual dry and starved mode tests performed on the

full scale test facility (presented in sections 2.4.1 and 2.4.2). As

the model is not intended to simulate the wet mode, it was not compared

to those experimental results. The experimental and model results are

compared in Tables 2.6.1 and 2.6.2.

As can be seen from tables 2.6.1, the model overpredicts the dry

mode experimental results by approximately 15%. As formulated, (see

section 2.4.2.1) the model assumes the oil thickness on the disc is

uniform and constant over the entire surface of the disc. This assumed

thickness is evaluated where the disc passes through the oil layer

and enters the air stream.

When operated in the dry mode, however, the disc in entering the

water also passes through another oil layer. This layer establishes

the thickness of oil on the disc while under the water. The mechanisms

TABLE 2.6.1

DRY MODE

Run	ε_{exp}	ε_M	$\Delta\varepsilon(\%)$	Q_{exp}	Q_M	$\Delta Q(\%)$
1	.26	.289	11.1	2330	2577	10.6
2	.25	.281	12.4	2440	2756	13.0
3	.224	.269	20	2440	2911	19.3
4	.25	.293	17.2	2490	2913	17.0

ε = effectiveness

Q = rate of heat rejected per disc   (BTU/Hr)

subscripts: exp: experimental results

M: predicted by model

$$\Delta X(\%) = \left(\frac{X_M - X_{exp}}{X_{exp}}\right) \times 100$$

of the oil coating the disc is the same for the air and water sides, except that in the air stream the oil is drained by gravity forces, while in the water the oil is drained by buoyance forces. As the buoyancy forces for oil in water are much smaller than gravity forces, the oil thickness on the water side is much larger than that on the air side. Consequently, the model under-predicts the oil layer thickness under the water in the dry mode, and therefore underpredicts the resistance to heat transfer between the disc and the water (see section 2.5.2.4). This results in the overprediction of the rotor performance in the dry mode.

By the definition of starved mode, there is essentially no oil layer floating on the water where the discs enter the water stream. Hence, the oil on the disc is not replenished, and the oil thickness that is on the disc in the water is essentially the same as that which was on the air side. Therefore, in the starved mode, the model sufficiently predicts the oil film thickness and its interaction with the performance of the disc. This can be seen in Table 2.6.2, where the average percent difference between the simulated and experimental heat loads per disc was less than 1%, with a standard deviation of 4.3%

The model's predictive value for the outlet water temperature (T_{w_2}), outlet air temperature (T_{A_2}), water hot spot temperature (T_{w_3}), coolest disc temperature (T_{P_2}), and the thermal fluctuations of the disc $(T_{P_1} - T_{P_2})$ are compared with experimentally measured values in Table 2.6.3.

TABLE 2.6.2

STARVED MODE

Run	ε_{exp}	ε_M	$\Delta\varepsilon(\%)$	$Q_{exp_{dry}}$ $(Q_{meas}-Q_{evap})$	Q_M	$\Delta Q\%$
1	.264	.290	9.8	2380	2575	8.2
2	.221	.246	11.3	2945	2897	-1.6
3	.242	.240	-0.8	3018	3054	1.2
4	.231	.243	5.2	2961	3109	5.0
5	.232	.243	4.7	3068	3082	0.5
6	.228	.230	0.9	3578	3582	0.1
7	.208	.232	11.5	2769	2915	5.3
8	.307	.318	3.6	2793	2683	-3.9
9	.231	.242	4.8	2995	3105	3.7
10	.313	.323	3.2	2774	2671	-3.7
11	.294	.293	-0.3	2764	2722	-1.5
12	.279	.296	6.1	2764	2329	2.4
13	.336	.330	-1.8	2401	2187	-8.9
14	.244	.252	3.3	3248	3285	1.1
15	.264	.287	8.7	3339	3470	3.9

$$\overline{X} = 4.7 \qquad\qquad \overline{X} = 0.8$$
$$S = 4.2 \qquad\qquad\quad S = 4.3$$

ε = effectiveness

Q = rate of heat rejection per disc (BTU/hr·disc)

Subscripts: exp: experimental results, after accounting for evaporation

M: predicted by model

$$\Delta X(\%) = (\frac{X_M - X_{exp}}{X_{exp}}) \times 100$$

$\overline{X}$ = average $\Delta X(\%)$, S = Standard deviation from average

TABLE 2.6.3

SPECIFIC SYSTEM TEMPERATURE, AS MEASURED & MODELED

Run	T_{w_2}		T_{A_2}		T_{w_3}		T_{p_2}		$T_{p_1} - T_{p_2}$	
	exp	model	exp	model	exp	model	exp	model	exp	model
1	125.8	125.9	89.7	91.3	128	132.0	117	116.5	5.0	7.4
2	122.6	123.5	90.6	92.1	125	134.9	114.9	112.9	6.1	8.3
3	121.6	122.6	94.5	94.7	124	129.8	-	111.4	-	8.8
4	121.4	121.6	87.9	88.6	123	129.0	114.8	110.3	6.8	8.9
5	121.2	122.1	88.7	89.5	122	125.1	110.0	111.0	6.3	8.8
6	119.8	121.2	87.3	37.4	120.5	123.2	116.8	111.0	3.0	4.7
7	125.5	126.8	98.2	99.9	128.5	132.1	-	116.2	-	8.3
8	128.3	128.9	91.8	92.5	130	132.9	117	119.1	5.0	7.7
9	127.9	128.0	98.8	99.4	129	132.6	-	116.7	-	8.9
10	127.8	128.2	91.3	92.0	130	131.6	118.1	118.4	5.4	7.7
11	126.9	127.9	-	97.2	-	129.6	-	118.0	-	7.8
12	125.6	126.0	-	95.3	-	127.3	-	117.9	-	3.7
13	128.5	129.1	99.5	98.2	130	130.5	120.2	121.1	4.8	6.3
14	125.4	125.8	95.4	95.8	127.5	127.9	113.8	113.9	7.0	9.4
15	127.8	128.0	89.1	90.6	130	131.3	117.7	115.3	6.8	10.0

Terms defined in Figure 2.5.1

There is generally a good agreement between the experimental and predicted values for T_{w_2}, T_{A_2}, T_{w_3}, and T_{P_2}. The disagreement between predicted and measured changes in disc temperature $(T_{P_1} - T_{P_2})$ results from the way in which the system is modeled. The experimentally measured values were determined by thermocouples embedded in the disc. Thus they directly measure the disc temperature. In the model (see section 2.4.2.5) the heat capacities of the disc and the oil are lumped together and the temperature fluctuations given in Table 2.6.3 are the average temperatures for that one, lumped, heat capacity.

In reality, the oil temperature fluctuates a great deal more than the disc temperature, as the oil covers the disc and a temperature gradient is needed to transfer heat to and from the disc, through the oil layer. Consequently, the average temperature of the oil and disc system given by the analytical model is expected to be greater than the measured disc temperature.

3. OIL STUDIES

3.1 DESCRIPTION OF OIL SYSTEM

One of the main assets of the Periodic Cooling Tower (P.C.T.) is its ability to perform as a dry tower, while requiring only a fraction of the capital investment required by a conventional finned-tube dry cooling tower. This ability is ultimately dependent on the oil layer which is floated on the surface of the water. It is therefore of interest to analyze the inter-actions between the rotating disc, the condenser water and the oil layer.

In contrast with the finned-tube heat exchanger, the water and air streams in the P.C.T. are not separated by a solid surface, but rather share a common free surface. Therefore, it was necessary to study means of sup-pressing evaporation in the P.C.T. Water evaporates from both the trough water free surface, and from the water adhering to the rotating discs. Since the area of the discs exposed to the air stream is several orders of magnitude larger than the trough water free surface area, most of the evaporation takes place on the discs.

One way of reducing evaporation would be to mechanically remove the water adhering to the discs by means of wipers. Because of the large number of discs involved ($\sim 10^6$), this added complexity is not desirable. In a first approach to this problem, Robertson [4] used discs with a hydrophobic surface. He tested bare aluminum and teflon coated surfaces. Evaporation rates were reduced to 50% (Aℓ) and 20% (Teflon coated) of that occurring in a conventional wet tower of equal capacity. However, the high cost of the teflon coating, and the deterioration of the aluminum surface performance (due to fouling) rendered these designs impractical. Robertson then tried floating an oil layer on the water free surface (Fig 3.1.1). This resulted in the entire disc surface (both air and water sides) being coated by a thin
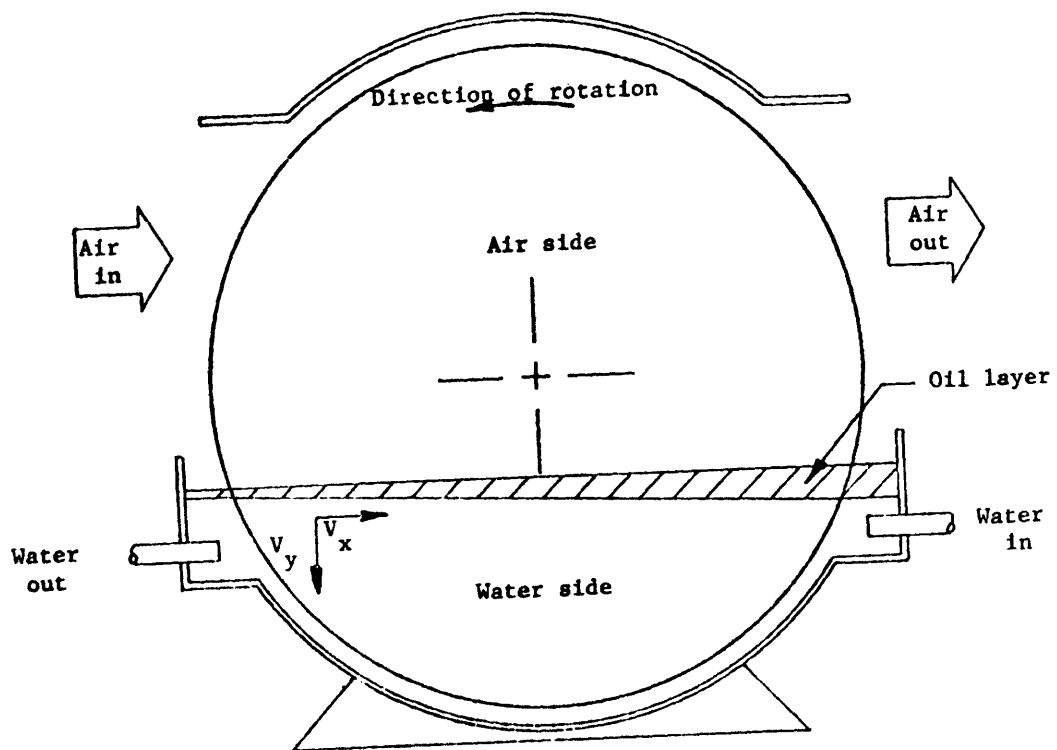
OIL SOLUTION TO WATER EVAPORATION

FIGURE 3.1.1

oil film. This film, in conjunction with the oil layer, functioned as a wiper which prevented any water from being carried to the air side.

The oil layer solution to the evaporation problem has been investigated in some detail, and appears to be a practical one. Two aspects of the oil system were given special consideration (1) determination of the thickness of the oil film coating the discs, (2) determination of the effect that the angular velocity of the disc, as well as the oil properties and the geometric configuration could have on the ability of the oil layer to suppress evaporation.

The oil film thickness is an important parameter because it determines the additional heat transfer resistance caused by the oil coating the disc. This resistance dominates on the water side, and represents about 15% of the total heat transfer resistance on the air side. It must therefore be included in the heat transfer analysis. An analytical model describing the oil film thickness distribution on the disc surface, as well as experimental measurements taken both on the air and water sides, are included in Part 3.2.

It is of interest to determine the constraints on the angular velocity of the disc, since the performance of the P.C.T. is affected by this velocity. This is the case in so far as the heat capacity of the discs is proportional to their angular velocity. For low angular velocities the P.C.T. performance increases sharply as velocity is increased, and then approaches asymptotically a maximum value for infinite angular velocity. Therefore, as long as the maximum allowable angular velocity is past this region of rapid increase in performance, this constraint does not represent a real limitation on the P.C.T. performance. The dependence of the maximum allowable angular velocity on oil properties, and other parameters such as oil layer

thickness, water level and disc spacing, was empirically determined and is included in Part 3.3.

Other aspects of the oil system which need to be considered are oil evaporation and emulsivness. They are discussed in Part 3.4.

Before making any quantitative measurements, an attempt was made to determine qualitatively the mechanisms by which the oil layer prevents water from being carried to the air side.

The apparatus used for making these observations is shown schematically in Fig (3.1.2). The single 20 inch diameter disc, made out of galvanized steel sheet metal, was partially immersed in a water trough. The trough was made out of clear plexiglass, so that the oil layer and the oil film on the water side could be observed. The water in the trough was circulated through a heat exchanger, and its temperature could be set within ±1 F° in a range from 80-150 °F. The portion of the disc immersed in the water could be varied by changing the water level. The disc was driven by a variable speed motor with a 0-20 RPM range.

3.1.1 Dry and Starved modes of operation .

It has been observed, that the oil layer is noticeably thicker on the side where the discs leave the water, as indicated in Fig (3.1.1). This side will hereafter be referred to as the WOA side, the letters representing the order in which the disc crosses the water-oil and oil-air interfaces. The opposite side will be referred to as the AOW side. Two different mechanisms were found to contribute to the oil accumulation on the WOA side:

1. Shear forces on the oil layer.

2. Net outflow of oil from the AOW side and net inflow to the WOA side.

To compensate for the higher heat transfer resistance on the air side (as compared to the water side), it is necessary to set the water level
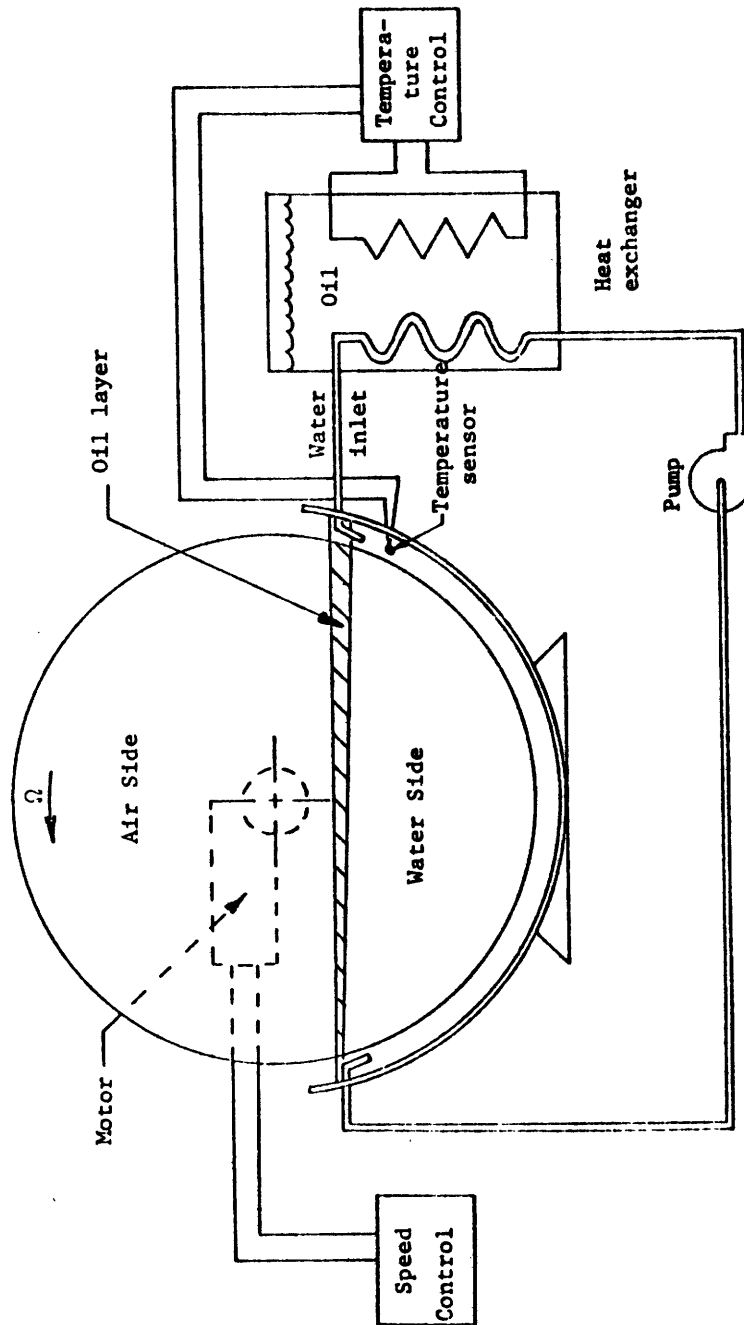
SCHEMATIC REPRESENTATION OF EXPERIMENTAL SETUP

FIGURE 3.1.2

77.

well below the axis of the disc, so that a larger fraction of the disc sur-

face is exposed to the air stream. This in turn means that the portion of

the disc surface in contact with the oil layer has a horizontal velocity

component, as shown in Fig. (3.1.1). Due to this horizontal velocity, the

discs exert a shear force on the oil layer, which tends to move the oil

towards the WOA side.

When barriers were set across the oil layer to impede the hori-

zontal displacement of the oil (thus neutralizing the effect of the shear

forces induced by the disc rotation), it was found that the oil would still

accumulate on the WOA side. This meant that oil was being carried from the

AOW to the WOA side on the disc surface, as shown in Fig. (3.1.3). This

was due to the fact that the oil film remaining on the disc surface on the

water side is considerably thicker than that remaining on the air side. As

will be shown later, these thicknesses are in the ratio of gravity to flo-

tation forces. This means that for the range of oils being used in the P.C.T.,

the oil film on the water side is roughly 2 to 3 times thicker than that on

the air side.

The rotating discs act as a pump, which moves the oil from the

AOW to the WOA side. The oil is driven back to the AOW side by the pressure

head resulting from the difference in oil layer thickness between the two

sides. As the angular velocity of the discs is increased, this pumping effect

also increases, and eventually the oil layer thickness on the part of the

AOW side is reduced to zero, as shown in Fig (3.1.4). This condition has been

termed starved mode operation, as opposed to dry mode operation. The latter

refers to a situation in which the oil layer covers the entire water surface.

Starved mode operation has the advantage of making the oil film on the water side

Oil carried out of
the oil layer on
disc surface

WOA side of
oil layer

Oil flow induced by
horizontal component
of disc velocity

Air side

Ω

Water side

AOW side of
oil layer

Oil carried into
the oil layer on
disc surface
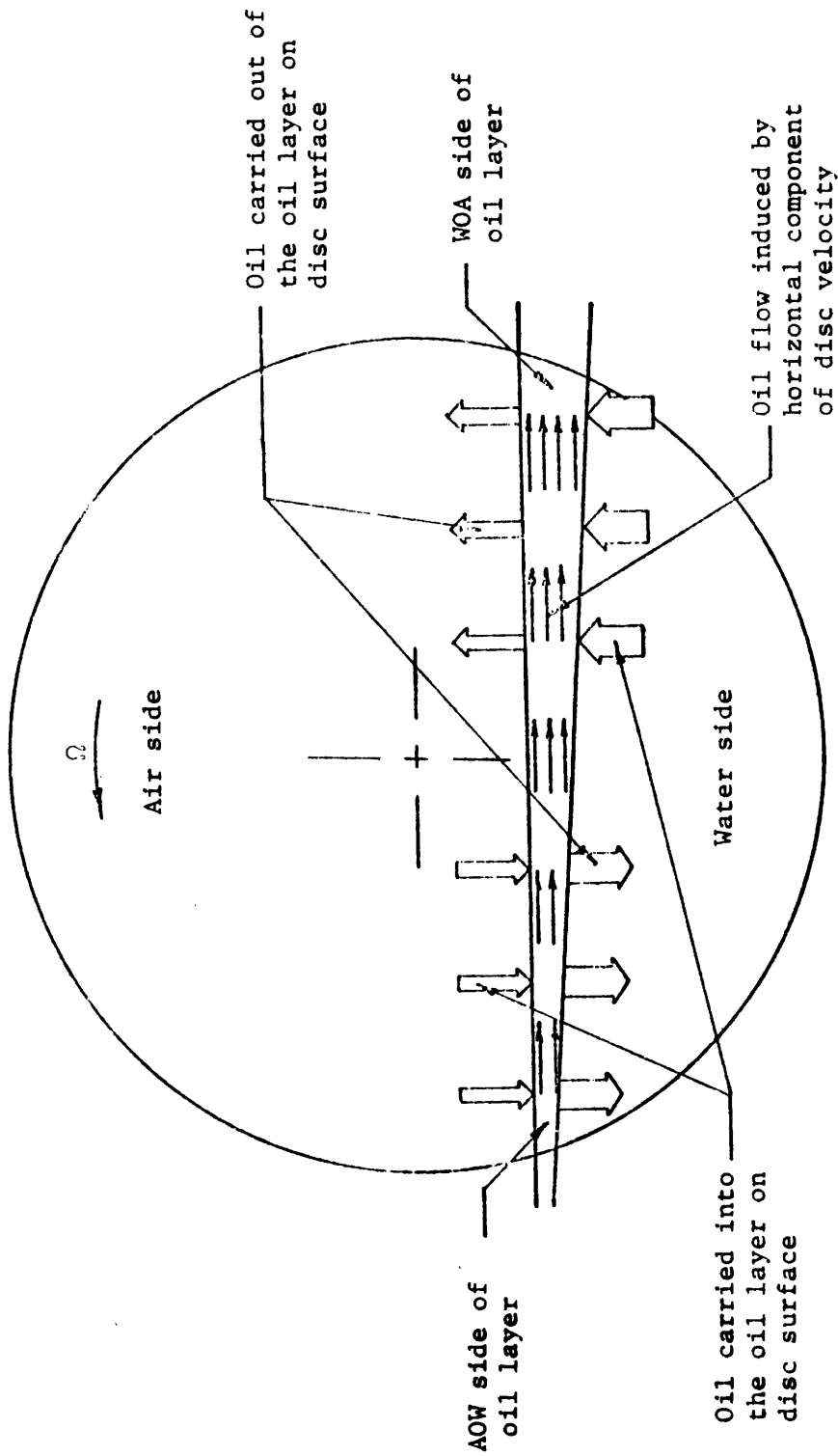
MECHANICMS OF OIL ACCUMULATION ON THE WOA SIDE OF THE OIL LAYER

FIGURE 3.1.3
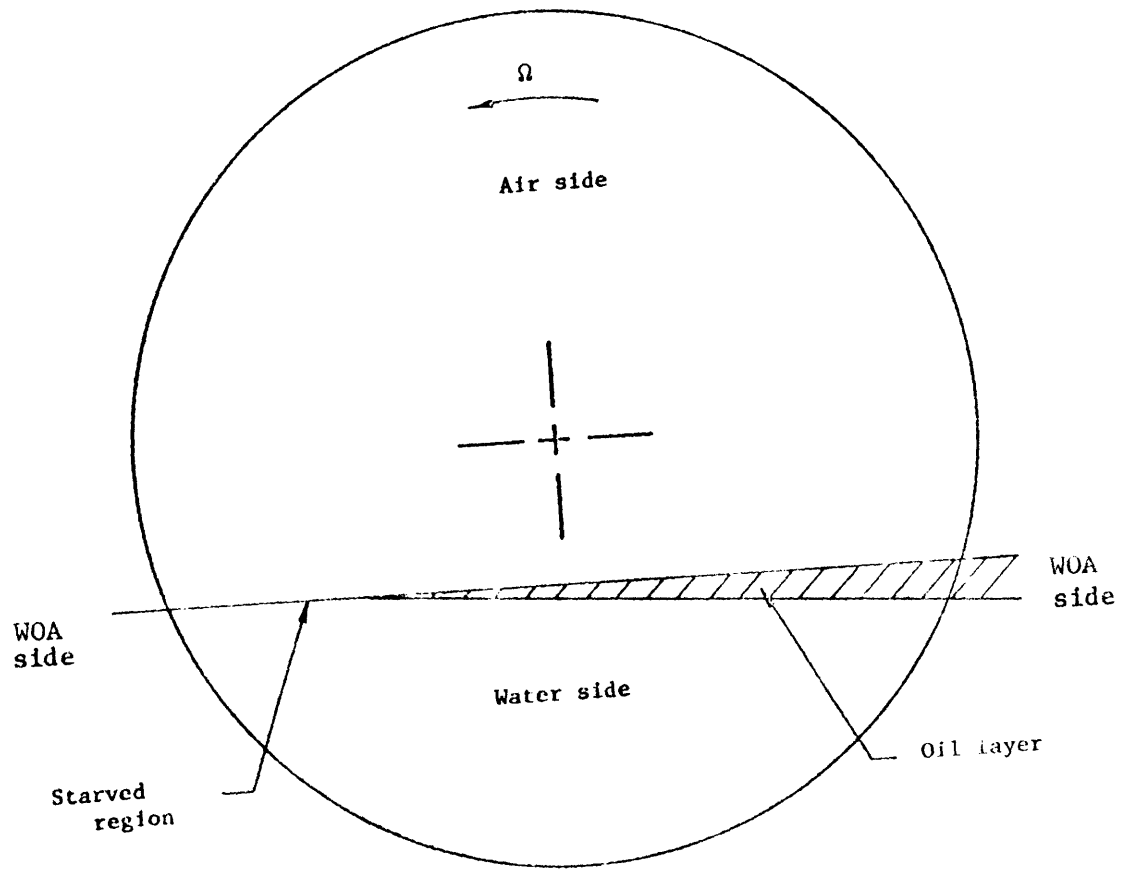
STARVED MODE OF OPERATION

FIGURE 3.1.4

thinner, since the disc cannot pickup oil on the AOW side. This in turn increases the heat transfer performance. It has the slight disadvantage of leaving part of water surface covered with, at most, a monolayer of oil, through which evaporation can take place. However, the fraction of the water free surface area not covered by oil is small as compared to the total heat transfer area, and therefore, evaporation is minimal.

3.1.2. Oil film on the disc surface

It is perhaps necessary to emphasize the distinction between the expressions 'oil film' and 'oil layer'. Oil film refers to the oil on the disc surface, while oil layer refers to the oil on the water surface.

Tinted oil was used in the observations of the oil film. The disc was painted white so as to be able to infer changes in film thickness from changes in color tone. On the air side two regions were identified, as shown in Fig. (3.1.5). It was observed that no oil would flow into a circular region around the center of the disc (region II in Fig. (3.1.5). This region extended almost down to the oil layer. Between this circle and the rim of the disc (region I), the surface was covered by an oil film of varying thickness. The oil film seemed to be thinner along the boundaries of region I, with the exception of two zones forming part of the 'oil ridge'. The expression 'oil ridge' refers to a narrow circular arch, of noticeably thicker oil film that divided region I in two. The oil ridge is more noticeable at lower water levels, and becomes very faint as the water level approaches the center of the disc. This suggests that it is formed by oil flowing down towards the rim of the disc, as indicated by the arrows in Fig. (3.1.5). Changes in the angular velocity of the disc did not affect the boundaries of the regions just described, nor did they affect the position of the oil ridge.
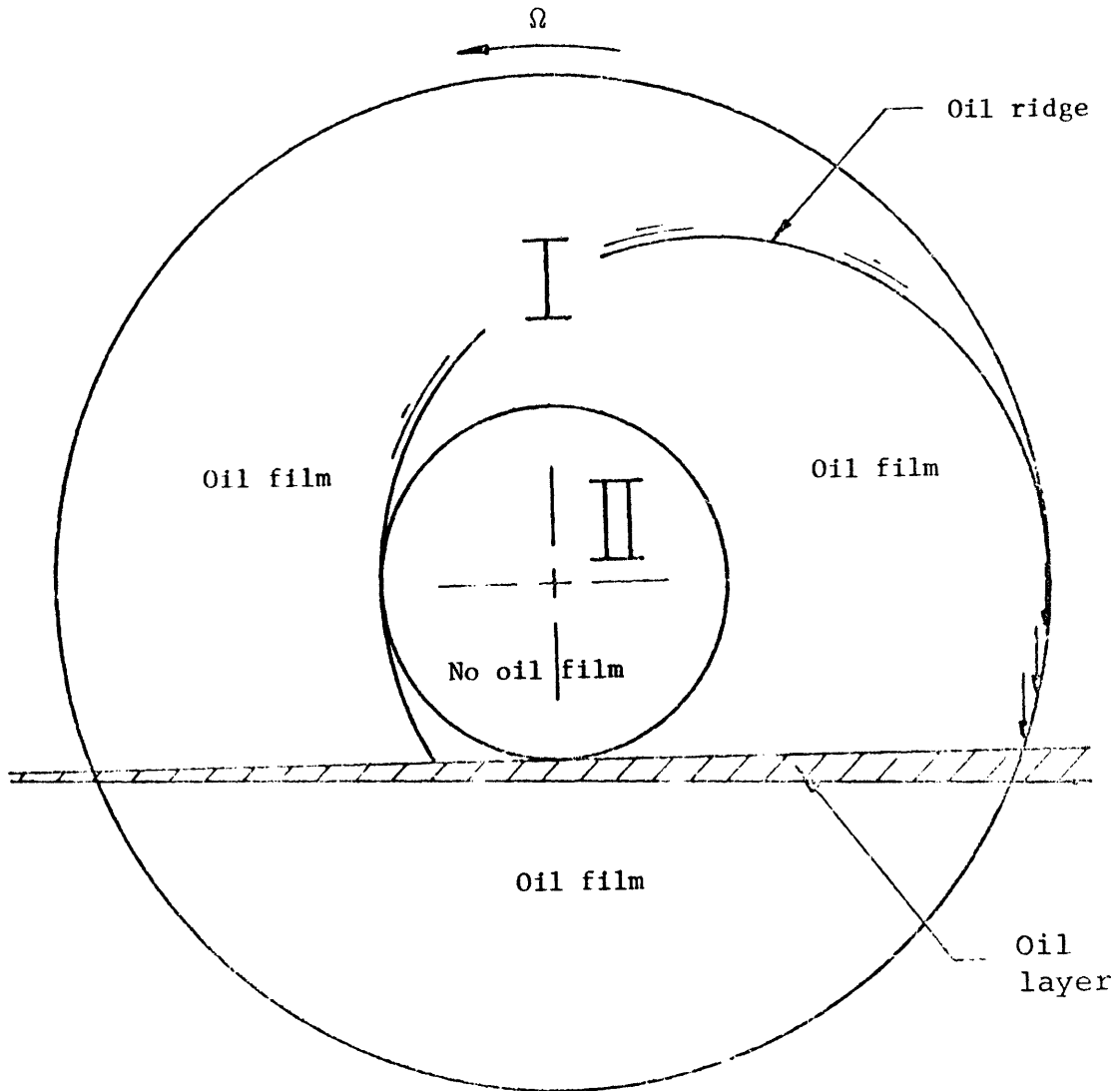
REGIONS OF THE DISC SURFACE COVERED BY AN OIL FILM

FIGURE 3.1.5

The oil film thickness nevertheless, increased with increasing angular velocity.

On the water side the film thickness appeared to be much thicker than on the air side, but no distinct regions were observed. At high angular velocities ($\simeq$20 RPM) the film would become unstable and ripples would appear on its surface. Some of these ripples would sporadically break, and oil droplets would be released into the water stream. This occurred at angular velocities higher than those contemplated for the P.C.T. and therefore it does not represent a real constraint.

3.1.3 Water beading on disc surface

It has been observed that under certain operating conditions water beads are carried to the air side on the disc surface. These beads appear to be covered by a monolayer of oil. Nevertheless, they have been shown to significantly increase the water evaporation rate; which is an undesirable effect. It is therefore of interest to determine the conditions under which water beading occurs, so as to avoid them in the design of the P.C.T. There are three different circumstances which may cause beading on the disc surface. They are:

1) Accumulation of water droplets in the oil layer.

2) Water wetting the disc surface.

3) Water breaking through the oil layer.

Water droplets are continuously being shed into the oil layer as the discs cut through it. This can be seen in the photographs shown in Fig. (3.1.8). If these droplets do not readily coalesce, they accumulate in the oil layer, forming a water-in-oil dispersion. The size of the drops ranges from hundredths of an inch to about 1/16". Some of the smaller beads are picked up by the disc and carried to the air side. These droplets ride

along inside the oil film and probably do not contribute to water evapo-

ration. The rate of coalescence of the water droplets in the oil layer is

a strong function of the viscosity and interfacial tension of the oil.

Therefore, with a proper selection of oil, this effect can be eliminated al-

together and still maintain other required properties.

The second beading mechanism is also related to oil properties,

specifically to the metal wetting ability of the oil. Some oils, particularly

synthetic oils with high interfacial tension, do not wet the disc well. They

are partially displaced by water, especially near the rim of the disc. Water

adhering to these bare spots on the disc is pulled through the oil layer. It

then forms a water pocket under the oil film on the air side, as shown in

Fig (3.1.6). Gravity forces squeeze the water out of these pockets, forming

in turn large beads ($\sim$ 1/8" diameter) which ride on top of the oil film. As

will be shown later, high interfacial tension plays an important role in

keeping the water from breaking through the oil layer. In addition, high

interfacial tension is an important factor in accelerating, the coalescence

of water drops in the oil layer. On the other hand, it reduces the wetting

ability of the oil. Because of this tradeoff, the optimum value of the

interfacial tension was not apparent, and had to be empirically determined.

The third beading mechanism is related to the oil properties, as

well as angular velocity, oil layer thickness, water level and spacing be-

tween the discs. Fig. (3.1.7) shows a photograph of the water breaking

through the oil layer and beading up on the disc surface. Blue dye was added

to the water to improve visualization. In. Fig. (3.1.8) a series of photo-

graphs is shown, which depicts the WOA side at increasing angular velocities.

When the disc was operated in the dry mode, water would never break
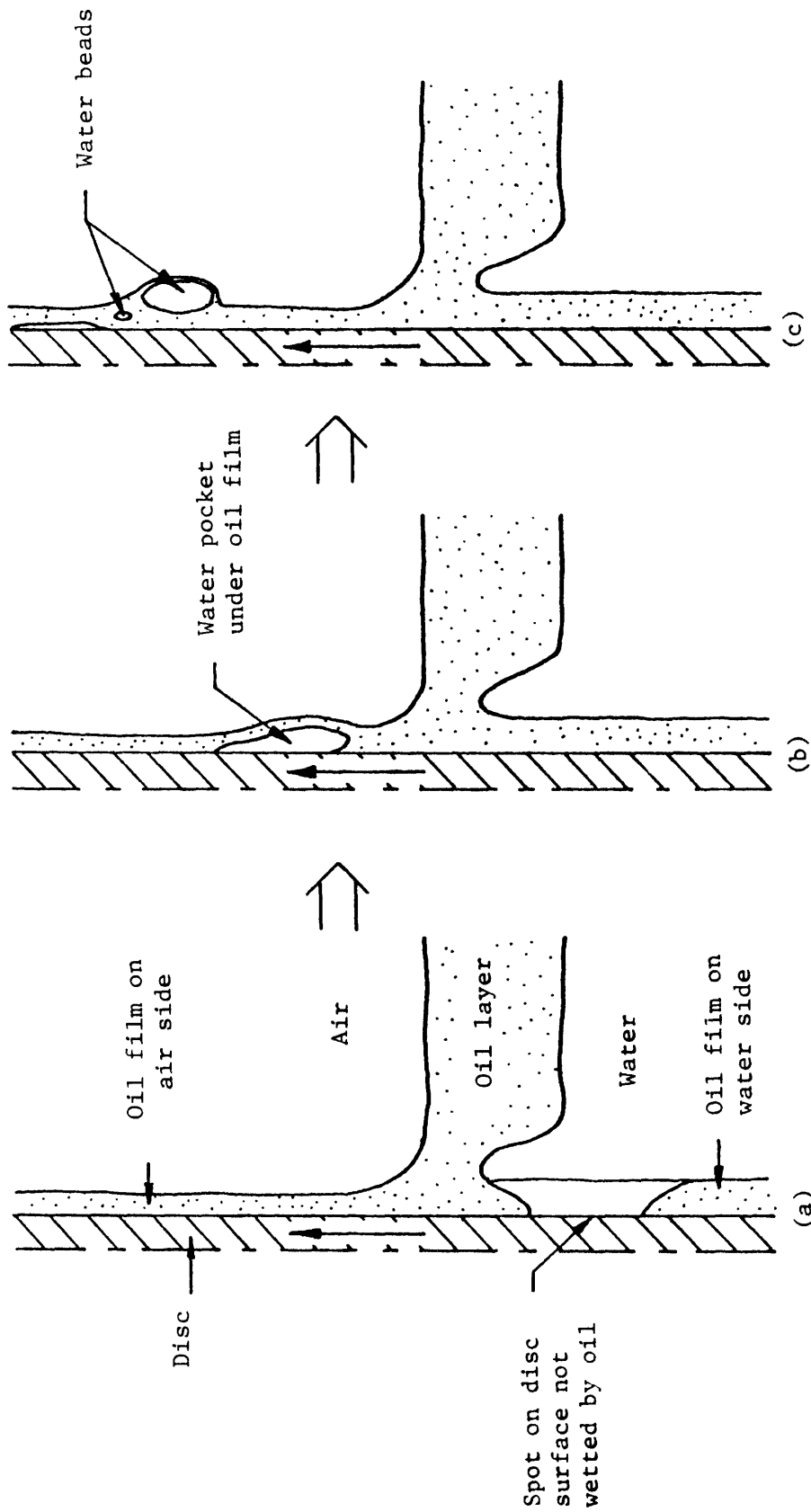
WATER BEADING ON THE DISC SURFACE CAUSED BY POOR METAL WETTING

PROPERTIES OF THE OIL

FIGURE 3.1.6

WATER BEADING OF THE DISC'S SURFACE

Figure 3.1.7

(a) Ω = 3.6 RPM

(b) Ω = 6 RPM

(c) Ω = 9 RPM
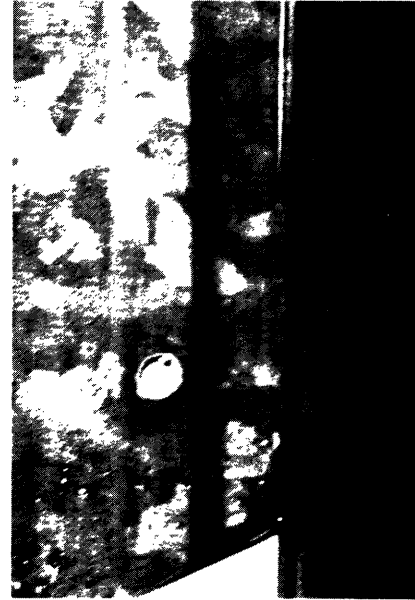
(d) Ω = 11 RPM

OIL LAYER AT DIFFERENT ANGULAR VELOCITIES

Figure 3.1.8

through the oil layer. Only at high angular velocities a very thin water

filament was pulled under the oil film near the rim of the disc. This fila-

ment would then break into small beads as illustrated in Fig. (3.1.9a). In

the starved mode, as the angular velocity was increased, a similar phenomena

occurred. However, as the angular velocity was further increased, water

would break through in a progressively larger region near the edge. The

water breaking through the oil layer would then form beads which would be

carried around on the disc surface, forming a beaded band around the rim of

the disc, as shown in Fig. (3.1.9b).

The main difference between the dry and the starved modes of opera-

tion is the thickness of the oil film on the water side. This fact, along

with the difference in beading between the two modes, suggests that the

water-stripping ability of the oil layer is strongly dependent on the oil

film thickness on the water side.

As the disc rotates through the water, a water layer is dragged

along on top of the oil film. When this water layer reaches the water-oil

interface on the WOA side, it can either bend sharply under the oil layer

or break through it into the air side, depending on the forces present.

Fig. (3.1.10) shows cross-sections of the oil layer on the WOA side. It de-

picts three possible combinations of oil film thickness on the water and

air sides. At (a) the film thickness on the water side, h_w, is larger

than the film thickness on the air side, h_a. This implies that the disc is

bringing more oil into the oil layer than it is taking away. Oil will there-

fore flow from the disc into the oil layer (as indicated by the arrows),

forcing the water to flow under the oil layer. Under these circumstances, the

water cannot break through the oil layer, regardless of the normal velocity
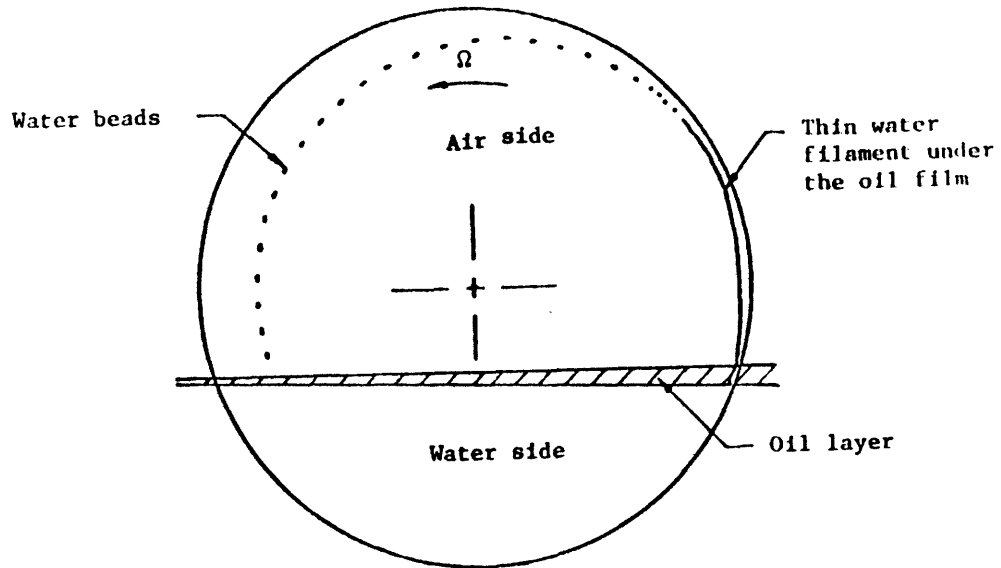
(a)   Dry mode of operation
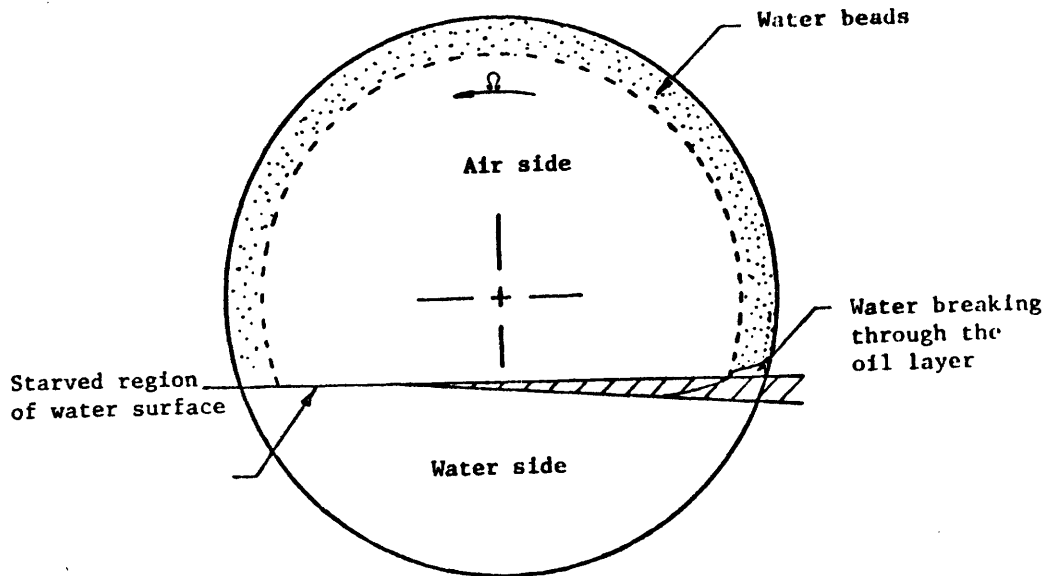
(b)   Starved mode of operation

WATER BEADING ON DISC SURFACE

FIGURE 3.1.9

(a) Dry mode operation

(b) Starved mode operation
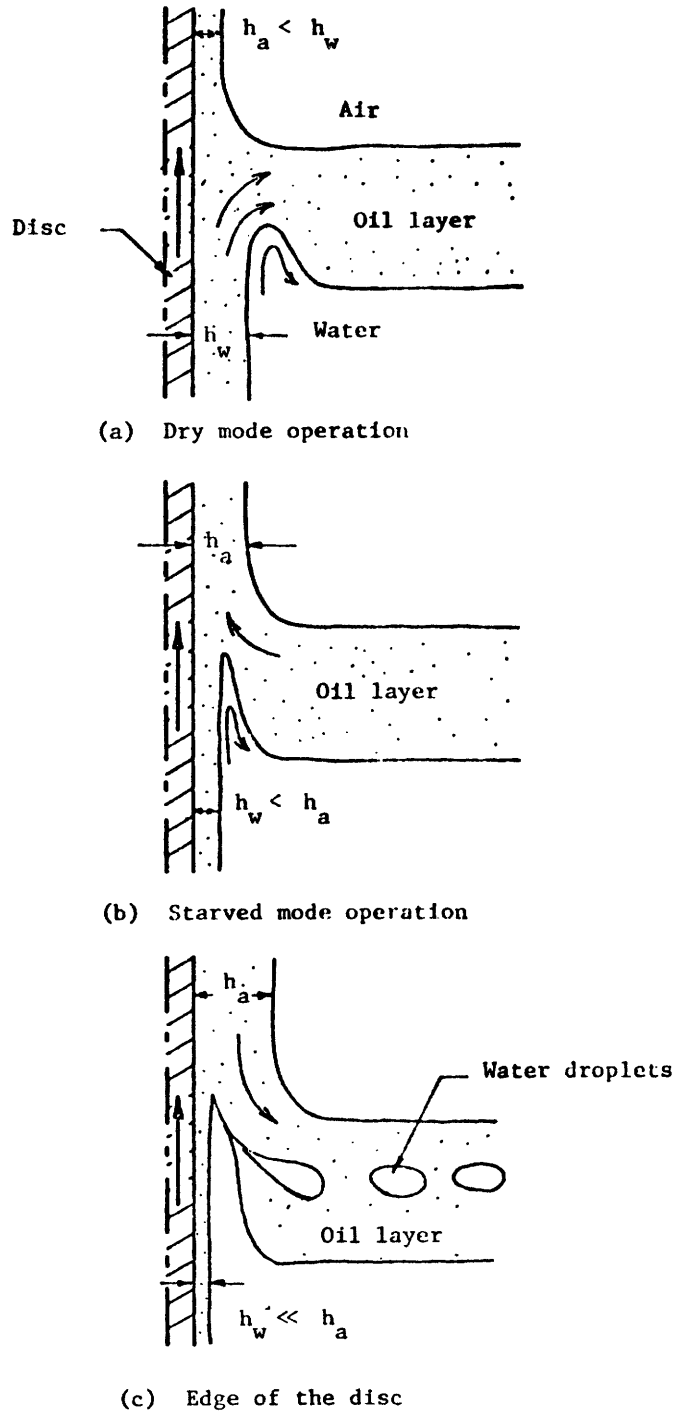
(c) Edge of the disc

WATER STRIPPING ACTION OF THE OIL LAYER

FIGURE 3.1.10

of the disc at that point. This is apparently the situation existing through-
out the WOA side in dry mode operation, except at the very edge of the disc,
where the film thickness on the water side is reduced to zero.

In Fig. (3.1.10,b) the opposite situation is shown, $h_w < h_a$. Oil
must now flow from the oil layer to the disc, as indicated. For the water
not to break through the oil layer, gravity and interfacial tension forces
must exceed the shear drag and momentum forces trying to pull the water
through. Both interfacial tension and gravity forces are bounded. That is,
they cannot exceed some maximum values which depend on the interfacial tension
in the first case, and on the oil layer thickness in the second. Therefore,
if the disc velocity normal to the oil layer is increased sufficiently, shear
and momentum forces will dominate, and water will break through to the air
side. This is believed to be the condition existing under starved mode
operation.

Near the edge of the disc, the oil film thickness on the water side
goes to zero, for both dry and starved modes of operation. Therefore, the
situation in the oil layer before water breaks through, should be similar in
both cases. As was already mentioned in the description of the oil film,
the film on the air side is very thick near the edge of the disc. Oil accumu-
lates in this region, forming a ridge. It has been observed that oil flows
downward on the surface of this ridge, giving rise to the situation depicted
in Fig. (3.1.10,c). Water is dragged into the oil layer as far as the
meniscus region on the air side, where it is washed off by the oil flowing
down the disc. The water then breaks into drops which are entrained in the
oil layer. Fig. (3.1.11) shows a photograph of the disc edge on the WOA
side, which was taken through the oil layer. In this photograph the situation

EDGE VIEW OF DISC ON
SIDE WHERE DISC PASSES
FROM WATER, THEN OIL,
TO AIR (WOA SIDES)

Figure 3.1.11

just described can be seen. When the angular velocity is increased suffi-
ciently, a thin water filament is pulled up under the oil film.

The starved mode of operation may be preferred to the dry mode, because
it reduces the oil film heat transfer resistance on the water side. There-
fore, water break-through is a problem that has to be dealt with. It is of
special interest for the optimization of the P.C.T. design to determine how
the maximum angular velocity (before beading starts) is affected by para-
meters such as oil layer thickness, water level and disc spacing. It has
been observed that this maximum angular velocity increases with increasing
oil thickness and disc spacing, and decreases with increasing water level.
It is also important to determine how the oil properties affect this maximum
angular velocity, in order to make an appropriate selection of the oil to
be used in the P.C.T.

3.2 OIL FILM THICKNESS DISTRIBUTION ON DISC SURFACE

Measurements of the thickness of the oil film coating the discs were made earlier by Fink [14]. His results showed that the film thickness varied with position on the disc surface, as well as the angular velocity and the water temperature. All these measurements were made on the air side, and only one type of oil was used. Silicon oil was being used at the time because it has a very low vapor pressure, which results in a negligible oil loss due to evaporation. However, the high cost of silicon oils may make it desirable to accept a higher oil evaporation rate and use cheaper hydrocarbon oils. Furthermore, as pointed out in section 3.1.1, the film thickness on the water side is also an important parameter, since it constitutes the largest heat transfer resistance on that side. Therefore, it was necessary to obtain a more general solution to the oil film thickness distribution; a solution which included the effects of different oil properties and different operating conditions (angular velocity and water level).

3.2.1 Theoretical Model

In developing the theoretical model, the disc surface was initially divided into two regions: one formed by that part of the disc which is in the air stream at any instant of time, and the other by the portion submerged in the water. The analysis for both regions is very similar, the main difference being that gravity forces are substituted by flotation forces on the water side. The coordinate system used in the analysis is shown in Fig. (3.2.1). The angular velocity Ω is taken as positive for counterclockwise rotation.

The film thickness h is several orders of magnitude smaller than the characteristic dimension of the disc, its radius R. The oil flow in the
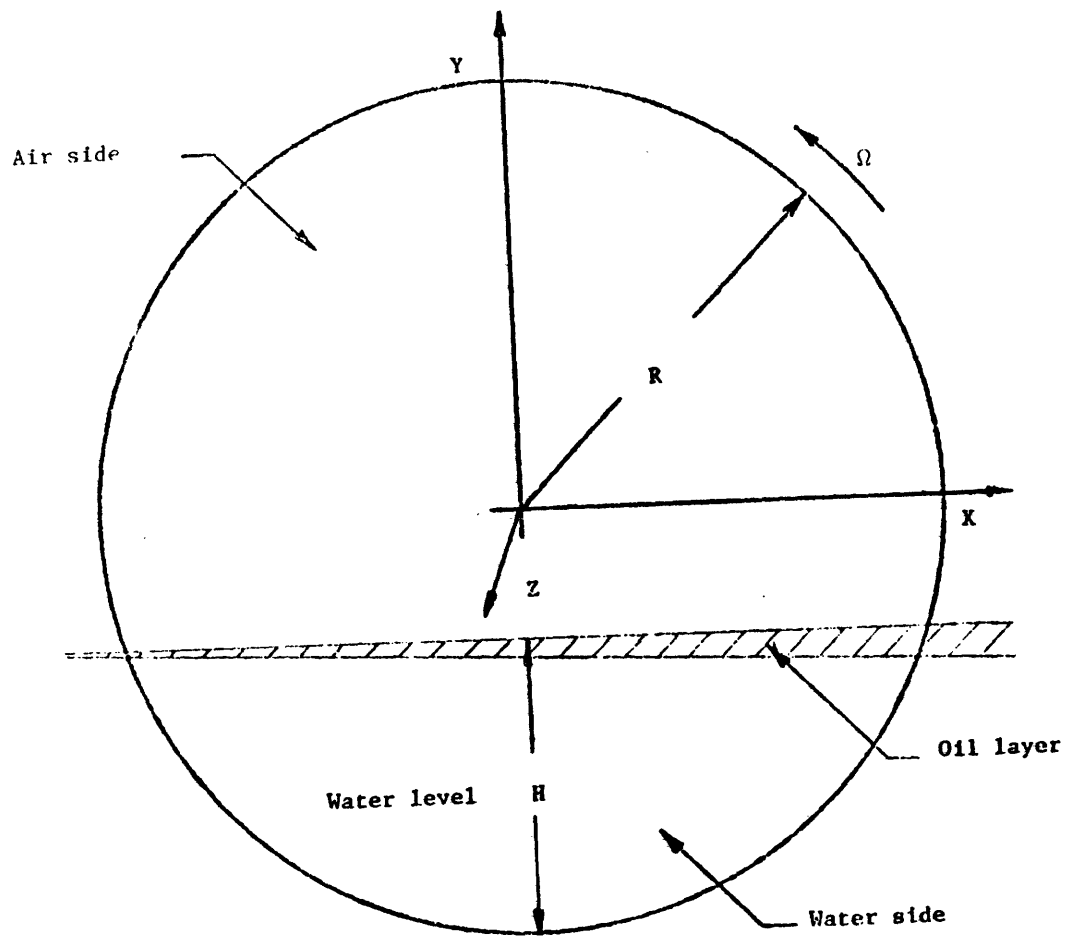
SYSTEM OF COORDINATES

FIGURE 3.2.1

film is therefore similar to a three-dimensional boundary layer flow and can
be described by the equations [15]:

$$u \frac{\partial u}{\partial x} + v \frac{\partial u}{\partial y} + w \frac{\partial u}{\partial z} = - \frac{1}{\rho} \frac{\partial p}{\partial x} + \nu \frac{\partial^2 u}{\partial z^2} + g_x \qquad (3.2.1)$$

$$u \frac{\partial v}{\partial x} + v \frac{\partial v}{\partial y} + w \frac{\partial v}{\partial z} = - \frac{1}{\rho} \frac{\partial p}{\partial y} + \nu \frac{\partial^2 v}{\partial z^2} + g_y \qquad (3.2.2)$$

$$\frac{\partial u}{\partial x} + \frac{\partial v}{\partial y} + \frac{\partial w}{\partial z} = 0 \qquad (3.2.3)$$

The analysis of the oil flow on the disc surface will follow these
steps:

1) From order of magnitude considerations, the three-dimensional
boundary layer equations will be reduced to a simple form and then inte-
grated to yield the velocity profiles in the film.

2) The continuity equation will then be integrated across the
film, using the velocity solutions from part (1), and a partial differ-
ential equation for the oil film thickness obtained.

3) Finally, this equation, along with semi-empirical boundary
conditions will be solved for the oil film thickness.

3.2.1.1 Air Side

On the air side, the pressure outside the film is uniform, equal
to the atmospheric pressure. The only pressure gradients in the film are
those arising from the curvature of the film surface. With the exception
of the meniscus, in the region where the dics leave the oil layer, the
surface of the film is nearly planar and this pressure effect is negligible.

Therefore,

$$\frac{\partial p}{\partial x} \sim \frac{\partial p}{\partial y} \sim 0$$

As the angular velocity of the discs is increased, a point is reached beyond which the oil film becomes unstable, as was observed on the water side. This instability would cause waves on the oil-air interface, and the previous assumption of a planar surface would no longer be valid. This condition however, develops at higher angular velocities than those contemplated for the P.C.T. and therefore, need not be considered here.

Since the film is very thin, and there is practically no shear at the oil air interface, the velocity of the oil can be assumed to be very close to the velocity of the disc at that same point. An order of magnitude analysis then yields:

$$u \sim \Omega y \quad ; \quad \frac{\partial u}{\partial x} \sim 0 \quad ; \quad \frac{\partial u}{\partial y} \sim \Omega \quad ; \quad \frac{\partial^2 u}{\partial z^2} \sim \frac{\Omega R}{h^2}$$

$$v \sim \Omega x \quad ; \quad \frac{\partial v}{\partial x} \sim \Omega \quad ; \quad \frac{\partial v}{\partial y} \sim 0 \quad ; \quad \frac{\partial^2 v}{\partial z^2} \sim \frac{\Omega R}{h^2}$$

The continuity equation (3.2.3) becomes:

$$\frac{\partial w}{\partial z} \sim 0$$

Since w equals zero at the disc surface, w must be equal to zero everywhere.

There is no body force in the x direction, and gravity is the only body force in the y direction.

On the left hand side of Eqs. (3.2.1) and (3.2.2) the only remaining terms are then

$$v \frac{\partial u}{\partial y} \quad \text{and} \quad u \frac{\partial v}{\partial x}$$

These correspond to the centrifugal acceleration induced by the discs' rotation. By comparing them with the other terms in Eqs. (3.2.1) and (3.2.2) it is seen that they can be neglected as long as

$$\Omega << \frac{\nu}{h^2} \qquad \text{and} \qquad \Omega^2 R << g \qquad (3.2.4)$$

Both these conditions are met in the range of operation of the P.C.T.

Incorporating all these order of magnitude considerations, a much simpler form of the three-dimensional boundary layer equations is obtained:

$$\frac{\partial^2 u}{\partial z} = 0$$

$$\frac{\partial^2 v}{\partial z^2} = \frac{g}{\nu} \qquad (3.2.5)$$

$$\frac{\partial u}{\partial x} + \frac{\partial v}{\partial y} = 0$$

These equations can be readily integrated twice to yield the velocity distributions:

$$u = C_1 z + C_2$$

$$v = \frac{g}{2\nu} z^2 + C_3 z + C_4$$

where C_1 through C_4 are functions of x and y, to be determined from the boundary conditions. The no slip condition at the disc's surface along with negligible shear stress at the oil air interface define the boundary conditions for the velocities.

$$u = \Omega y \qquad \text{at } z=o$$

$$v = \Omega x$$

$$\frac{\partial u}{\partial z} = \frac{\partial v}{\partial z} = o \qquad \text{at } z=h$$

The functions C_1, C_2, C_3, C_4 can then be evaluated to obtain the velocity distributions in the x and y directions

$$u = \Omega y \tag{3.2.6}$$

$$v = \frac{g}{2\nu} (z^2 - 2h) + \Omega x \tag{3.2.7}$$

where h is also a function of x and y.

Substitution of these expressions into the continuity equation (3.2.2), followed by integration across the film thickness, yields

$$\frac{\partial}{\partial x} (-\Omega y h) + \frac{\partial}{\partial y} (\Omega x h - \frac{1}{3} \frac{g}{\nu} h^3) = 0 \tag{3.2.8}$$

Carrying out the differentiation, a partial differential equation in h is obtained:

$$-\Omega y \frac{\partial h}{\partial x} + (\Omega x - \frac{g}{\nu} h^2) \frac{\partial h}{\partial y} = 0 \tag{3.2.9}$$

Equation (3.2.9) can be cast into a nondimensional form by substituting the variables:

$$\bar{x} = \frac{x}{R} \quad , \quad \bar{y} = \frac{y}{R} \quad \text{and} \quad \bar{h} = \frac{h}{\left(\frac{\nu \Omega R}{g}\right)^{1/2}} \tag{3.2.10}$$

to obtain:

$$-\bar{y} \frac{\partial \bar{h}}{\partial \bar{x}} + (\bar{x} - \bar{h}^2) \frac{\partial \bar{h}}{\partial \bar{y}} = 0 \tag{3.2.11}$$

Equation (3.2.11) describes the nondimensional film thickness variation on the disc surface. It must be solved in conjunction with some boundary condition, to obtain a closed form solution for $\bar{h}$ as a function of $\bar{x}$ and $\bar{y}$.

One form of obtaining a solution to Eq. (3.2.11) is to first determine the loci of uniform film thickness, defined by

$$d\bar{h} = \frac{\partial \bar{h}}{\partial \bar{x}} d\bar{x} + \frac{\partial \bar{h}}{\partial \bar{y}} d\bar{y} = 0$$

which can be rewritten as:

$$\frac{\partial \bar{h}}{\partial \bar{x}} d\bar{x} = - \frac{\partial \bar{h}}{\partial \bar{y}} d\bar{y} \qquad (3.2.12)$$

Eq. (3.2.11) can be rewritten as:

$$\bar{y} \frac{\partial \bar{h}}{\partial \bar{x}} = (\bar{x} - \bar{h}^2) \frac{\partial \bar{h}}{\partial \bar{y}} \qquad (3.2.13)$$

Dividing equation (3.2.12) by equation (3.2.13) and rearranging results in

$$(\bar{x} - \bar{h}^2) d\bar{x} = - \bar{y} d\bar{y}$$

This equation can be integrated between a boundary point $(\bar{x}_o, \bar{y}_o)$ and an arbitrary point $(\bar{x}, \bar{y})$ to yield:

$$\int_{\bar{x}_o}^{\bar{x}} (\bar{x} - \bar{h}^2) d\bar{x} = - \int_{\bar{y}}^{\bar{y}} \bar{y} d\bar{y}$$

or

$$\frac{\bar{x}^2}{2} - \bar{h}^2 \bar{x} - \frac{\bar{x}_o^2}{2} + \bar{h}^2 \bar{x}_o = - \frac{\bar{y}^2}{2} + \frac{y_o}{2}$$

By rearranging and adding $\bar{h}^4$ to both sides to complete the squares, the equation describing the loci of uniform thickness is obtained.

$$(\bar{x} - \bar{h}^2)^2 + \bar{y}^2 = (\bar{x}_o - \bar{h}^2)^2 + \bar{y}_o^2 \qquad (3.2.14)$$

With a boundary condition of the form

$$\bar{h} = f (\bar{x}_o, \bar{y}_o) \tag{3.2.15}$$

the right hand side of Eq. (3.2.14) is a constant for any given $\bar{h}$.
From the form of Eq. (3.2.14) it can be seen that the loci of uniform thickness are circles centered on the $\bar{x}$ axis, at $(\bar{h},0)$. The radius of these circles is determined by the boundary condition.

The most appropriate boundary condition would seem to be the film thickness distribution at the line $\bar{y} = \bar{y}_o$, where the disc leaves the oil layer. Levich [16] has formulated an equation for estimating the thickness of the liquid film adhering to a flat plate of infinite length being drawn from a liquid. This equation is

$$h = \left[\frac{\mu V}{\rho g}\right]^{.5} f \left(\frac{\mu V}{\sigma}\right)$$

where

$$f \left(\frac{\mu V}{\sigma}\right) = \begin{cases} .93 \left(\frac{\mu V}{\sigma}\right)^{1/6} & \text{for} \quad \frac{\mu V}{\sigma} << 1 \\ 1 & \text{for} \quad \frac{\mu V}{\sigma} >> 1 \end{cases} \tag{3.2.16}$$

Eq. (3.2.16) was derived by Levich for a plate pulled vertically from a liquid with a constant velocity V. The thickness h is achieved at some distance above the liquid surface which is large as compared to the meniscus height. These conditions do not apply strictly to the situation at hand. First, the boundary condition is required along a line immediately above the liquid surface, and second, the velocity of the disc at the point where it leaves the oil layer is not normal to the oil layer. In addition, the value of $\frac{\mu V}{\sigma}$ is close to unity in the range of interest. Nevertheless, an attempt was made at using Eq. (3.2.16) as boundary condition. It was assumed that the film thickness depended only on the disc's velocity component normal to the oil alyer, $V = \Omega x$. Since both solutions included in Eq. (3.2.16) give similar results for $\frac{\mu V}{\sigma}$ in the neighborhood of one, the

average value was used. The resulting boundary condition is shown in Fig. (3.2.2). Eq. (3.2.14) was used to draw two circles of uniform thickness $\bar{h}_1$ and $\bar{h}_2$, corresponding to two boundary points $(\bar{x}_1, \bar{y}_1)$ and $(\bar{x}_2, \bar{y}_2)$. The circles intersect each other, implying that the boundary condition specified by Eq. (3.2.16) does not give a unique solution. In addition, this boundary condition would also imply that the whole surface of the disc on the air side is covered by an oil film. This is contrary to experimental observation, which indicates that there is a dry region around the center of the disc. Eq. (3.2.16) is therefore not applicable in this situation.

It can be expected however, that the film thickness along the line $\bar{y} = \bar{y}_o$ is a monotonically increasing function of the normal velocity $V_{\bar{y}}$. In addition, the film is very thin, and therefore, the relative displacements of the oil with respect to the disc are small. Thus, it can also be expected that the general shape of the film thickness distribution does not change in going from the line $\bar{y} = \bar{y}_o$ to the $\bar{x}$ axis. In particular, this implies that along the $\bar{x}$ axis, the film thickness will reach a maximum value at point B in Fig. (3.2.3,a). Point B is on the rim of the disc and therefore beyond it the film thickness along the $\bar{x}$ axis must be zero. Consequently, in the neighborhood of point B, the oil film thickness distribution must be as indicated in Fig. (3.2.3,b). Surface tension forces will tend to round up the profile at the edge, but since $h < < R$, it can be expected that in a very small region around B, the film thickness takes all the values between zero and some h_{max}.

In conjunction with Eq. (3.2.14), this boundary condition requires that all circles of uniform thickness, $o < \bar{h} < \bar{h}_{max}$, be tangent to the line $\bar{x} = 1$ at point $(1, 0)$. This solution is shown graphically in Fig. (3.2.4).
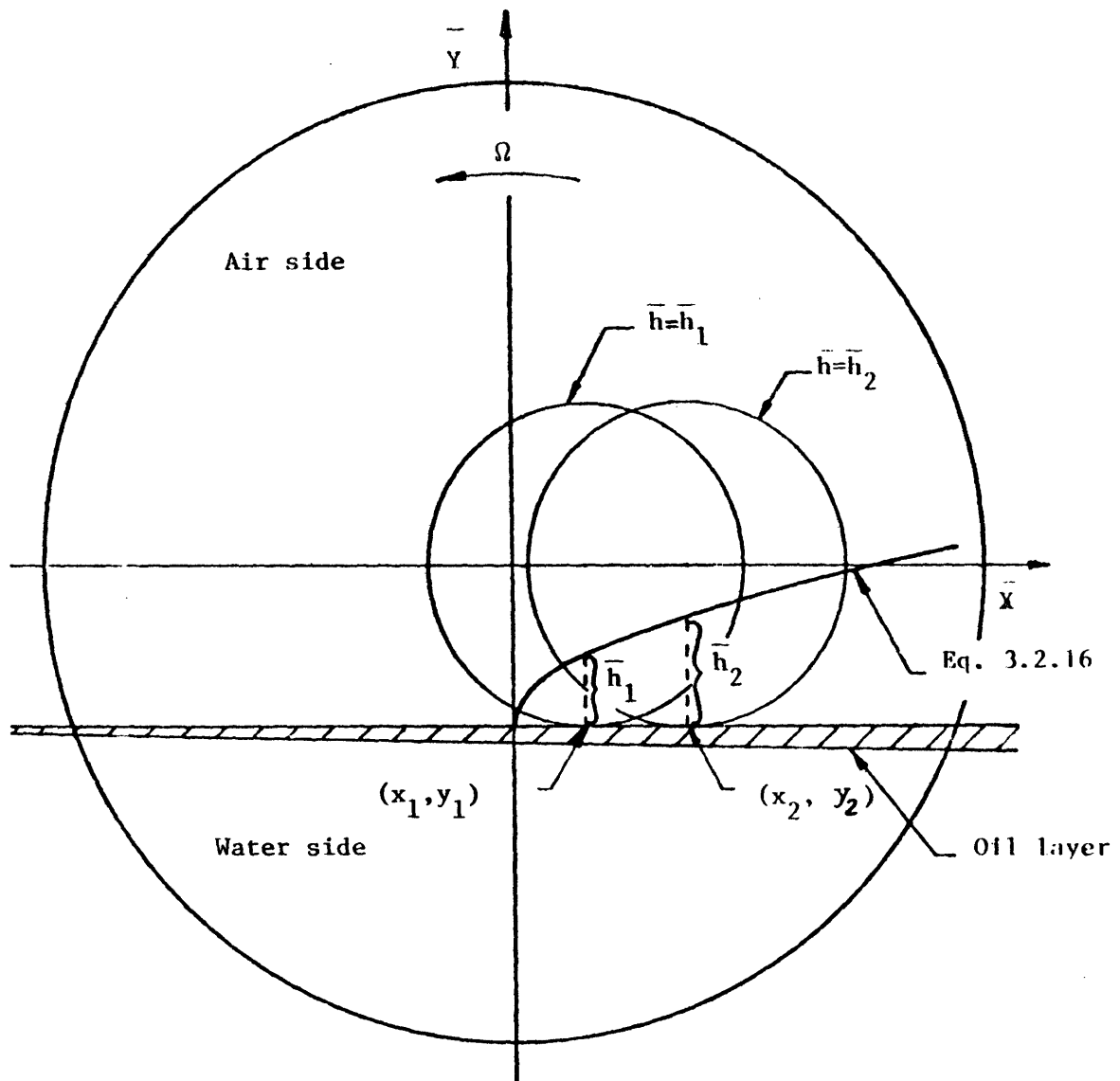
LEVICH'S BOUNDARY CONDITION

FIGURE 3.2.2

(a)

(b)
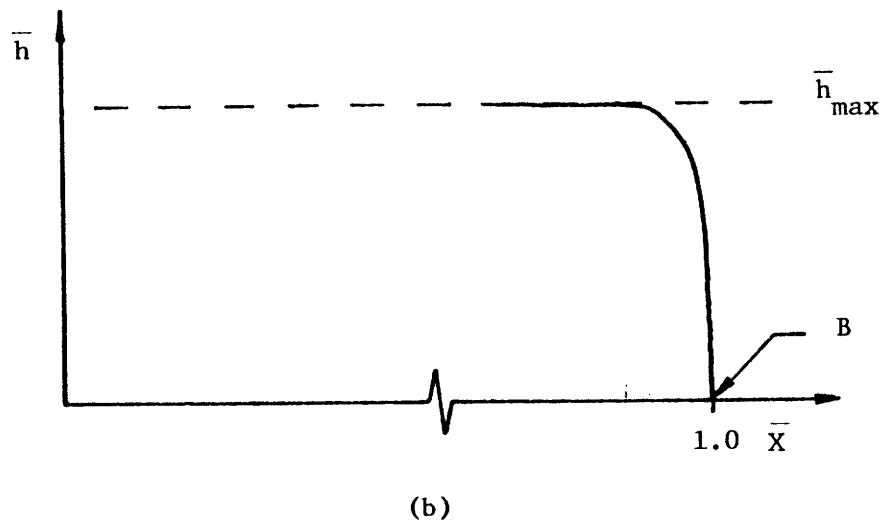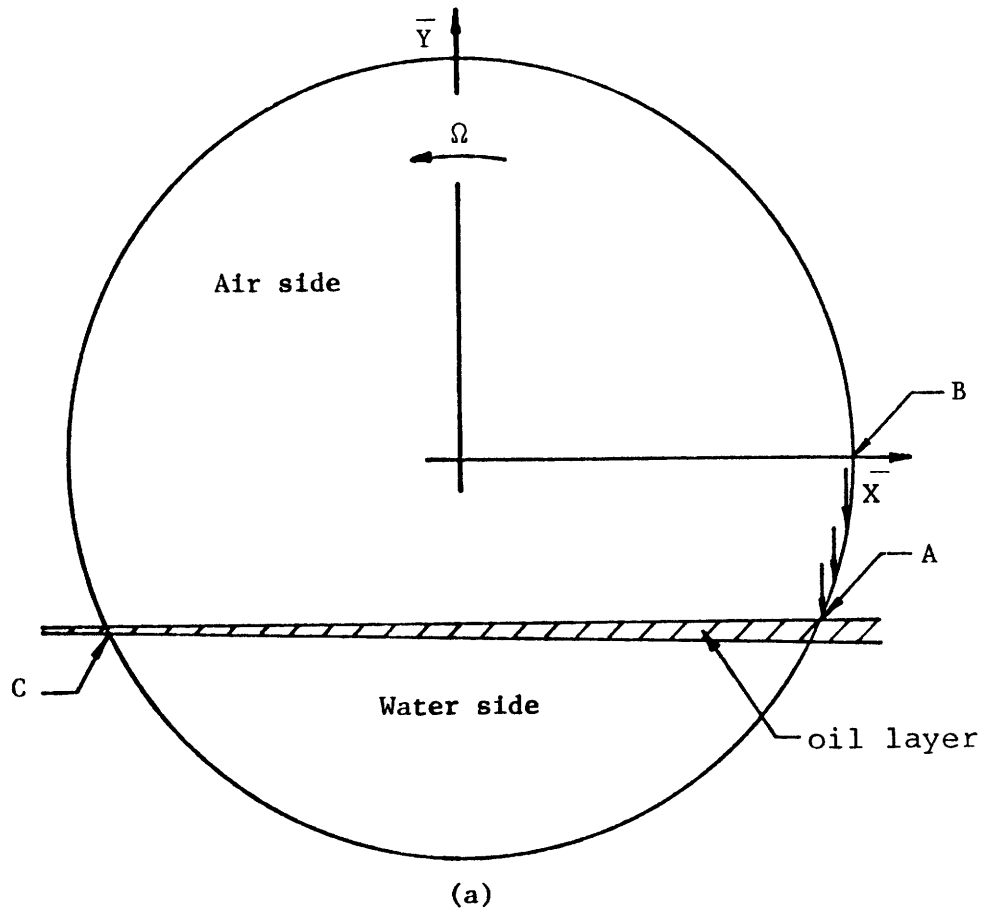
EDGE BOUNDARY CONDITION

FIGURE 3.2.3
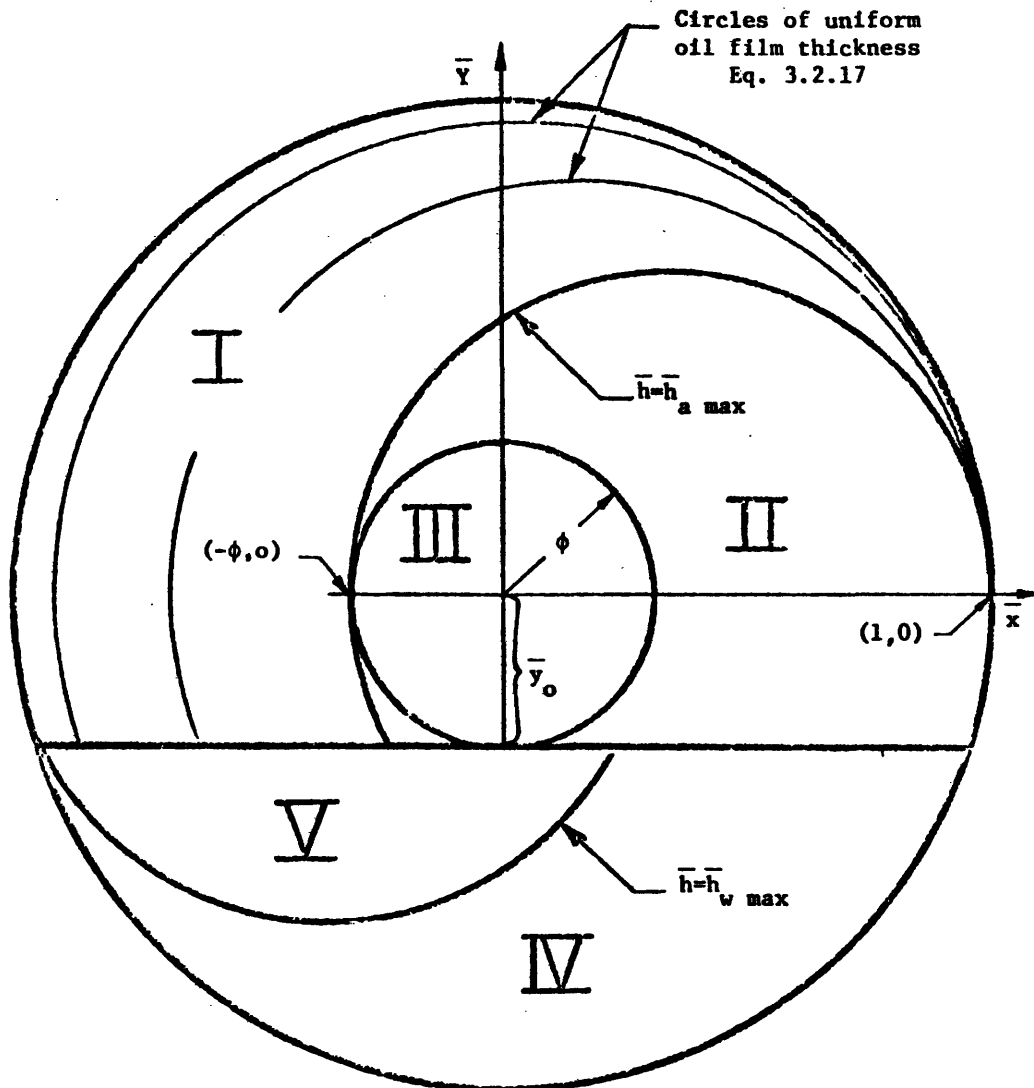
REGIONS OF DIFFERENT ANALYTICAL SOLUTIONS TO THE
OIL LAYER THICKNESS DISTRIBUTION

FIGURE 3.2.4

Substituting the boundary coordinates

$$\bar{x}_o = 1$$

$$\bar{Y}_o = 0$$

into (3.2.14), a closed form solution for $\bar{h}$ within region I is obtained:

$$\bar{h} = \left[\frac{1 - (\bar{x}^2 + \bar{y}^2)}{2(1 - \bar{x})}\right]^{1/2} \tag{3.2.17}$$

A second boundary condition is needed to generate the solution in region II. It has been observed that the oil does not flow within a circle around the axis of the disc (region III in Fig. (3.2.4)). The radius, ϕ, of this circle is slightly smaller than $\bar{y}_o$ (distance between the center of the disc and the oil layer surface), and can be expressed as

$$\phi = \bar{y}_o - \varepsilon \ (\bar{y}_o, \ \Omega) \tag{3.2.18}$$

The function ε has been empirically determined and is shown in Fig. (3.2.5). In the range $o < \bar{y}_o < .5$ the value of ε is small compared to $\bar{y}_o$ and it could be neglected. Since the oil layer thickness is small compared to the disc radius, $\bar{y}_o$ can be expressed in terms of the water level H as

$$\bar{y}_o = 1 - \frac{H}{R} = 1 - \bar{H}$$

As indicated by Eq. (3.2.17), the film thickness in region I is zero at the point (-1,0), and then increases monotonically as region III is approached along the $-\bar{x}$ axis. This implies that the film thickness in region I will reach a maximum value along the $-\bar{x}$ axis at the point $(-\phi,0)$ (Fig. (3.2.4)). Since the film thickness is zero within region III, a boundary condition similar to the one described for point (1,0) must exist

$$\bar{y}_o = 1 - \frac{H}{R}$$

Distance from the oil layer to the center of the disc

RADIUS OF REGION III

FIGURE 3.2.5

$$\epsilon = \bar{y}_o - \phi$$
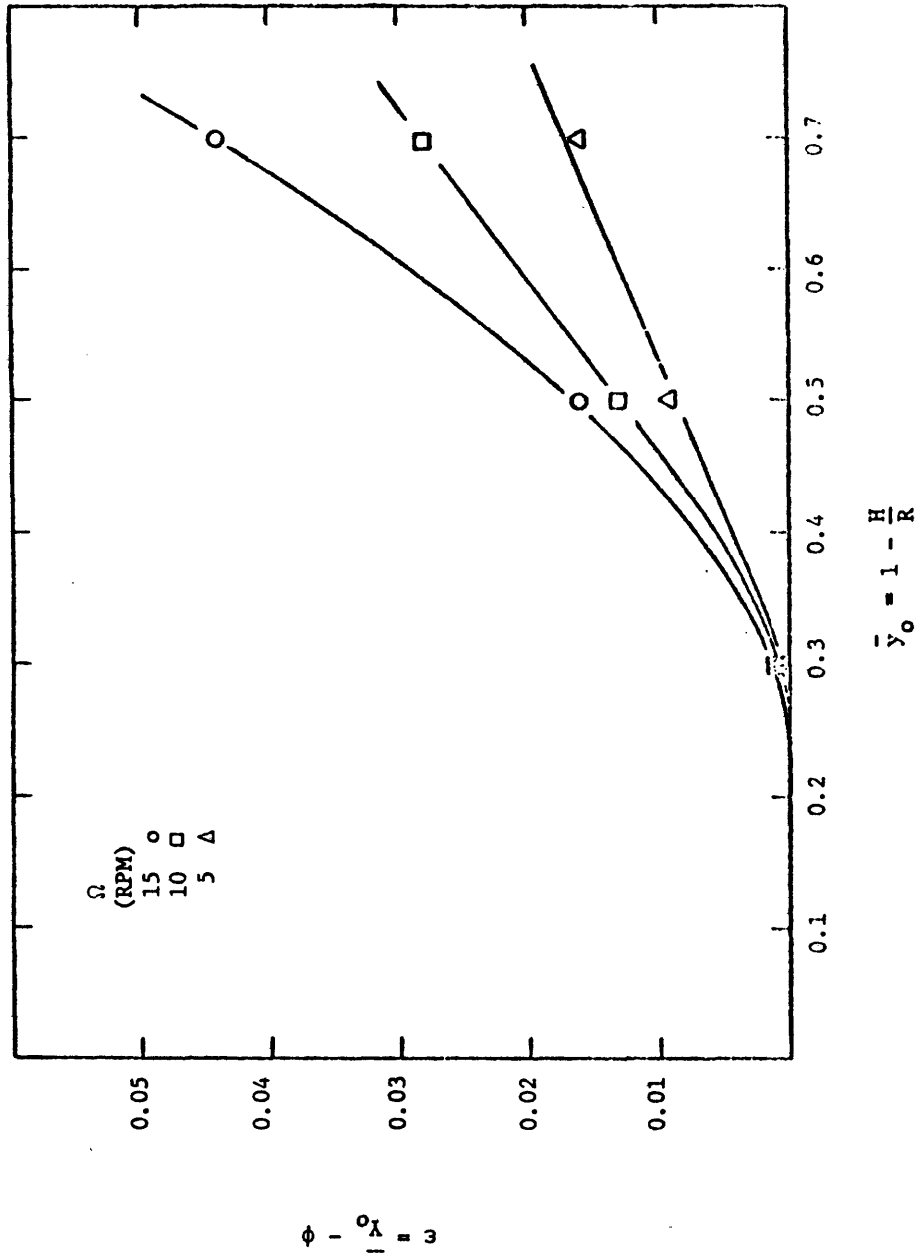
Correction for the radius of region III.

at point $(-\phi,0)$; that is, in a very small region around point $(-\phi,0)$, the film thickness must take all the values between zero and some h_{max}.

Substitution of this boundary condition into Eq. (3.2.14), yields an expression for $\bar{h}$, which is valid within region II:

$$\bar{h} = \left[\frac{(\bar{x}^2 + \bar{y}^2) - \phi^2}{2(\bar{x} + \phi)}\right]^{1/2} \tag{3.2.19}$$

The surfaces defined by Eqs. (3.2.17) and (3.2.19) intersect in the circle of maximum thickness $\bar{h}_{a\ max}$. The value of $\bar{h}_{a\ max}$ can then be determined by evaluating Eq. (3.2.19) at point $(1,0)$, or by evaluating Eq. (3.2.17) at point $(-\phi,0)$, to yield

$$\bar{h}_{a\ max} = \left[\frac{1-\phi}{2}\right]^{1/2} \tag{3.2.20}$$

or in terms of the water level,

$$\bar{h}_{a\ max} \simeq \left[\frac{H}{2R}\right]^{1/2}$$

3.2.1.2 Water side

The analysis of the oil film motion on the portion of disc below the water level, will follow the same steps as those of the air side analysis. The three-dimensional boundary layer equations will be reduced to a simpler form and then integrated to obtain the velocity profiles in the x and y directions. Integrating the equation of conservation of mass across the film thickness, a partial differential equation in $\bar{h}$ will be obtained. This equation will be solved in conjunction with some boundary conditions to obtain $\bar{h}$.

All the order of magnitude considerations made in simplifying the boundary layer equations on the air side, are also valid for the water side,

with the exception of the zero pressure gradient condition. On the water side, the pressure outside the film can be assumed to vary hydrostatically.

$$\frac{dP}{dy} = - \rho_w g$$

The boundary layer equations (3.2.1) and (3.2.2) then become

$$\frac{\partial^2 u}{\partial z^2} = 0 \qquad (3.2.21)$$

$$\frac{\partial^2 v}{\partial z^2} = \frac{g}{\nu} (1 - \frac{\rho_w}{\rho_o}) \qquad (3.2.22)$$

The boundary conditions for the velocities are:

At $z = 0$ $\quad u = -\Omega y$

$\qquad\qquad v = \Omega x$

At $z = h$ $\quad \dfrac{\partial u}{\partial z} = \dfrac{\tau_x}{\mu_o}$ $\qquad$ and $\qquad \dfrac{\partial v}{\partial z} = \dfrac{\tau_y}{\mu_o}$

where τ_x and τ_y are the shear stresses at the oil water interface. Integrating Eqs. (3.2.21) and (3.2.22) twice, and introducing the boundary conditions yields

$$u = \frac{\tau_x}{\mu_o} z - \Omega y \qquad (3.2.23)$$

and

$$v = \left[\frac{g(1 - \frac{\rho_w}{\rho_o})}{2\nu} \right] z^2 + \left[\frac{\tau_y}{\mu_o} - g \frac{(1 - \frac{\rho_w}{\rho_o})}{\nu_o} h \right] z + \Omega x \qquad (3.2.24)$$

The order of magnitude of the shear stresses can be estimated from

$$\frac{\tau}{\mu_o} \sim \frac{\mu_w \frac{\partial V}{\partial z}}{zo} \sim \frac{\mu_w}{\mu_o} \frac{\Omega R}{S}$$

where S is the spacing between the discs.

Therefore the shear stress term can clearly be neglected in Eq. (3.2.23).

It can also be neglected in Eq. (3.2.24) as long as

$$\frac{\Omega R}{S} << \frac{(1 - \frac{\rho_o}{\rho_w}) h}{\nu_w} \tag{3.2.25}$$

This condition is met in the range of operation of the P.C.T. and therefore,

Eqs. (3.2.23) and (3.2.24) are reduced to:

$$u = -\Omega y \tag{3.2.26}$$

$$v = \frac{(1 - \frac{\rho_w}{\rho_o})}{2\nu_o} (z^2 - 2hz) + \Omega x \tag{3.2.27}$$

Substituting these velocities into the continuity equation (3.2.3) and inte-

grating across the film thickness, a partial differential equation describing

the film thickness variation on the water side is obtained:

$$-\Omega y \frac{\partial h}{\partial x} + \Omega x + g \frac{(\frac{\rho_w}{\rho_o} - 1) h^2}{\nu_o} \frac{\partial h}{\partial y} = 0 \tag{3.2.28}$$

Substitution of the nondimensional variables defined in Eq. (3.2.10) yield

$$- \bar{y} \frac{\partial \bar{h}}{\partial x} + [\bar{x} + (\frac{\rho_w}{\rho_o} - 1)\bar{h}^2] \frac{\partial \bar{h}}{\partial \bar{y}} = 0 \tag{3.2.29}$$

By making the differential $d\bar{h}$ equal to zero, the equation defining the loci of

uniform thickness $\bar{h}$ is obtained:

$$[\bar{x} + (\frac{\rho_w}{\rho_o} - 1)\bar{h}^2]^2 + \bar{y}^2 = [\bar{x}_o + (\frac{\rho_w}{\rho_o} - 1)\bar{h}^2] + \bar{y}_o^2 \tag{3.2.30}$$

In order to find a solution for $\bar{h}$, boundary conditions must be specified. The arguments used in deriving the boundary condition at point B on the air side also apply to point C (Fig. 3.2.3,a) on the water side. Therefore, one boundary condition is that at point C, $\bar{h}$ takes all the values between zero and some $\bar{h}_{wmax}$. Substitution of the coordinates of point C, $(-\sqrt{1-\bar{y}_o^2}, -\bar{y}_o)$, into Eq. (3.2.30) yields:

$$\bar{h} = \frac{1}{[\frac{\rho_w}{\rho_o} - 1]^{1/2}} \left[\frac{1 - (\bar{x}^2 + \bar{y}^2)}{2(\bar{x} + \sqrt{1 - \bar{y}_o^2})} \right]^{1/2} \tag{2.3.1}$$

This solution is valid in region IV. A second boundary condition is required to specify the value of $\bar{h}_w$max and to generate a solution valid in region V (Fig. (3.2.3)).

The governing equations for the film thickness in the air and water sides are of the same form. It can therefore be expected that the film thickness distribution at the boundary where the disc enters the water, has a form similar to that along the boundary where the disc enters the air side. On the air side the thickness distribution along the line $\bar{y} = -\bar{y}_o$, $\bar{x} > 0$, can be obtained from Eq. (3.2.19)

$$\bar{h} = \left[\frac{\bar{x}^2}{2(\bar{x} + \bar{y}_o)} \right]^{1/2}$$

The term ε from Eq. (3.2.18) has been neglected. Similarly at line, $\bar{y} = -\bar{y}_o$, $\bar{x} < 0$, the thickness on the water side would then be :

$$\bar{h} = \frac{1}{\left[\frac{\rho_w}{\rho_o} - 1\right]^{1/2}} \left[\frac{\bar{x}^2}{2(\bar{y}_o - \bar{x})}\right]^{1/2} \qquad (3.3.32)$$

Eq. (3.2.32) in conjunction with Eq. (3.2.30) gives the film thickness distribution in region V.

$$\bar{h} = \frac{1}{\left[\frac{\rho_w}{\rho_o} - 1\right]^{1/2}} \left[\frac{(\bar{x}^2 + \bar{y}^2) - \bar{y}_o}{2(\bar{y}_o - \bar{x})}\right]^{1/2} \qquad (3.2.33)$$

The maximum film thickness on the water side is then obtained by substituting the coordinates of point C into Eq. (3.2.33)

$$\bar{h}_{w\ max} = \frac{1}{\left[\frac{\rho_w}{\rho_o} - 1\right]^{1/2}} \left[\frac{1 - \bar{y}_o^{\ 2}}{2(\bar{y}_o + \sqrt{1 - \bar{y}_o^2})}\right]^{1/2} \qquad (3.2.34)$$

From Eqs. (3.2.34) and (3.2.20) it can be seen that the ratio of maximum thickness for the air and water sides is approximately:

$$\frac{\bar{h}_{a\ max}}{\bar{h}_{w\ max}} \approx \left[\frac{\rho_w}{\rho_o} - 1\right]^{1/2} \qquad (3.2.35)$$

This means that for an oil with a specific gravity of .85, the film under the water would be around 2.5 times thicker than the oil film on the air side.

When the discs are operated in the starved mode, as shown in Fig. (3.2.6), the boundary condition at line $\bar{y} = -\bar{y}_o$, $\bar{x} < 0$, changes. For $\bar{x} < \bar{x}_1$, the discs do not go through the oil layer and the film thickness is therefore given by the solution in region I:

$$\bar{h} = \left[\frac{1 - (\bar{x}^2 + \bar{y}_o^{\ 2})}{2(1 - \bar{x})}\right]^{1/2} \qquad (3.2.36)$$
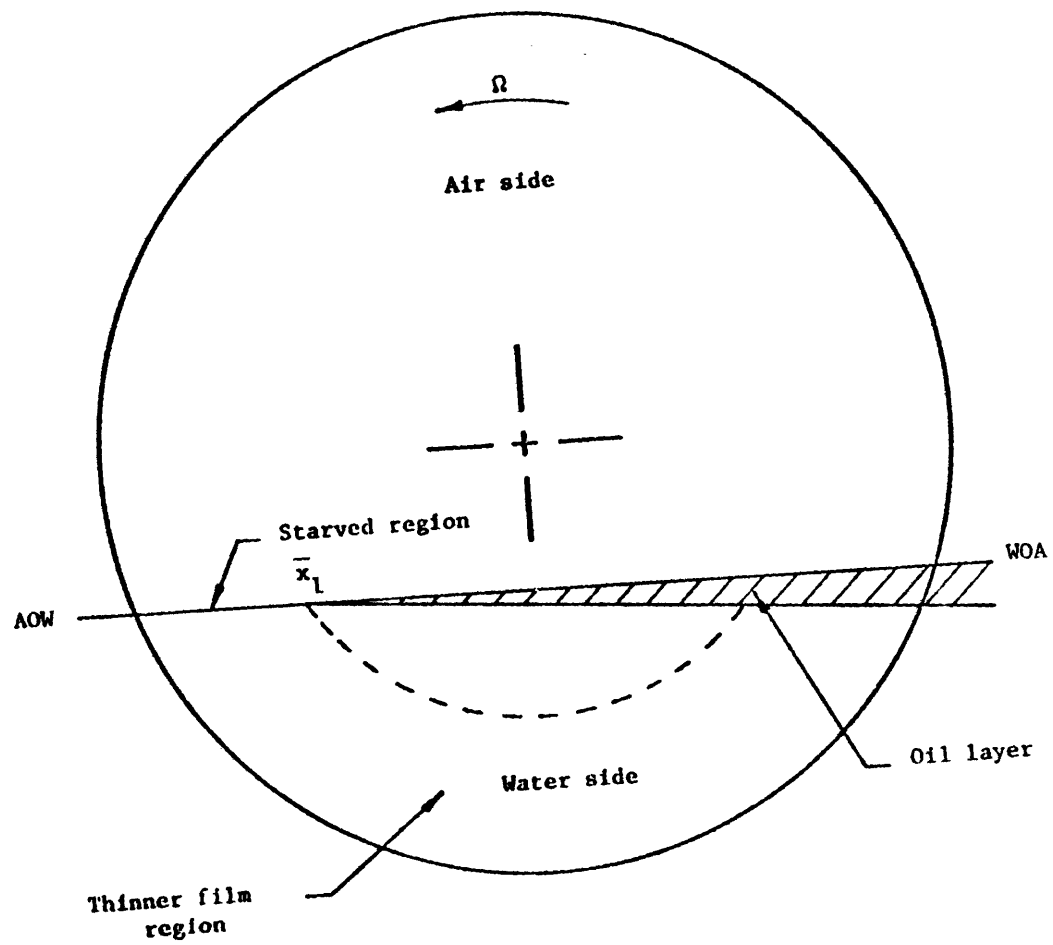
STARVED MODE OPERATION

FIGURE 3.2.6

For $\bar{x} > \bar{x}_1$, Eq. (3.2.32) still holds.

To obtain the film thickness at an arbitrary point on the water side under starved mode operation, the boundary condition Eqs. (3.2.32) and (3.2.36) must be solved simultaneously with Eq. (3.2.30). The form of Eq. (3.2.30) lends itself to a graphical solution as shown in Fig. (3.2.7). The boundary condition is drawn at the line $\bar{y} = \bar{y}_0$, $\bar{x} < 0$. The center of the loci of uniform thickness $\bar{h}$ is given in Eq. (3.2.30) as

$$\bar{x} = - \left[\frac{\rho_w}{\rho_o} - 1 \right] \bar{h}^2 \qquad (3.2.37)$$

This parabola is drawn with $\bar{h}$ along the $\bar{Y}$ axis. The circle of uniform thickness represented in Eq. (3.2.30) can then be drawn as indicated in Fig. (3.2.7). The size of the starved region is a function of both the angular velocity and the oil layer thickness. It can vary from zero (dry mode operation) to the intersection of the curves represented by Eqs. (3.2.32) and (3.2.36). Beyond this point, the film thickness on the air side is larger than that on the water side. This means that oil is being added to the oil layer as the disc goes through it, and therefore, the oil layer thickness cannot be zero.

In summary, the expressions derived for the oil film thickness on the different regions of the disc surface are:

Air side:

Region I $\qquad \bar{h} = \left[\dfrac{1 - (\bar{x}^2 + \bar{y}^2)}{2\,(1-\bar{x})} \right]^{1/2}$

Region II $\qquad \bar{h} = \left[\dfrac{(\bar{x}^2 + \bar{y}^2) - \phi^2}{2\,(\bar{x} + \phi)} \right]^{1/2}$

$$\bar{h}_a \mathrm{max} = \left[\frac{1-\phi}{2} \right]^{1/2}$$
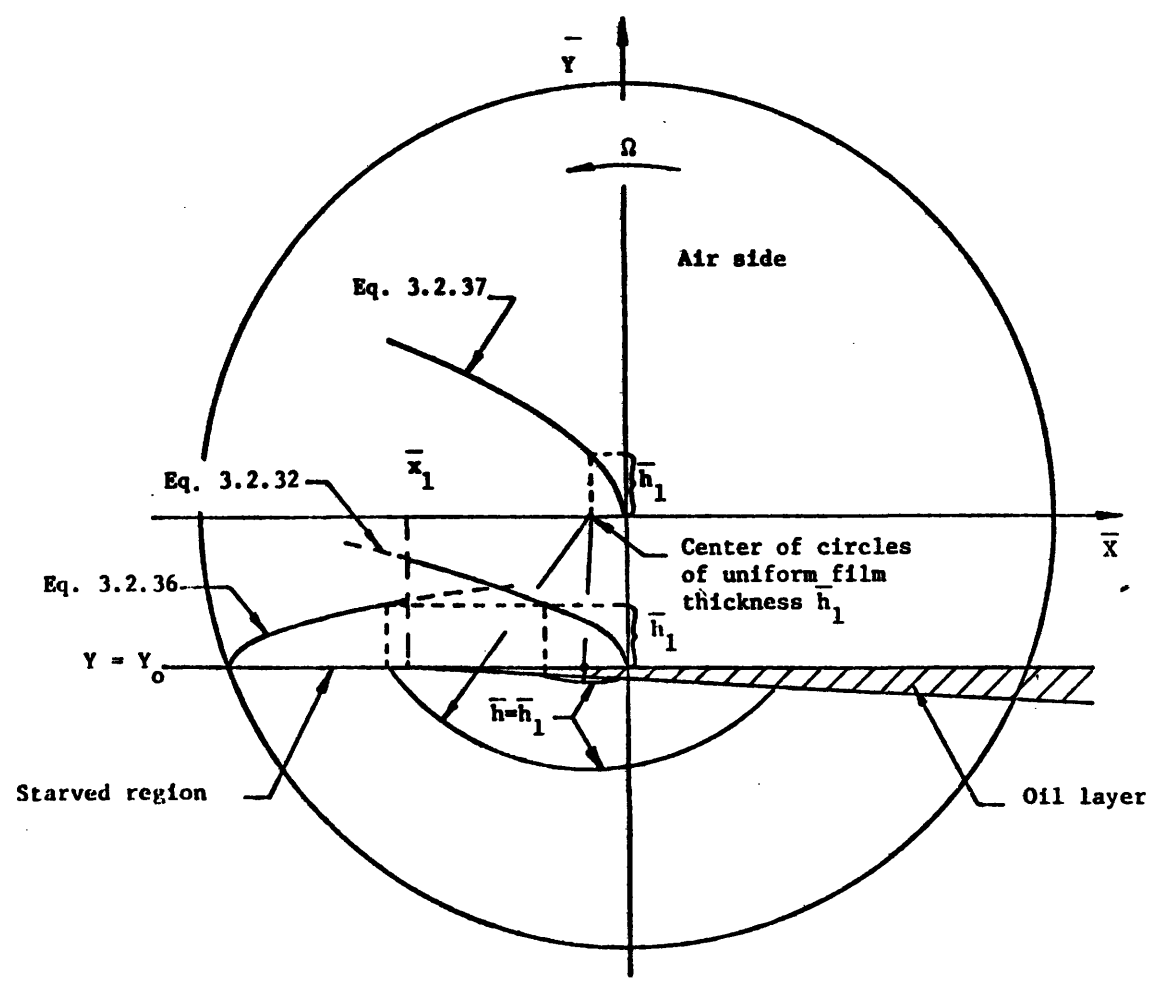
GRAPHICAL SOLUTION TO THE OIL FILM THICKNESS

DISTRIBUTION ON THE WATER SIDE UNDER STARVED MODE OPERATION

FIGURE 3.2.7

Water side:

Region IV
$$\bar{h} = \frac{1}{\left[\frac{\rho_w}{\rho_o}-1\right]^{1/2}}\left[\frac{1-(\bar{x}^2+\bar{y}^2)}{2\,(\bar{x}+\sqrt{1-\bar{y}^2})}\right]^{1/2}$$

Region V
$$\bar{h} = \frac{1}{\left[\frac{\rho_w}{\rho_o}-1\right]^{1/2}}\left[\frac{(\bar{x}^2+\bar{y}^2-\bar{y}_o^2)}{2\,(\bar{y}_o-\bar{x})}\right]^{1/2}$$

$$\bar{h}_{w\,max} = \frac{1}{\left[\frac{\rho_w}{\rho_p}-1\right]^{1/2}}\left[\frac{1-\bar{y}_o^2}{2\,(\bar{y}_o+\sqrt{1-\bar{y}_o^2})}\right]^{1/2}$$

For starved mode operation, a closed form solution for $\bar{h}$ has not been found, but its value can be obtained from Eqs. (3.2.36) and (3.2.30) by an iterative procedure, or by the graphical method described above.

Region III on the air side does not participate in the heat transfer process, since it remains constantly in the air stream. Therefore, the thickness of the oil film in this region does not affect the performance of the P.C.T. Empirical observations indicate that the film thickness here is close to zero.

The equations describing the boundaries between the different regions are:

Air side:

Regions I and II
$$[\bar{x}-\bar{h}^2]^2+\bar{y}^2=[1-\bar{h}_{a\,max}^2]^2 \qquad (3.2.38)$$

Regions II and III
$$\bar{x}^2+\bar{y}^2=\phi^2 \qquad (3.2.39)$$

Water side:

$$\text{Regions IV and V} \qquad [\bar{x} + \bar{h}^2_{w\ max}]^2 + \bar{y}^2 = [(1-\frac{H}{R}) + \bar{h}^2_{w\ max}]^2 \qquad (3.2.40)$$

The film thickness distribution for $\bar{y}_o = .3$ is shown graphically in Fig. (3.2.8).

According to the model developed here, the parameters which affect the thickness of the oil film are: water level; disc tip speed; kinematic viscosity; and specific gravity of the oil. Their effect on the oil film thickness is shown graphically in Figs. (3.2.9) and (3.2.10).

3.2.2 Experimental Measurements

The empirical oil film thickness distribution was determined from measurements of the oil volume flow rate across small sections of the disc surface. Measurements were taken at three positions: along lines 1 and 3 on the air side and along position 2 on the water side (Fig. (3.2.11)). The experimental setup was the same as described in section (3.1) and shown schematically in Fig. (3.1.2). The oil used was Texaco TI-10150, which has a specific gravity of .85 and a kinematic viscosity of 11.06 centistokes @ 130°F. The oil layer thickness was approximately one inch, and for all but one set of measurements, it covered the entire water surface. The one exception was when measurements were taken on the water side under starved mode operation. In this case, vertical barriers were set across the oil layer at the $\bar{x}$=o position. Due to the pumping action of the rotating discs, the oil accumulated on the WOA side of the oil layer (x>o in Fig. 3.2.11), leaving the other side starved of oil.

3.2.2.1 Apparatus

To measure the oil volume flow rate, the oil film across a small
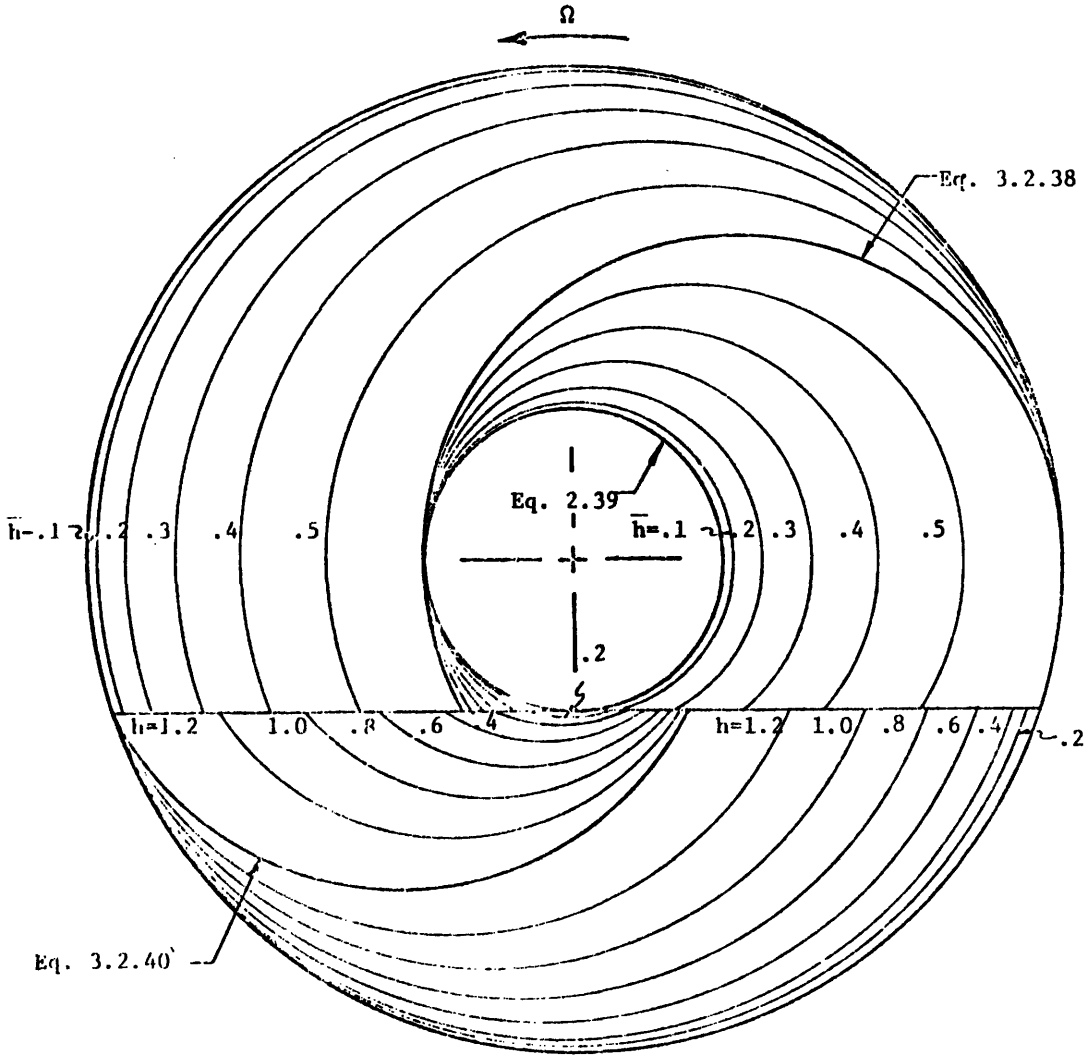
ANAYLTICAL SOLUTION TO THE OIL FILM THICKNESS

DISTRIBUTION SHOWING CIRCLES OF UNIFORM THICKNESS

FIGURE 3.2.8

$$h_{w_{max}}\left[\frac{g\left(\frac{\rho_w}{\rho_o}-1\right)}{v_o \Omega R}\right]^{1/2}$$

$$h_{a_{max}}\left[\frac{g}{v_o \Omega R}\right]^{1/2}$$

Maximum oil film thickness $\bar{h}_{max}$

$$\bar{H} = \frac{H}{R}$$

Nondimensional water level
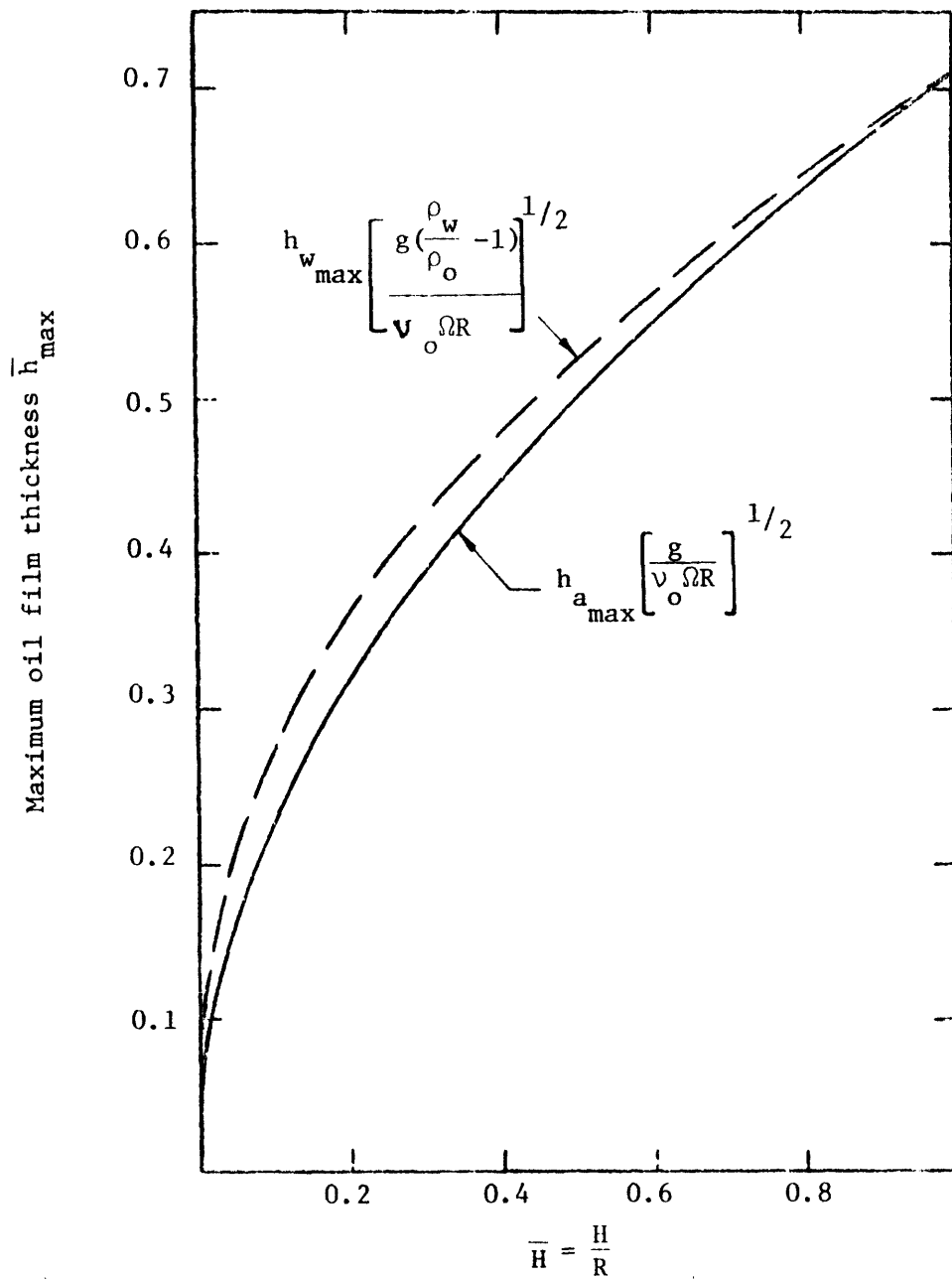
MAXIMUM OIL FILM THICKNESS AS A FUNCTION OF

WATER LEVEL

FIGURE 3.2.9

The graph shows curves labeled with viscosity values. The y-axis is "Oil film thickness $\frac{h}{h}$ (mils)" with gridlines at 10, 20, 30, 40, 50. The x-axis is "Ω R — Tip speed (RPM - inch)" with values at 50, 100, 150.

Curve labels: $\nu = 1.50 \frac{Ft^2}{hr}$, 1.25, 1.00, 0.75, 0.50, 0.25, 0.10
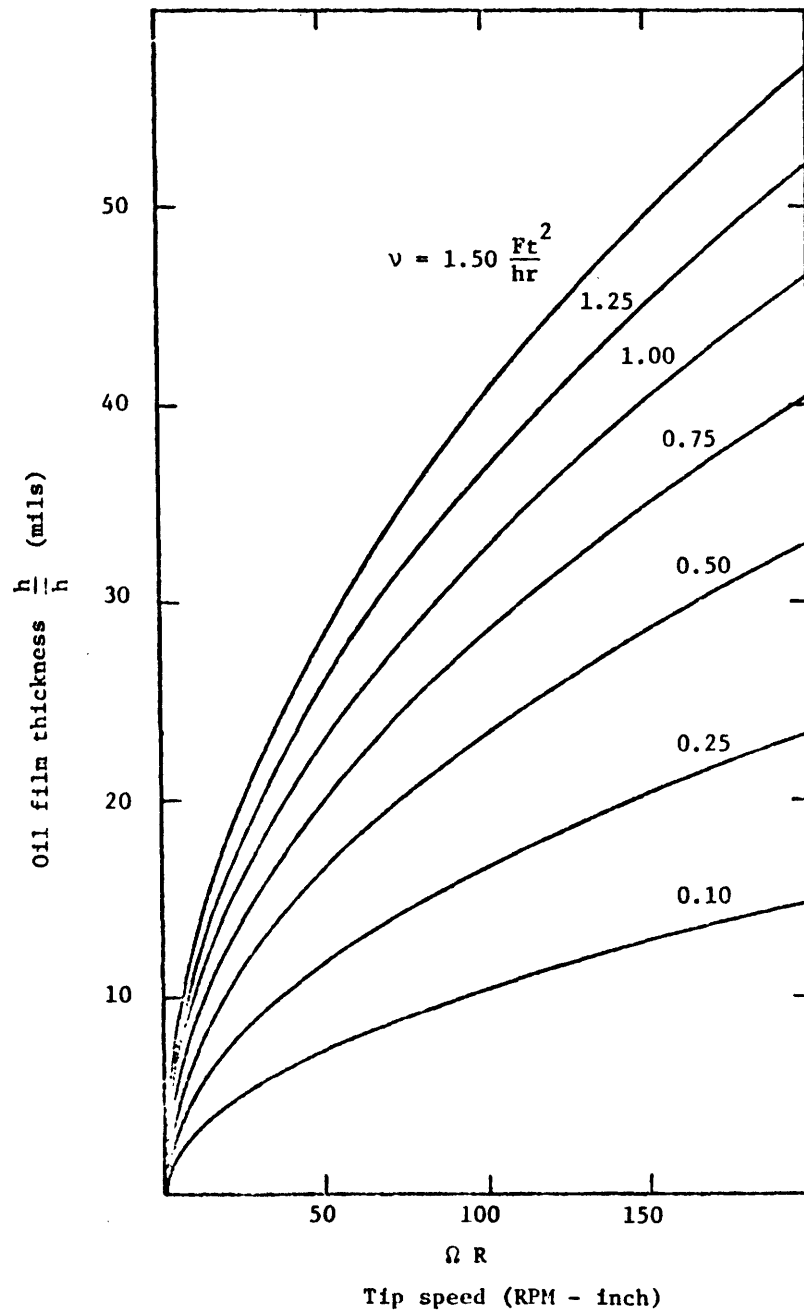
OIL FILM THICKNESS AS A FUNCTION OF TIP SPEED AND OIL VISCOSITY

FIGURE 3.2.10
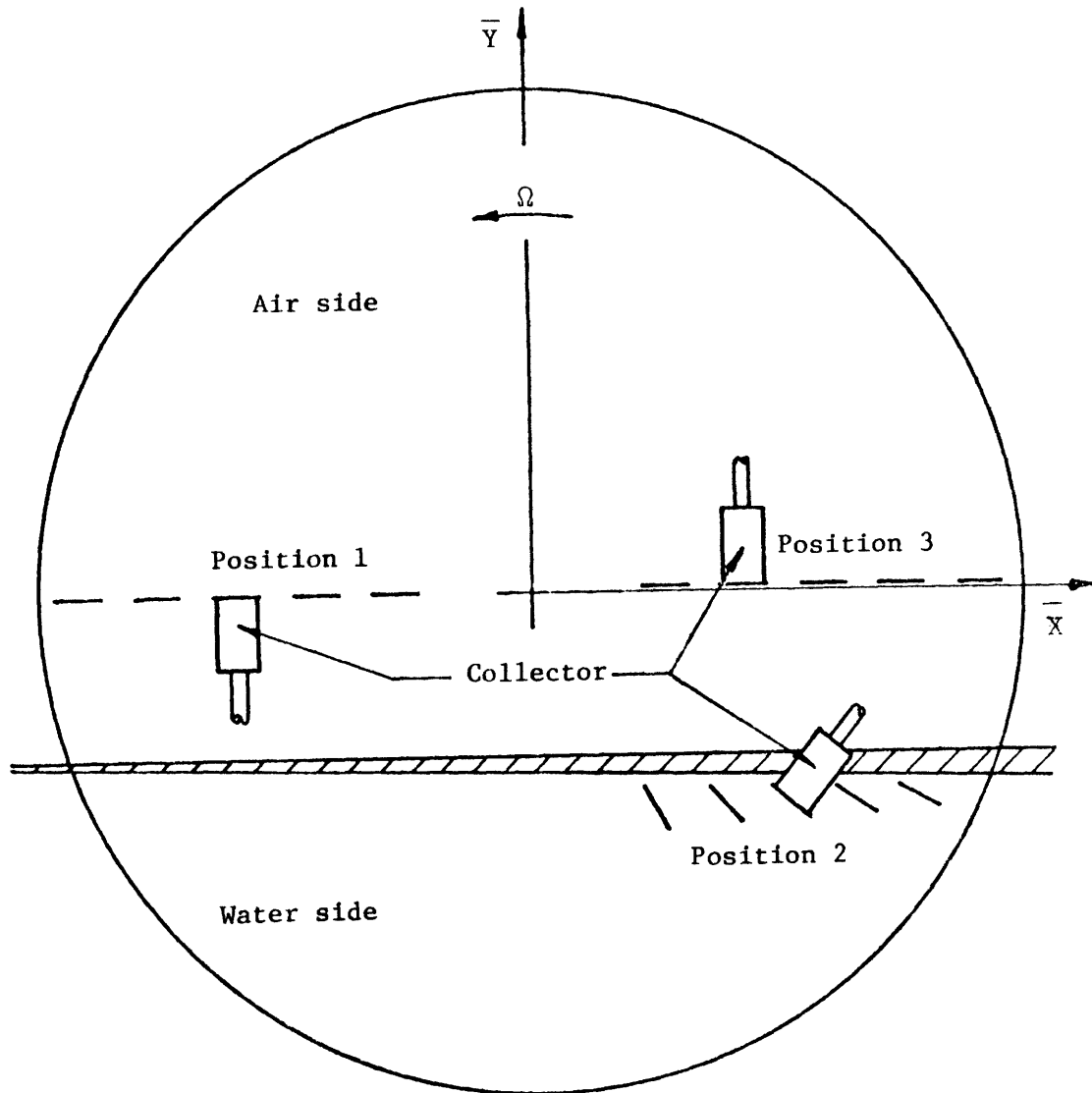
LOCATION OF OIL FILM THICKNESS MEASUREMENTS

FIGURE 3.2.11

section of the disc was wiped off, for a specified number of revolutions, and the oil was then collected in a graduated cylinder. At position 1 on the air side, and position 2 on the water side, the oil flowed freely into the collecting device, due to gravity and flotation forces. The collector used at these two positions is shown in Fig. (3.2.12,a). It consisted of a rectangular box with a U-shaped opening on one side. This opening was 15/16" wide, and was lined with a rubber wiper. A 1/4" plastic hose connected the collector to a 50ML graduated cylinder.

At position 3 on the air side, the situation is somewhat different. The velocity of the disc at this position is upward, and therefore, the collector must be placed with its opening facing down. Gravity forces tend to pull the oil away from the collector. To override this effect, it was necessary to apply suction to the collector. A faucet pump was used for this purpose. It was also observed at this position, that unless all the oil in contact with the collector was sucked away, the film thickness ahead of the collector was disturbed. This, in turn, would cause the measurements to be in error. Different collector geometries were tested, and the one shown in Fig. (3.2.12,b) was found to have the least effect on the surrounding oil film.

For measurements on the air side, the collectors were hand held against the disc. A typical measurement involved holding the collector at the desired position for a specified number of revolutions and recording both the time and the total volume of oil collected.

On the water side, the collector was positioned with its opening perpendicular to the radial direction and held against the disc by a spring loaded arm. The oil was removed from the collector by means of a siphon.
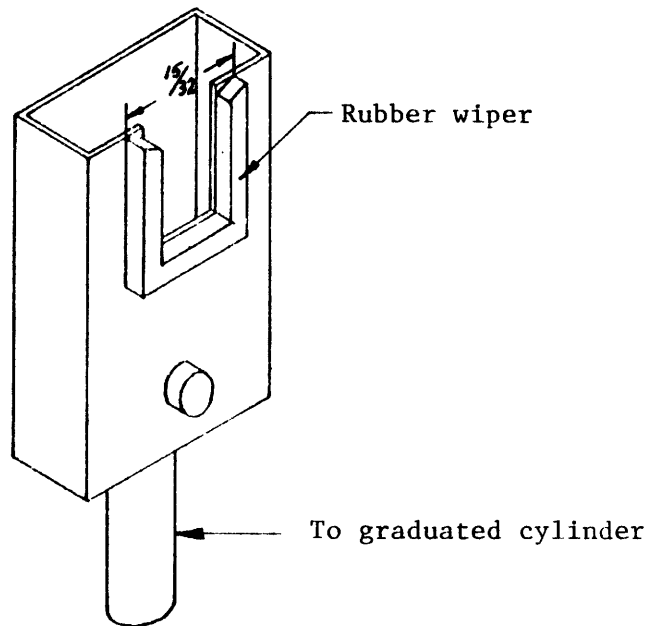
(a) Collector used at positions 1 and 2
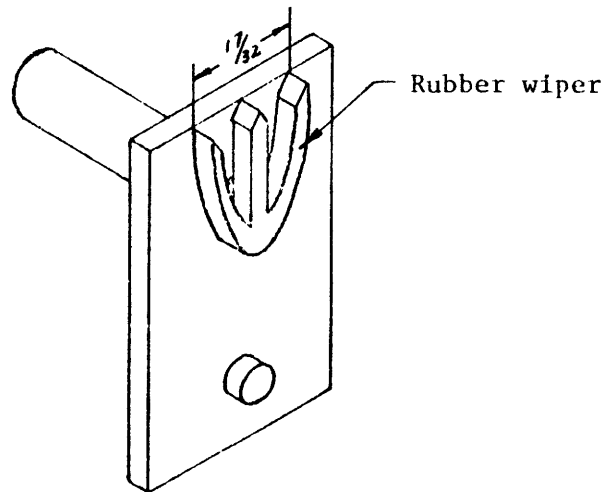
(b) Collector used at position 3

OIL COLLECTORS

Figure 3.2.12

The flow out of the collector could be regulated by raising or lowering the siphon outlet, which was mounted on a screw drive. When taking a measurement, the oil flow out of the collector was set equal to that being wiped off the disc, so that the oil water interface inside the collector remained static. Oil was then collected for a specified number of revolutions as on the air side.

3.2.2.2 Data Reduction

To determine the oil film thickness, h, from the volume of oil collected, the relative motion of the oil with respect to the disc surface must be considered. At positions 1 and 3, y=o and the velocity distribution within the film can be obtained from Eqs. (3.2.6) and 3.2.7)

$$u = o$$

$$v = \frac{g}{2\nu} (z^2 - 2hz) + \Omega x$$

By integrating the velocity across the film, the volume flow rate per unit width in the y direction can be obtained

$$Q_y = \int_o^h v dz = \Omega x h - \frac{g}{3\nu} h^3 \tag{3.2.41}$$

Q_y can also be expressed in terms of the measured oil volume V, the collection time t and the collector opening d:

$$Q_y = \frac{V}{td} \left|\frac{x}{x}\right| \tag{3.2.42}$$

Equating the left side of Eqs. (3.2.41) and (3.2.42), an expression for h is obtained

$$h^3 - \left(\frac{6\pi\nu Nx}{gt}\right) h + \frac{3\nu V}{gtd} \left|\frac{x}{x}\right| = 0 \tag{3.2.43}$$

where N is the number of revolutions. There exists a standard solution to this equation which is included in Appendix (3.A). Once h is obtained, it can be nondimensionalized using the variables defined in Eq. (3.2.10).

Measurements on the water side at position 2 involve flows in both the x and y directions. The velocity profile in the oil film on the water side is given by Eqs. (3.2.26) and (3.2.27)

$$u = -\Omega\, y$$

$$v = g \frac{(1 - \dfrac{\rho_w}{\rho_o})}{2\,\nu_o} \; (z^2 - 2hz) + \Omega\, x$$

Integration of these equations yield the volume flow rate per unit width in the x and y directions:

$$Q_x = \Omega\, y\, h$$

$$Q_y = \Omega\, x\, h \; + \; g\, \frac{(\dfrac{\rho_w}{\rho_o} - 1)}{3\,\nu}\, h^3 \qquad\qquad (3.2.44)$$

The volume flow rate per unit width in a direction normal to the radius is given by

$$Q_r = +\, Q_x \sin\beta + Q_y \cos\beta$$

where β is the angle measured from the x axis in the clockwise direction. The sine and cosine can be expressed in terms of x and y

$$\sin\beta = -\frac{y}{\sqrt{x^2 + y^2}} \qquad , \; \cos\beta = \frac{x}{\sqrt{x^2 + y^2}}$$

Therefore

$$Q_r = \left[2\pi N \; \frac{\sqrt{x^2 + y^2}}{t} \right] h \; + \left[\frac{x \; g \; (\frac{\rho_w}{\rho_o} - 1)}{3 \; \nu \; \sqrt{x^2 + y^2}} \right] h^3 \tag{3.2.45}$$

In terms of the measured quantities Q_r is given by:

$$Q_r = \frac{V}{td}$$

Combining with Eq. (3.2.45) and rearranging

$$h^3 + \left[\frac{6\pi \nu N \; (x^2 + y^2)}{g(\frac{\rho_w}{\rho_o} - 1) \; t \; x} \right] h \; - \; \frac{3\nu \; V \; \sqrt{x^2 + y^2}}{g \; (\frac{\rho_w}{\rho_o} - 1) \; t \; d \; x} = 0 \tag{3.2.46}$$

From Eq. (3.2.46) the film thickness on the water side is obtained. The solution to this equation is also included in Appendix (3.A).

3.2.2.3 Error Analysis

The constant coefficients and the coefficients multiplying h in Eqs. (3.2.43) and (3.2.46) are large as compared to unity. Therefore,

approximate solution for h can be obtained by neglecting the cubic term

$$h \simeq \frac{V}{2\pi r \; Nd} \tag{3.2.47}$$

where r stands for $\sqrt{x^2 + y^2}$

All the quantities on the right side of Eq. (3.2.47) correspond to measurements, and therefore involve some experimental error. Assuming a normal error distribution for each of the quantities measured, the overall error for the film thickness can be expressed as:

$$\left(\frac{\Delta h}{h}\right)^2 = \left(\frac{\Delta V}{V}\right)^2 + \left(\frac{\Delta r}{r}\right)^2 + \left(\frac{\Delta N}{N}\right)^2 + \left(\frac{\Delta d}{d}\right)^2 \tag{3.2.48}$$

The average values of the measured quantities and their estimated errors are:

V = 25 ± .5   ML

r = 5 ± .1   inches

N = 12 ± .1 rev

d = .5 ± 1/64   inches

Substitution of these values into Eq. (3.2.48) yields

$$\left|\frac{\Delta h}{h}\right| = .043$$

Therefore, the measured film thickness can be expected to be within 5%
of its actual value.

3.2.3   Comparison of Measurements with Theoretical Model

The parameters which influence the film thickness distribution
on the disc surface are the water level, H, and angular velocity, Ω.
Measurements were therefore taken for different combinations of H and Ω.
In Figures (3.2.13) through (3.2.20) these measurements are compared with
the results obtained from the theoretical model.

3.2.3.1   Air Side

On the air side, measurements were taken at positions 1 and 3
(Fig. 3.2.11). The results obtained at position 1 are shown in Fig.
(3.2.13). Film thicknesses under five different operating conditions are
included in this graph. The broken lines represent the analytical solution
given by Eq. (3.2.17). In each set of measurements there was a noticeable
increase in the film thickness in the vicinity of $\bar{x} = \frac{H}{R}$. This was due
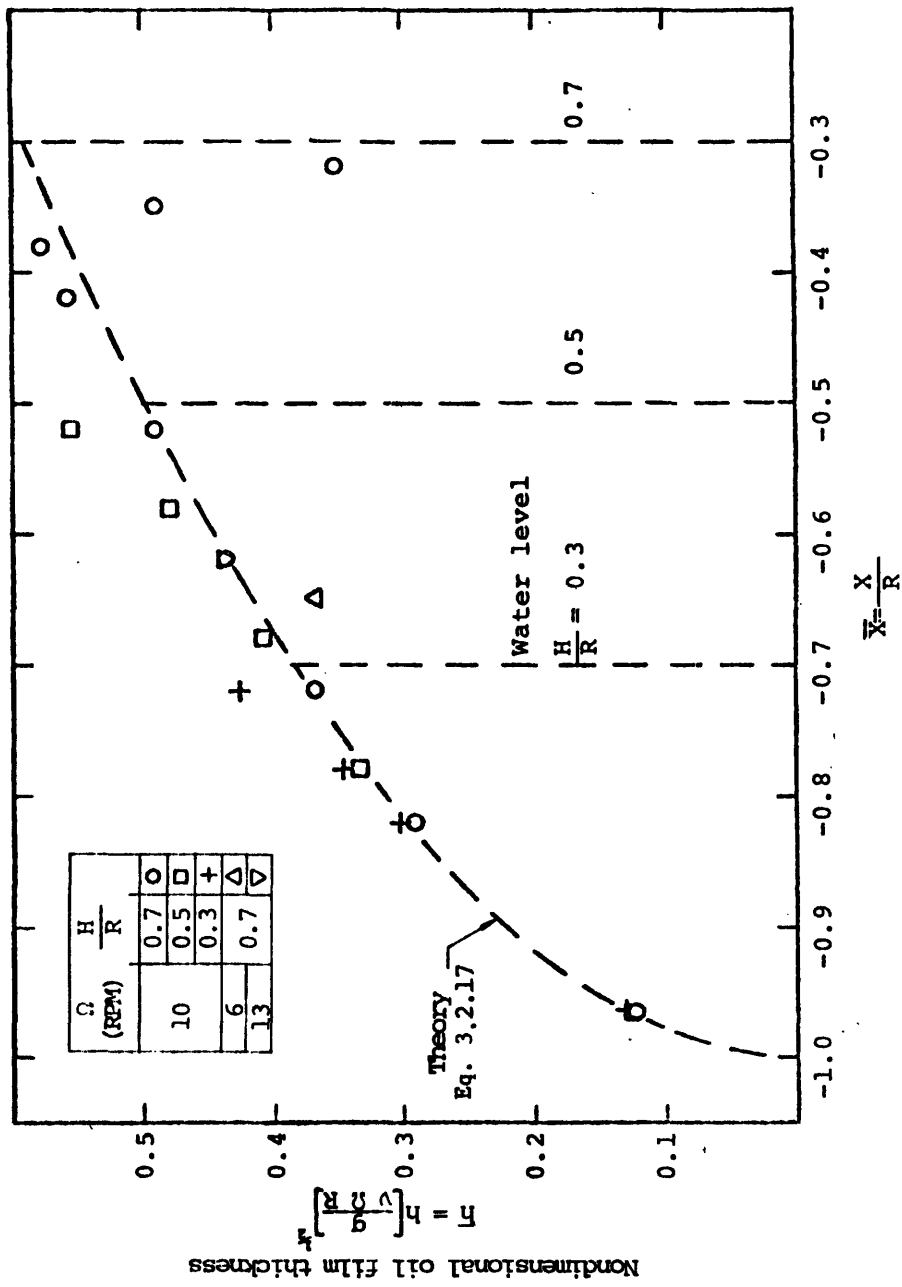
Horizontal axis of the disc

OIL FILM THICKNESS AT POSITION 1

FIGURE 3.2.13

to the presence of the oil ridge described in section (3.1.2) To determine whether surface tension effects from this oil ridge had any influence on the overall film thickness, the ridge was temporarily eliminated by means of a rubber wiper. The film thickness was then measured and the results are shown in Fig. (3.2.14). It can be seen, that the film thickness remains the same throughout the $-\bar{x}$ axis, and only the peak at $-\bar{x} = \dfrac{H}{R}$ disappears. This result is in agreement with the analytical model which indicates that the film thickness distribution in region I (Fig. (3.2.3)) is independent of the value of the maximum thickness at point (1,0). Furthermore, although the oil film in the ridge is thicker than predicted by the model, the width of the ridge is very small as compared to the radius of the disc. Therefore, the increase in overall oil volume flow rate due to the presence of the ridge is also small, and could not affect the overall thickness distribution significantly.

A similar set of measurements was taken at position 3. They are shown in Fig. (3.2.15). The broken lines represent the solutions as given by Eq. (3.2.19) with $\phi = (1 - \dfrac{H}{R})$. The dotted lines correspond to this same equation, with the values of ϕ corrected according to Fig. (3.2.5). Again, the presence of the oil ridge is revealed by the marked increase in thickness near $\bar{x} = 1$. This is the only significant deviation from the analytical solution, and as was shown by the measurements at position 1, its effect is localized.

3.2.3.2 Water side

The film thickness measurements taken on the water side at position 2 are shown in Figs. (3.2.16) and (3.2.17). They were taken with a water level H = 0.5 and three different angular velocities, 5, 10
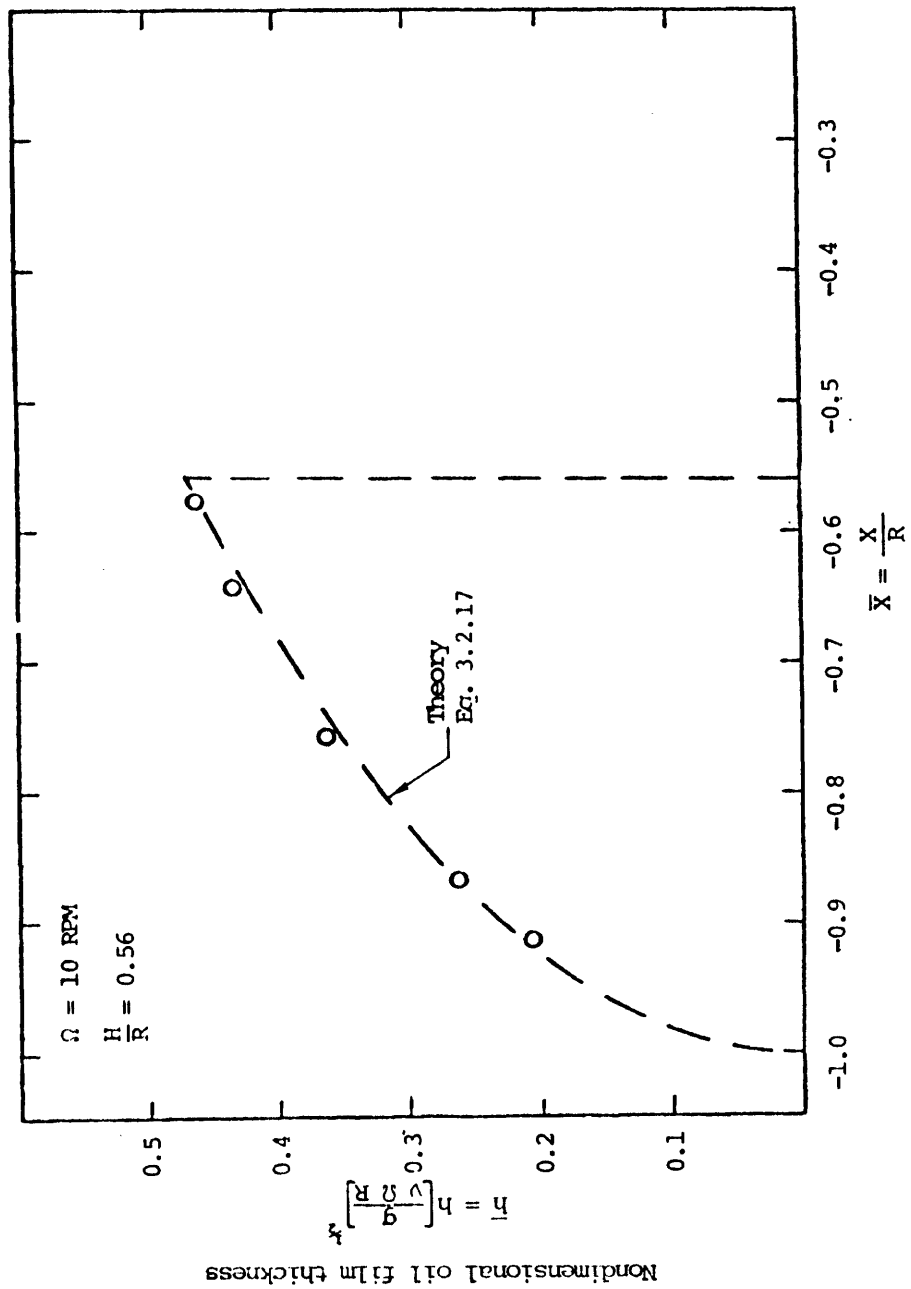
Horizontal axis of the disc

OIL FILM THICKNESS AT POSITION 1 WITH OIL RIDGE REMOVED

FIGURE 3.2.14

Horizontal axis of the disc

$$\bar{X} = \frac{X}{R}$$
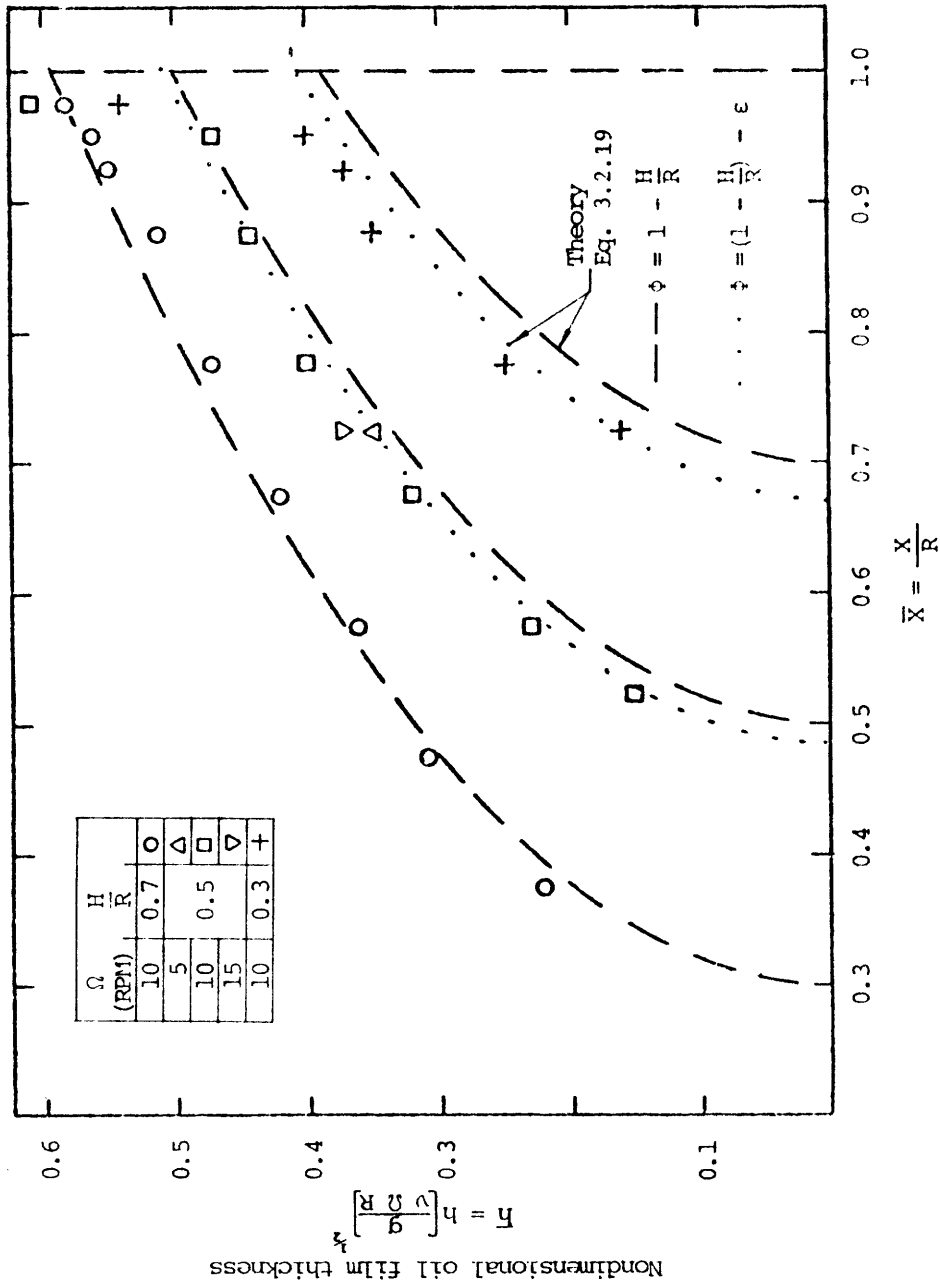
OIL FILM THICKNESS AT POSITION 3.

FIGURE 3.2.15
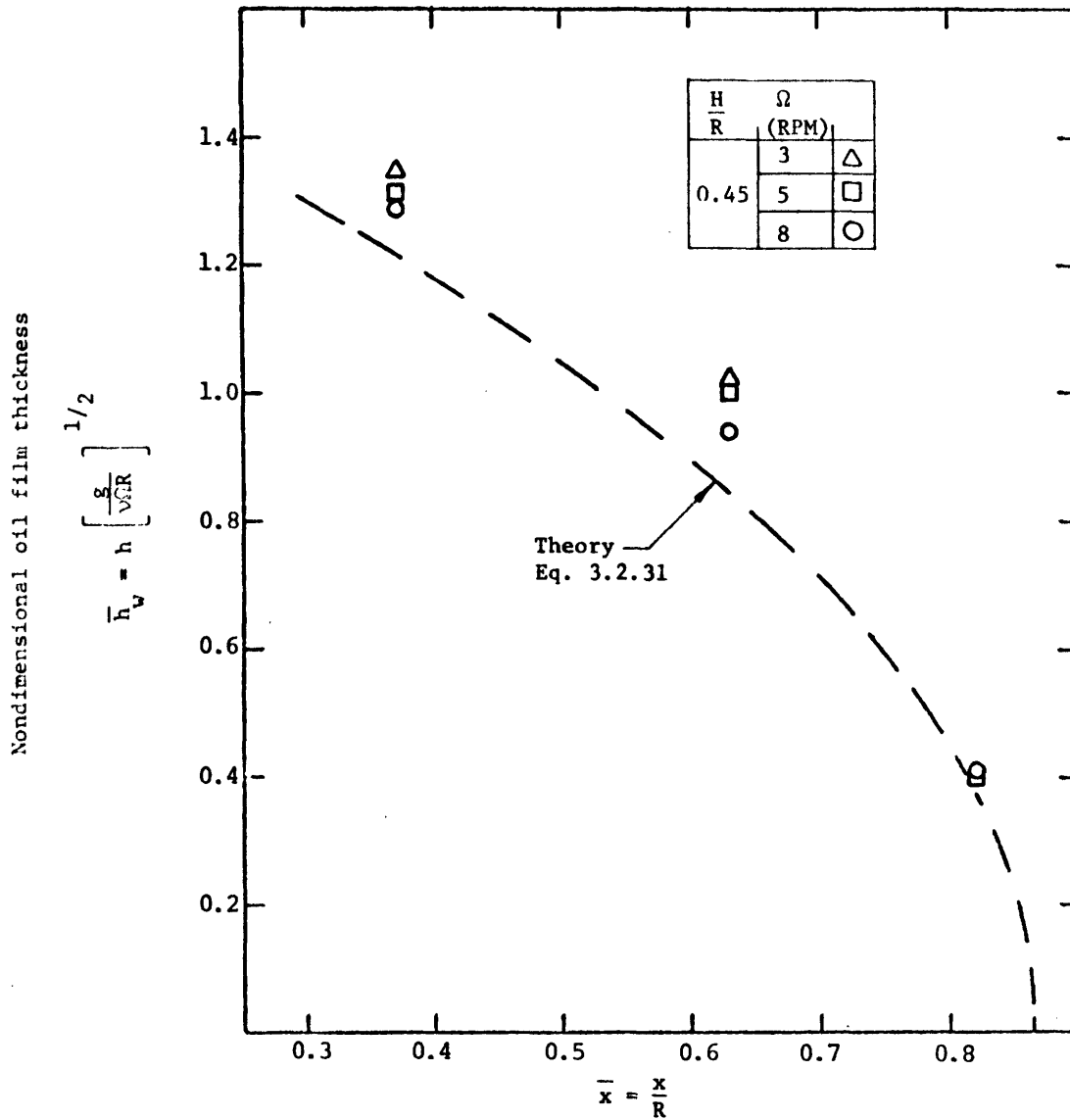
Line parallel to horizontal axis of disc at $\overline{Y}=-0.5$

OIL FILM THICKNESS ON THE WATER SIDE AT
POSITION 2 UNDER DRY MODE OPERATIONS

FIGURE 3.2.16
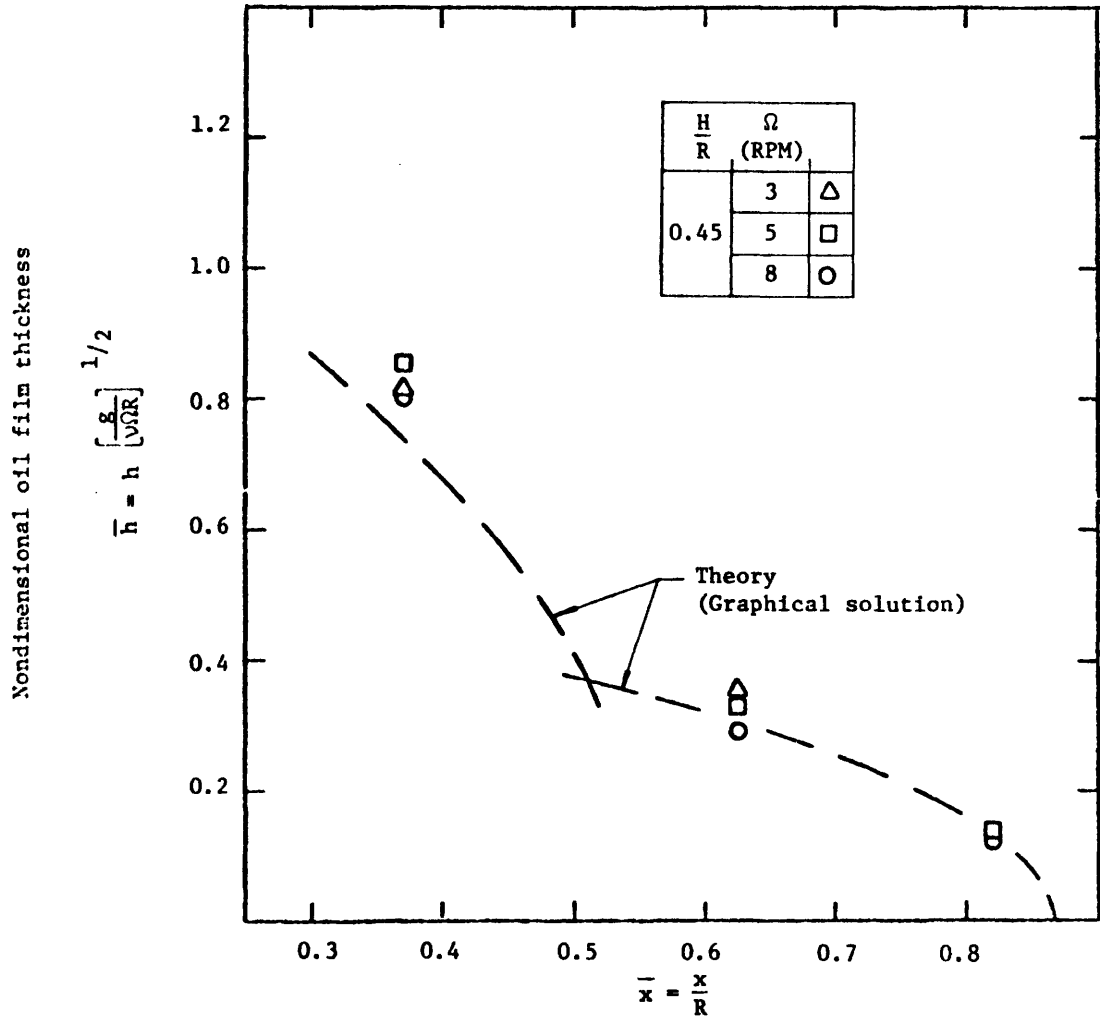
Line parallel to horizontal axis of the disc at $\overline{Y}$ = -0.5

OIL FILM THICKNESS ON THE WATER SIDE AT POSITION
2 UNDER STARVED MODE OPERATION

FIGURE 3.2.17

and 15 RPM. Fig. (3.2.16) corresponds to the unstarved operation mode and the broken line represents the solution given by Eq. (3.2.31). The results shown in Fig. (3.2.17) were taken under starved conditions with $\bar{x}_1 \simeq$ -o.6. The broken line represents the analytical solution obtained using the boundary conditions given by Eqs. (3.2.32) and (3.2.36).

3.2.3.3 Finks' Data

Measurements of the oil film thickness on a rotating disc were previously made by Fink [14]. His measurements were taken on a 5 foot diameter disc using Silicon oil. He measured the film thickness at several positions on the air side for different operating conditions. Figs. (3.2.18), (3.2.19) and (3.2.20) show the thicknesses measured along the $+\bar{x}$ axis, the $+\bar{y}$ axis and the $-\bar{x}$ axis respectively. The broken lines represent again the analytical solutions.

It can be seen from Figs. (3.2.18) through (3.2.20) that the analytical solution is generally within experimental error of the empirical measurements. The only real discrepancy arises in the measurements taken at 129°F along the $+\bar{x}$ axis (Fig. 3.2.18). There are reasons to believe that these measurements might be in error. First, unlike all other film thickness measurements, these measurement do not collapse into a single curve when represented in the nondimensional variables $\bar{x}$, $\bar{y}$ and $\bar{h}$. Second, the data for 129°F along the $+\bar{x}$ axis indicates that the oil film thickness is reduced towards the edge of the disc. This is contrary to the results of all other measurements taken at this location. Finally, as described in section (3.2.2.1), it is not unlikely that erroneous measurements are obtained at this position, resulting from the disturbance of the oil film due to the presence of the collector.

TEMP °F	Ω (RPM)	DISC SIDE	
58	4	Front	O
			△
129		Back	▽

Nondimensional oil film thickness

$$\bar{h} = h \left[\frac{g}{\nu \Omega R} \right]^{1/2}$$

Eq. 3.2.19

$$\phi = 1 - \frac{H}{R}$$

$$\bar{x} = \frac{x}{R}$$

Horizontal axis of the disc
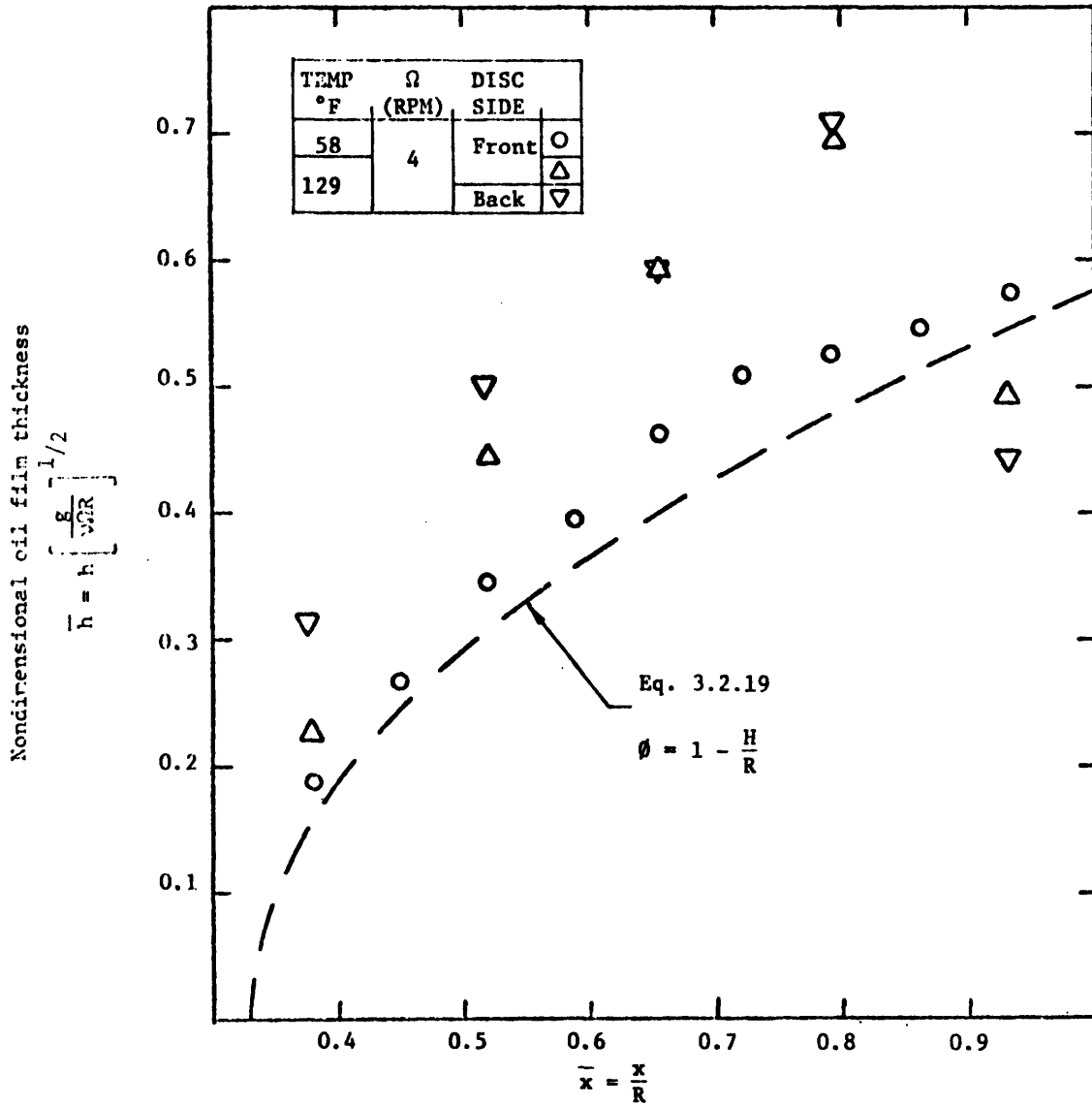
OIL FILM THICKNESS ALONG + $\bar{x}$ AXIS
(Data taken by Fink [14])

FIGURE 3.2.18

TEMP °F	Ω (RPM)	DISC SIDE	
	2		+
58	4	Front	O
	6		□
129	4		△
		Back	▽

Nondimensional oil film thickness

$$\bar{h} = h \left[\frac{g}{\nu \Omega R} \right]^{1/2}$$

Theory Eq. 3.2.17

Theory Eq. 3.2.19

$$\bar{Y} = \frac{Y}{R}$$

Vertical axis of the disc
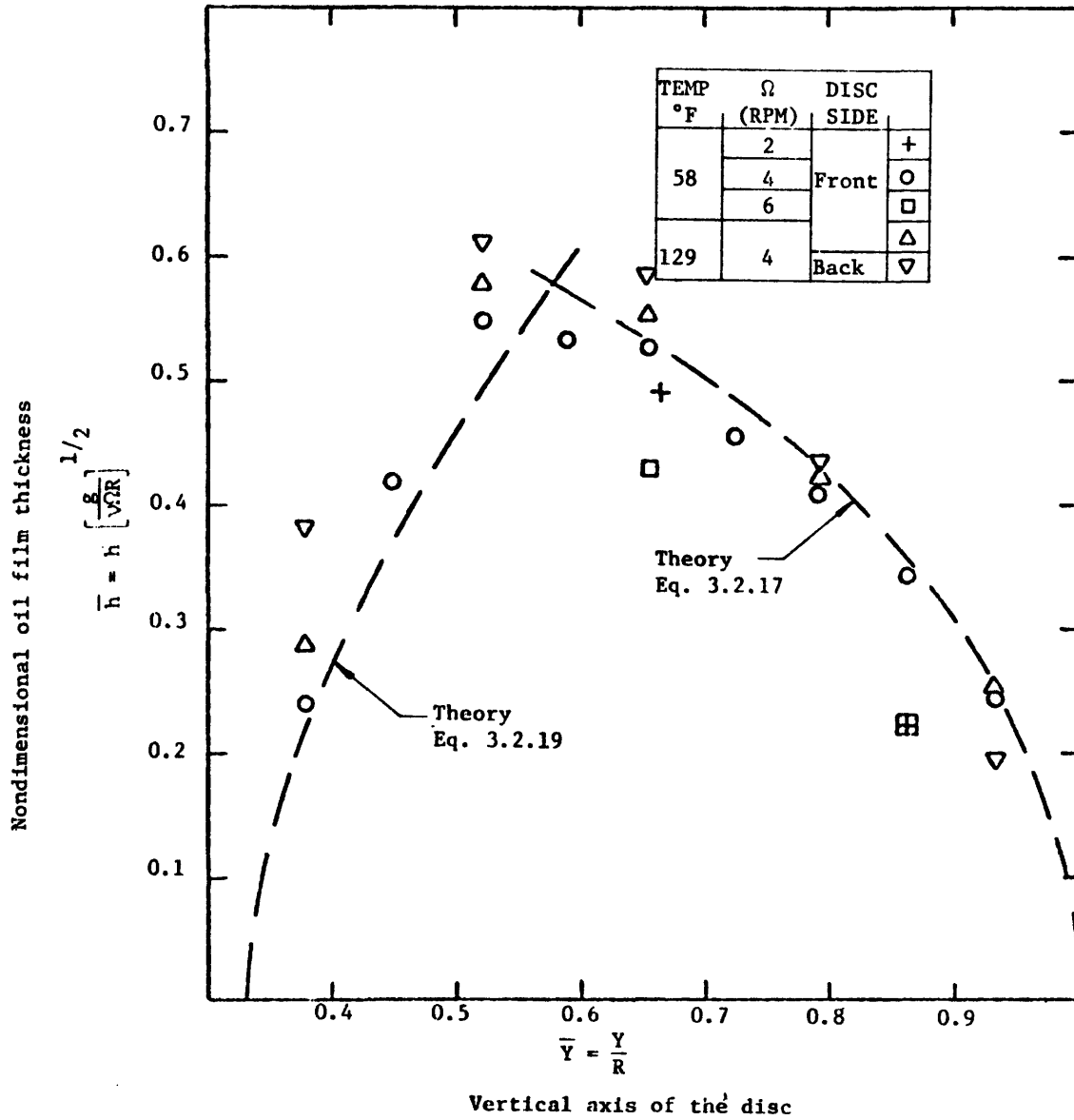
OIL FILM THICKNESS ALONG + $\bar{Y}$ AXIS
(Data taken by Fink [14])

FIGURE 3.2.19

TEMP °F	Ω (RPM)	DISC SIDE	
58		FRONT	○
129	4		△
		BACK	▽

Theory
Eq. 3.2.17

$$\bar{h} = h \left[\frac{g}{\nu \Omega R} \right]^{1/2}$$

Nondimensional oil film thickness

$$\bar{x} = \frac{x}{R}$$

Horizontal axis of the disc
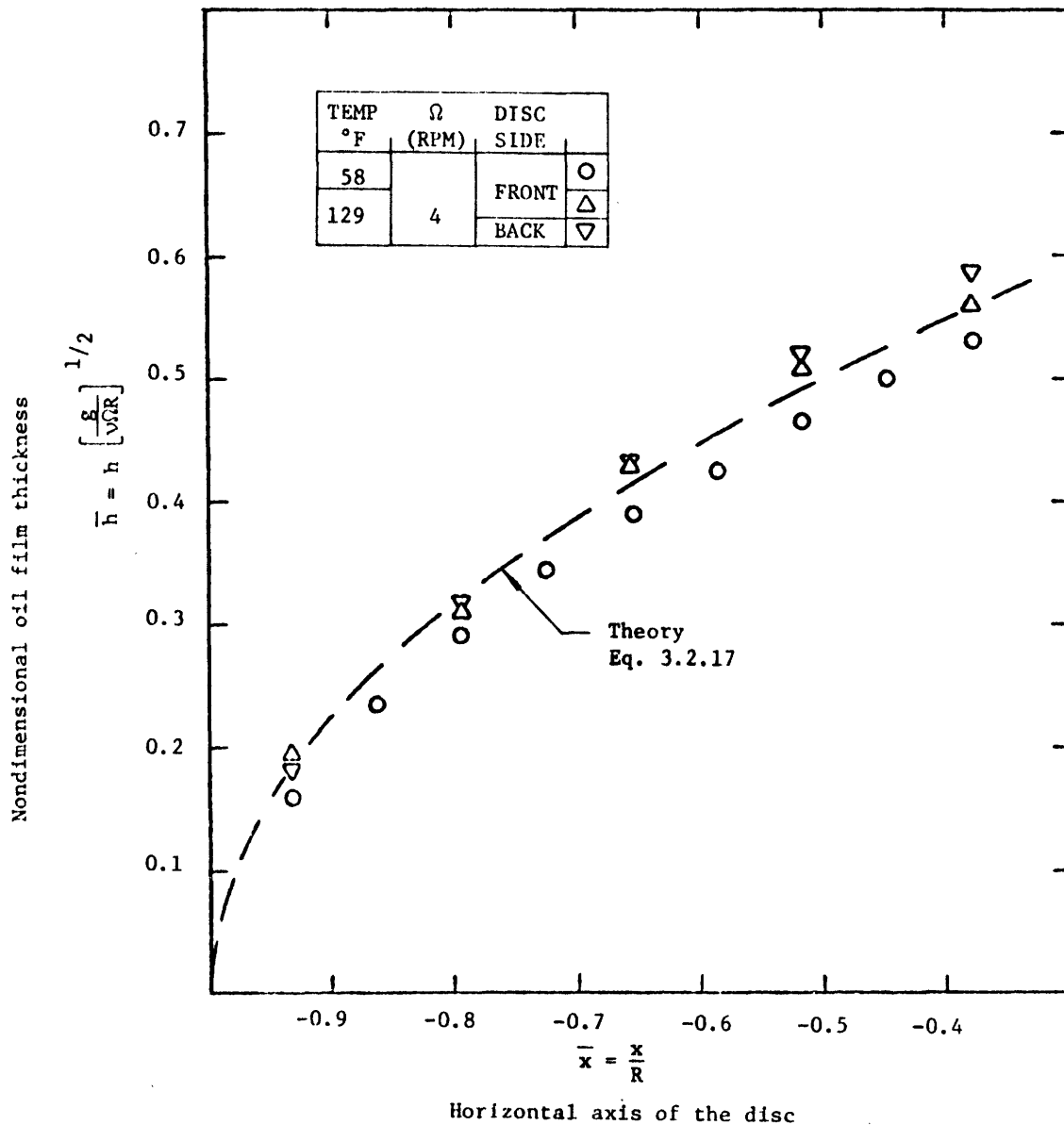
OIL FILM THICKNESS ALONG THE $-\bar{x}$ AXIS
(Data taken by Fink [14])

FIGURE 3.2.20

From the data shown in Figs.(3.2.12) through (3.2.20), it can be concluded, that the analytical solution derived in section (3.2.1) yields a good approximation to the oil film thickness distribution, within the range of operation of the P.C.T. The expressions derived in section (3.2.1) can therefore be used to calculate the film thickness and from it the heat transfer resistance of the oil film.

3.3 MAXIMUM ANGULAR VELOCITY DEPENDANCE ON THE OIL LAYER

The periodic Cooling Tower transfers heat from the water to the air stream through the matrix of rotating discs. Consequently , the performance of the P.C.T is a function of the heat capacity of the discs, as well as the heat capacities of the water and air streams. This performance increases as the magnitude of the heat capacities increase, and it is most sensitive to changes in the smallest heat capacity.

For given values of the water and air heat capacities, the performance of the P.C.T. will increase as the discs' heat capacity is increased. The performance will increase rapidly at first, when the discs' heat capacity is the smallest of the three, and then will reach asymptotically a maximum value as the disc's heat capacity approaches infinity. It is therefore desirable to operate the P.C.T beyond this region of rapid increase in performance. To do so, the heat capacity of the discs must be comparable in magnitude to that of the air or water stream, whichever is smaller.

The heat capacity of the discs is proportional to the product of the mass of the discs and their angular velocity. Consequently, any prescribed value of the heat capacity can be obtained by a suitable combination of the mass and angular velocity. However, the capital cost of the P.C.T. is roughly proportional to the weight of the discs, and therefore it is perferable to make them as light as possible (the limit being the structural stability of the disc matrix). The desired heat capacity can then be obtained by increasing the angular velocity. It has been observed, however, that as the angular velocity of the discs is increased, a point is reached beyond which any further increase in the angular velocity results in water beading

of the disc surface, as described in Section (3.1.3). These water beads substantially increase the water evaporation rate of the P.C.T. and should therefore be avoided. This section is concerned with Ω_c, the critical angular velocity at which water beading begins.

The parameters which affect Ω_c are the oil properties, such as specific gravity, viscosity, surface and interfacial tension, and the geometric configuration of the disc-oil system. The latter includes oil layer thickness, water level below the center of the disc and spacing between the discs. The effect of these parameters on Ω_c was determined empirically. A theoretical model describing the physical mechanism involved has yet to be formulated. Preliminary attempts in that direction are included at the end of the section.

3.3.1 Experimental setup

The apparatus used in these measurements was the one already described in Section (3.1), and shown in Fig. (3.1.2). A typical set of measurements involved the following steps: (1) the angular velocity of the disc was increased until the first water beads appeared near the rim of the disc; (2) the time constant (sec per revolution) as well as the oil layer thickness was then recorded; (3) oil was then added to the oil layer and the process was repeated. All measurements were taken with barriers in the oil layer simulating starved mode operation.

Four different oils were used in these tests: two hydrocarbon oils, Rubrex-100 and Texaco TL-10150, and two synthetic oils, Synfluid and Silicon oil. The characteristics of these oils are included in Appendix (3B).

While testing Rubrex-100 it was found that its performance substantially improved with time. It was also observed that a white, cream-like, phase would accumulate at the oil water interface. This suggested that some water soluble surface active agent was being dissolved out. To test this hypothesis, some R-100 oil was thoroughly mixed with water in a blender, and then filtered to remove the white precipitate formed with the mixing. The oil then obtained had a considerably higher interfacial tension, and performed much better than regular R-100. This oil was labeled AR-100. Mobil Oil Co., producers of R-100, were consulted with regard to the nature of the substance being precipitated out. According to them R-100 was a pure base oil, which contained no additives. Therefore, the R-100 used in these tests must have been contaminated, and it was this contaminant that was dissolved out.

In determining the effect of interfacial tension on Ω_c, tests were made using base Texaco oil TL-10150 which contained different concentrations of a sulfonate base additive. These oils were labeled T-xxx, where xxx corresponded to the additive concentration in parts per million. The interfacial tension variation with additive concentration is also included in Appendix (3B).

3.3.2 Experimental results

The number of parameters which affect the critical angular velocity is quite large. Therefore, no attempt was made at testing all possible variations of the parameters. Instead, the parameters were divided into two groups according to the way in which they affected the performance of the P.C.T. These groups were:

1. Specific gravity $(\frac{\rho_o}{\rho_w})$, kinematic viscosity (ν), surface tension (σ_i) and oil layer thickness (D).

2. Water level (H) and disc spacing (S)

The first group, only affects the heat transfer performance of the P.C.T. insofar as it affects Ω_c. Consequently, the values of these parameters should be chosen so as to maximize Ω_c. The parameters in the second group, however, not only influence Ω_c, but they also affect the characteristics of the P.C.T. through other mechanisms as well. Changes in the spacing between the discs will also affect the heat transfer coefficients and the air pressure drop across the tower. The water level in turn, also determines the ratio of heat transfer areas between the air and water sides.

A larger fraction of the disc surface should be exposed to the air stream to compensate for the lower heat transfer coefficient on the air side. This can be achieved by setting the water level below the center of the discs. In doing so, however, part of the disc stays on the air side all the time (region III in Fig. (3.2.3). That fraction of the disc surface is wasted, since it does not contribute to the heat transfer. This problem was analyzed by Robertson [4]. He found that for a solid disc, the optimum water level was one third of the disc radius below the center of the disc. This solution, however, did not consider variations of the angular velocity with changes in water level. Also being considered is the possibility of using an annular disc rather than a solid one. This would eliminate the wasted area around the center of the disc, and thus allow for greater freedom in choosing the water level.

From the previous considerations, it is clear that the optimum disc spacing and water level can only be determined from an overall optimization

it is first necessary to know how these parameters affect the critical angular velocity Ω_c.

Returning to the first group of parameters, Fig. (3.3.1) shows the variation of Ω_c with oil layer thickness. Each curve corresponds to a different oil. The properties of these oils are also indicated in the figure.

From the data obtained, it can be seen that Ω_c increases as the oil layer thickness is increased. The rate of increase is highest for low values of D. While taking these data, it was observed that as D was increased, a point was reached beyond which the water oil interface in the oil layer became unstable. Large numbers of water droplets accumulated in the oil layer, and eventually a froth was formed. Due to its high water content, this froth had a density very close to that of water. This meant that froth globules which were separated from the oil layer as a result of the churning action of the discs, did not readily return to the oil layer. Instead, they were carried away in the water stream. The thickness at which this condition developed was different for each oil. It corresponded approximately to the upper limit of the region of rapid increase in Ω_c with D. In addition, the cost of the initial change of oil is directly proportional to the oil layer thickness. It is, therefore, preferable to use a relatively thin oil layer.

Another parameter that appears to play an important role in determining Ω_c is the interfacial tension. Of the oils tested, there are two pairs of oil which differ only in their interfacial tensions. These are: R-100, AR-100 and T-345, T-5000. In both cases it can be observed that higher interfacial tension permits a higher angular velocity before water beading starts. However, as described in section (3.1.3) an interfacial tension which is too high, may also cause beading. In this case, the beading is due to poor

		T °F	$\frac{\rho_o}{\rho_w}$	ν st.	σ_s d/cm	σ_i d/cm
○	AR-100	130	.85	.11	25	17
□	R-100	130	.85	.11	25	2.5
+	T-345	130	.85	.11	31	8
✗	T-5000	130	.85	.11	31	3.8
△	Synf.	70	.81	.25	29	19
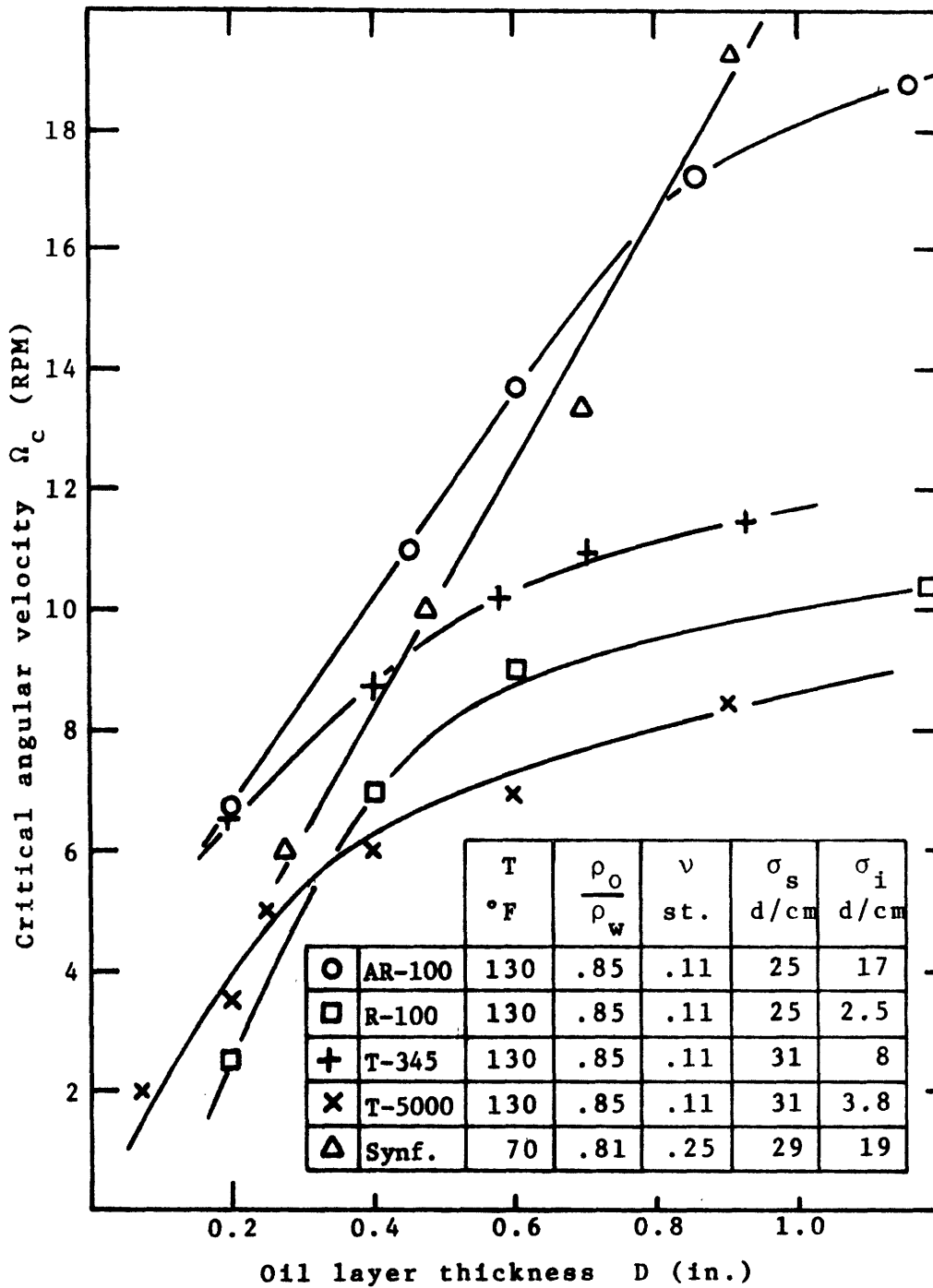
VARIATION OF THE CRITICAL ANGULAR VELOCITY WITH OIL
LAYER THICKNESS FOR A 20" DIAMETER DISC

Figure 3.3.1

wetting of the disc by the oil. Both Synfluid and AR-100 showed some signs of wetting problems. When Silicon oil (σ_i=35) was tested, the wetting problem was so severe that no data could be taken.

This problem was further investigated by mixing Texaco TL-10150 oil with a sulfonate base additive. Oil samples with additive concentration ranging from 40 ppm to 5000 ppm were prepared. The main effect of the additives was to lower the interfacial tension. It was found that the interfacial tension had to be reduced to approximately 9 dynes /cm before the wetting problem would subside. This corresponds to an additive concentration of about 340 ppm.

The surface tension seems to affect Ω_c in the opposite way. Comparing the data for R-100 with that of T-5000 it can be seen that higher surface tension results in lower Ω_c.

The water temperature in the P.C.T. may be subject to smaller variations about its design value. Some data were taken to determine how this would affect Ω_c. The oil used in this test was AR-100. The water level was maintained at 5 inches below the center of the disc. The total volume of oil used remained constant throughout the experiment, as it would in the actual operation of the P.C.T. The oil film thickness however did change, as indicated in Fig. (3.3.2). This change was due to the increase in the viscosity of the oil at lower temperatures. A higher viscosity implies a thicker oil film on the disc surface and therefore less oil remains in the oil layer.

The data shown in Fig. (3.3.2), indicate a substantial increase in Ω_c with temperature. Only a small fraction of this change was due to the variation in oil layer thickness. The extent of this effect can be appreciated from the two data points taken at 88°F. The major influence in Ω_c can be
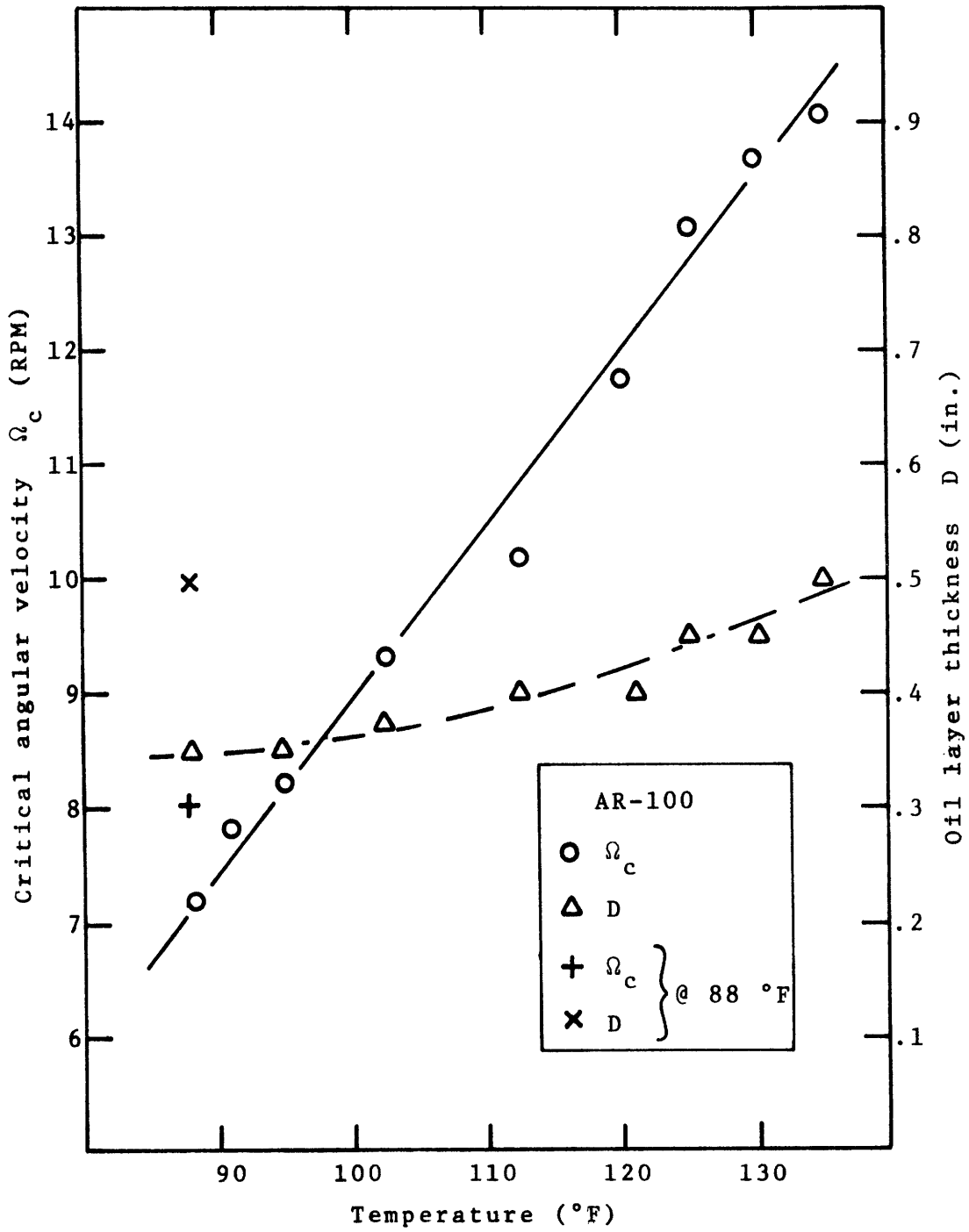
VARIATION OF THE CRITICAL ANGULAR VELOCITY WITH
TEMPERATURE FOR A 20" DIAMETER DISC

Figure 3.3.2

traced back to variations in oil properties with temperature. The oil proper-
ties most affected by temperature are interfacial tension and viscosity. The
interfacial tension varies inversely with temperature and therefore cannot
account for the observed variation in Ω_c. On the contrary, as was pointed
out above, a decrease in interfacial tension would tend to reduce Ω_c. There-
fore, it can be concluded, that the increase in Ω_c is due to the decrease in
viscosity.

The only oil property whose effect on Ω_c has not yet been clearly
stablished is the specific gravity. There is reason to believe, however,
that a lower specific gravity will increase Ω_c. This supposition is based
on the data taken for AR-100 at 100°F and for Snyfluid at 70°F. At those
temperatures both oils have approximately the same properties, except for
the specific gravity. Synfluid has a specific gravity of 0.81 and AR-100
one of 0.86. For an oil layer thickness of 0.5 inches, Synfluid has an Ω_c
of 10.5 RPM, as compared to 9 RPM for AR-100. Furthermore, the data for
AR-100 was taken with a lower water level than that for Synfluid. As will
be shown below, this implies that the value of Ω_c obtained for AR-100 should
be reduced before comparing it with the value obtained for Synfluid. Con-
sequently, a lower specific gravity results in a higher Ω_c.

The second group of parameters, mentioned at the beginning of this section,
involved the water level and the spacing between the discs. To determine
their effect on Ω_c, two series of data were taken using AR-100. The water
temperature was maintained at 130°F, and the oil layer thickness at 0.5
inches. To study the effect of disc spacing, two discs separated by spacers
were used. The water level was maintained at 5" below the center of the disc.
Wipers were set across the oil layer on the outside of the discs, to eliminate

any possible effects in Ω_c resulting from the variation in the distance between the discs and the trough walls. The oil was allowed to flow freely between the discs.

The data obtained from these tests are shown in Figs. (3.3.3) and (3.3.4). The critical angular velocity increased with decreasing water level and with increasing disc spacing. Again, it should be emphasized, that these results can only be considered in the context of an overall optimization of the P.C.T.

3.3.3 Theoretical Model

As described in section (3.1.3) the mechanism behind the water stripping action of the oil layer probably depends on the balance between shear, momentum and interfacial tension forces. The problem appears to be quite involved and no simple analytical model which would predict the performance of the oil layer has yet been found. In addition, a precise prediction of Ω_c is not necessary for the optimization of the P.C.T. Only the relative variation of Ω_c with changes in other parameters is important, since the actual level of Ω_c can be adjusted by changing the oil layer thickness.

It can be expected that the tip speed $(\Omega R)_c$ at which water beading begins, is some function of the oil layer thickness (D), the relative density of the water in the oil layer $(\rho_w(1-\frac{\rho_o}{\rho_w})$, the viscocity of the oil (ν_o), the surface tension of the oil (σ_s), the interfacial tension of the oil (σ_i), the water level (H) and the disc spacing (S).

$$(\Omega R)_c = \phi(D, \ \rho_w(1-\frac{\rho_o}{\rho_w}), \ \gamma_o, \ \sigma_s, \ \sigma_i, \ H, \ S) \qquad (3.3.1)$$
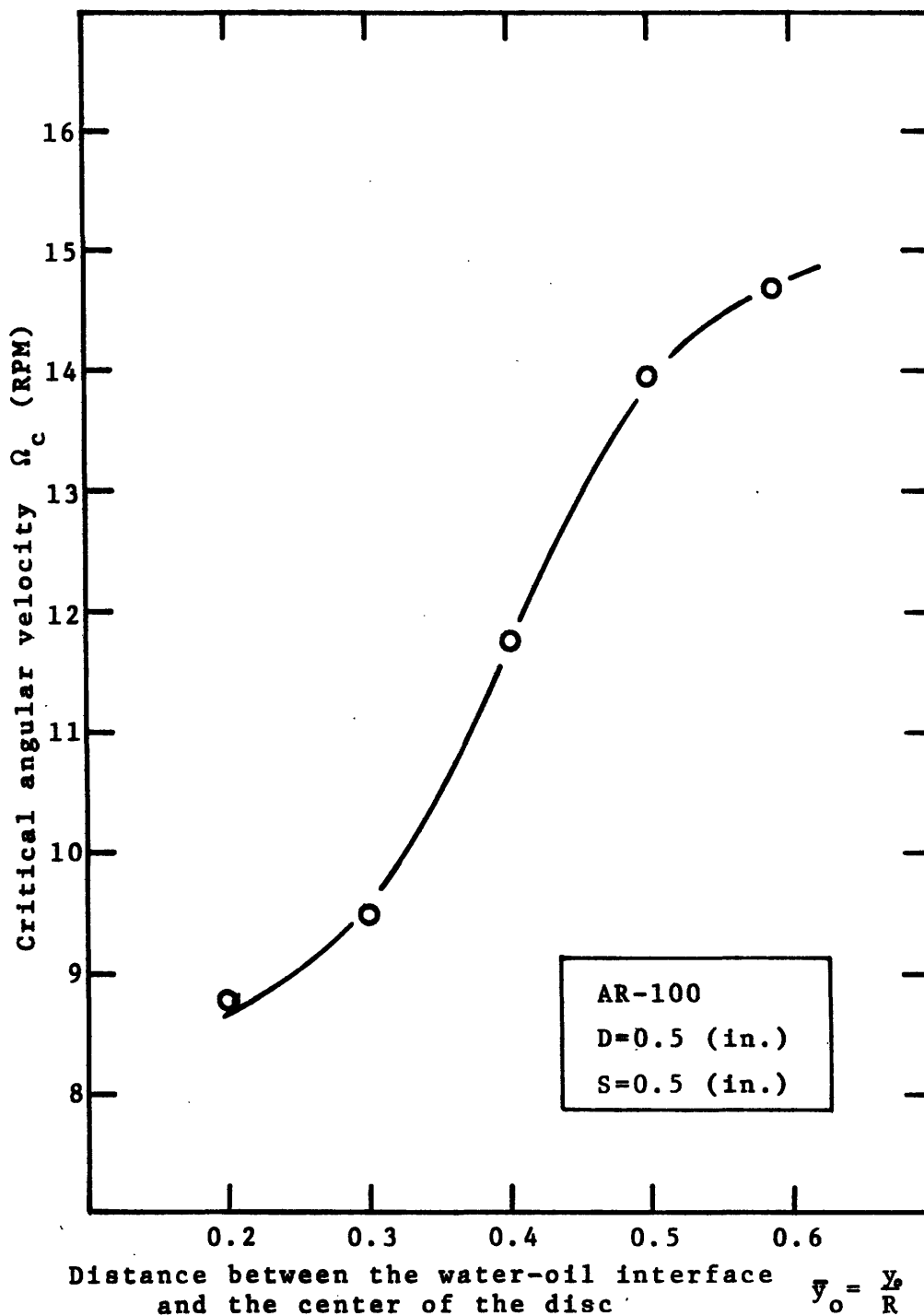
VARIATION OF THE CRITICAL ANGULAR VELOCITY WITH
WATER LEVEL FOR A 20" DIAMETER DISC

Figure 3.3.3
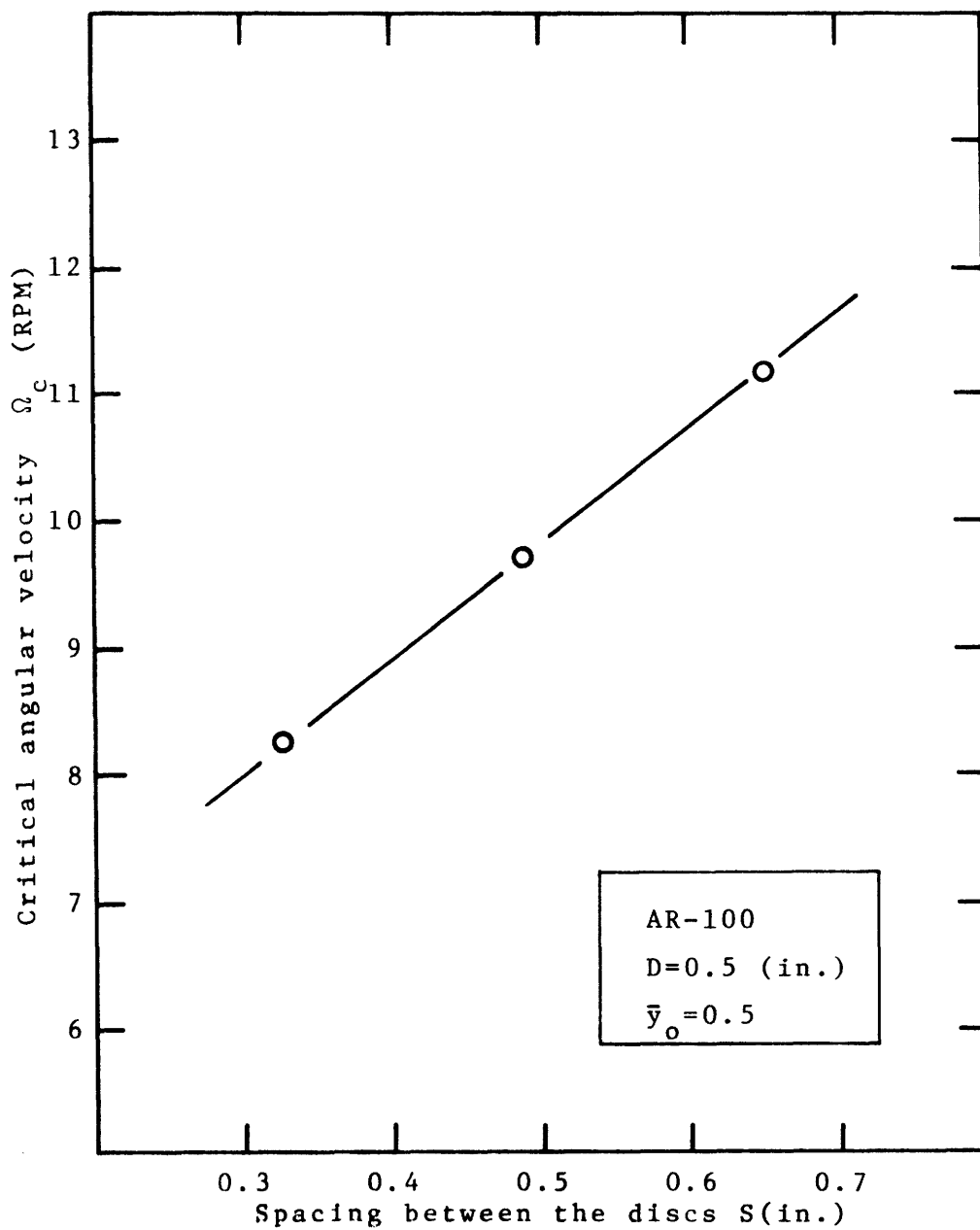
VARIATION OF THE CRITICAL ANGULAR VELOCITY WITH SPACING
BETWEEN THE DISCS FOR A 20" DIAMETER DISC

Figure 3.3.4

From dimensional analysis, this expression can be reduced to:

$$\left(\frac{\Omega R D}{V}\right)_{o\,c} = \pi\left(\frac{\sigma_i D}{\rho(1 - \frac{\rho_o}{\rho_w})v_o^2}, \frac{\sigma_s}{\sigma_i}, \frac{H}{R}, \frac{S}{D}\right) \qquad (3.3.2)$$

The data shown in Figure (3.3.1) were taken with constant value of H and S and therefore it should satisfy an expression of the form:

$$\bar{\Omega}_c = \bar{\Omega}(\bar{D}, \bar{\sigma}) \qquad (3.3.3)$$

where

$$\bar{\Omega} = \frac{\Omega R D}{v_o}; \quad \bar{D} = \frac{\sigma_i D}{\rho_w(1 - \frac{\rho_o}{\rho_w})v_o^2}; \quad \bar{\sigma} = \frac{\sigma_s}{\sigma_i}$$

These data have been replotted using $\bar{\Omega}$ and $\bar{D}$ as variables and $\bar{\sigma}$ as a parameter (Figure (3.3.4)). It can be seen that the data for the hydrocarbon oils @ 130°F appear to satisfy a relationship of the form of Eq. (3.3.3). However, the data for Synfluid, AR-100 @ 90°F and T-500 @ 75°F does not follow the same pattern. This suggests that there are still other variables which should have been included in Eq. (3.3.1). These variables could be the viscocity of the water and, quite possibly, the nature of the surface active agent present in the oil. More data from a wider range of oils and different temperatures would be needed in order to derive such a correlation.

It can also be observed in Figure (3.3.5) that for each of the conditions tested, the data fall on a straight line when plotted on a log-log scale of $\bar{\Omega}_c$ vs $\bar{D}$. A simple empirical equation relating $\bar{\Omega}_c$ and $\bar{D}$ can therefore be formulated:

$$\bar{\Omega}_c = a\,\bar{D}^b \qquad (3.3.4)$$
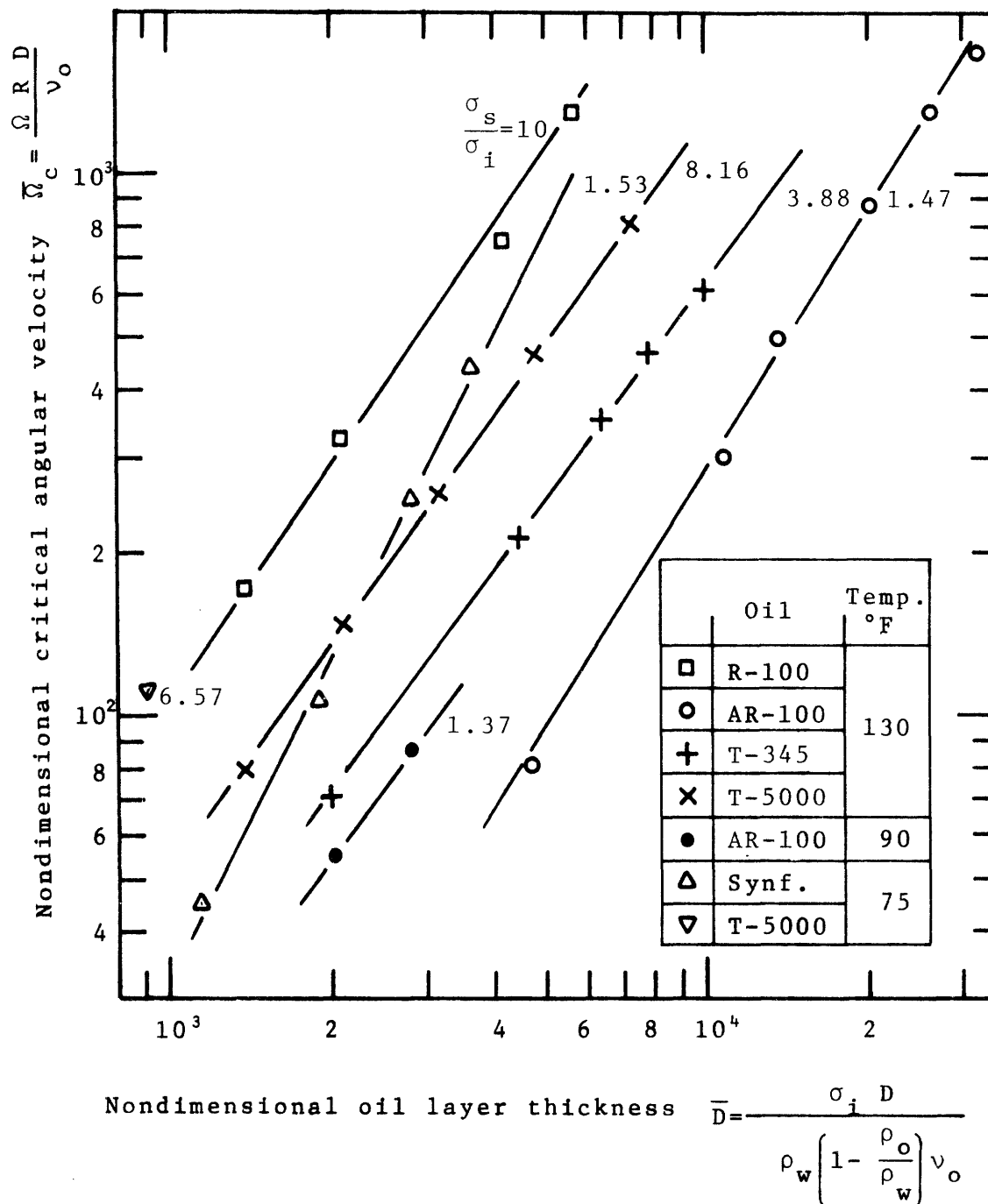
VARIATION OF THE CRITICAL ANGULAR VELOCITY
AS A FUNCTION OF THE OIL LAYER THICKNESS
AND OIL PROPERTIES

Figure 3.3.5

where a and b are constants to be determined empirically for each oil and operating temperature. For the oils already tested, the values of a and b as given in Table 3.1.

Table 3.1

Type of Oil	a	b	Temp(°F)
T - 345	2.79×10^{-3}	1.34	130
T - 5000	3.58×10^{-3}	1.39	130
R - 100	4.52×10^{-3}	1.46	130
AR-100	1.51×10^{-4}	1.57	130
Synfluid	3.85×10^{-5}	1.97	170

Eq. (3.3.4), however, only takes into account the variations in $\overline{\Omega}_c$ due to the difference in oil properties and oil layer thickness. A general expression for $\overline{\Omega}_c$ must also include the effects of varying the water level $(\overline{H} = 1 - \overline{Y}_o)$, and the spacing between the discs (S). As a first approximation it will be assumed that the effects of the different parameters on $\overline{\Omega}_c$ are uncoupled. This suggests an expression for $\overline{\Omega}_c$ of the form:

$$\overline{\Omega}_c = f_1(\overline{D}) \cdot f_2(\overline{Y}_o) \cdot f_3(S) \qquad (3.3.5)$$

where the function $f_1(\overline{D})$ corresponds to Eq. (3.3.4), and the functions $f_2(\overline{Y}_o)$ and $f_3(S)$ will be derived from experimental measurements.

The dependence of Ω_c on the water level was shown in Fig. (3.3.3) As the water level was lowered ($\overline{Y}_o$ increased), the critical angular velocity increased. This was to be expected since Ω_c is a function of the disc velocity normal to the oil-water interface, V_n (Fig. (3.3.6)). This components of the
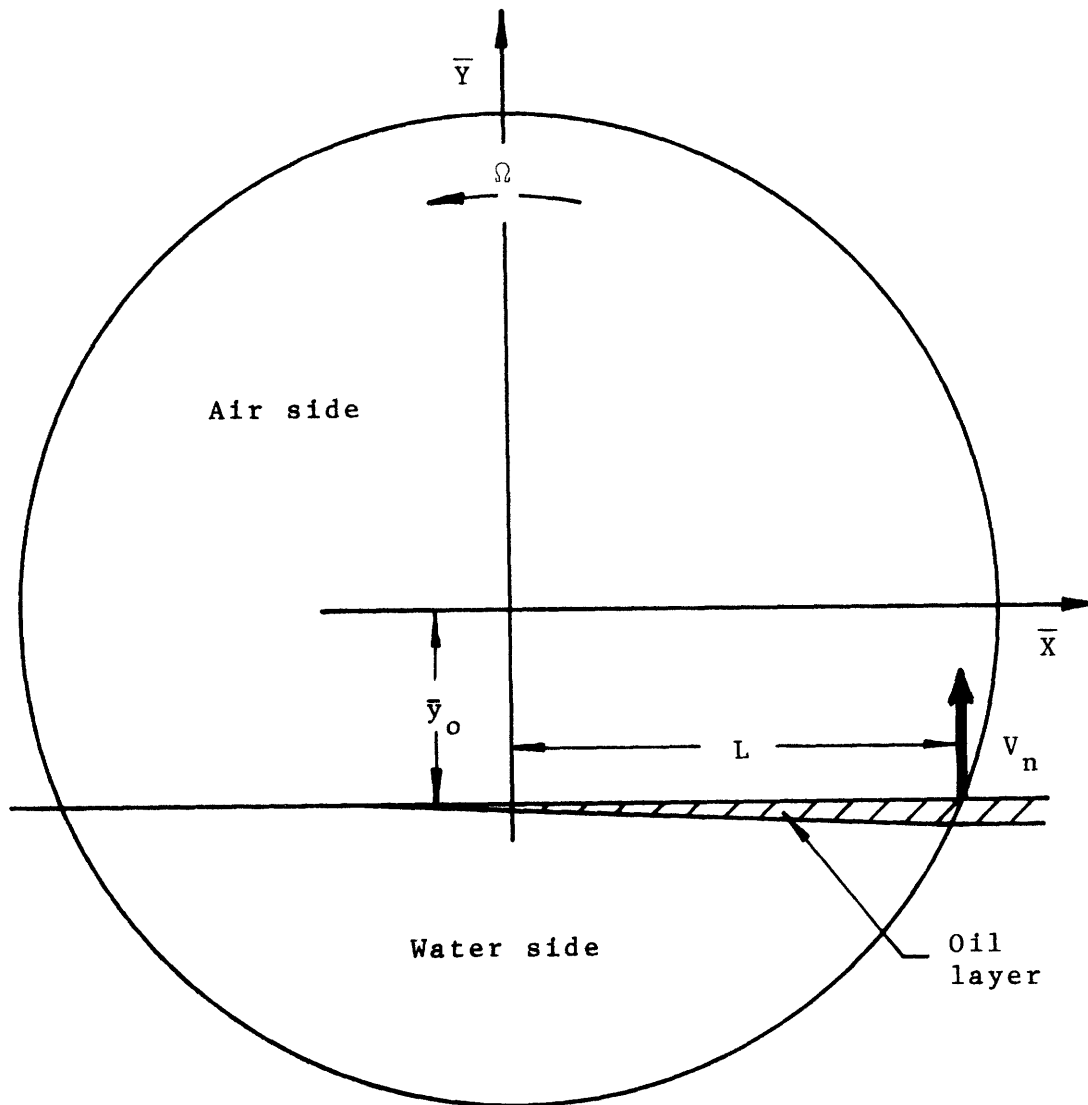
DISC VELOCITY NORMAL TO THE OIL LAYER

Figure 3.3.6

disc velocity is proportional to the semichord length L, which gets increasingly smaller as the water level is lowered. However, as shown in Fig. (3.3.7a), the critical disc normal velocity, $V_{nc} = \Omega_c L$, is not constant. It increases as the water level is lowered, reaches a maximum around $\overline{Y}_o = .55$ and then decreases as the water level is lowered further. One possible explanation for this phenomenon can be found in the way the oil film thickness on the air side changes as the water level is changed.

As mentioned in section (3.1.3), the oil ridge plays an important role in preventing the water from breaking through the oil layer in the region around the edge of the disc. This mechanism is illustrated again in Fig. (3.3.8). The oil ridge is formed by the oil picked up by the disc along line $\overline{OP}$. Gravity forces push this oil towards the rim of the disc where it accumulates in a thick ridge. Due to the thickness of the ridge, the weight of the oil exceeds the shear drag of the discs, causing the oil on the surface of the ridge to actually flow down towards the oil layer. It is this oil flowing down the ridge which washes off the water film pulled into the oil layer by the rotating disc, as shown in Fig. (3.3.8b). The amount of oil flowing down is a function of the angular velocity, the water level and the properties of the oil. The non-dimensional oil volume flow rate, defined as:

$$\overline{Q} = \frac{Q}{(\Omega R)^{3/2} (\frac{\nu}{g})^{1/2}}$$

is however, only a function of the water level. Using the expressions for the oil velocity distribution derived in section (3.2), the non-dimensional oil volume flow rate along the ridge was calculated for different water levels, and is shown in Fig. (3.3.7b). It can be seen, that both the oil volume flow rate down the ridge and the critical disc normal velocity have a similar dependence on the water level. This suggests that a cause-effect
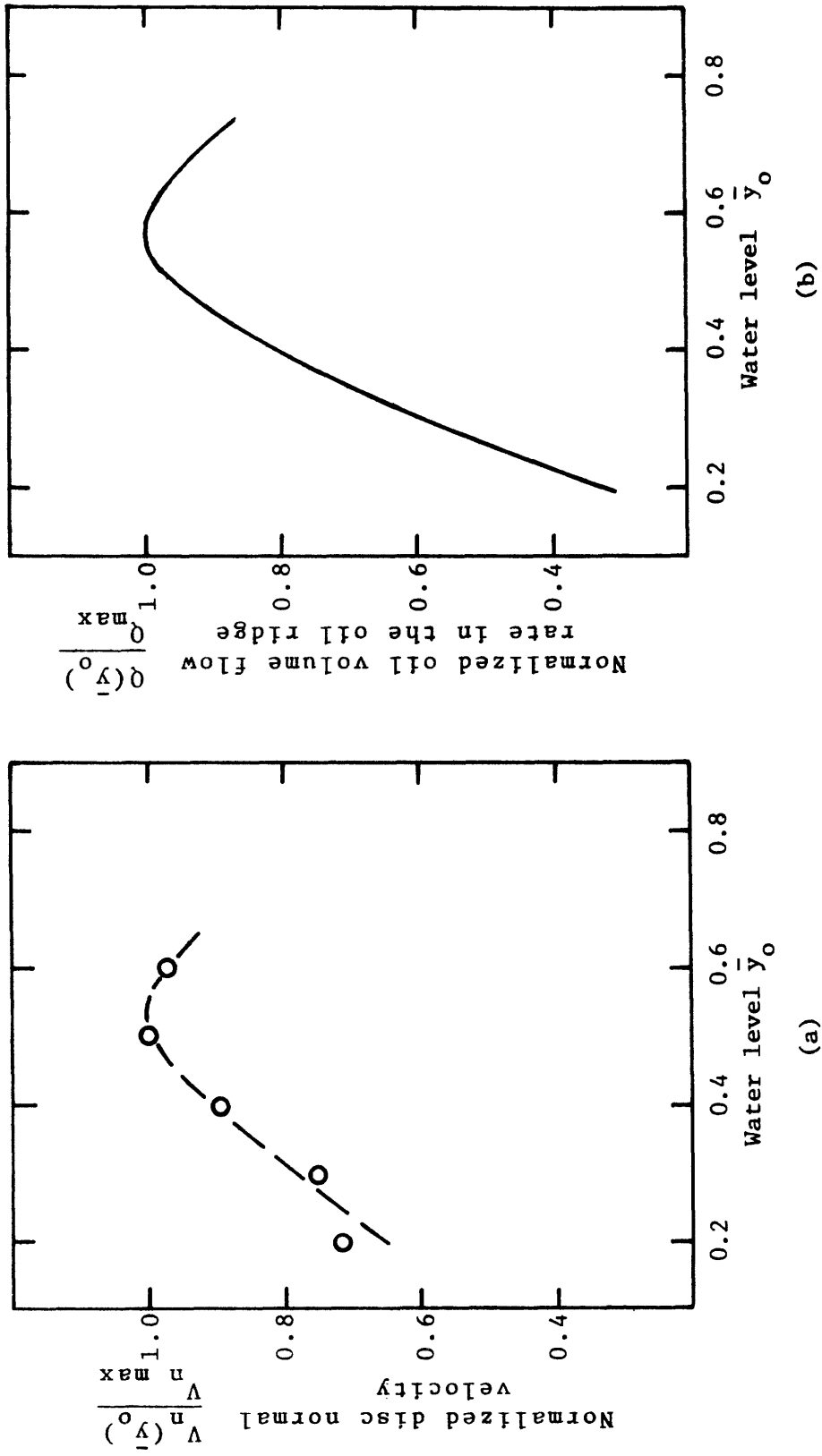
RELATIONSHIP BETWEEN THE OIL RIDGE AND THE CRITICAL ANGULAR VELOCITY

Figure 3.3.7

Disc

V_n

Oil ridge

Air
side

Water
side

(b) Front view

$\bar{X}$

Circle of maximum
thickness $h=h_a$ max

Water droplets

P

O

Oil layer

$\bar{y}_o$
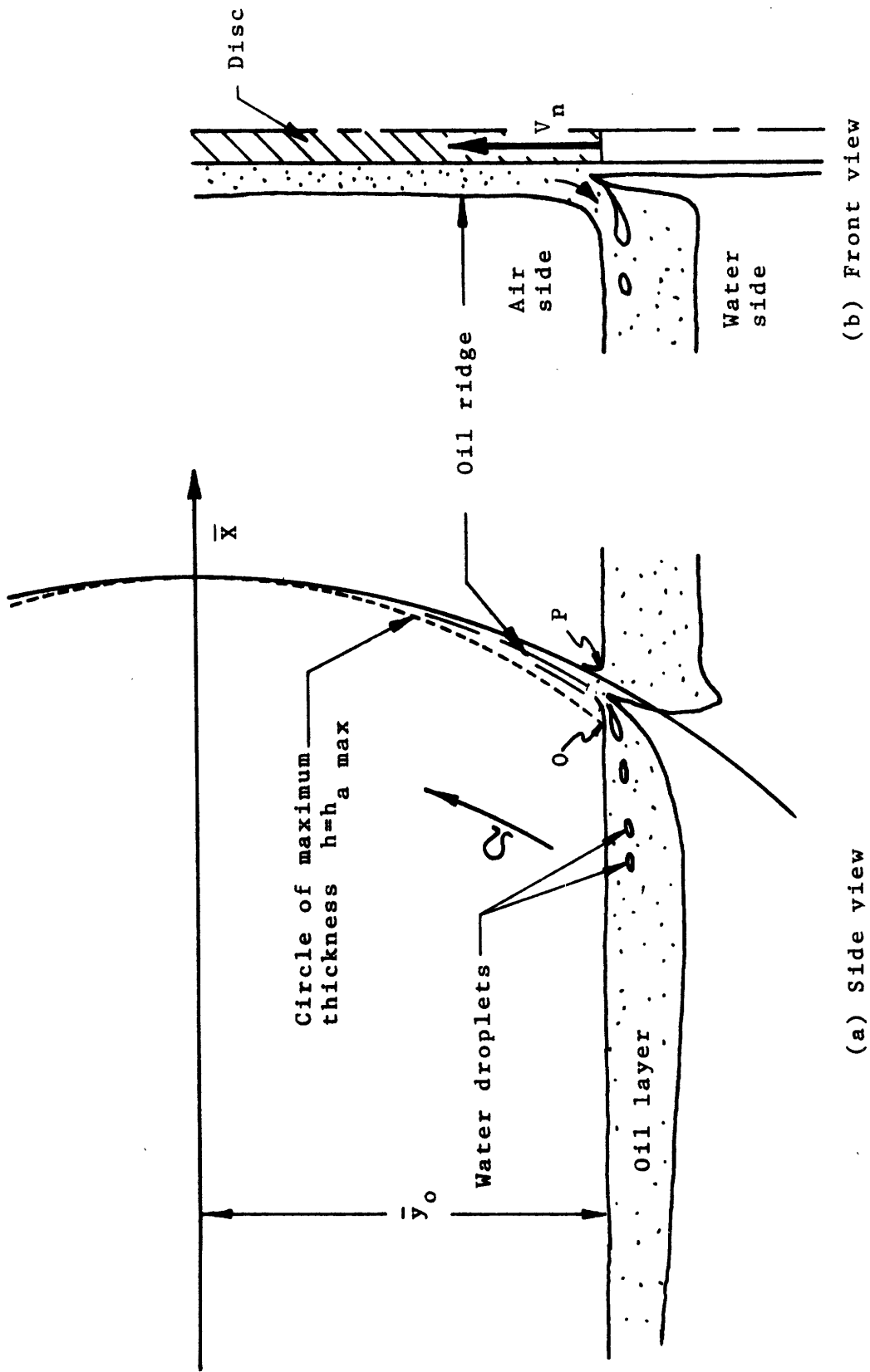
(a) Side view

WATER STRIPPING ACTION OF THE OIL RIDGE

Figure 3.3.8

relationship may exist between them. If this is the case, the critical

disc normal velocity can be expressed as:

$$\frac{V_{nc}}{V_{nc\ max}} = C\ f'(\overline{Y}_o)$$

where C is a function of the oil properties, the oil layer thickness and

the spacing between the discs. The critical angular velocity is related

to V_{nc} by:

$$V_{nc} = \Omega_c R(1 - \overline{Y}_o^2)^{1/2}$$

Therefore the critical angular velocity dependence on the water level can

be expressed as:

$$\overline{\Omega}_c = C'\ \frac{f'(\overline{Y}_o)}{\sqrt{1 - \overline{Y}_o^2}}$$

The function $f(\overline{Y}_o)$ was empirically determined by fitting a third degree

polynomial to the measured data, as indicated by the dashed line in Fig.

(3.3.7a).

$$f'(\overline{Y}_o) = 1 - 0.0536(\overline{Y}_o - .55) - 6.22(\overline{Y}_o - .55)^2 - 9.40(\overline{Y}_o - .55)^3 \qquad (3.3.6)$$

The last parameter that needs to be considered is the spacing between

discs (S). Varying the disc spacing affects the performance of the oil in

several ways. When S is increased, the shear drag between the discs and

the oil layer is reduced. In addition, the head gradient forces and the shear

forces between the water and the oil layer increase. Both of these tend to

move the oil back to the AOW side. The net result is that the tendency of

the oil to accumulate on the WOA side is reduced. This in turn implies that

the onset of starved mode operation occurs at a higher angular velocity. Another consequence of increasing the spacing between the discs is that for a given angular velocity the shear drag between the discs and the water decreases. This means that the discs can be operated at a higher angular velocity without beading of the disc surface, since it is the drag force of the discs on the water which pulls the water through the oil layer and causes beading (Fig. (3.3.9)). Consequently, it can be expected, that the critical angular velocity will increase as the spacing between the discs is increased. Furthermore, since the drag between the discs and the water becomes very large as S approaches zero, Ω_c must also go the zero for small S. One functional dependence of the critical angular velocity on the disc spacing which satisfies the previous conditions is:

$$(\Omega R)_c = C'' S^d \tag{3.3.7}$$

where C'' is a function of the oil properties, oil layer thickness and water level. The values of these coefficients were obtained by fitting the experimental data with a curve of the form of Eq. (3.3.7), as shown in Fig. (3.3.10).

$$C'' = 1.12 \text{ ft/sec-in}^4$$

$$d = 0.4$$

Combining Eqs. (3.3.4) (3.3.6) and (3.3.7), the desired expression for the critical angular velocity is obtained:

$$\Omega_c = 0.91 \ a\left[\frac{\sigma_1 D}{\nu_o^2 \rho_w(1 - \frac{\rho_o}{\rho_w})}\right]^b \frac{\nu_o S^{.4}}{DR(1 - \overline{Y}_o)^{2.5}}$$

$$[1 - .054(\overline{Y}_o - .55) - 6.22(\overline{Y}_o - .55)^2 - 9.40(\overline{Y}_o - .55)^3] \tag{3.3.9}$$
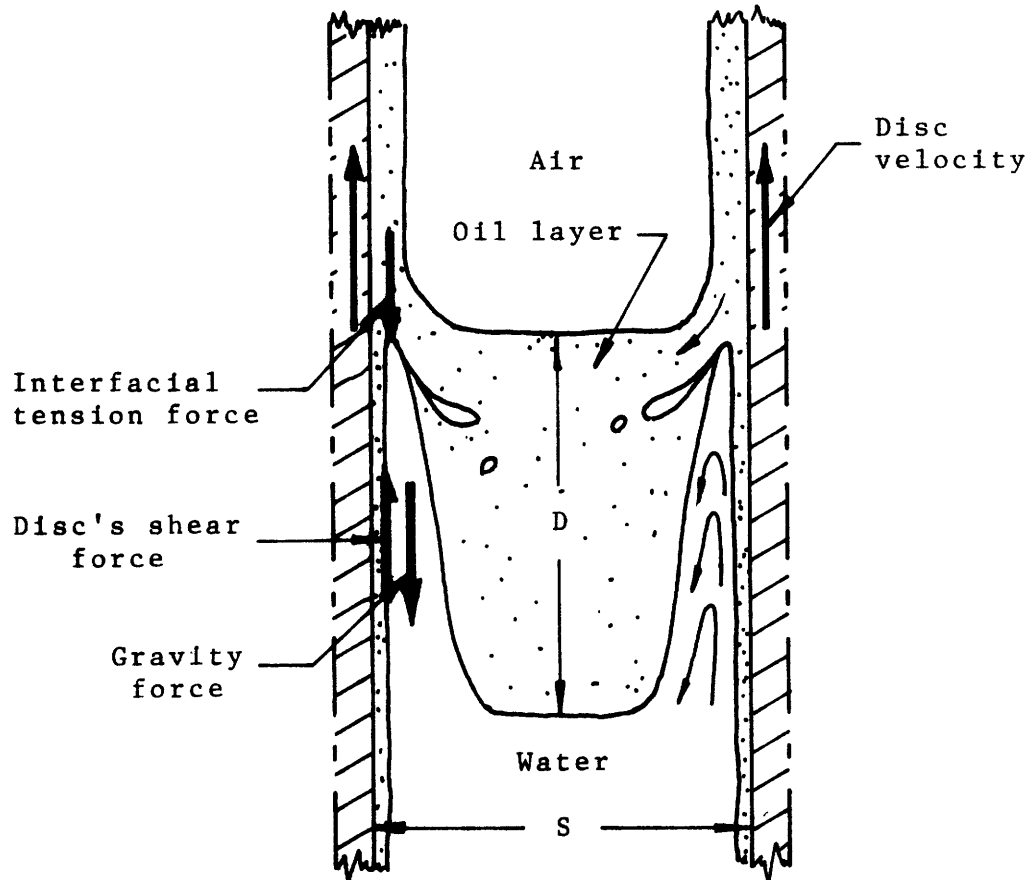
CROSSECTION OF THE OIL LAYER AT THE 'WOA' SIDE

Figure 3.3.9
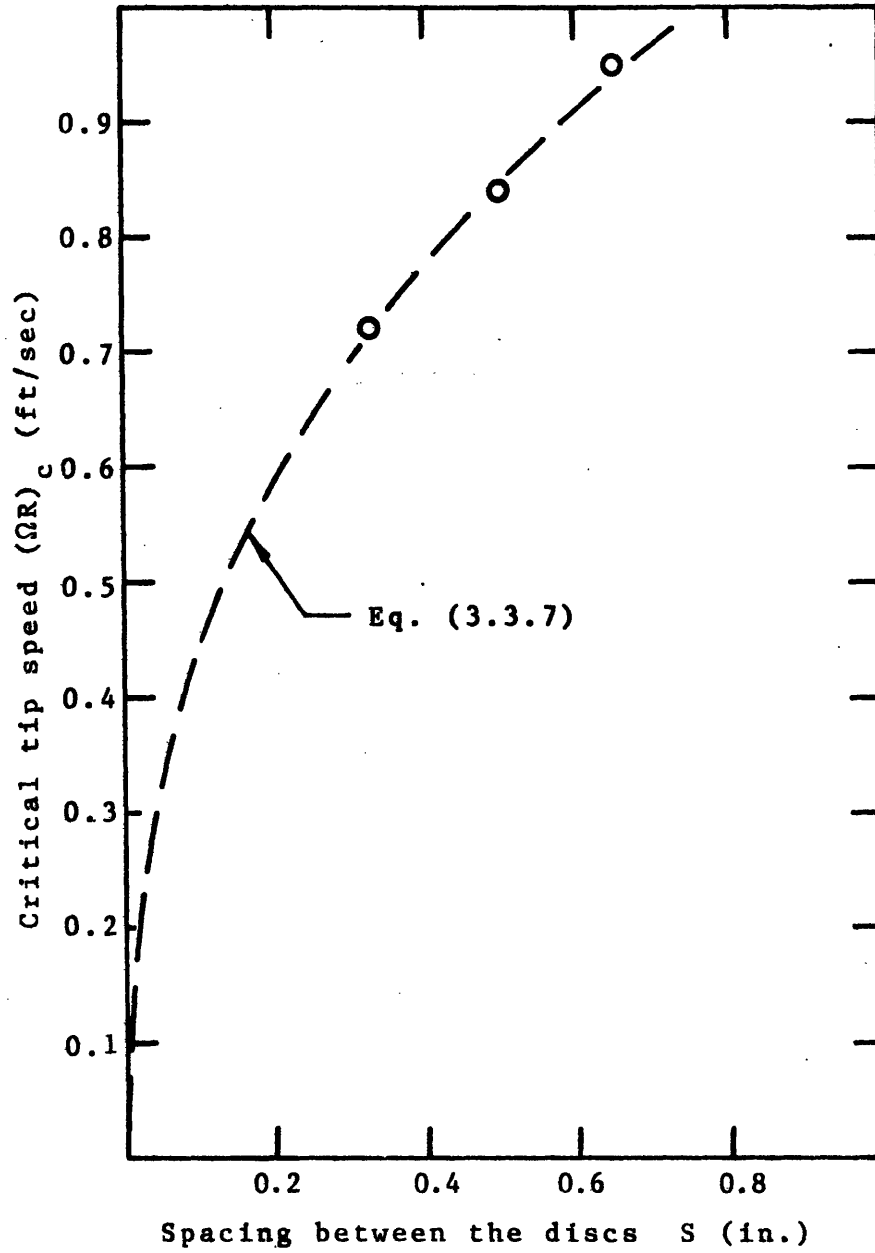
CRITICAL ANGULAR VELOCITY DEPENDANCE ON THE
SPACING BETWEEN THE DISCS

Figure 3.3.10

The parameters a and b are functions of the kind of oil used and the operating temperature. For the oils already tested, their values @ 130°F are given in Table (1). The units of S in Eq. (3.3.9) are inches.

3.4 Oil Stability

Along with the oil film thickness and the critical angular velocity, there are some other aspects of the P.C.T. oil system which deserve some consideration. They are:

1. Oil loss through evaporation.

2. Emulsification of the oil.

3. Oil contamination

These problems do not have immediate influence on the heat transfer perfor- mance of the P.C.T., but nevertheless must be considered in the selection of the oil.

3.4.1 Oil evaporation

The rate at which oil will evaporate from the P.C.T. is proportional to the product of the oil vapor pressure and the total oil free surface area. Although the vapor pressures of most oils are very small, the surface area (which includes all the heat transfer area) is large, and thus a significant amount of oil could evaporate. The environmental questions raised by the rejection of a quantity of oil vapor into the atmosphere, may well exceed the environmental drawback of a wet cooling tower. In addition, the cost of continuously replacing a large volume of oil may well render the P.C.T. economically impractical. Consequently, a negligible oil evaporation rate under the operating conditions of the P.C.T. is essential.

The details of the oil evaporation rate calculations are given in Appendix (3.C). The rate of oil lost by evaporation for a 1000 MW power plant, ranges from less than 2 lbm/hr for silicon oil to around 200 lbm/hr for hydro- carbon oils. These values, however, represent the upper limits for the evaporation rates, since they were calculated using the initial state vapor

pressures. The vapor pressure of most oils decreases with time of operation, as the lighter components of the oil are evaporated away. Therefore, the steady state evaporation rates would be somewhat lower than the values given above. Although the evaporation rate of silicon oil is significantly less than that of hydrocarbon oils, the environmental impact of rejecting silicon oil vapor to the atmosphere is not known. In addition, the cost of silicon oils is substantially greater, and therefore, it might be desirable to accept a higher reposition rate and use cheaper hydrocarbon oils.

3.4.2 Oil churning

Another consideration that must be borne in mind, when selecting the oil to be used in the P.C.T., is the emulsive characteristics of the oil; that is, the ease with which water in oil dispersions will separate. The importance of this has already been pointed out and can be summarized as follows.

In the operation of the P.C.T. water droplets are continuously being entrained in the oil layer. This process is closely related to the water stripping action of the oil layer. Therefore, even if the water entrainment can be held to a minimum by proper combination of angular velocity and oil layer thickness, it cannot be eliminated altogether. If these water droplets do not readily coalesce, they accumulate in the oil layer forming a water-in-oil dispersion. As long as the water content of the oil remains low (less than 20%) the presence of these water droplets does not affect the oil layer performance. However, if the water content in the oil layer becomes much higher, several problems arise. As described in section (3.1.3), some water beads are carried by the disc to the air side and make the oil film thicker. Furthermore, the large number of water droplets increase the apparent viscosity of the oil and this leads to a lower critical angular velocity. Finally, there is the problem described in section (3.3.2) of oil froth globules

being separated from the oil layer and carried away in the water stream.

This latter problem can possibly have the added complication of coating the

condenser tubes with a film of oil. This would not only increase the heat

transfer resistance in the condenser, but could also result in oil contamin-

ation of the boiler water. Consequently, it is necessary to keep the water

content of the oil layer low. This can be best achieved by a proper selection

of the oil.

The rate at which water droplets coalesce in a water-in-oil dis-

persion is, in general, a function of viscosity, specific gravity and inter-

facial tension. Viscosity and specific gravity affect the motion of the

water droplets within the oil. The lower the viscosity, and the lower the

specific gravity, the easier it is for the water droplets to settle out.

Also, a high interfacial tension results in more energy being stored at the

oil water interface. This, in turn, increases the tendency of the water

droplets to coalesce in order to reduce the stored energy.

To determine the relative magnitude of these effects, a series of

tests were made. The tests consisted of thoroughly mixing equal amounts of

oil and water, and then recording the rate at which they separated. The

apparatus used for these experiments is shown schematically in Fig. (3.4.1).

It consisted of a 40 ML graduated centrifuge tube immersed in an oil bath.

The temperature of the oil bath could be set to within 0.5°F in a range from

75 to 200°F. Most of the measurements were taken at the operating tempera-

ture of the P.C.T; that is, 130°F. The stirrer was a galvanized sheet metal

strip .4 inches wide and 4 inches long. It was driven by a 3600 RPM electric

motor. For each test, 15 ML of oil and 15 ML of tap water were used. The

stirring time was two minutes.
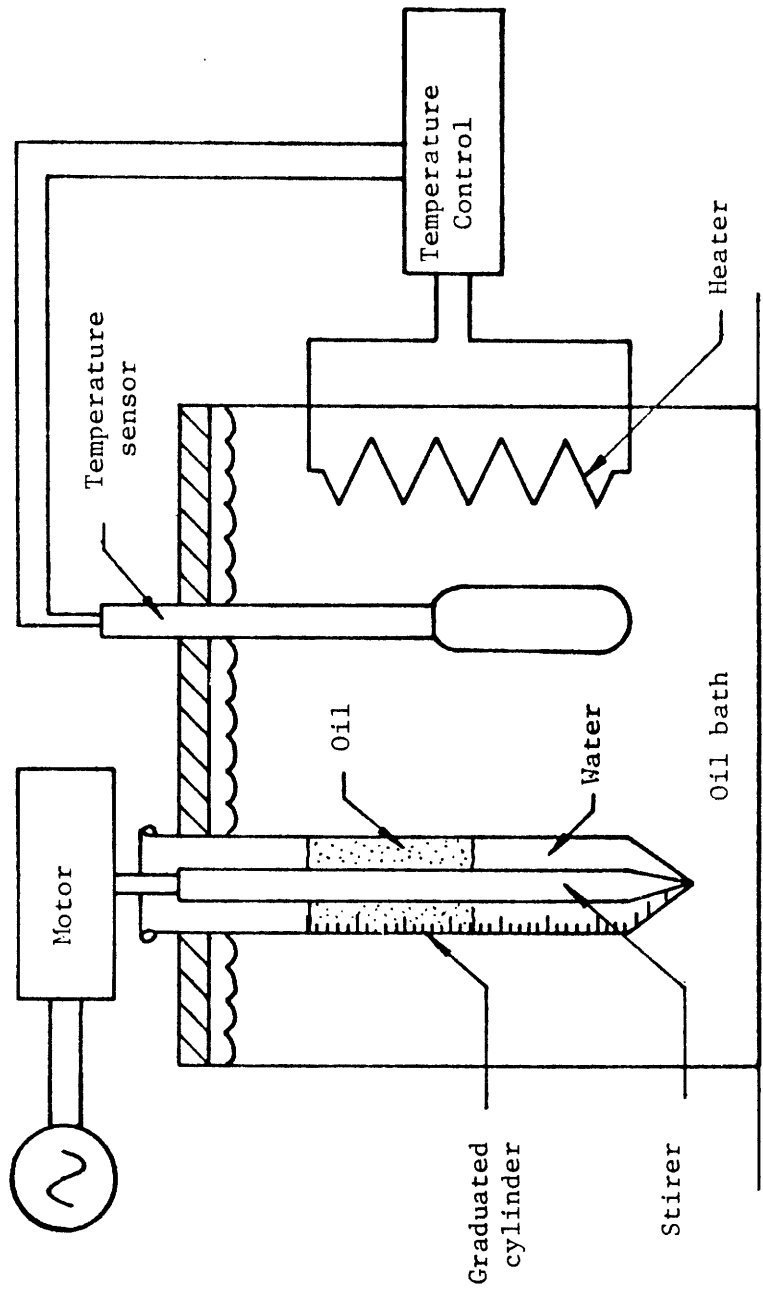
EMULSION TEST APPARATUS

Figure 3.4.1

The separation rates for the different oils tested are shown in Fig. (3.4.2). The upper half of the graph represents the percent of the oil which has separated from the dispersion as a function of time. The lower half represents the water separation rate.

The effect of viscosity on the separation rate can be appraised from the data for base Texaco oil (T-0) at 75°F and at 130°F. The viscosity of the oil at 130°F is about one third of that at 75°F. It can be concluded therefore, that reducing the viscosity of the oil significantly accelerates the coalescence of the water droplets.

The other oil property which was different for each oil tested is the interfacial tension. Its effect on the coalescence rate is not straight-forward. Comparisons between oils of the same kind, that is T-0 with T-5000 and R-100 with AR-100, indicate that a higher interfacial tension results in a faster separation of the water and oil. However, the opposite is true when the data for AR-100 and T-5000 are compared. This apparent inconsistency seems to indicate that it is not just the value of the interfacial tension, but also the kind of surface active agent present that is important. The additive present in AR-100 is water soluble, and this must be the factor which causes slower separation. The same phenomena is probably responsible for the slow responce of R-100.

3.4.3 Oil contamination

The oil in the P.C.T. will be continuously collecting dirt particles present in the air stream. This contamination may deteriorate the performance of the oil, and therefore, partial filtration or periodic change of oil will probably be required. Observations in the full scale model [17] as well as in the 20 inch rig indicate, however, that even with a substantial amount of
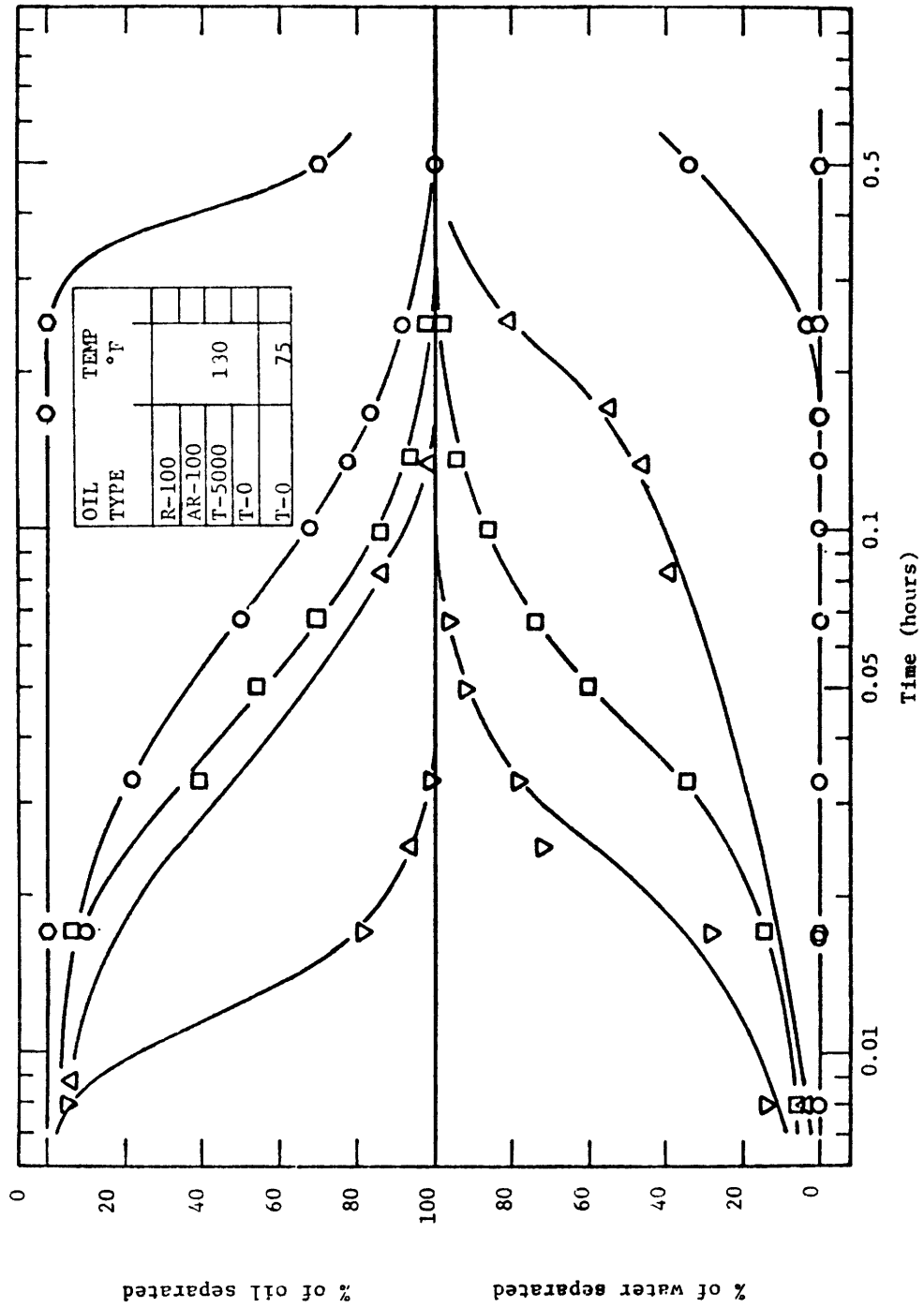
EMULSIVE CHARACTERISTICS OF DIFFERENT OILS

FIGURE 3.4.2

dirt present, the performance of the oil is not significantly affected.

In a series of tests done with T-350, dirt (off the lab shelves) was sprinkled on the rotating disc. It was observed that while some particles remained in suspension, most of them soon migrated to the water oil interface. At the interface they formed a film-like structure. The oil circulation in the oil layer drove the film towards the WOA side, as shown in Fig. (3.4.3). After a short time, portions of this film dropped out of the oil layer due to the higher density of the film. The dirt particles were then carried away in the water stream. This experiment was repeated several times throughout four days of continuous operation of the rig. The results were always the same, and no deterioration in the performance of the oil was observed. The entrainment of the oil-and-dirt film in the water stream may again present problems in the condenser, as discussed in section (3.4.2). More detailed experimentation has been performed to determine the effect the presence of oil has on condenser performance. This study is discussed in detail in Section 6. The results of this study, conducted without dust or dirt contaminants, indicates a negligible effect of oil on condenser performance. Pending further tests, and depending on the level of contamination of the air stream, it might be necessary to filter the water as well as the oil.
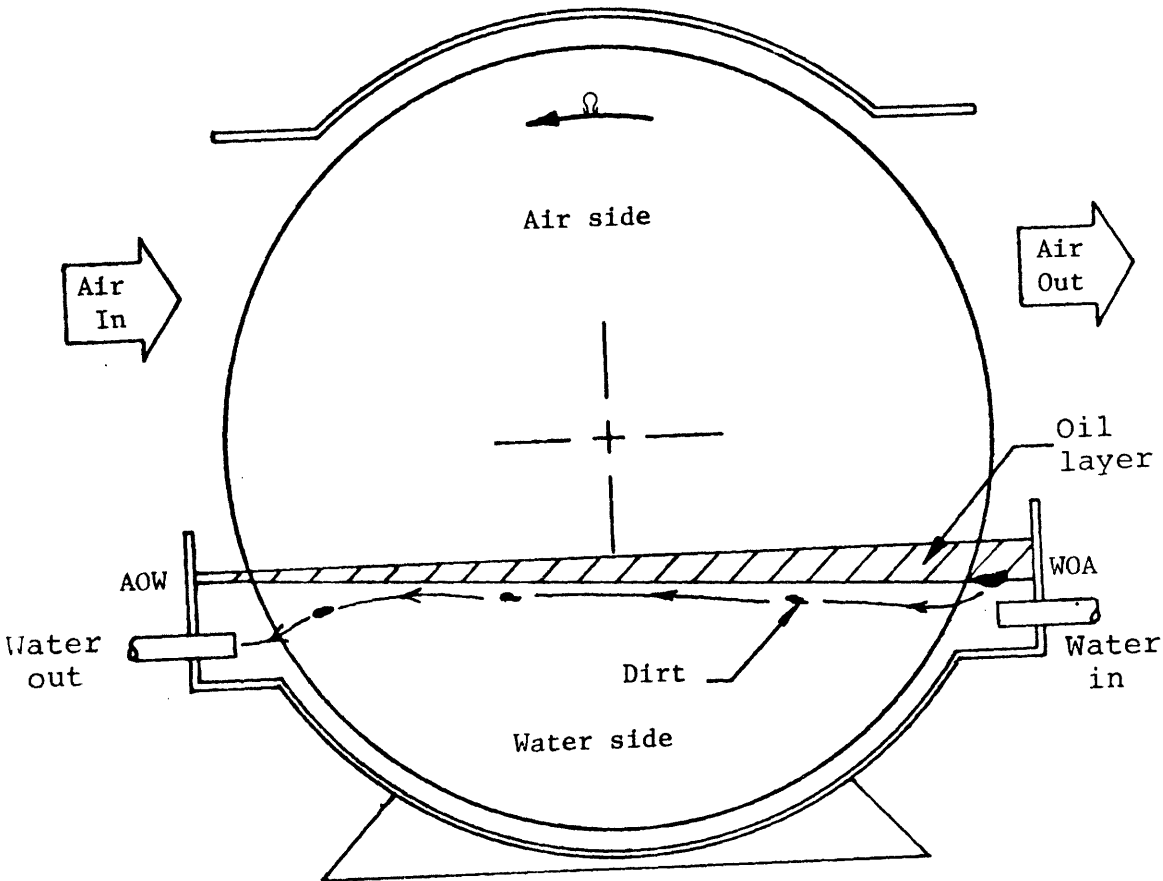
OIL CONTAMINATION

FIGURE 3.4.3

4. Augmentation of Disc Performance by Surface Roughening

4.1 Introduction

As with all liquid-gas heat exchangers, the major resistance to heat transfer lies on the gas side. Any augmentation of the air side heat transfer coefficient will increase the performance of the heat exchanger.

As reported in the second year's report [5], adding square-rib roughness elements to smooth surfaces will increase air side heat transfer coefficients. An economic optimization indicated that for a 1000 MW electric power plate, the use of such surface roughening elements would decrease the incremental and capital costs of the rotary heat exchanger by about 20%.

This previous ribbed surface study was based on existing correlations to predict the heat transfer coefficient and friction factor. However, the correlation was not based on the same geometry and flow conditions as exhibited by the rotary heat exchanger. For instance, the coating oil layer will change the square-rib profiles by rounding all sharp edges or corners and may affect the heat transfer coefficient and friction factor. Further, as the ribs are on a rotating disc, the angle between the rib and the flow directions is constantly changing from 0° to 180° and will affect the heat transfer coefficient and friction factor also.

To realistically evaluate disc ribbing, the functional dependence of heat transfer and friction on rib shape and angle of attack must be determined for the Reynold's flows that the discs will experience. This

more detailed study was examined both analytically and experimentally, and is discussed in the following sections.

4.2 Objectives of the Investigation

The results of previous investigations in surface roughening cannot be applied to the proposed periodic heat exchanger surface directly due to the different geometry and flow conditions. For such an application, a number of problems had to be investigated carefully.

Turbulent heat transfer and friction in tubes or annul j with repeated-rib roughness had been investigated quite extensively, but most of the investigators [12-15] concentrated on small ratios of rib height to flow hydraulic diameter, e/D_h (about 0.001 to 0.01) and high Reynolds number flows (about 10^5 to 10^6). In the periodic heat exchanger, there is an oil layer on the water surface to prevent water from evaporation. When the disc rotates, the oil will coat the disc surface, so a large rib height is necessary in order to protrude through the oil layer and trip the laminar boundary layer of the air. Since the rib height is large, low Reynolds number is appropriate for modest pumping power. In this study, e/D_h was varied from 0.032 to 0.102, and the Reynolds number was varied from 3,000 to 30,000.

For a pitch to height ratio p/e, greater than 10, there is a significant quantity of existing data; however, for a p/e ratio less than 10, very little data has been taken. It was of interest to find out whether a p/e greater or less than 10 would provide an optimal thermal and hydraulic performance under the same flow conditions.

In the proposed periodic heat exchanger, the flow attack angle of the air to the rib may be varied as the disc rotates (see Fig. 4.2.1). The effect of different flow attack angles on friction and heat transfer by other investigations has not been previously examined precisely. Such an examination was carried out in this study.

In the periodic heat exchanger, when the disc rotates, the oil will coat the disc, filling the corners and rounding out the edges of the square ribs. The effect of different rib shapes on friction and heat transfer must be determined. Little existing data is available.

The purpose of this investigation was to establish a friction and heat transfer correlation based on experiments, the law of the wall similarity and heat-momentum transfer analogy and which includes the effect of the above four conditions. Then, the friction and heat transfer correlations can be employed to design and predict the optimum thermal-hydraulic performance conditions of the periodic cooling tower by using an optimum computer design program.
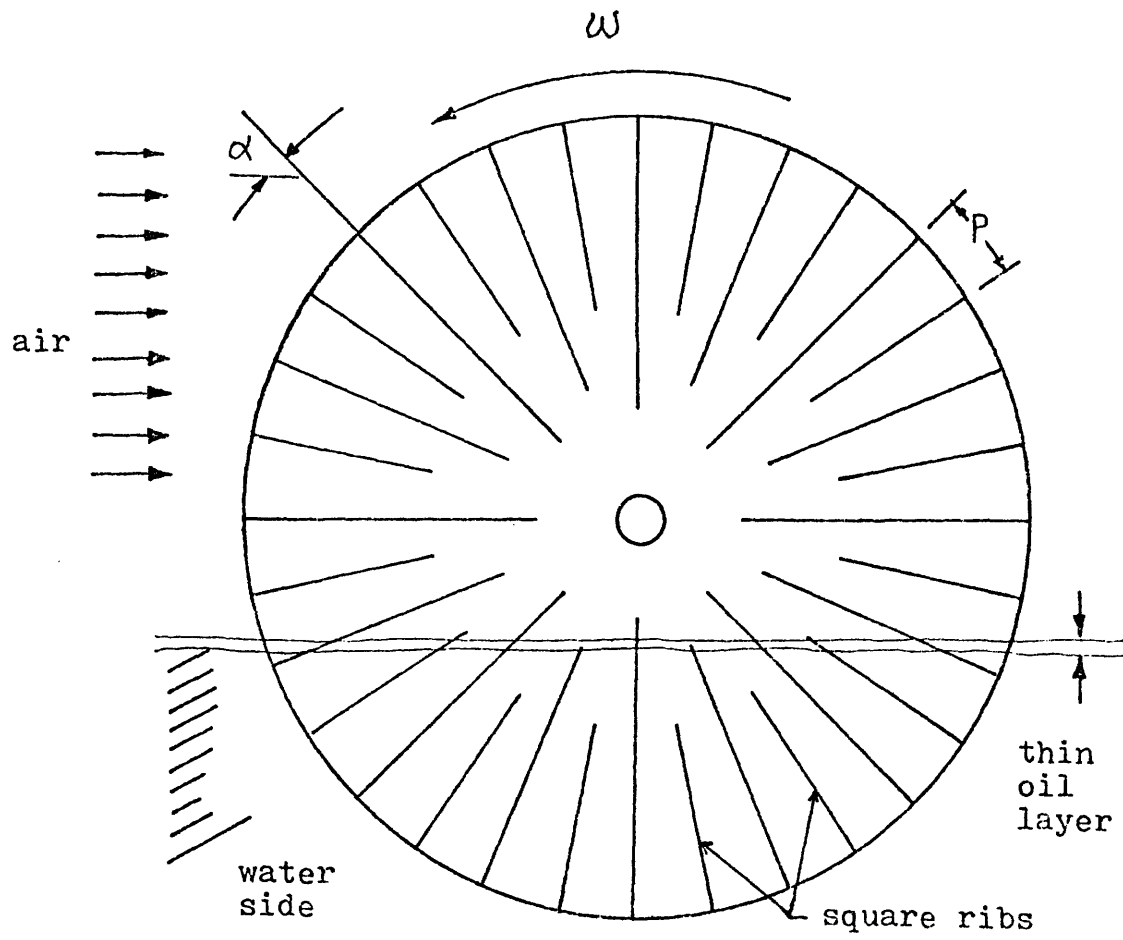
Figure 4.2.1 Square Ribs in Radial Direction on Smooth Plate

4.3 Experimental Program, Results and Correlations

4.3.1 Introduction

The rotary heat exchanger has a number of discs which are assembled with a common rotating axis. Since the disc rotational speed is slow relative to the air flow velocity (5 rpm relative to 20 fps), an infinite parallel plates model can be applied. In other words, two stationary parallel plates can be used as a model for experimental purposes.

An electric heating system, producing a constant heat flux, was used for the entire experiment. Although a constant wall temperature more realistically models the rotary heat exchanger than does a constant heat flux, electric heating was used because of (1) the difficulty and complexity involved in fabricating and operating a constant temperature apparatus, and (2) the difference in the fully developed turbulent thermal boundary layer for both cases is less than 5% [9].

Details of the test apparatus, its calibration, were discussed in last year's annual report [6].

4.3.2 The Effect of Rib Shape on Friction and Heat Transfer

For the friction tests, three different rib shapes were used, corresponding to a ϕ of 40°, 55° and 90° (Figure 4.3.1). Clay was employed to fill the outside corners of the ribs to create the shapes with 40° and 55° angles.

For the heat transfer test, the effect of clay on heat transfer must be considered. Because clay is a poor conductor, too much clay on the aluminum surface would create an insulating layer. Assuming
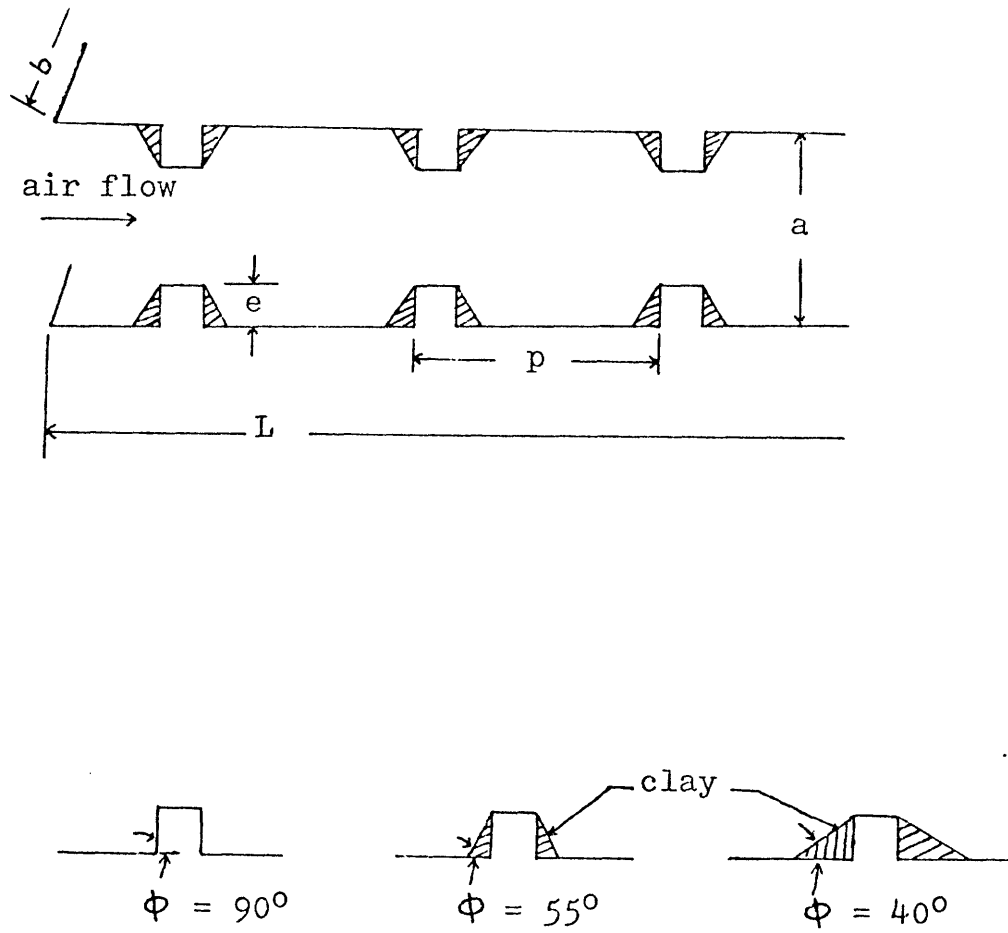
Figure 4.3.1 Model of rib shapes

the thermal conductivity of clay to be 0.5 BTU/hr-ft°F, the effect of

clay for different rib shapes is estimated in Appendix 4A. For a ϕ

of 55° the average thickness of the clay layer is about 0.05 inch. With

this thickness the presence of the clay will degrade the heat transfer

performance by less than 10% when compared with the 90° clay free, or

rib shape. However, for a ϕ of 40°, the average thickness of the clay

layer is about 0.1 inch. and the degradation of performance is about

20%. For this reason, only the rib shapes with ϕ = 55° and 90° are used

in the heat transfer tests.

Test results are presented in Figures 4.3.2 and 4.3.3. In Figure

4.4.3, the friction factor increased 20% when the rib shape was changed

from 90° to 55°, and decreased 30% when the rib shape was changed from

90° to 40°. It is expected that smaller ϕ's have even smaller pressure

drops. If the Reynolds number was less than 5,000, the Stanton number

decreased 10% when the rib shape was changed from 90° to 55°. For Reynolds

numbers greater than 5,000, the Stanton number was insensitive to the

rib shape (Figure 4.3.3). This can be understood by considering the

nondimensional parameter, e^+. As developed in last year's annual report [6]

e^+ is a nondimensional rib height. The magnitude of this nondimensional

height, in comparison to the thickness of the laminar sublayer (calculated

by the universal velocity distribution [10]), can be used to determine

if the rib is penetrating the laminar sublayer and interacting with the

turbulent core. For $e^+ < 5$, the rib is totally within the laminar sublayer

while for $e^+ > 30$, the rib is penetrating into the turbulent core.

Intermediate values of e^+ are transitional cases. When the Re is greater

Figure 4.2.2 Friction factor versus Reynolds
number for different rib shapes
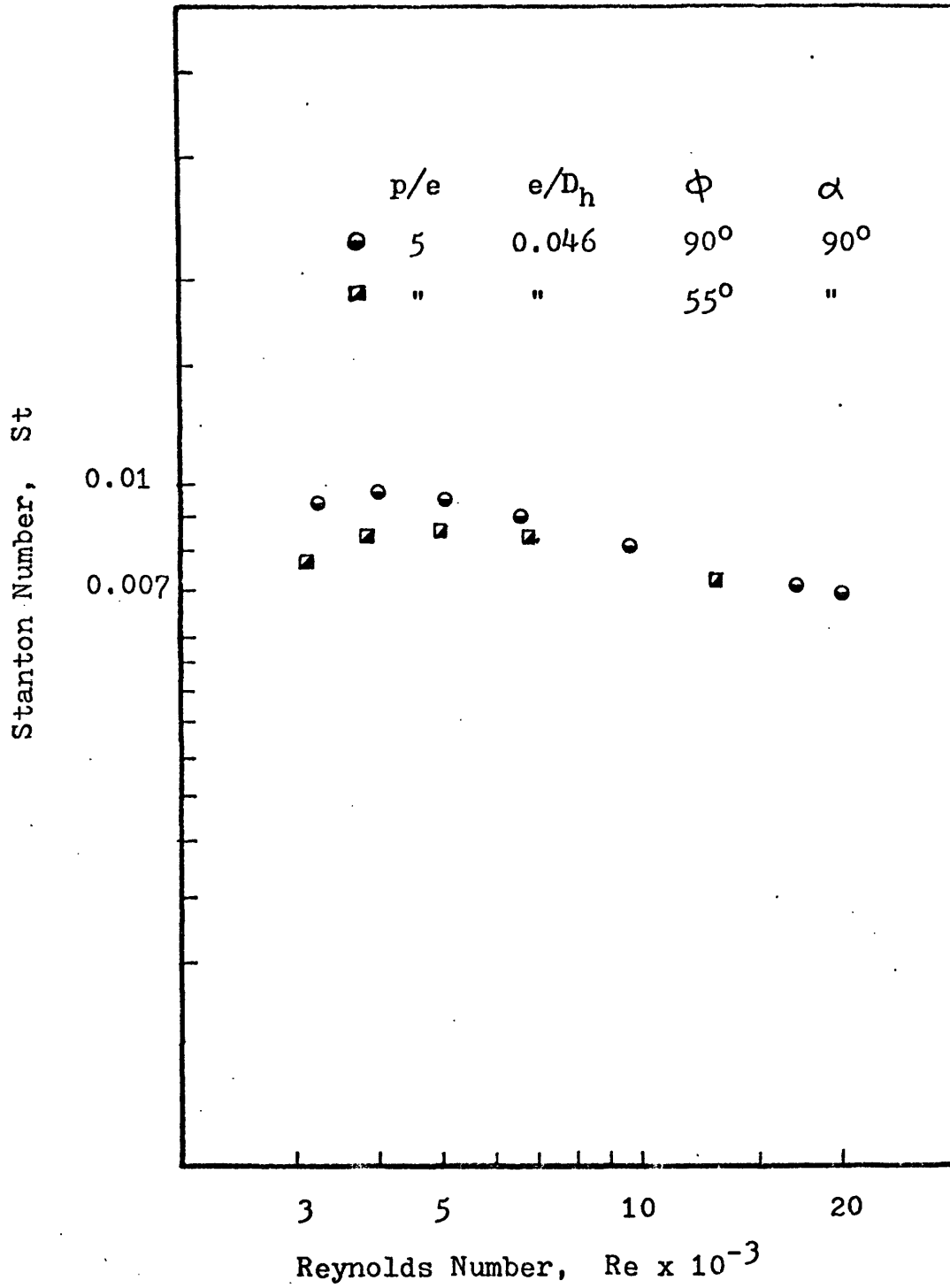
Figure 4.3.3 Stanton number versus Reynolds number for different rib shapes

than 5,000, e^+ is greater than 30, the ribs are penetrating into the turbulent core and the rib shapes have no effect on heat transfer rate; however when Re is less than 5,000, e^+ is less than 30, the ribs penetrate only into the transition regime and the rib shapes have an effect on local flows and the heat transfer rate. No heat transfer tests were performed with a rib shape of 40°.

4.3.3 The Effect of Rib Pitch on Friction and Heat Transfer

The original machined-ribs were 0.1 inch square. Machining 0.033 inch off the top of each rib changed the p/e ratio from 5 to 7.5. The rib then had the dimensions of 0.1 inch width by 0.067 inch height. For a given e/D_h and p/e ratio, such a small change in the dimension of the square rib cross section had been found to have a negligible effect on the friction factor and the heat transfer coefficient [26]. Machining alternate ribs off changes the p/e ratio from 7.5 to 15.

To obtain a surface with the p/e equaling 10, 0.188 inch square steel ribs were glued onto two pieces of aluminum flat plates (1/4" x 12" x 60") using a quick setting epoxy. The glueing was done in such a way that the two surfaces were in uniform contact and there were no air bubbles in the glue layer. Taking alternate ribs off changed the p/e ratio from 10 to 20.

The glue had no effect on the friction factor, but the effect of the glue on the heat transfer coefficient must be considered. Because glue is a poor conductor, too much glue on the aluminum surface might create an insulating layer. Assuming the thermal conductivity of glue to be 0.1 BTU/hr-ft°F and a thickness of 0.1 inch, it is found that the heat transfer

coefficient is decreased by about 5% when compared with a surface without glue. Thus, a thin glue layer has a negligible effect on heat transfer.

The pitch to height ratios of 5, 7.5, 10, 15 and 20 were tested. All data are plotted in figures 4.3.4 and 4.3.5. From Figure 4.3.4, it is quite clear that a p/e of 10 had the highest friction factor. p/e's of 5 and 7.5 have the same magnitude of friction factor at the same Reynolds number, both being 10% lower than that of a p/e equaling 10. In the heat transfer portion of figure 4.3.5, a p/e equaling 10 had the highest heat transfer coefficient. The Stanton number decreased by 5% when the p/e was increased to 15 and decreased 10% when p/e wad decreased to 5.

A possible explanation of the experimental results follows: For the case of a shorter rib pitch (p/e = 5), flow separates after the rib, but reattachment cannot occur between ribs. Flow vortices which induce pressure loss and heat transfer occur between ribs (see Fig. 4.3.6). So in case of p/e equaling 5, both the pressure drop and heat transfer increase when compared with the smooth surface. In the case of p/e equaling 10, the flow separates and reattachment occurs shortly before reaching the next rib. Between the separation point and the reattachment point, reverse flows (vortices) occur. After the reattachment point, the boundary layer tends to grow, but it is broken by the next rib, and the flow pattern is repeated. In this flow pattern, since there is a thin boundary layer near the reattachment region, there are much larger pressure loss and heat transfer than the vortex flow region (i.e., p/e = 5). In case of a larger rib pitch (p/e = 20), the flow pattern is the same as before, but because of the larger pitch, the boundary layer is allowed to grow over a
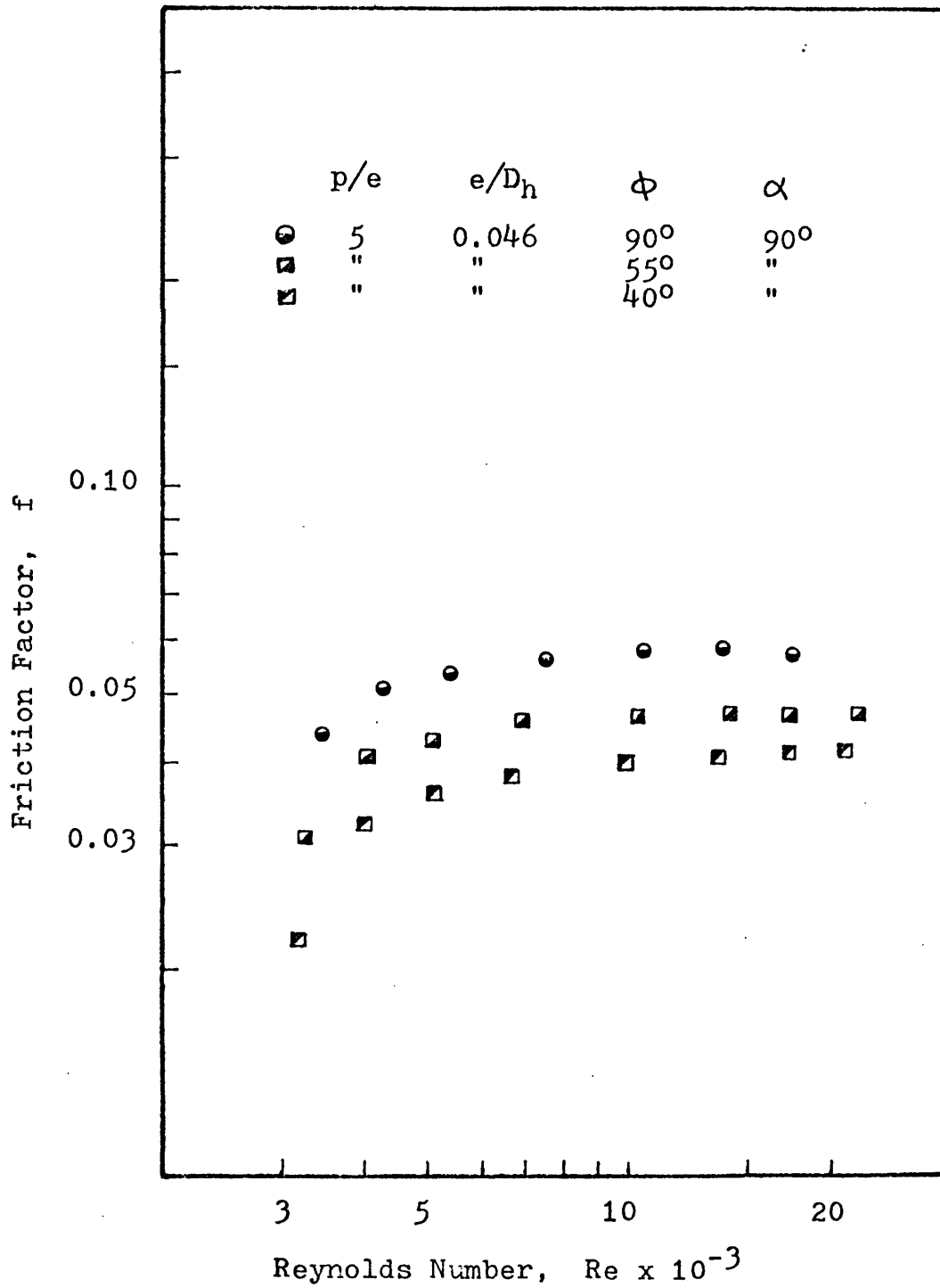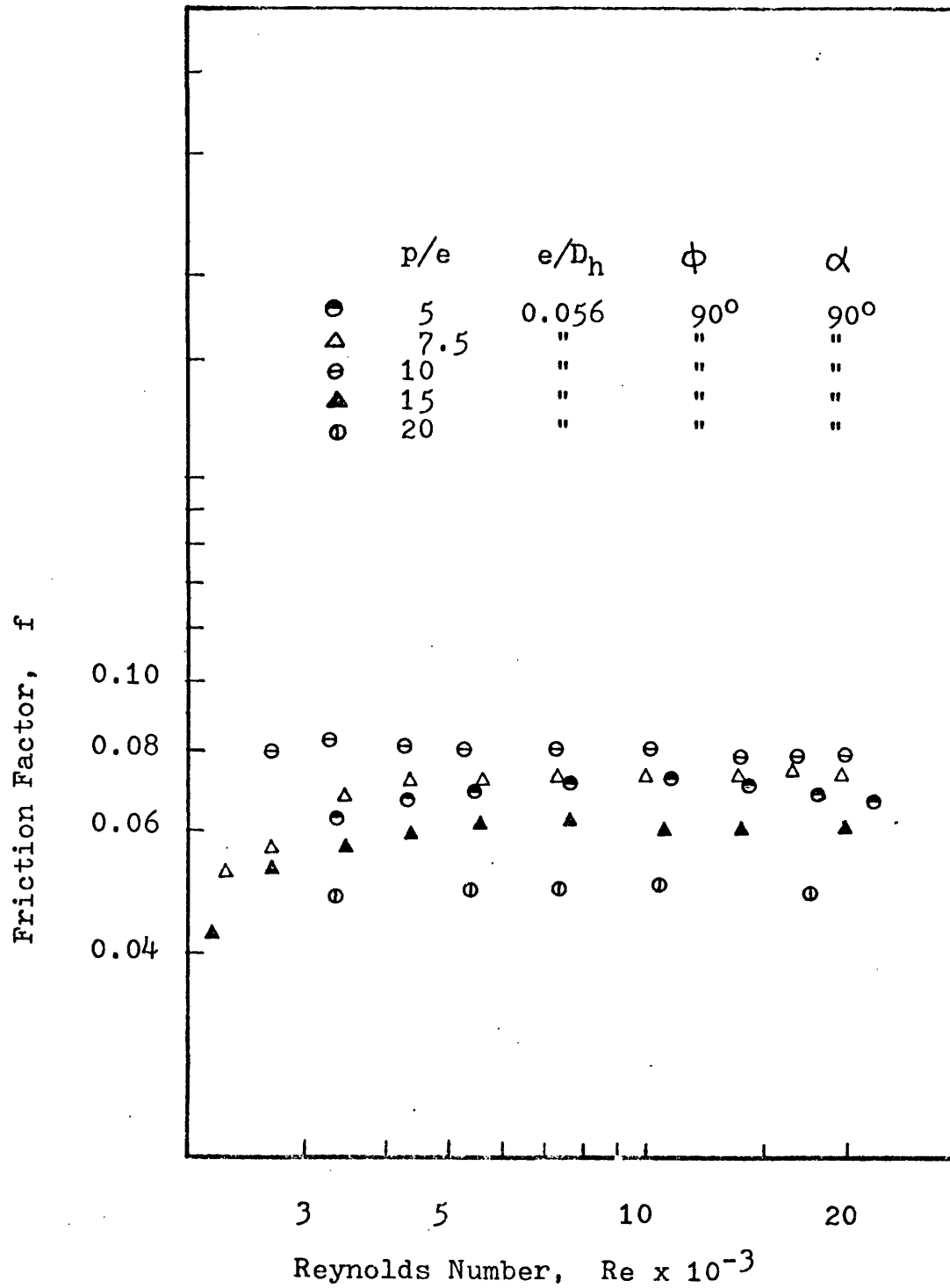
Figure 4.3.4 Friction factor versus Reynolds
number for different p/e ratios
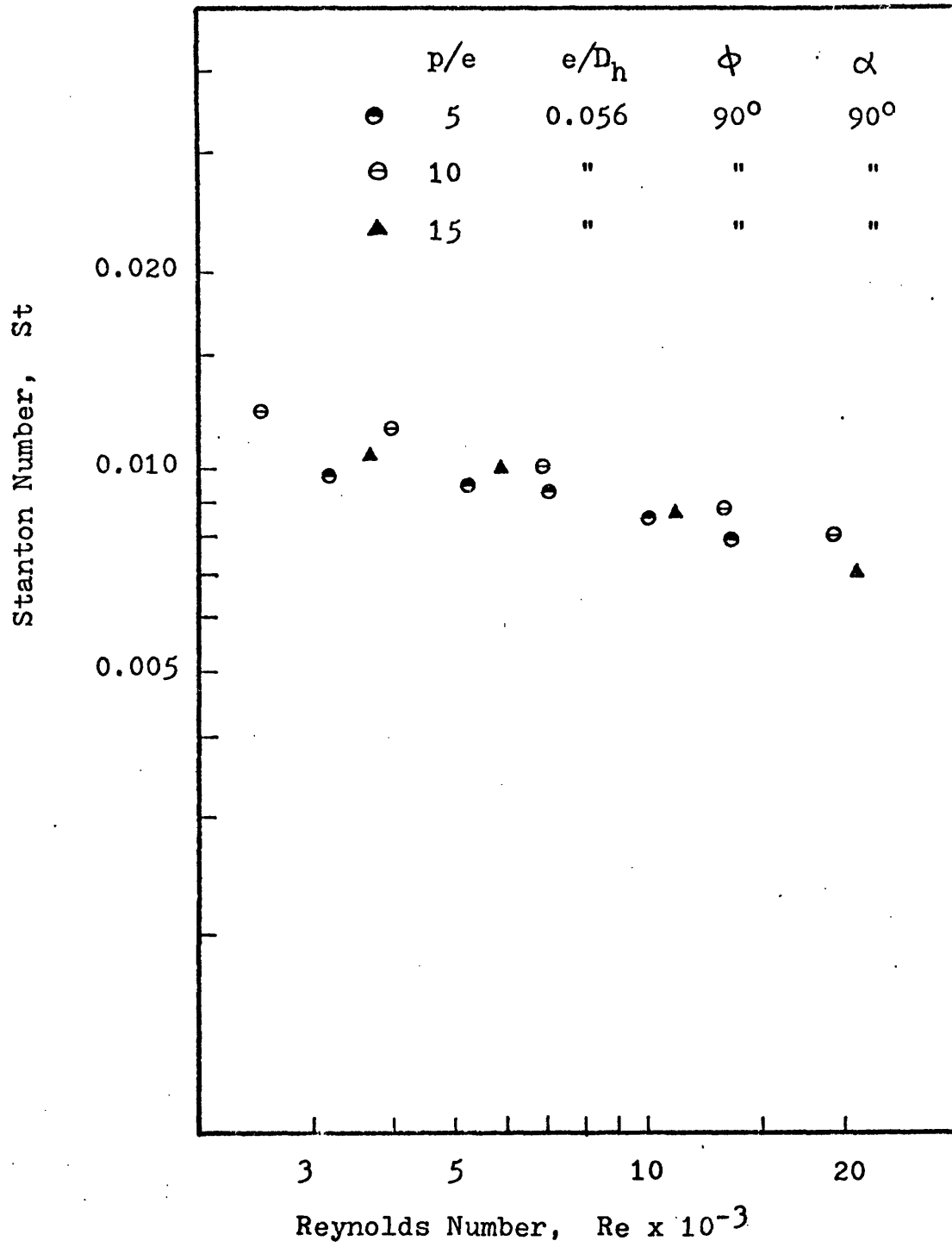
Figure 4.3.5   Stanton number versus Reynolds

number for different p/e ratios
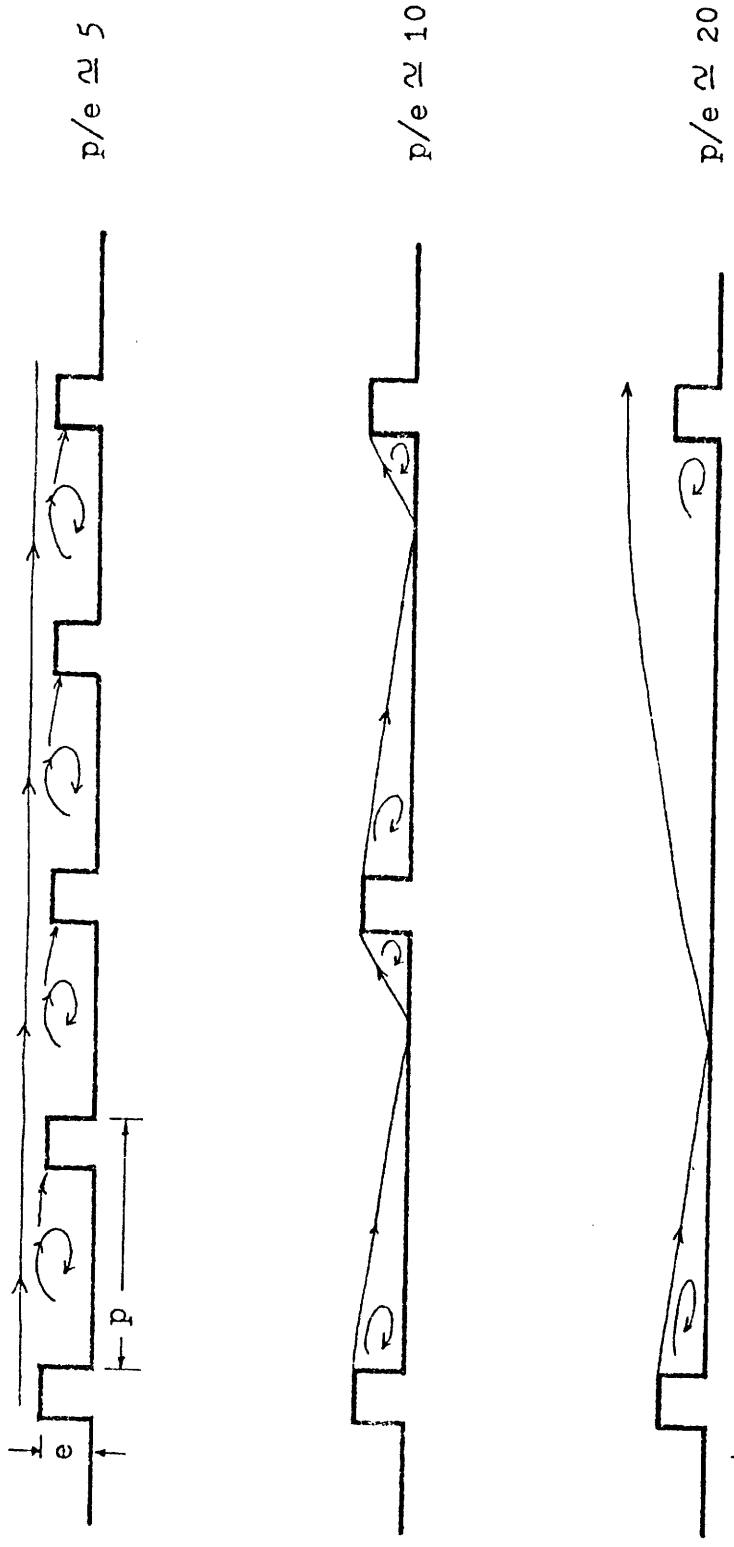
Figure 4.3.6 The Effect of Rib Pitch on the Flow Pattern

longer distance before being broken by the next rib. This thick boundary
layer reduces the pressure loss and heat transfer capability. Hence
when p/e equals 20, the friction factor and heat transfer decrease from
that when p/e equals 10.

4.3.4 The Effect of Flow Attach Angle on Friction and Heat Transfer

In order to experimentally examine the effect of flow attack angle
on the friction factor and heat transfer coefficient, the flow attack angle
was varied from 90°, 45° to 20° with p/e, e/D_h, and ϕ kept constant at
10, 0.102, and 90°, respectively. The experimental data for these
conditions are plotted in Figures 4.3.7 and 4.3.8. A second series of
tests were performed with p/e = 20, e/D_h = 0.102, ϕ = 90°, and the flow
attack angle varying from 75°, 45° to 20°. The experimental data for this
series of tests are plotted in Figures 4.3.9 and 4.3.10. The pitch as
used in this discussion is defined as the space between ribs in the flow
direction.

In Figures 4.3.7 and 4.3.8 it is important to point out that while
the friction factor drops 45% when the flow attack angle is changed from
90° to 45° at a given Reynolds number, the Stanton number only drops 5%.
If the flow attack angle is further decreased to 20°, the friction factor
has decreased a total of 70% while the Stanton number has decreased a total
of 60% for the same Reynolds number. In other words, a flow attack angle
of 45° represents the best thermal-hydraulic performance. At this point,
the heat and momentum analogy is not applicable to a surface with
different flow attack angles. The reason is that the form drag (which
makes no contribution to the heat transfer mechanism) will be reduced when

Figure 4.3.7 Friction factor versus Reynolds number for different flow attack angles
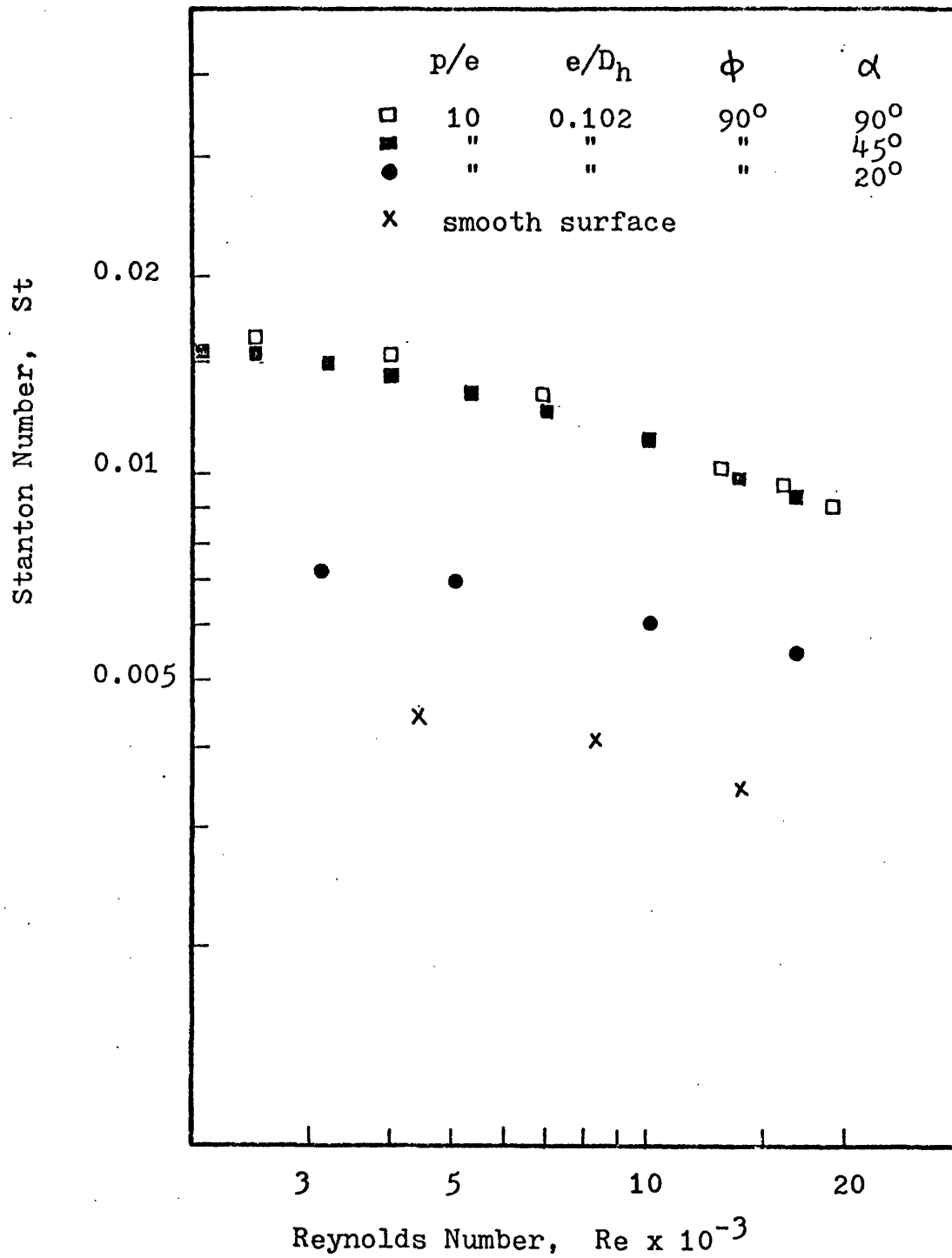
Figure 4.5.8 Stanton number versus Reynolds number for different flow attack angles

the flow attack angle is changed from 90° to 45°. Hence, while the rib with a 45° flow attack angle or greater still has the capability to break down the laminar sublayer of the turbulent flow, and reattachment occurs shortly before reaching the next rib (which is the mechanism that causes a high heat transfer), the form drag is being reduced. If the flow attack angle is further decreased to 20° (and beginning to appear almost like a smooth surface), both the friction factor and the heat transfer coefficient decrease to lower values. Possibly at such low flow attack angles, the air stream near the wall is following the rib direction, rather than traveling across the rib. It is expected that the friction factor and Stanton number will approach that of a smooth surface as the flow attack angle approaches zero degrees.

Figures 4.3.9 and 4.3.10 show the same tendency for the tests when p/e equals 20. Figures 4.3.11 and 4.3.12 directly show the effect of flow attack angle on the friction factor and Stanton number for different p/e ratios.
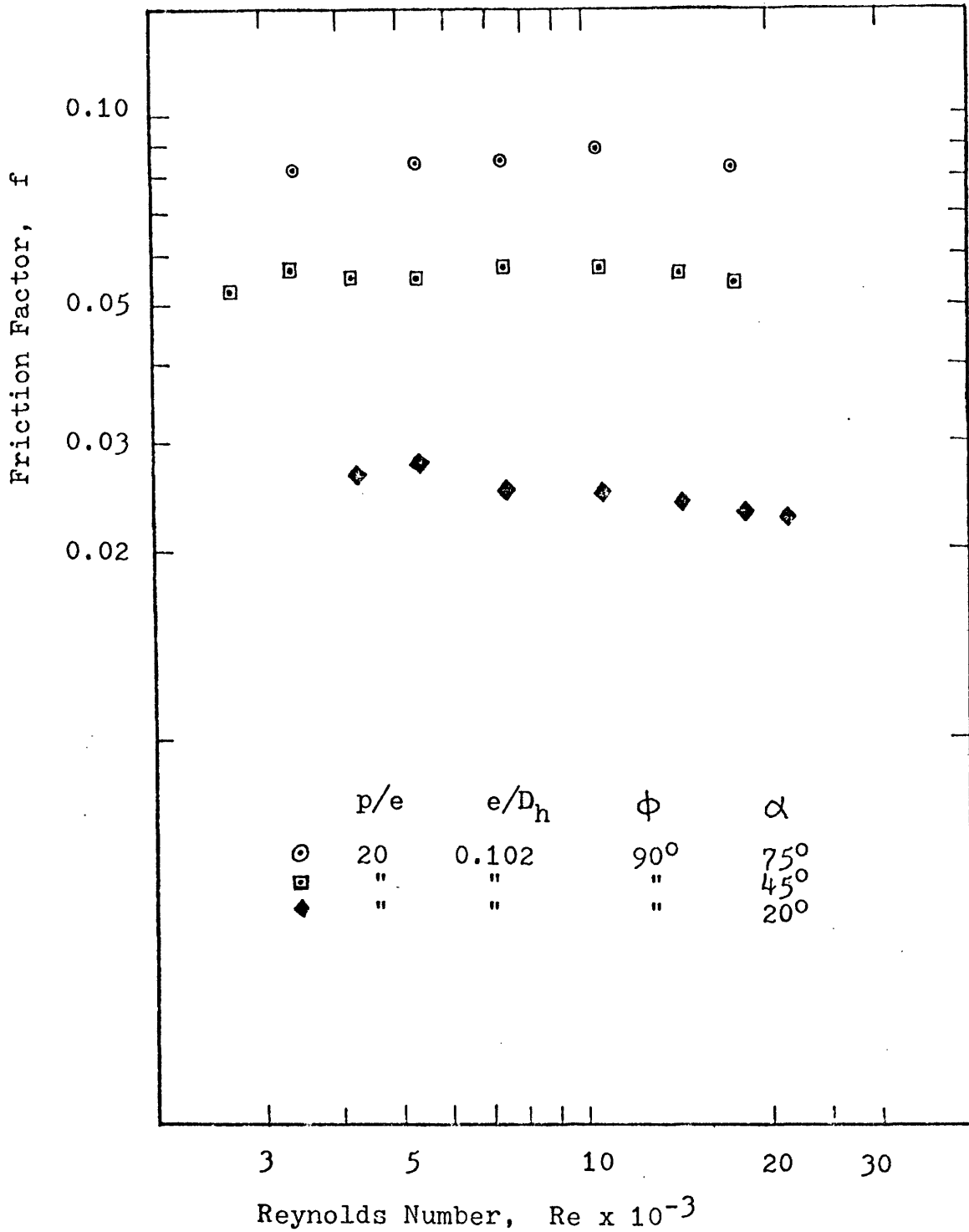
Figure 4.3.9 Friction factor versus Reynolds number
for different flow attack angles

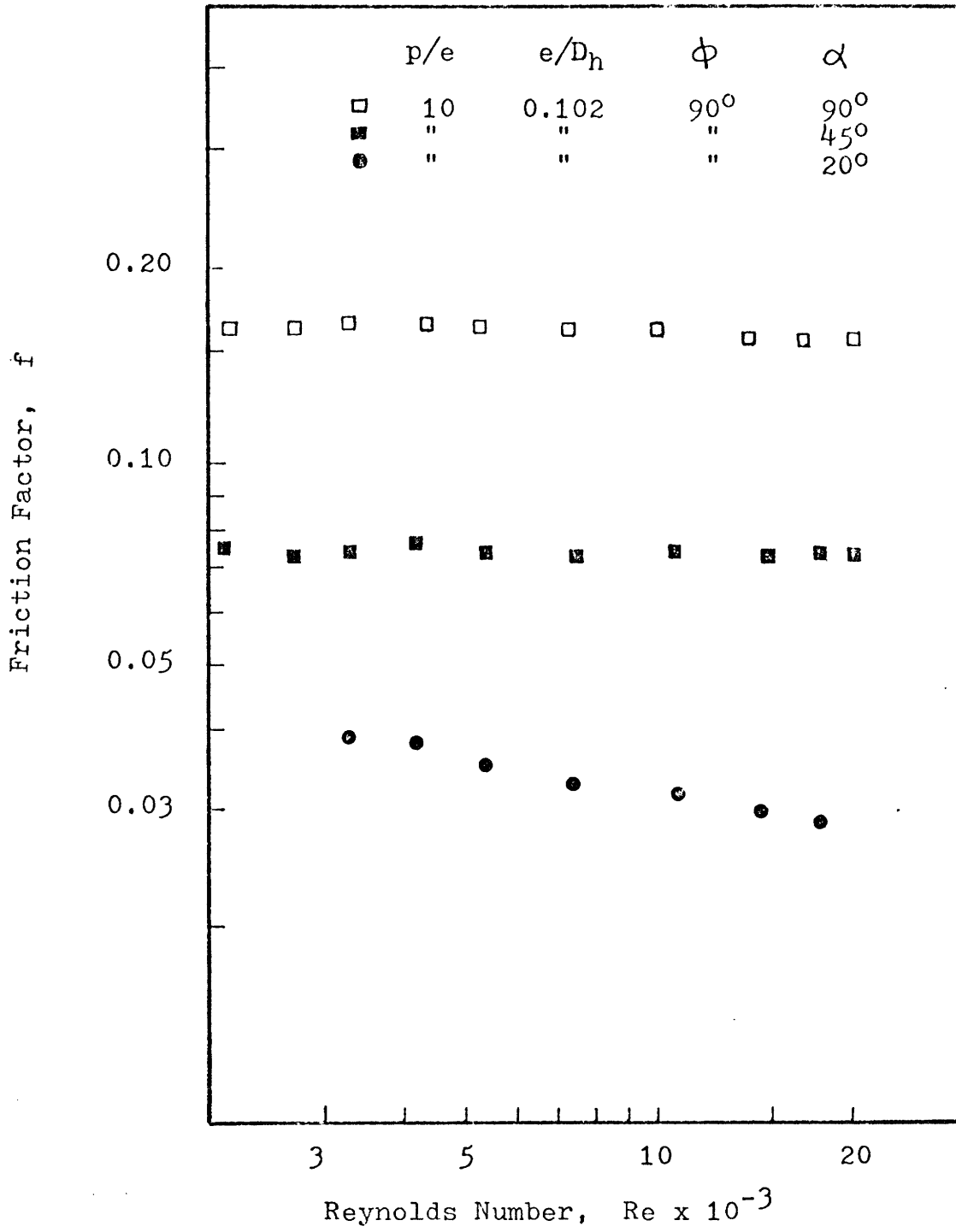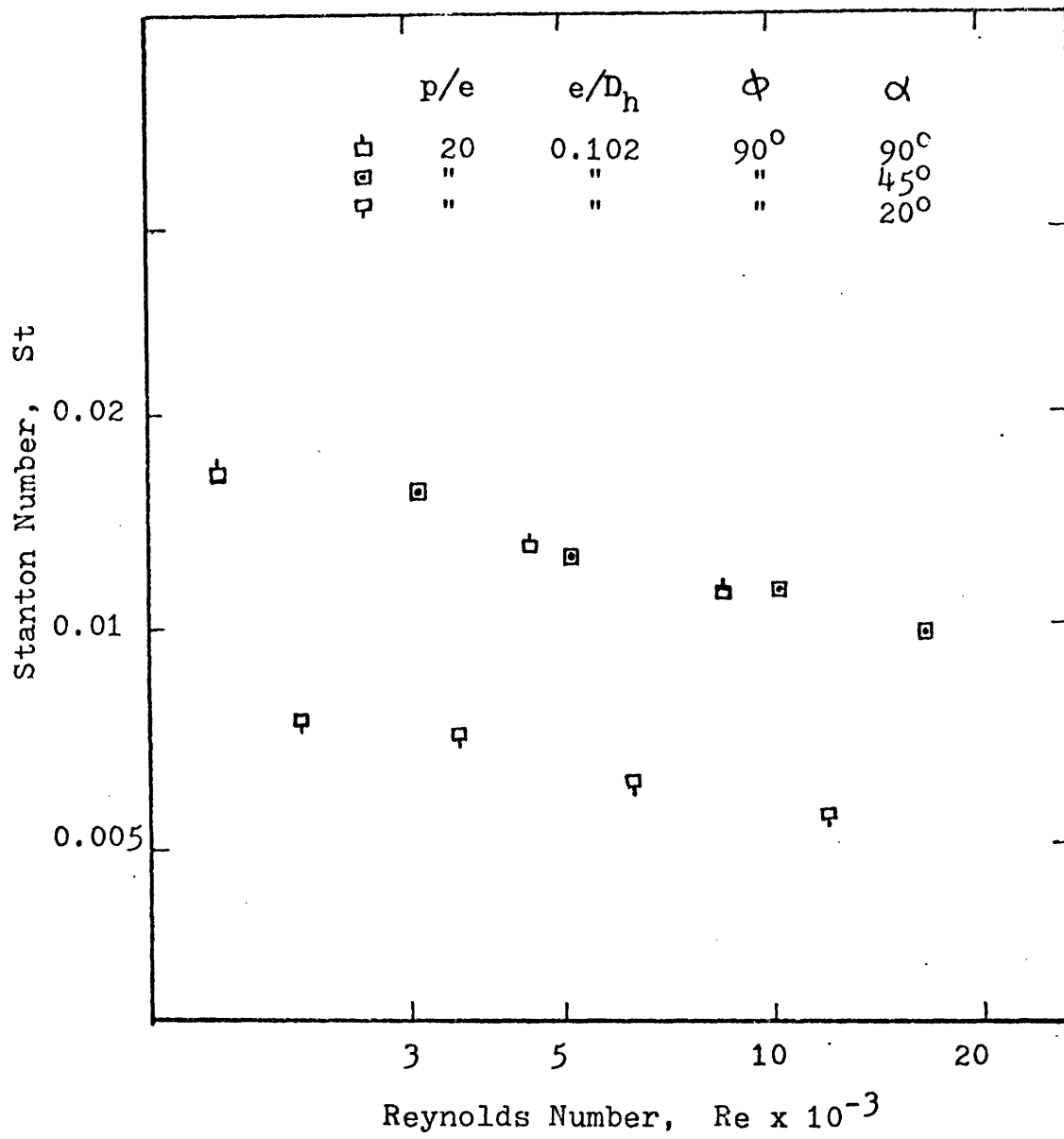Figure 4.3.1c Stanton number versus Reynolds number
for different flow attack angles
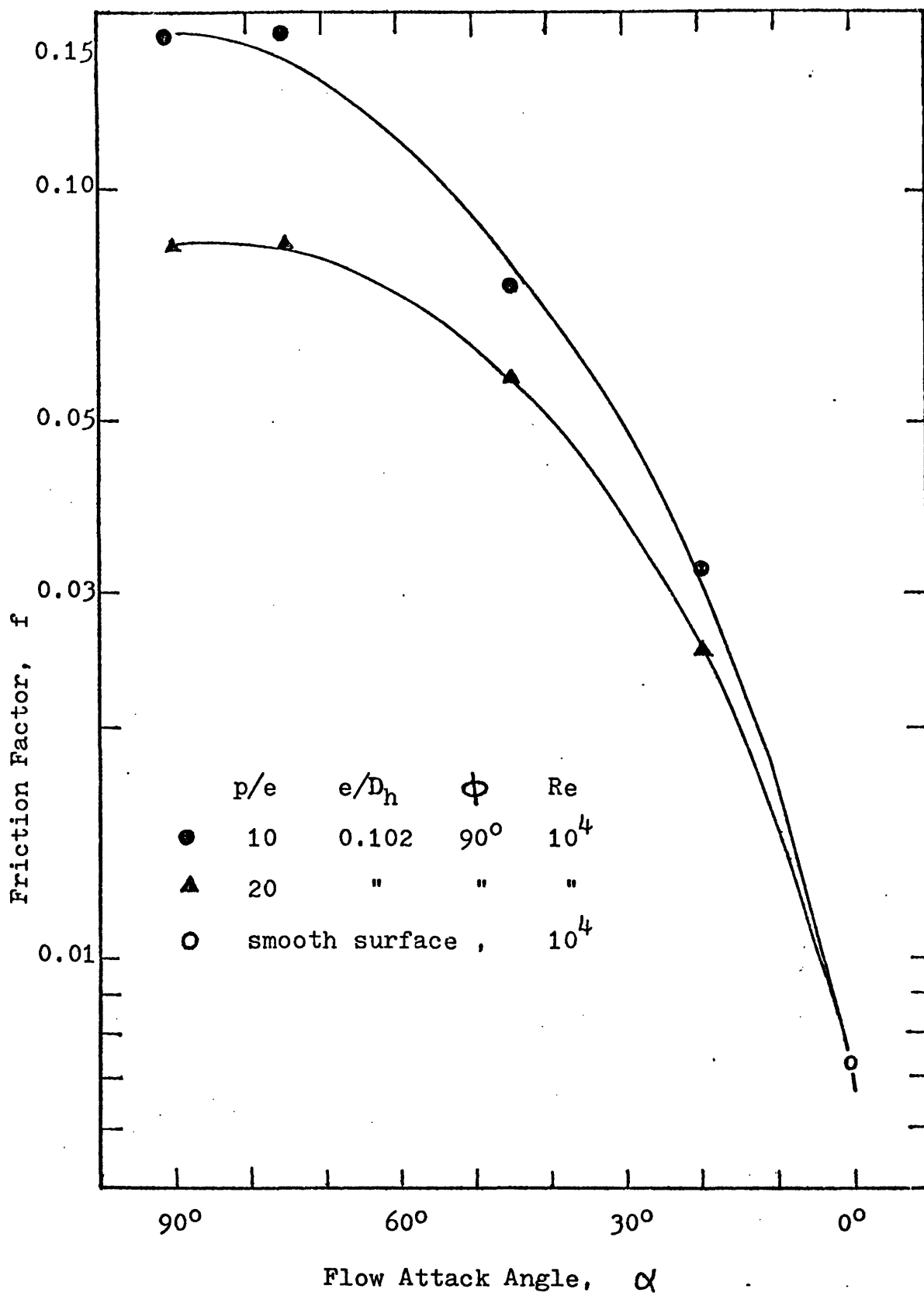
Figure 4.3.11 Friction factor versus flow attack angles
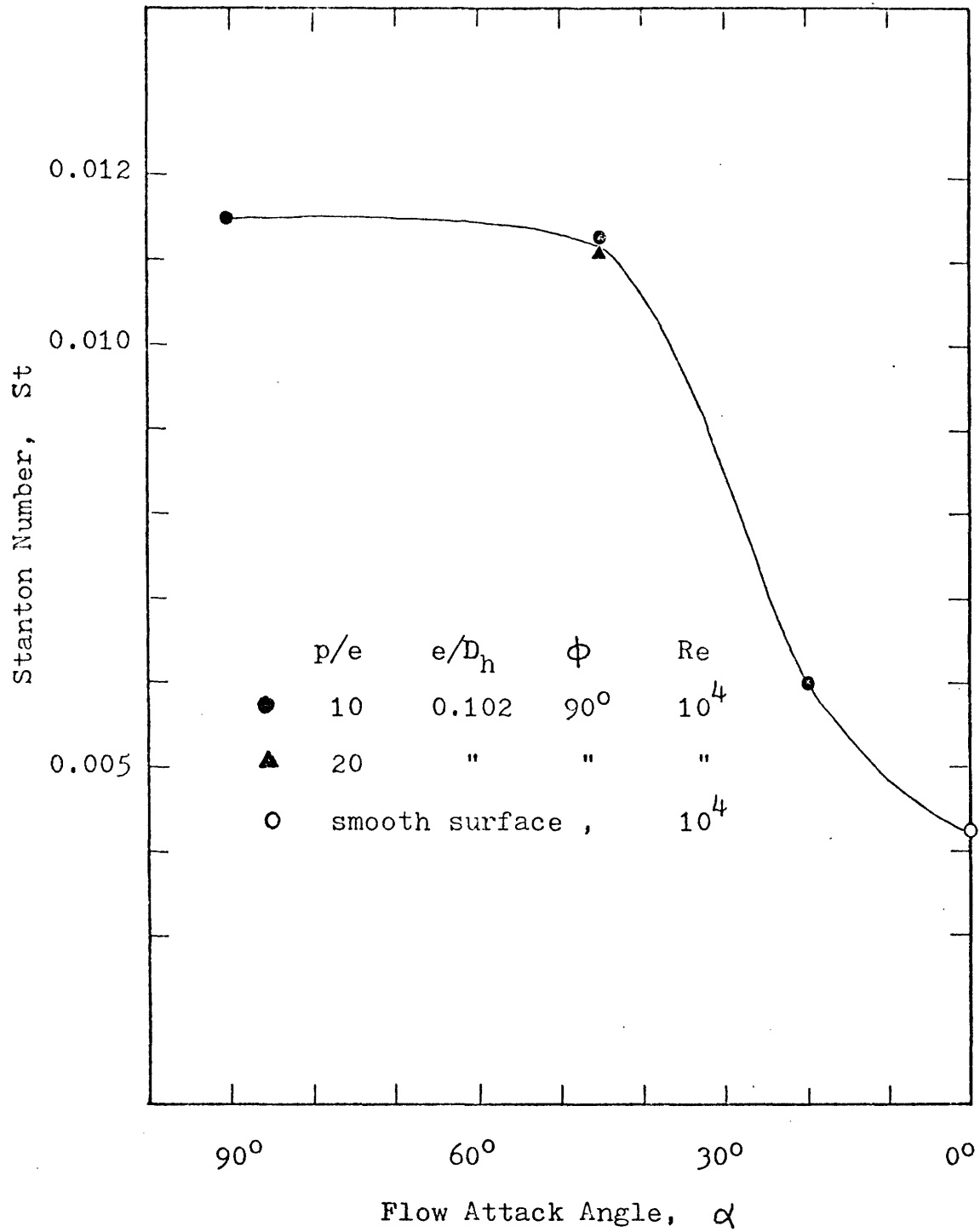
Figure 4.3.12 Stanton number versus flow attack angles

4.4 Correlation of Data

4.4.1 General Form of the Correlations

Both the heat transfer and the friction factor data were correlated using their respective similarity laws. These 'laws' are based upon the assumption that in turbulent flow there exists two separate regimes in any flow channel. One regime that exists away from the immediate vicinity of the wall where the core conditions are unaffected by the wall, and a second region near the wall where the velocity and thermal gradients depend upon local wall conditions.

The 'friction similarity law', originally derived by Nikuradse [27] is given by:

$$R_e^+(e^+) = \sqrt{2/f} + 2.5 \ln(2e/D_h) + 3.75 \qquad (4.4.1)$$

where the roughness function Re^+ is a general function of e^+ determined empirically for each roughness shape. e^+ is defined as $e^+ = (e/D_h)Re \sqrt{f/2}$.

In a similar fashion, the 'heat transfer similarity law', originally derived by Dipprey and Sabersky [28], is given by,

$$H_e^+(e^+, Pr) = R_e^+(e^+) + \frac{\dfrac{f}{2 St} - 1}{\sqrt{f/2}} \qquad (4.4.2)$$

H_e^+ is the so-called heat transfer function, and is dependent upon both e^+ and the Prandtl number. It must be emphasized that both R_e^+ and H_e^+ depend upon the specified type of geometrically similar roughness and are experimentally determined for each roughness type.

In general, the similarity laws can be applied to any type of roughness geometry by taking into account the geometrically non-similar roughness parameters. Not only the rib height and pitch but also the rib shape

and flow attack angle will change the flow pattern near the rough wall region (i.e., change the velocity distribution and the eddy diffusivity of heat and momentum). Hence, correlations for the friction and heat transfer data were sought in the following forms:

for the friction factor:

$$R^+(e^+) = R_e(e^+) \ f_1(p/e) \ f_2(\phi) \ f_3(\alpha) \qquad 4.4.3$$

for heat transfer:

$$H^+ = H_e^+(e^+, \ Pr) \ f_4(p/e) \ f_5(\phi) \ f_6 \ (\alpha) \qquad 4.4.4$$

where $R_e^+(e^+)$ and $H_e^+(e^+, \ Pr)$ are given by equations 4.4.1 and 4.4.2, respectively, and where $R^+(e^+)$, H^+, and the functional relations for p/e, ϕ, and α, were experimentally determined.

By taking into account the effect of the rib shape and the flow attack angle, the general friction and heat transfer functions were investigated in this study. All data on varying e^+, p/e, ϕ, and α were correlated into equations 4.4.3 and 4.4.4. In this way, the friction and heat transfer similarity laws of equations 4.4.1 and 4.4.2 were extended to equations 4.4.3 and 4.4.4 by taking into account the geometrically non-similar parameters, p/e, ϕ, and α. The final friction and heat transfer correlations are shown in Figures 4.4.1 and 4.4.2.
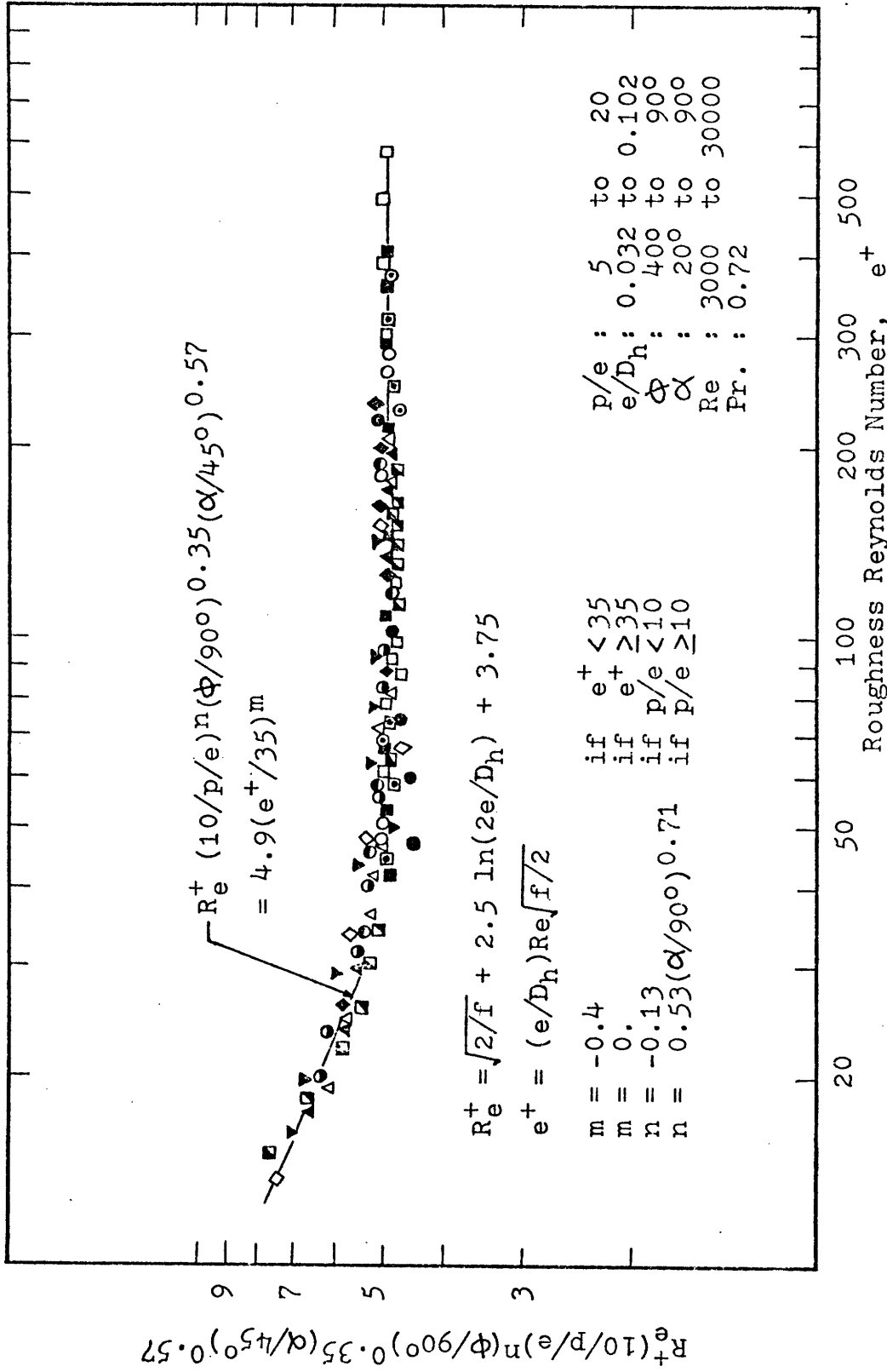
Figure 4.4.1 Final Friction Correlation

$$(H_e^+)(\alpha/45°)^j = 10.0\,(e^+/35)^i$$

$$H_e^+ = (f/2St - 1)/\sqrt{f/2} + R_e^+$$

$$R_e^+ = \sqrt{2/f} + 2.5\,\ln(2e/D_h) + 3.75$$

$$e^+ = (e/D_h)Re\sqrt{f/2}$$

$i = 0.$ if $e^+ < 35$
$i = 0.28$ if $e^+ \geq 35$
$j = -0.45$ if $\alpha \geq 45°$
$j = 0.5$ if $\alpha < 45°$

St based on total area
(including rib area)

p/e :   5   to   20
e/D_h : 0.032 to 0.102
φ   :   55° to   90°
α   :   20° to   90°
Re : 3000 to 30000
Pr : 0.72
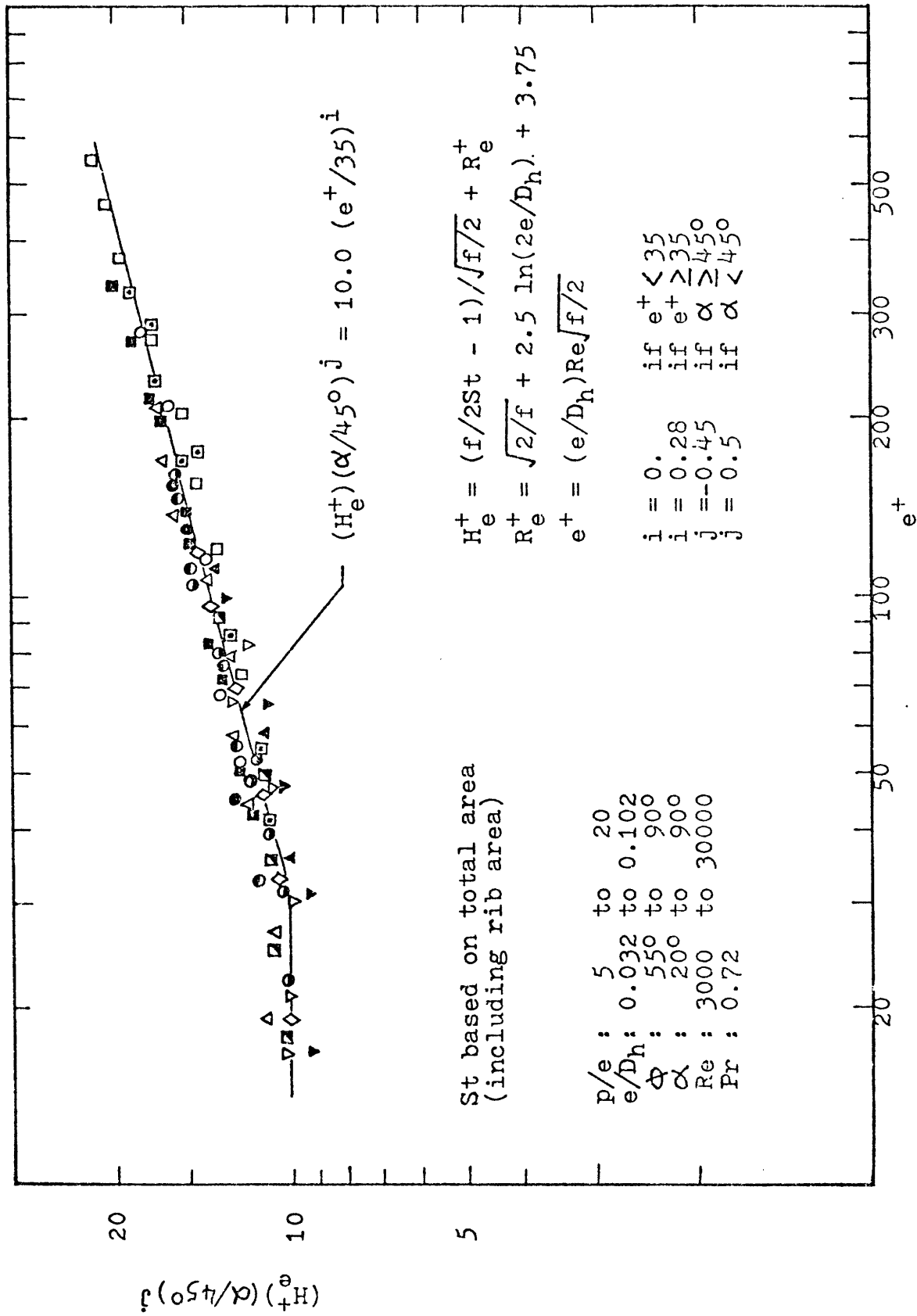
Figure 4.4.2   Final heat transfer correlation

4.4.2 Final Friction Factor Correlation

The data can be correlated into a single curve by multiplying R_e^+ with $(\phi/90°)^{0.35}(10/p/e)^n(\alpha/45°)^{0.57}$. This is shown in Figure 4.4.1. In this figure, R_e^+ equals $4.9(e^+/35)^m$. In algebraic form,

$$R_e^+(e^+)(\phi/90°)^{0.35}(10/p/e)^n(\alpha/45°)^{0.57} = 4.9(e^+/35)^m \qquad (4.4.5)$$

where

$$R_e^+(e^+) = \sqrt{2/f} + 2.5 \ln(2e/D_h) + 3.75 \qquad (4.4.1)$$

(the so called "friction similarity law")

$$e^+ = (e/D_h)Re\sqrt{f/2}$$

$$m = -0.4 \qquad \text{if } e^+ < 35$$

$$m = 0 \qquad \text{if } e^+ \geq 35$$

$$n = -0.13 \qquad \text{if } p/e < 10$$

$$n = 0.53(\alpha/90°)^{0.71} \qquad \text{if } p/e \geq 10$$

Equations 4.4.5 and 4.4.2 can be rewritten as:

$$\sqrt{2/f} = \frac{4.9(e^+/35)^m}{(\phi/90°)^{0.35}(10/p/e)^n(\alpha/45°)^{0.57}} - 2.5 \ln(2e/D_h) - 3.75 \qquad (4.4.6)$$

It was assumed that the effect of e^+, p/e, ϕ, and α on R^+ are not interrelated, but is of the form of $R^+ = Re^+(e^+) \ f_1(p/e)f_2(\phi)f_3(\alpha)$. However the experimental correlation of equation 4.4.5 shows p/e is dependent upon ϕ when $p/e \geq 10$.

Equation 4.4.6 represents the general form of the correlation between the friction factor and e/D_h, p/e, ϕ, α, and Re. For given characteristic values of the roughness and the flow condition, the friction factor can be calculated from equation 4.4.6.

4.4.3 Final Heat Transfer Coefficient

Under the assumption of equation 4.4.4, the data can be correlated by multiplying H_e^+ by $(\alpha/45°)^j$. This is illustrated in Figure 4.4.2. Note that the experiments have shown that H_e^+ is not a function of ϕ or of p/e ($40° \leq \phi \leq 90°$, $5 \leq$ p/e ≤ 20). From figure 4.4.2 it can be seen that H^+ equals $10.0(e^+/35)^i$, therefore,

$$(H_e^+)(\alpha/45°)^j = 10.0(e^+/35)^i \qquad (4.4.7)$$

where

$$H_e^+ = (f/2St - 1)/\sqrt{f/2} + R_e^+$$

$$R_e^+ = \sqrt{2/f} + 2.5 \ln(2e/D_h) + 3.75 \qquad (4.4.1)$$

$$e^+ = (e/D_h)Re\sqrt{f/2}$$

$$i = 0.0 \qquad \text{if } e^+ < 35$$

$$i = 0.28 \qquad \text{if } e^+ \geq 35$$

$$j = -0.45 \qquad \text{if } \alpha \geq 45°$$

$$j = 0.5 \qquad \text{if } \alpha < 45°$$

Equation 4.4.7 represents the general form of the correlations between the Stanton number, e/D_h, p/e, ϕ, α, f and Re. For a given R_e^+, f, e^+ and α, the Stanton number can be calculated from this equation. To take into account the Prandtl number effect, H_e^+ will be replaced by (H_e^+) $(0.72/Pr)^{0.57}$, in equation 4.4.7, where the Prandtl number varies from 0.71 to 37.6. This is suggested by Webb, Eckert, and Goldstein [21]. These equations can be rewritten as:

$$\frac{(f/2St) - 1}{\sqrt{f/2}} = \frac{10.0(e^+/35)^i}{(\alpha/45°)^j (\frac{.72}{PR})^{.57}} - \sqrt{2/f} - 2.5 \ln(2e/D_h) - 3.75 \qquad (4.4.8)$$

4.4.4 Summary of Correlations

1. Heat transfer augmentation has been studied for turbulent flow between parallel plates using repeated-rib roughness. Repeated-ribs behave as a "turbulence promotor" to break down the laminar sublayer of the turbulent flow and induce more turbulence near the wall region. It was found experimentally that the friction factor and heat transfer coefficient not only depend on the Reynolds number, the ratio of rib height to hydraulic diameter and pitch to height ratio, but also on the rib shape and flow attack angle. Also, for a given Reynolds number, a height to hydraulic diameter ratio and rib shape, the optimal thermal-hydraulic performance is given by a pitch to height ratio of 10, and flow attack angle of 45°.

2. A friction correlation has been developed for turbulent flow between parallel plates having a repeated-rib roughness. The friction correlation is based on the law of the wall similarity with a logarithmic velocity distribution. This is the same method employed by Nikuradse for the sand-grain roughness. The general friction correlation has been obtained by taking into account the effect of geometrically non-similar parameters. All experimental friction data well correlated in Fig. 4.4.1, or algebraically, in the form of equation 4.4.6.

3. The heat transfer correlation developed for turbulent flow between parallel plates having a repeated-rub roughness, is based on the application of a heat momentum transfer analogy by Dipprey and Sabersky for the sand-grain roughness. The general heat transfer correlation has been obtained by taking into account the effect of geometrically non-similar

parameters. All experimental heat transfer data are well correlated in Figure 4.4.2, or algebraically, in the form of equation 4.4.8.

Since the effect of pitch to height ratio and rib shape on the heat transfer function (H_e^+) is very small, pitch to height ratio and rib shape does not show up in equation 4.4.8. Equation 4.4.8 is for air flow only $(Pr = 0.72)$. To take into account the Prandtl number effect, H_e^+, should be replaced by $(H_e^+)(0.72/Pr)^{0.57}$ in equation 4.4.8, (suggested by Webb, Eckert, and Goldstein [21]).

4. The friction and heat transfer correlations of equation 4.4.6 and equation 4.4.8 are based on experimental data for air flow with $0.032 \leq e/D_h \leq 0.102$, $5 \leq p/e \leq 20$, $40° \leq \phi \leq 90°$, $20° \leq \alpha \leq 90°$, and $3,000 \leq Re \leq 30,000$. The correlations can be extended to a wider range of e/D_h ratio by the law of the wall similarity. Given a roughness parameters of e/D_h, p/e, ϕ, and α, the friction factor and Stanton number can be determined as follows. First select any value of e^+, and use equation 4.4.1 to calculate R_e^+ and f directly. Then Re can be computed from $Re = e^+/((e/D_h)\sqrt{f/2})$. Equation 4.4.3 can be used to determine St. Then select another value of e^+ to get the corresponding R_e^+, f, Re and St. and so on. The graphs of f and St versus Re can now be plotted For given values of e/D_h, p/e, ϕ, α, and Re, f and St can be read directly off the graph.

5. By using the equivalent hydraulic diameter (D_h) friction and heat transfer correlations of equation 4.4.6 and equation 4.4.8 can be applied to design any type of heat exchangers.

4.5 Economic Comparison of Smooth and Rough Surfaces

4.5.1 Introduction

In section 4.4, the general friction and heat transfer correlations for roughened surfaces were obtained experimentally. These friction and heat transfer correlations can be applied to design any kind of heat exchangers with air (or water) as a working fluid. These correlations were specifically developed to aid in the designing of the periodic cooling tower for a large scale electric power generation plants.

An optimum computer design routine [7,8] which was used to design the dry cooling tower with standard tubes will be introduced here and modified to design a periodic coooling tower with annular discs using a rib roughened surface. The projected costs for cooling towers with smooth and rough surfaces will be compared.

4.5.2 Concept of the Optimum Computer Design Program

A computer model [7,8] was developed to design the best possible heat exchanger by optimizing heat transfer and the thermodynamic relations with economic trade-offs. An example of one of the economic trade-offs that must be considered is the turbine outlet water temperature. The amount of heat rejected is proportional to the surface area of the cooling tower times the temperature difference between the inlet air and inlet water. For a given ambient air temperature and thermal load, the higher the water temperature the less surface area is needed. As the heat transfer surface area becomes smaller, the capital cost of the cooling tower is reduced. However, the higher water temperature causes a lower Rankine cycle efficiency, and a lower cycle efficiency requires a larger boiler capacity, greater fuel consumption, and more heat rejection for the same MW generation.

In optimizing the design of the cooling tower coupled with the power plant, the most important cost is the incremental increase in the average yearly cost of power generation (mills/kwh) resulting from the use of a dry cooling tower. The incremental cost can be calculated from capital costs, operating and maintenance costs, increased fuel and boiler costs resulting from decreased thermal efficiency, and the cost of replacement power due to lost capacity at higher ambient air temperatures.

Using standard finned tubes, the dry cooling tower considered is an indirect cooling system, induced draft, single pass cross flow heat exchanger. The nominal power plant output is 1,000 MgW. With heat exchanger surface cost data, turbine heat rate versus back pressure performance, andpower generation all given, the heat transfer and cost equations may be reduced to six independent variables which must be optimized for a dry cooling tower with standard finned tubes. A systematic method of searching combinations of the six variables throughout the allowable range of each variable was used to find the lowest incremental cost design.

The model is general and may be adapted to fossil fuel and nuclear plants and to different locales, costs, and heat exchanger surfaces merely by changing the input data which includes fuel costs, costs of lost capacity per kilowatt-hour, maintenance and interest rates, turbine heat rate versus back pressure, boiler costs, yearly air temperature of the locale, friction and heat transfer coefficients for the heat transfer surface. Land costs and piping costs from the turbine to the heat exchanger are also included. A more detailed description of optimum design program is given in reference [7] and reference [8].

Assumptions and input data values are listed in Tables 4.5.1 and 4.5.2. This cost data is noticeably out of date as it is data for about 1970. This dated information is used in the prior cooling tower studies at MIT. This allows rapid comparisons between the optimal PCT and other cooling systems.

TABLE 4.5.1

Assumptions:

1. Turbine performance varies with outlet temperature as given by General Electric data incorporated in Estimated Turbine Generation Heat Rate Variation with Elevated Pressures.

2. Air side pressure drop to be kept above some minimum value (4 lbf/ft^2).

3. A percentage of the fan velocity is recovered (50%).

4. The yearly cost of operation is the sum of

   - the interest on capital costs (fixed charge rate of 15.8%)

   - the cost of operating the required fans and pumps

   - the cost of additional fuel required due to increased thermal efficiency

   - maintenance costs

   - the cost of lost capacity at off design temperatures

5. Capital costs are broken down into

   - cost of heat exchanger surface ($.4/ft^2$)

   - cost of motors for fans and pumps ($30/hp)

   - cost of the fan blades ($7.5/ft^2$ area covered)

   - cost of increased boiler capacity due to lower themal efficiency ($45/kw)

   - land costs ($11,600/acre)

6. Maintenance cost is expressed as a percent of the capital cost (1.09%).

Table 4.5.2

Values for Input Data**

INPUT	VALUE
Plant size	1,000 MW
Fuel Cost	$.50/Million BTU's
Replacement power costs	15 Mills/Kw-hr
Fixed charge rate	15.8% of capital
Maintenance cost of cooling systems	1.09% of capital
Boiler costs	$45/KW
Electric motor costs	$30/HP
Fan propeller costs	$7.5/ft^2
Fan air velocity	150 ft/sec @ fan
Surface cost	$.4/ft^2
Land cost	$11,600/acre
Capacity factor	75%
Thermal efficiency	40%
Fan and pump efficiency	85%
Temperature data (New York City)	U.S. Weather Bureau
Pressure drop	4 psf
Water pipe diameter	8 ft
Water pipe cost	$173/ft

** costs are for comparative purposed only, and do not reflect 1976 prices.

4.5.3 Modified Optimum Computer Design Program for the Periodic

Cooling Towers

The optimum computer design program for the dry cooling tower with

standard finned tubes was modified and applied to optimize the periodic

cooling tower [4 5]. There are seven variables which should be optimized

for the power plant using a periodic cooling tower with smooth heat

transfer surfaces. (1) D: the distance between plates, (2) T_{wl}: the

water temperature at the tower inlet, (3) T_D: the design ambient air temperature

at   which the power plant can deliver its fully rated power, (4) V_{Al}:

the air velocity through the tower, (5) V_{wl}: the water velocity through the

tower, (6) D_o: the diameter of the disc, and (7)δ_d: the disc thickness.

The seven variables are reduced to five by confining our optimization search

to a disc diameter of five feet and disc thickness to 0.03 inches.

4.5.3.1 Disc with Rough Surface

Since more than half of the total cost of a dry cooling tower

is the cost of the heat transfer surface [5] a reduction in the required

heat transfer surface area significantly lowers the capital cost. For a

given heat rejection rate and temperature difference between hot water and

cold air, an increase in the surface heat transfer coefficient reduces the

total heat transfer area needed. The resultant capital cost savings is

the basic motivation of this investigation. From the experimental results

of section 4.4, the friction factor and heat transfer coefficient depend

not only on the Reynolds number but also on the rig height, pitch, shape

and flow attack angle. The general friction and heat transfer correlations

of equations (4.4.6) and (4.4.8) will be used to design the periodic heat

exchanger. In other words, e/D_h, p/e, ϕ, and α are additional system

variables which have to be optimized for the periodic cooling tower design.

4.5.3.2 Annular Disc Design

Experimental observations of solid discs showed that the variation in temperatures in the central region of disc was much smaller than the outer region [6]. This is because the central region has no contact with the hot water (Figure 4.5.1), and implies that the central region of disc bears a negligible fraction of the heat load in comparison to the outer region. On top of this, the central region has a drag force on the surface, which can be translated into a pressure drop and fan power. Therefore, a design which eliminates the central region (an annular design) would lower cooling tower costs by (1) a more efficient use of material and (2) reducing fan power requirements.

For the annular disc design, the air inflow and outflow can be assumed to be flowing approximately in the radial direction (Figure 4.5.2) Therefore ribs on the annular disc can be assumed to have a constant flow attack angle of 45°, which was experimentally established in section 4.4 to give the best thermal-hydraulic performance. The rotor is modeled as described in section 2.5, with the added simplification that the water side is a single well mixed heat exchanger.

In the modified optimum computer design program, the outer disc diameter (D_o) is a system variable which has to be optimized. In order to maintain the air inflow and outflow to be flowing approximately in the radial direction, the ratio of the inner disc diameter (D_i) to the outer disc diameter has to be restricted to be greater than some lower bound (Figure 4.5.2). In this program, the D_i/D_o ratio is allowed to vary between 0.6 and 1.0
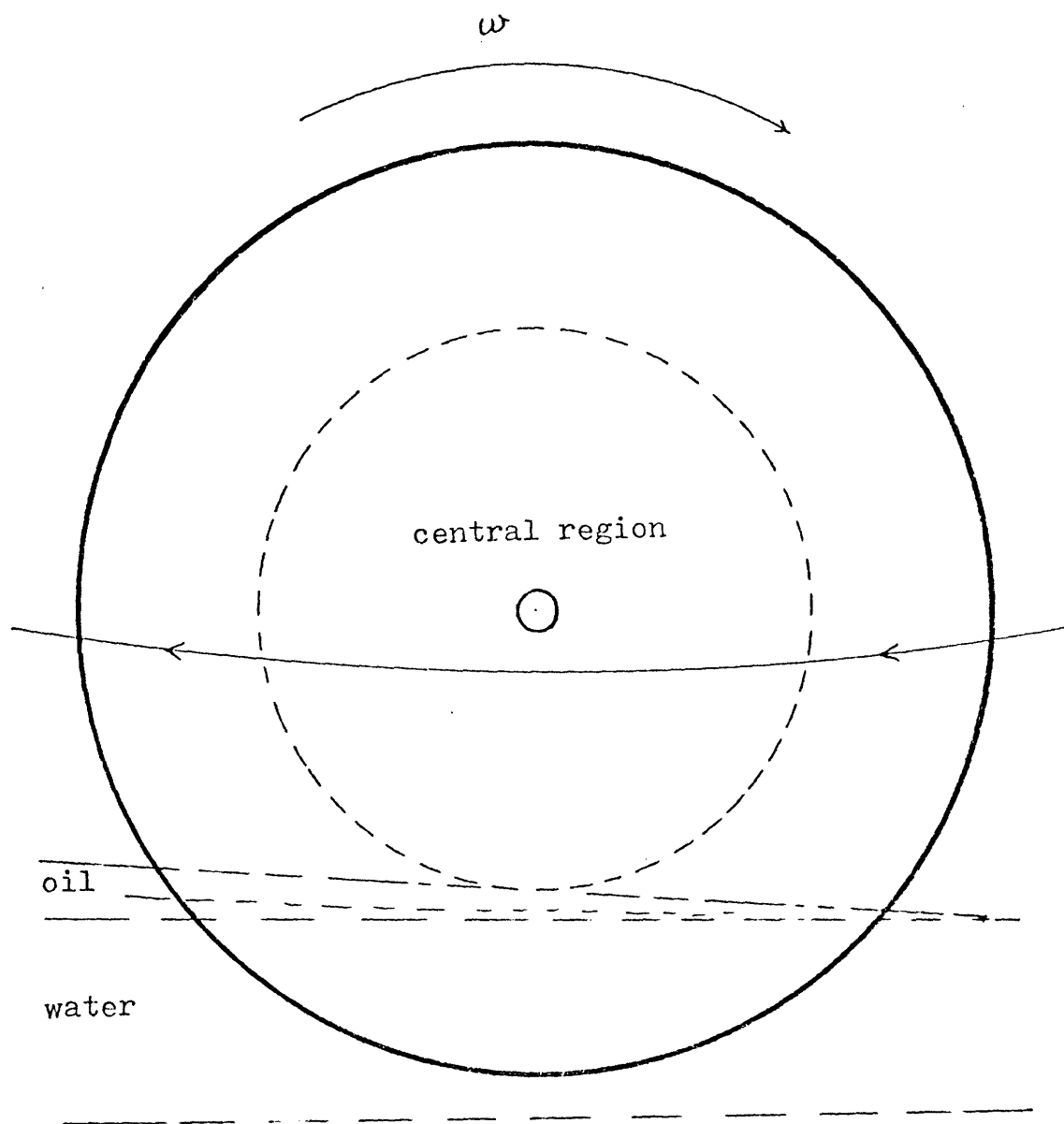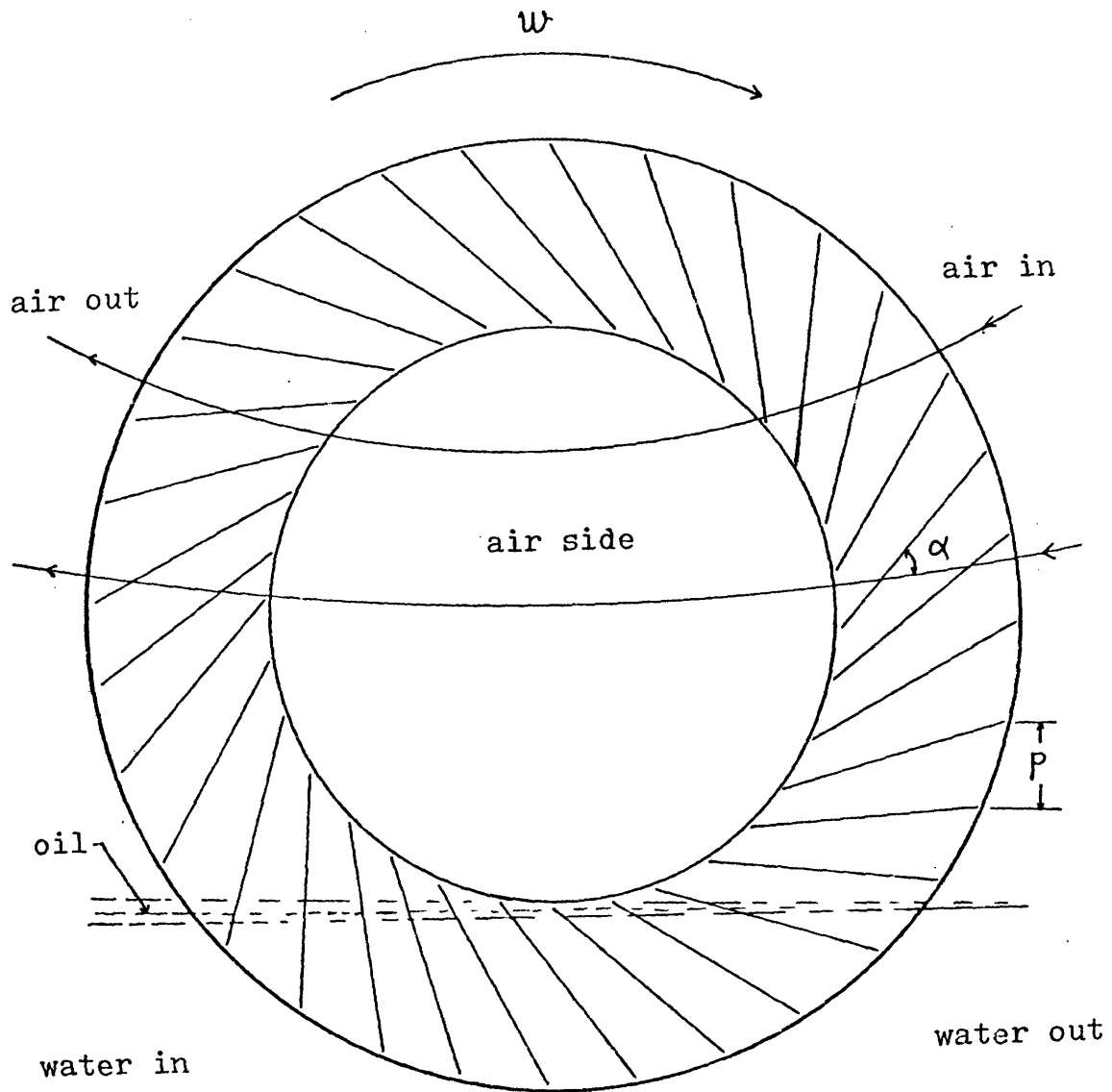
Fig 4.5-1 Solid disc model

w

air out

air in

air side

α

oil

P

water in

water out

air side : two passes cross flow
water side : well mixed

Figure 4.5.2 Annular disc model with repeated-rib rougheners

The water level is another parameter that should be considered. If the water level is below the hollow region of the annulus, there would be some region of the annulus not in contact with the hot water; the material in this nonwetted region is not being efficiently used, and is similar to the central region of the solid disc design. If water level reaches into the hollow region of the annulus, it has been found (see section 3) that oil droplets are generated at the inner boundary of the annulus (Figure 4.5.3). These oil droplets fall, and can be entrained in the air stream. A significant and unacceptable quantity of oil can be lost from the system by this mechanism. Therefore, in terms of heat transfer capability and the oil loss problem, the optimal water level is at the inner radius of the annulus.

The disc rotational speed is still another parameter to be considered. The number of heat transfer units, NTU, is exponentially proportional to the disc rotational speed [4]. However, as noted in section 3, too high a rotational speed, i.e., too high a tangential speed at the outer boundary of the annulus, would cause oil droplets to form on the disc surface. It has been experimentally determined that a rotational speed of about 5 rpm can be achieved for the 5' diameter disc with minimal oil problems. This limiation on the rotational speed is not a significant deterrent to the heat transfer performance. The following relation was used to constrain the rotational speed of the different disc parameters.

$$rpm = (5)(5'/D_o) \tag{5-1}$$
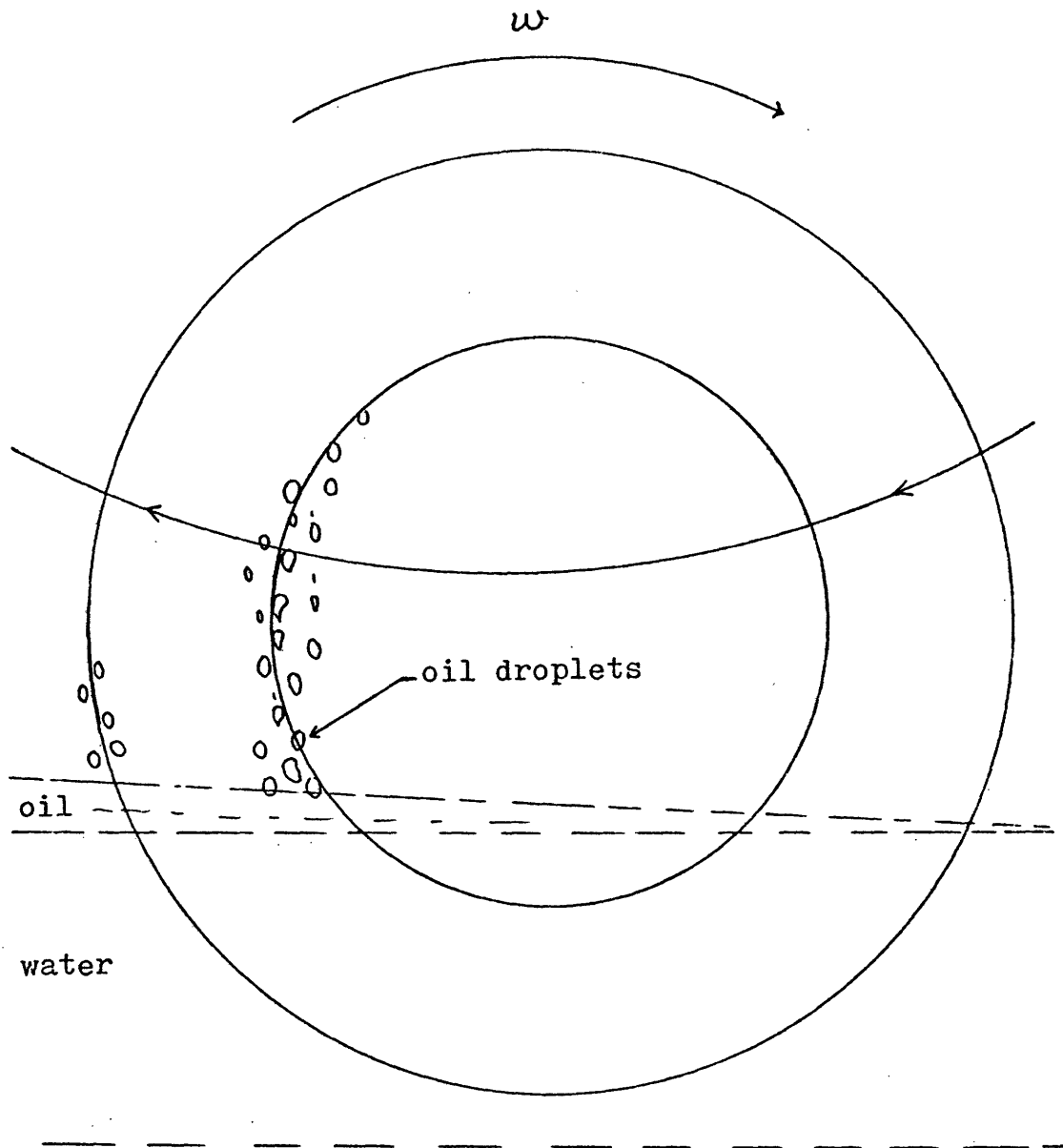
ω

oil droplets

oil

water

Figure 4.5.3 Annular disc model with oil droplets

Finally, consider the disc surface cost. Assuming that discs of
different thickness have the same manufacturing and assembling cost, then
the disc surface cost will be directly proportional to the disc thickness.
Although thinner discs are cheaper, too thin a disc will have a "buckling"
problem, so that the disc thickness is determined not only by the cost but
also by the desired stiffness of the material. As previously noted, to
reduce the complexity of the optimization routine, the optimization search
was limited to disc thicknesses of 0.03 inches.

4.5.4 Cost Comparison of Periodic Cooling Towers

Optimum computer outputs are plotted in Figures 4.5.4 to 4.5.11.
Each point in these figures represents the minimum costs in the given
design conditions.

Figures 4.5.4 and 4.5.5 show the effect of flow attack angle on
capital (see Table 4.5.1 for what is included in capital cost) and
incremental costs versus ambient air design temperature. It indicates
that a 45° flow attack angle has a 5.7% saving on capital and a 5.4%
saving on incremental cost when compared with a 90° flow attack angle.
This is because a 45° flow attack angle represents the best thermal-
hydraulic performance as mentioned in section 4.4.

Figures 4.5.6 and 4.5.7 show the effect of rib shape on capital and
incremental costs versus ambient design temperature. There is only a
nominal (1%) difference between the 90° rib shape and the 45° rib shape.
The overall thermal-hydraulic performance does not change much with rib
shape, thus the shape of ribs as distroted by the oil layer should have
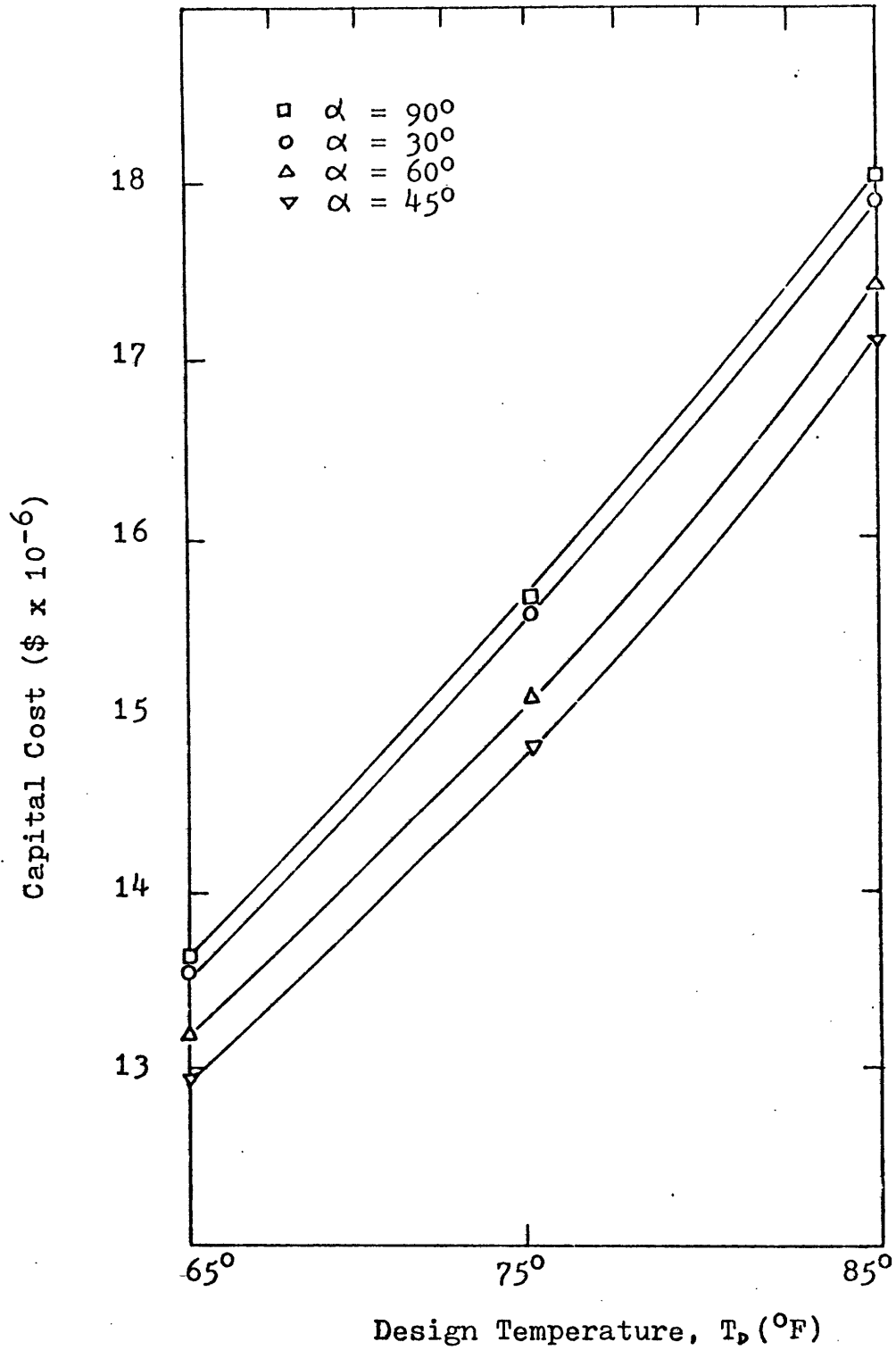minor effect on the performance of the tower.

Figure 4.5.4 Capital cost versus design temperature for different flow attack angles
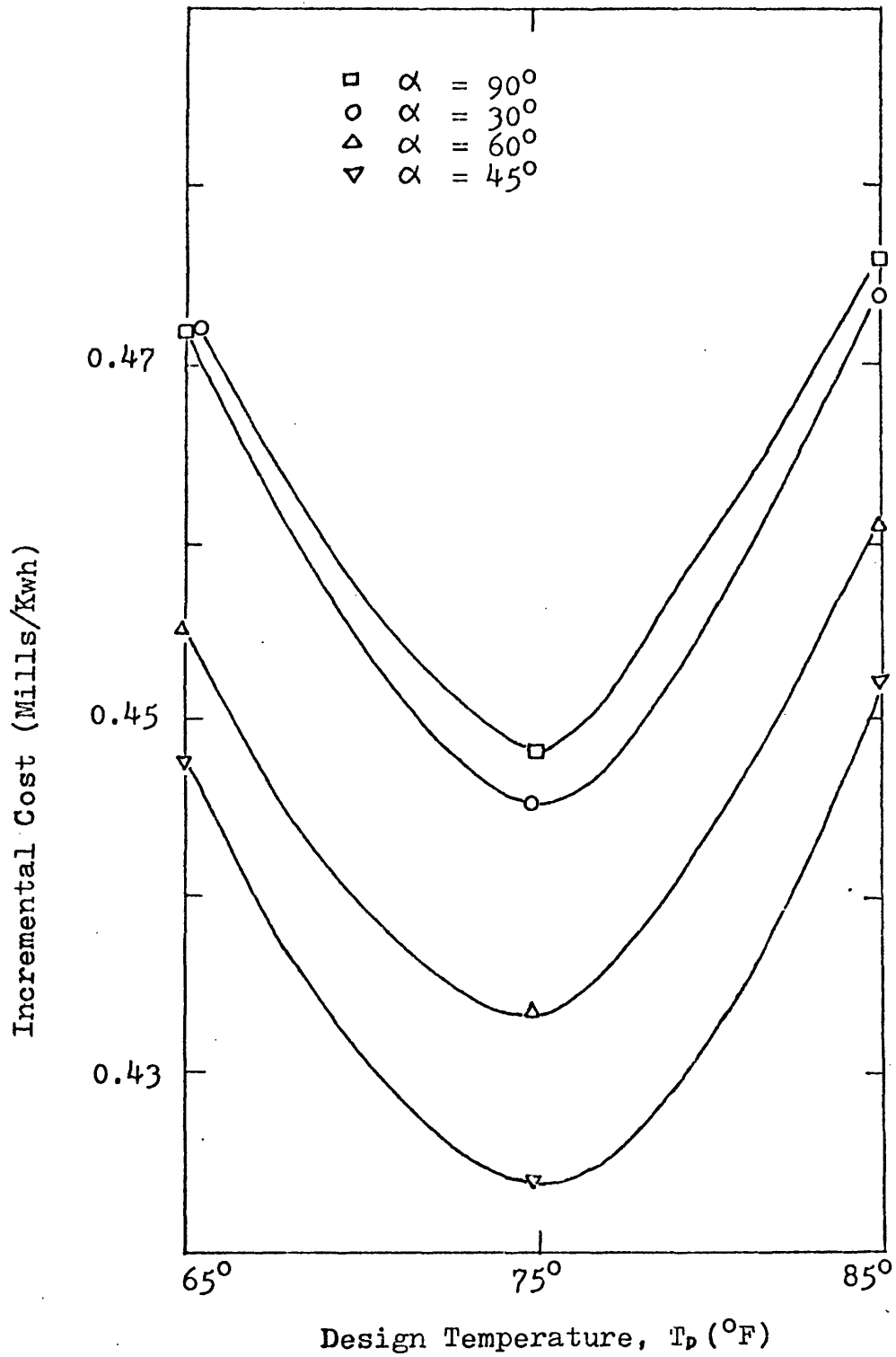
Figure +.5.5 Incremental cost versus design temperature
for different flow attack angles

Figure 4.5.6 Capital cost versus design temperature
for different rib shapes
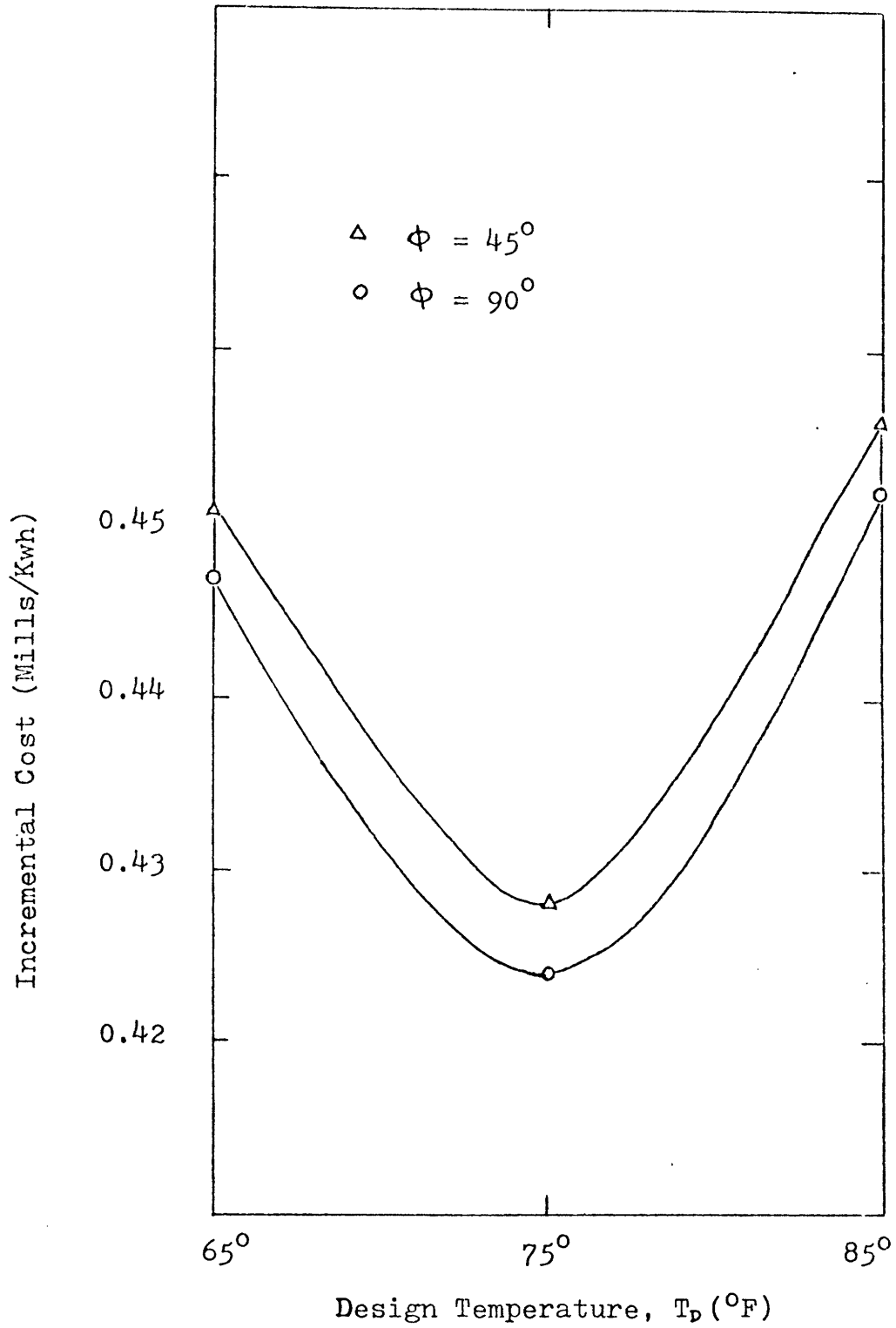
Figure 4.5.7 Incremental cost versus design temperature
for different rib shapes

Figures 4.5.8 and 4.5.9 show the effect of disc outer diameter on capital and incremental costs versus ambient design temperature. The graphs show that the 10ft disc outer diameter has a 5% higher capital expenditure and 5% higher incremental cost than the 5 ft. disc outer diameter, but that the 3ft out diameter disc has 2% savings on capital and incremental cost compared to the 5 ft disc. This is because with a given pressure drop across the heat exchanger, the overall air side heat transfer coefficient of a larger disc is lower than that of a smaller disc (Appendix 4.B). As judged by the optimization routine, the smaller disc is better. However, fabrication and assembly costs vary with disc size and this is not properly reflected in the costing model. As larger discs are easier to fabricate than smaller discs, proper cost modeling may radically change the 2% advantage the 3'disc has over a 5' disc.

A typical comparison between smooth discs, rough discs, and finned tubes is listed in Tables 4.5.3 and 4.5.4. Figures 4.5.10 and 4.5.11 also show the advantage of using roughened discs. The roughened disc has a 13% lower capital cost and a 12.3% lower incremental cost than the smooth disc under the same conditions (see Table 4.5.3). The roughened disc has a 40% lower capital cost and 35% lower incremental cost than the finned tubes for a 1,000 MgW power plant. The optimal rib geometry and flow conditions are given by a height to hydraulic diameter ratio between 0.05 and 0.08, a pitch to height ratio of about 10, and a Reynolds number for the air of about 10,000. Assumed in this analysis is that the ribs are square and sharp-edged, and that the flow attack angle is equal to 45°.
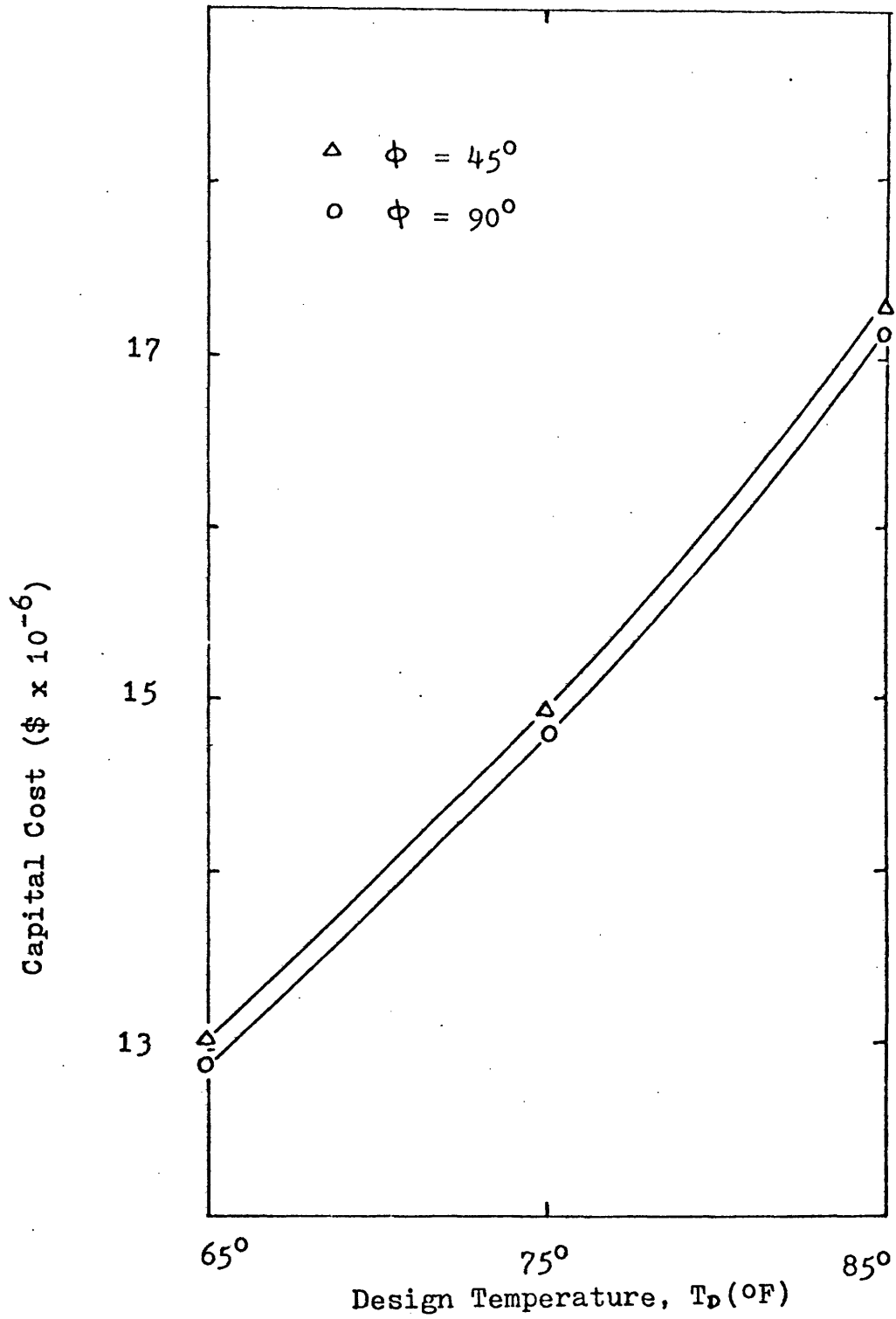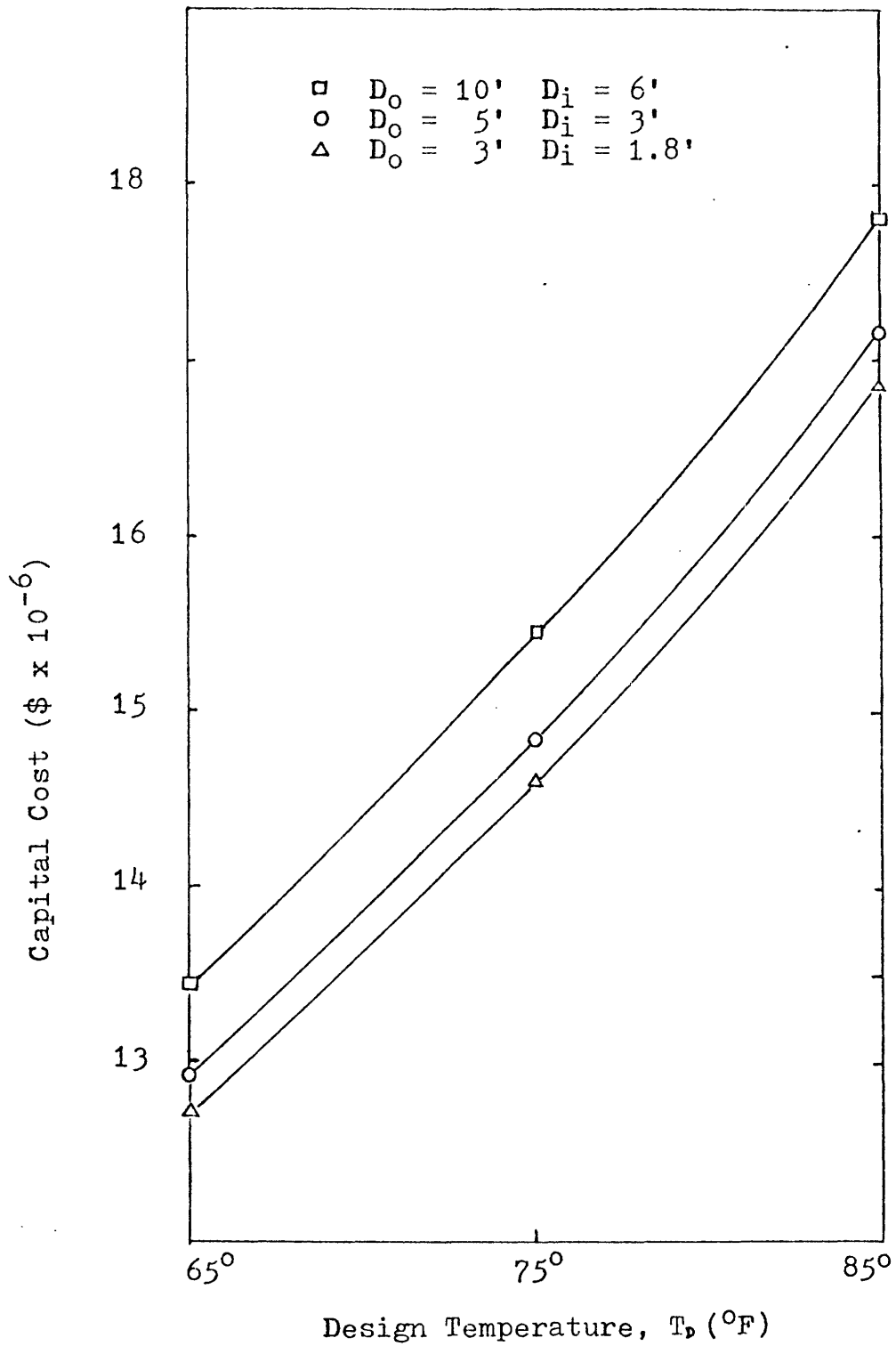
Figure 4.5.8 Capital cost versus design temperature
for different disc diameters
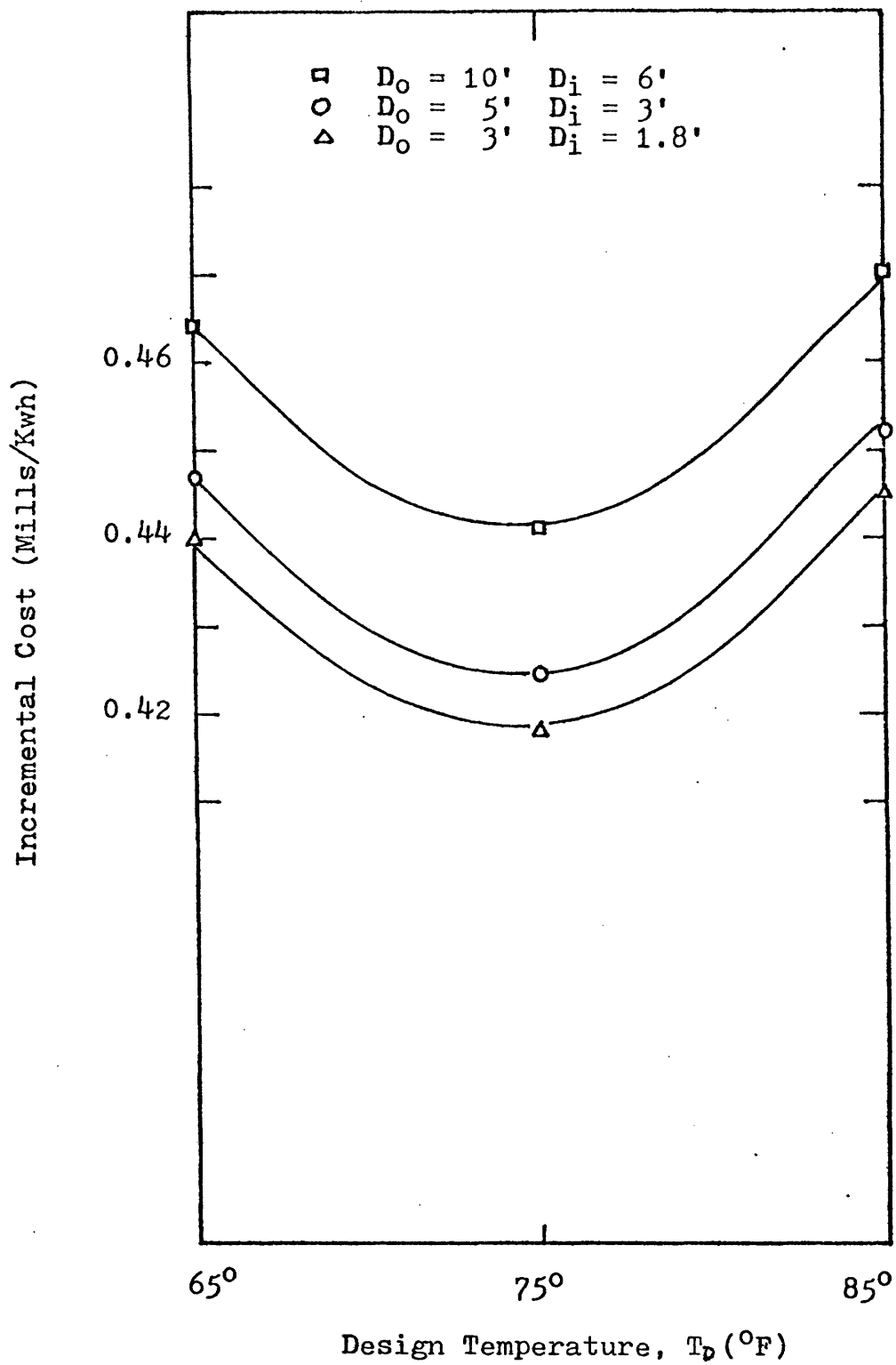
Figure 4.5.9 Incremental cost versus design temperature
for different disc diameters
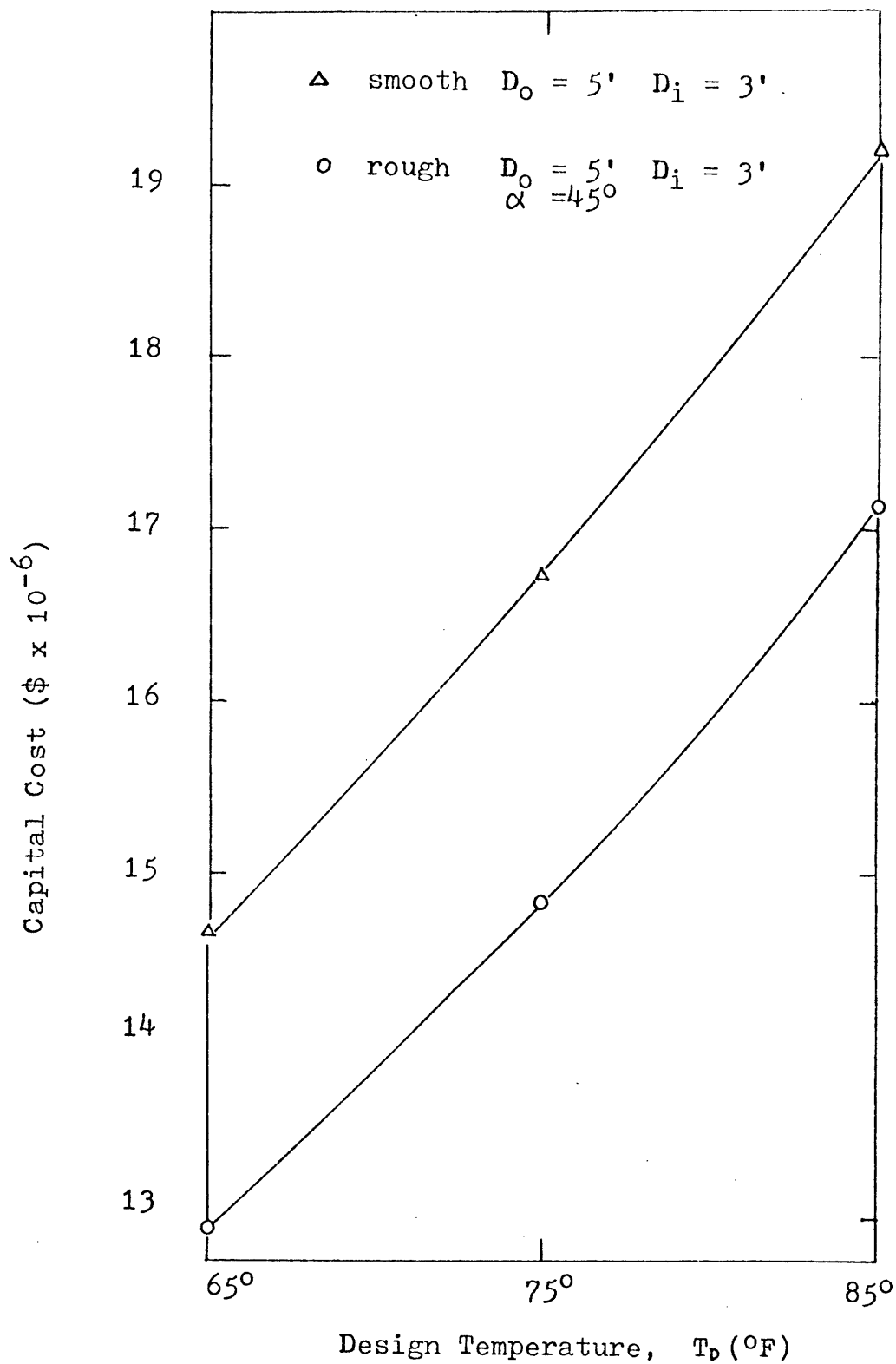
Figure 4.5.10 Capital cost comparison between
smooth and rough discs
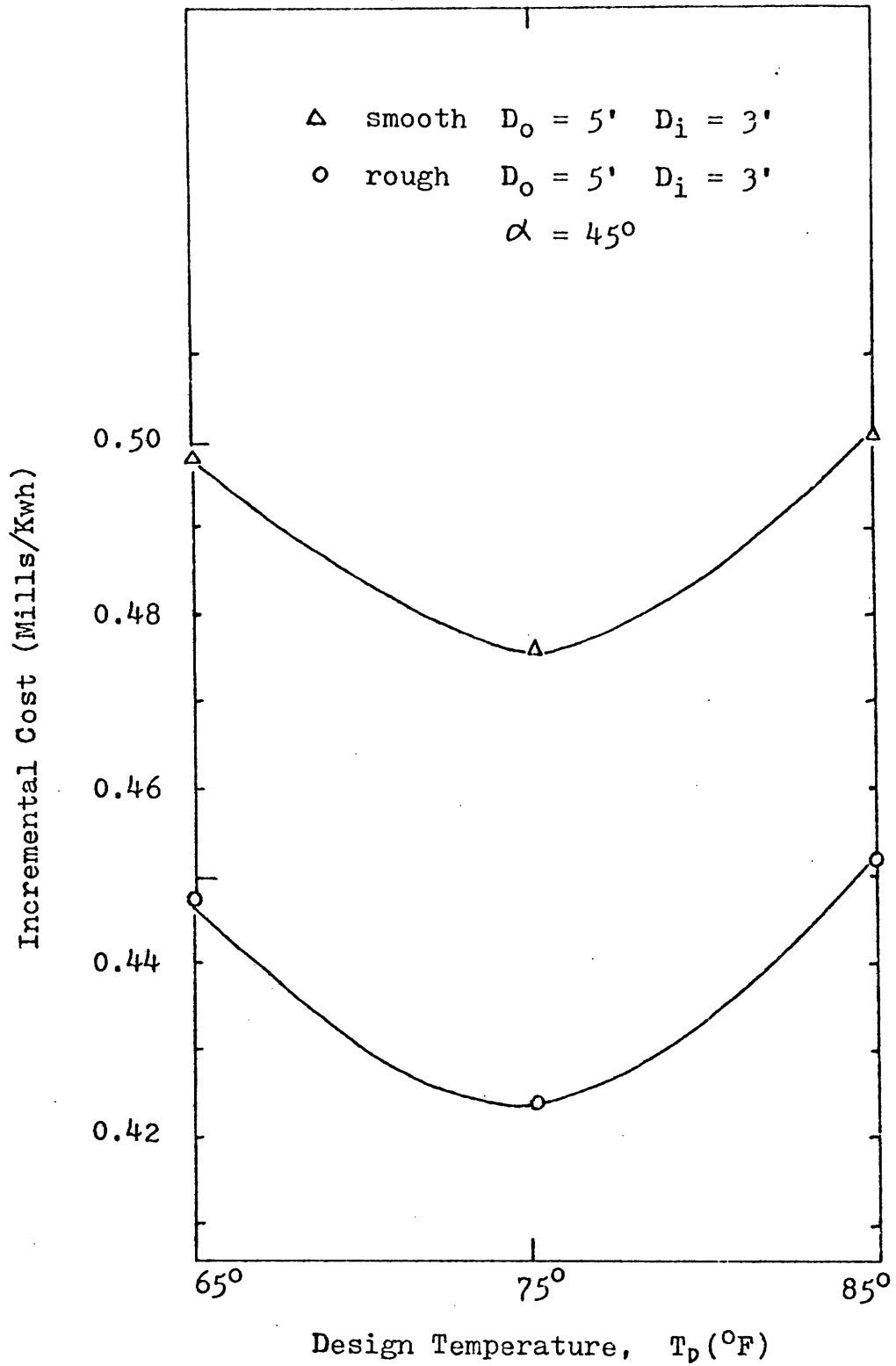
Figure 4.5.11 Incremental cost comparison between smooth and rough discs

Table 4.5.3

Typical Comparison Between Rough & Smooth Discs

	Smooth Discs	Rough Discs
T_D, °F	75	75
$T_w 1$, °F	128	127
V_{A1}, fps	39.32	23.76
V_{W1}, fps	0.09	0.06
D, inch	0.186	0.334
D_o, ft	5	5
D_i, ft	3	3
δ_d, inch	0.03	0.03
Number of discs	1.43×10^6	1.24×10^6
Land area (ft^2)	1.1×10^5	1.73×10^5
α, degree		45°
ϕ, degree		90°
p/e		10.1
e/D_h		0.048

TABLE 4.5.4

COMPARISON BETWEEN PERIODIC AND FINNED TUBE TOWERS

(COSTS RELATIVE TO FINNED TUBE [8])

	SMOOTH DISC	ROUGHENED DISC	FINNED TUBE [8]
SURFACE COST INCLUDING ASSEMBLY	.20	.20	1.0
COST OF HEAT EXCHANGER	.69	.61	1.0
COST OF INCREASED BOILER SIZE	.77	.71	1.0
COST OF LAND	.33	.56	1.0
WATER PUMPING POWER (KW)	8010	8780	3100
AIR SIDE PUMPING POWER (KW)	25700	21300	25500
TOTAL CAPITAL COST	.80	.71	1.0
INCREMENTAL COST OF POWER GENERATION	.84	.74	1.0

For an optimized air velocity of about 20 fps, the hydraulic diameter is about 1 inch, rib height is about 0.05 inch to 0.08 inch, and rib pitch is between 0.5 and 0.8 inch. From the computer results, rib shape is not an important factor in determining the capital and incremental costs.

5. Improvement of Rotor Performance by Cross-Coupling Rotor Systems

The conventional view of the periodic cooling tower has consisted of a number of trough or disc systems connected in parallel with each other. Hence each trough performs identically, as all inlet streams are at the same temperature (T_{in}), and all outlet streams are at T_{out}. As previously noted, the disc rotation within the trough induces flows which are sufficiently great to mix almost the entire trough of water to one temperature. Hence, the entire trough is at the same temperature as the water leaving the heat exchanger. This 'well mixed' condition has significant implications on the system performance. The energy transport from the bath to the atmosphere is dependent upon the temperature differential between these two fluids. Since the bath is well mixed, the heat transfer is limited by the temperature at which water is to be returned to the condenser (the trough outlet temperature and bath temperature). Yet the inlet stream isobviously at a higher temperature than the mixed temperature and hence has a potential for greater heat transport as it has a large temperature differential between it and the atmosphere.

The inlet stream's higher temperature may be used to advantage by placing a rotor system immediately upstream of the existing rotor. The well mixed trough temperature of this upstream system will be higher than the downstream trough temperature. This higher temperature results in a larger temperature difference between the trough and the atmosphere, and consequently has the potential for greater heat transport.

This concept leads to series connections of rotors, as well as parallel connections.

Obviously, as one increases the number of rotors in series, one increases the effectiveness of the system (an infinite number of rotors with both air and water streams connected in series is a counter-flow heat exchanger). However, these increases in effectiveness are accomplished only be greatly increasing the number of discs involved in the system. As discs are the principal cost of the rotary heat exchanger, a more realistic constraint is to maximize the system effectiveness for a fixed number of rotors employed. Another way of viewing this constraint is: with a fixed number of rotors available, what is the most advantageous way of coupling rotors in series and parallel to maximize the quantity of heat transferred.

As an example of the potential gain of rotors in series, consider a simplistic example involving two rotors.

If the rotors are connected in parallel (as in Figure 5.1.1a) each trough temperature is at T_{w2}. Consequently, the heat flux from rotor system 1 is:

$$(q/A)_1 = h_1(T_{w2}-T_a)$$

similarly, for rotor 2,

$$(q/A)_2 = h_2(T_{w2}-T_a)$$

If the rotors are connected in series, as in figure 5.1.1b, the temperature of trough 2 is higher than that in trough 1.

The heat flux from each is:

$$(q/A)_1{}^* = h_1{}^* (T_{w3}-T_a)$$

$$(q/A)_2{}^* = h_2{}^*(T_{w2}-T_a)$$
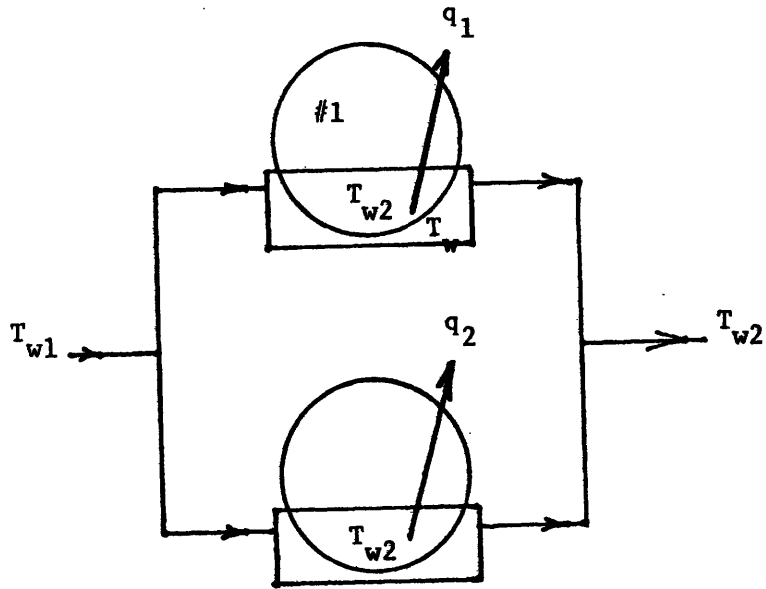
Figure 5.1.1a
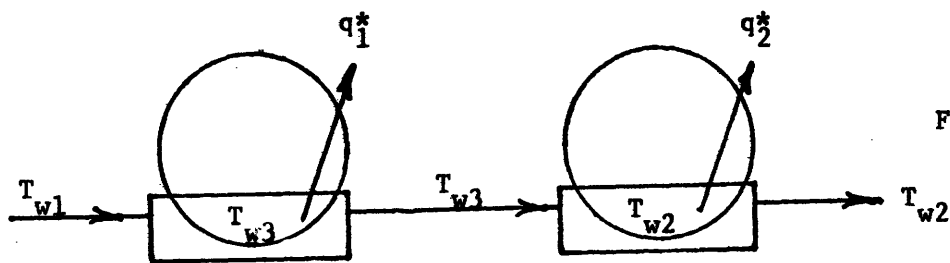
Figure 5.1.1b

Parallel & Series Connection of Rotors

Figure 5.1.1

unacceptable quantities of oil into the fluid streams. However, on the water side, as the trough circulation is presently overwhelmingly dominated by the disc induced flows, through flow rates would probably have to be greatly increased before oil entrainment would become a serious problem. Since series coupling increases the flow lengths and velocities, the pressure drop across the system also increases. This is primarily a problem on the air side of the heat exchanger system, for, as with all dry tower systems, the fan power requirements are already an appreciable quantity. Water side pressure drops are low, and although they would increase rapidly with series couplings, the magnitude of the water pumping power is small in comparison to the air fan power. Because the dominant constraint is the air side pressure drop, it was assumed that for this priliminary investigation no more than two rotors would be connected in series on the air side.

A computer routine was assembled to evaluate different flow arrangements. The routine was general, and could analyize the performance of up to ten rotors cross coupled in any manner. The cross coupling must be specified numerically as part of the input parameters. Each rotor was modeled as described in Section 2.5, with the exception that the water side of each rotor was modeled as a single, well mixed heat exchanger.

The basis of comparison is the ratios between the effectiveness of the system coupled as prescribed (ε_{system}) and the effectiveness of the same number of rotors coupled in parallel (ε_{base}). As both parallel and cross-coupled systems process the same quantity of fluids, this ratio of effectiveness is essentially the ratio of heat rejected from the cross-coupled system to that rejected from the parallel system.

In actual application, cooling towers must provide a specified heat rejection load and also return a fluid at a predetermined temperature. Hence, in the above example T_{w2} and T_a for both parallel and series couplings can be assumed to be identical. Also, specifying a heat load requires that each system process roughly the same quantity of water between T_w and T_w. Hence, in the parallel flow case, each trough processes half the total flow, while in the series case, the total flow passes through each trough. As the total flow rate remains constant, the flow rate per trough for two rotors is twice that of two rotors in parallel. Film coefficients between the discs and the water are proportional to the relative velocities between the disc and water. Consequently, film coefficients in the series configuration are higher than those in the parallel configuration. Based upon these observations,

$$(q/A)_1^* > (q/A)_1 \text{ since } T_3 > T_2 \text{ and } h_1^* > h_1$$

and

$$(q/A)_2^* > (q/A)_2 \text{ since } h_2^* > h_2.$$

Therefore the net heat flux from the series system $[(q/A_1)^* + (q/A)_2^*]$ is greater than that of the parallel system.

As the problem is presently constrained, there are practical limitations to the number of rotors that may be placed in series. The series coupling of rotors increases the fluid flow rates (air & water) per rotor. Increases above some as yet underdetermined level would be undersirable , as very high trough flow velocities would begin to entrain

Figure 5.1.2 illustrates the five different coupling systems chosen
to evaluate, and the resultant ratio of effectivenesses. As indicated
in Figure 5.1.2, the most significant increases in system performance
are made in linking the air streams in series due to increases in h
(compare system 1 to system 2). However, as noted previously, the series
linking of the air streams is probably realistically limited by the
increase in air side pressure drop. The further systems evaluated, limited
to two air streams in series, show only moderate changes in performance
from system 2.

Figure 5.1.2

IMPROVEMENT OF SYSTEM EFFECTIVENESS

by series & parallel arrangement

1.

$$\frac{\varepsilon_{system}}{\varepsilon_{base}} = 1.06$$

2.

$$\frac{\varepsilon_{system}}{\varepsilon_{base}} = 1.44$$

3.

$$\frac{\varepsilon_{system}}{\varepsilon_{base}} = 1.42$$

4.

$$\frac{\varepsilon_{system}}{\varepsilon_{base}} = 1.50$$

5.

$$\frac{\varepsilon_{system}}{\varepsilon_{base}} = 1.52$$
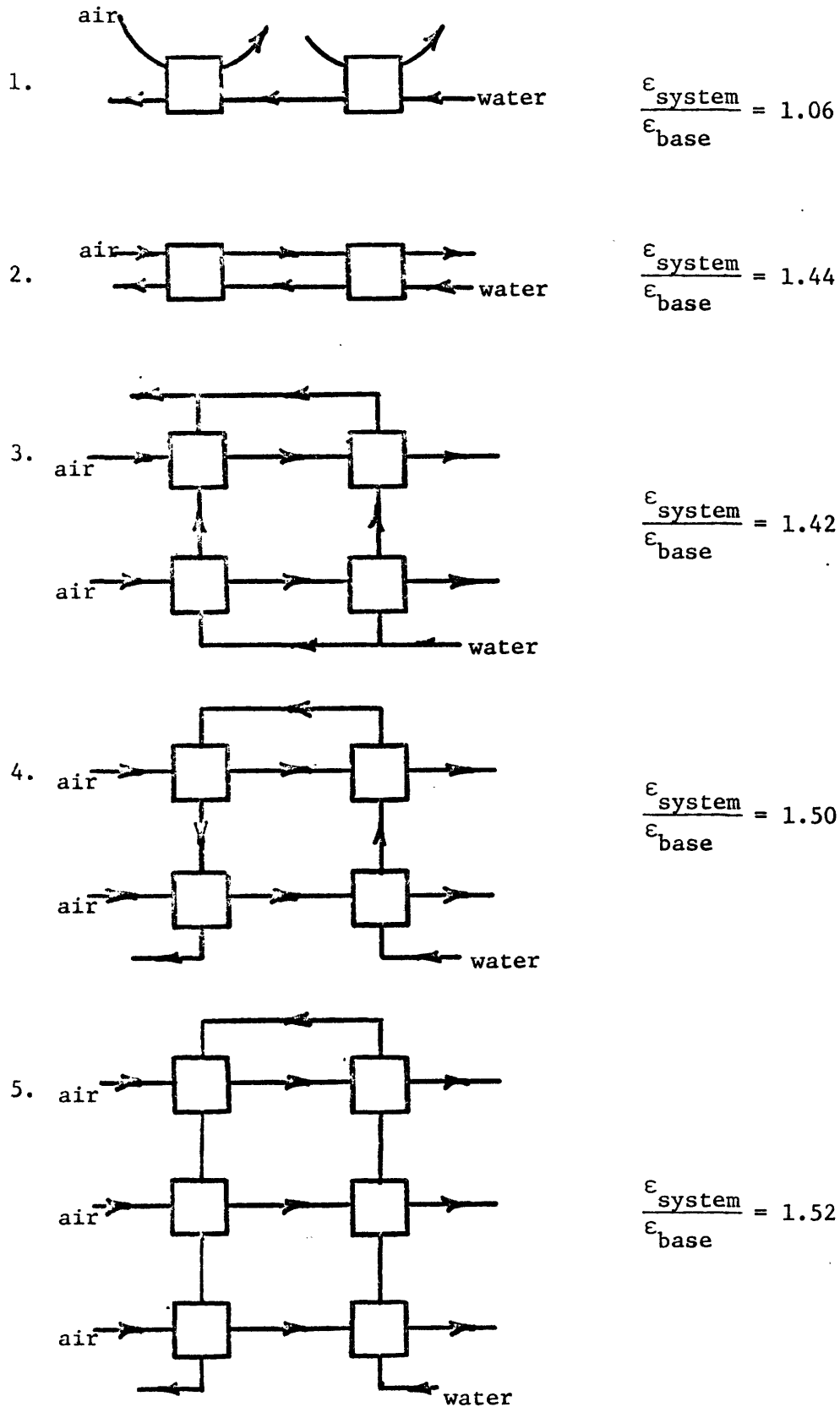
6. Condenser Fouling by Oil Contamination

6.1 Introduction

The presence of a floating oil layer on the water surface combined with the mechanical stirring provided by disc rotation and water through flow rates raises the possibility that oil droplets will be entrained in the water circulation system. The presence of oil in the water has the greatest potential deleterious effect in the steam condenser. If oil were deposited on the walls of the condenser tubes, the oil would represent an additional resistance to the heat transfer between the fluid media and the tube. Thus, the presence of an oil deposit on the interior tube walls would decrease the overall performance of the condensing system. Further, if a crack or leak were to develop in the condenser tube, the boiler feed water could be contaminated with oil. However, although feed water contamination by leaks is not a minor problem, it is a problem not soley inherent to the PCT. Hence, attention has been focused upon the impairment of condenser performance by oil fouling.

The significance of adding the thermal resistance of an oil layer in series with the convective heat transfer coefficient can be seen in the following equation:

$$h_{eff} = \frac{1}{\frac{1}{h} + \frac{\delta}{k}} \qquad (6.1)$$

This equation applies only if the oil thickness (δ) is small with respect to the radius of the tube. Here the resistance of the oil layer (k/δ) is coupled in series with the film coefficient between the flowing fluid and the oil layer (h) to yield an effective, or overall coefficient between the fluid and the tube wall (h_{eff}). Since oil has a low conductivity typically 0.076 BTU/hr-ft°F, the resistance of the oil can easily dominate

the equation. For example, using a typical value of h of 1000 BTU/hr-ft°F, and assuming an oil thickness of one half mil (0.0005"), h_{eff} is about 650 BTU/hr-ft^2°F. This is a 35% reduction in condenser performance solely because of a one half mil thick layer of oil.

It was expected that the water shear stresses between the water and the tube wall would be large enough to prevent a significant thickness of oil to accumulate on the inner surface of the pipe. A layer of oil which is sufficiently thin would have a negligible effect on the performance of the condenser. To evaluate the fouling potential of oil, it was decided to experimentally determine if a significant oil build up on the interior surface of the tube would occur and the effect this build up would have on the performance of the condenser.

As it would have been exceedingly difficult to physically measure the deposited oil thickness, the method employed was to measure the performance of the system and from this infer the oil thickness. The performance of the test system (to be described in Section 6.4) was measured with and without oil. From this difference in performance an effective oil thickness could be calculated using equation 6.1.

234.

6.2 Simulation and Analysis

The most accurate simulation of a real condenser system would be a steady

state   simulation. However, a steady state model would have had

temperatures too small for accurate measurement with thermocouples.

Therefore a transient response of a system to a step change in temperature

was used to measure the film coefficient. The transient method presents

large differences in temperature which are easier to measure with reasonable

accuracy.

In determining the film coefficients, it is important to know both

the skin temperature of the metal and the fluid temperature. If thermal

gradients exist in the test section, numerous thermocouples must be placed

within the metal wall to allow extrapolation to the surface temperature.

If a metal with a sufficiently high thermal conductivity is used, the

entire metal body appears isothermal, necessitating only one thermocouple

for skin temperature measurement. A measure of how isothermal a body will

appear is given by the Biot number (hd/k). Generally, if the Biot number

is less than 1/6 [10], the body can be considered isothermal. The Biot

number for the constructed copper test piece, based on expected film

coefficients, is on the order of 1/20. The test piece can therefore be

considered isothermal through any given test, and only one thermocouple

is required to determine the surface temperature.

In transient tests, the data to be gathered is the change in temperature

with time of a body after it has been exposed to a step change in ambient

conditions. Analysis of the curve of body temperature (T) vs. time (t)

will yield a heat transfer coefficient (h) between the body and the ambient.

Over a small time span (dt), the quantity of heat (dq) lost from an

isothermal body to the ambient is proportional to its change in temperature,

and is also proportional to the temperature diffence between the body and

the ambient. Mathematically,

$$dq = \rho V c \; dt = Ah(T-T_f) \; dt$$

Separation of variables and integration yields:

$$h = \frac{\rho V c}{At} \; \ln \frac{T_1 - T_f}{T_2 - T_f} \tag{6.2}$$

where T_1 and T_2 are the body temperatures at the beginning and end of

time span t, and T_f is the ambient temperature. ρ, V, c, and A are

geometric or thermophysical properties, and are readily obtainable. Hence,

knowledge of T_1 and T_2 as function of time t allows calculation of the

heat transfer coefficient (h).

6.3 Test Apparatus

A copper test section was fabricated and inserted in a section of

PVC pipe having the identical inner diameter. To ensure a fully developed

velocity profile over the test section, care was taken so that the

interfaces between the copper test section and the pipe were smooth, and

that the length of the PVC pipe upstream and downstream of the test

section were sufficiently long (L/D = 80 and 40, respectively).

High and low temperatures were supplied by hot and cold laboratory

water. Two valves were located in each line. One, a globe valve, allowed

for accurate control of flow rates, and the other, a gate valve, allowed

for a fast acting, step change in flow rate. Between the test piece

and the two water lines was an oil resevoir. The entire system drained

through a final valve into a weigh tank. Two thermocouples were placed

in the copper test piece (one for back up), and one in the cold water line. The thermocouple outputs were recorded as a function of time on an X-Y plotter.

A schematic of the system is shown in Figures 6.1.1 and 6.1.2.

6.4 Test Procedure

During the transient temperature test, it is important that the oil thickness remain constant. This necessitates that the fluids flushing the test section have identical flow conditions, and only differ in temperature. For example, were the second fluid to have a higher Reynold's number, the shear between the fluid and oil layer would be greater than with the first fluid, possibly causing a further reduction in the oil thickness. Hence, in equation 6.2, both test section temperature (T) and oil thickness (δ) would be changing with time. Further, since the oil thickness is a function of both the shear stress and oil viscosity, and oil viscosity is inversely proportional to temperature, a thinner steady state oil thickness would be achieved by flushing with hot water first. Flushing with hot water second would again cause both T and δ to change with time.

For experimental accuracy, it was therefore important to have identical flow conditions in the fluid streams, and also measure the test section's transient temperature/time history while being cooled. The hot water temperature used was about 120-130°F, which is about the normal operating temperatures of condensers; thus the steady state oil thickness was representative of actual operating conditions.
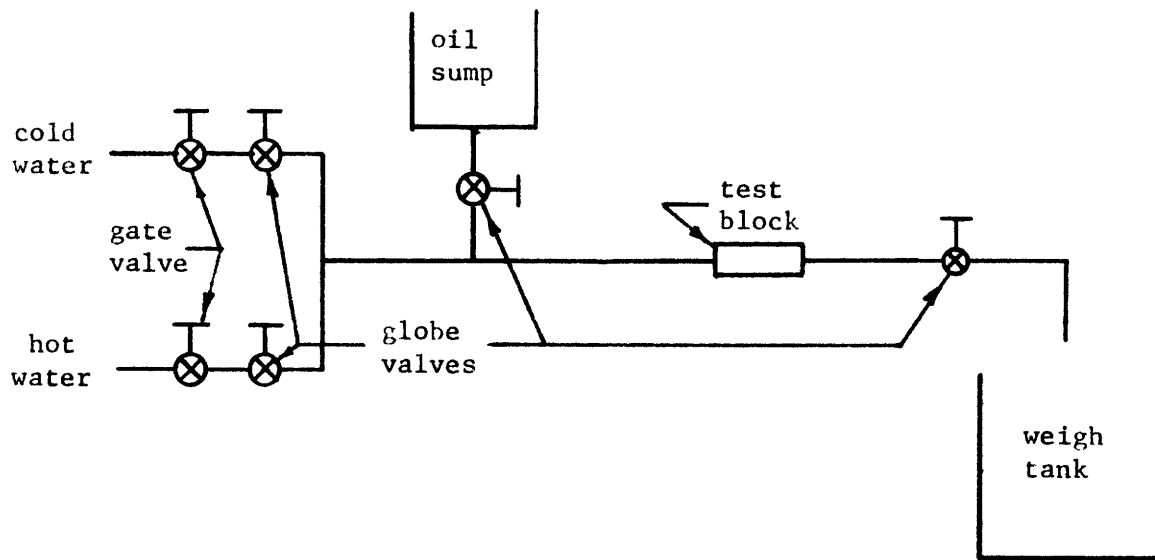
System Schema for Transient Testing

Figure 6.1
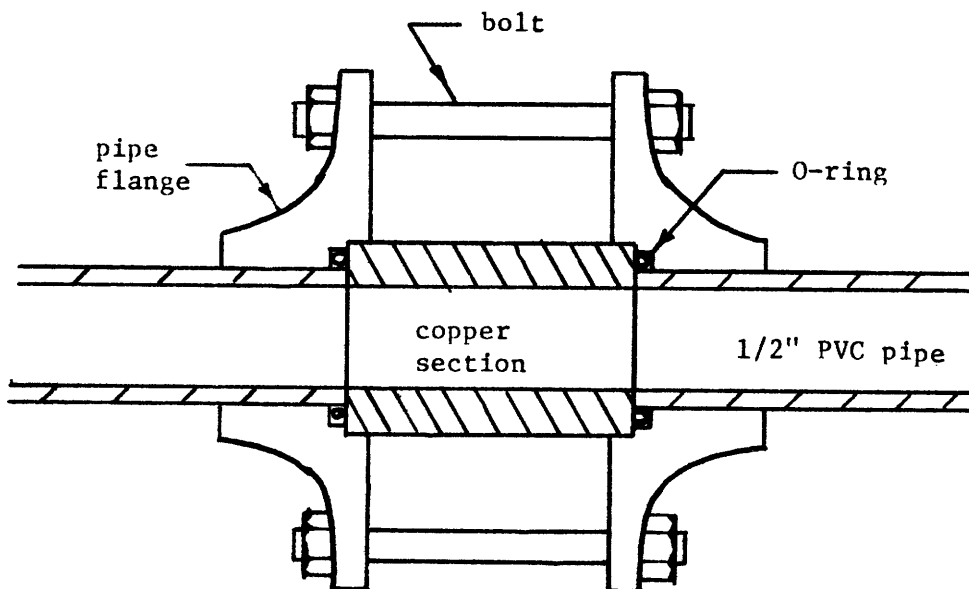
Detail of Test Block

Figure 6.2

Tests were initially made with no oil present. These results can be compared with accepted correlations (e.g. McAdams) to verify the calibration of the apparatus. Tests with oil were made after completion of water-only tests, to prevent contamination of the test piece with oil.

The test procedure was as follows:

1. Using globe valves, adjust hot and cold inlet flows to be identical (via weight tank measurements).

2. Using gate valves, turn off water flows and allow test section line to drain.

3. Allow oil from sump to enter test section. Allow the oil to sit in the line for several minutes by closing valve downstream of test section.

4. Drain oil from test section by gravity.

5. Open the gate valve in the hot water line, thereby heating the test section and establishing a steady state oil thickness on the tube wall.

6. Using gate valves, simultaneously turn hot water off, and cold water on.

7. Record time/temperature history of test piece, and cold water temperature.

8. Increment flow velocity, and repeat.

For the tests without oil, which were run initially, steps 2-4 were eliminated.

6.5 Results and Discussion

Each transient test generated a plot of thermocouple output vs. time. For the temperature used, the milivolt output of the copper-constant thermocouple is essentially linear. Thus the plot is actually temperature vs. time for the test piece. Figure 6.3 illustrates the output of a typical experimental run, and is seen to be an exponential decay of the test piece temperature with time. Ideally, the curve would have a discontinuity in its slope when passed by the initial front of cold water.
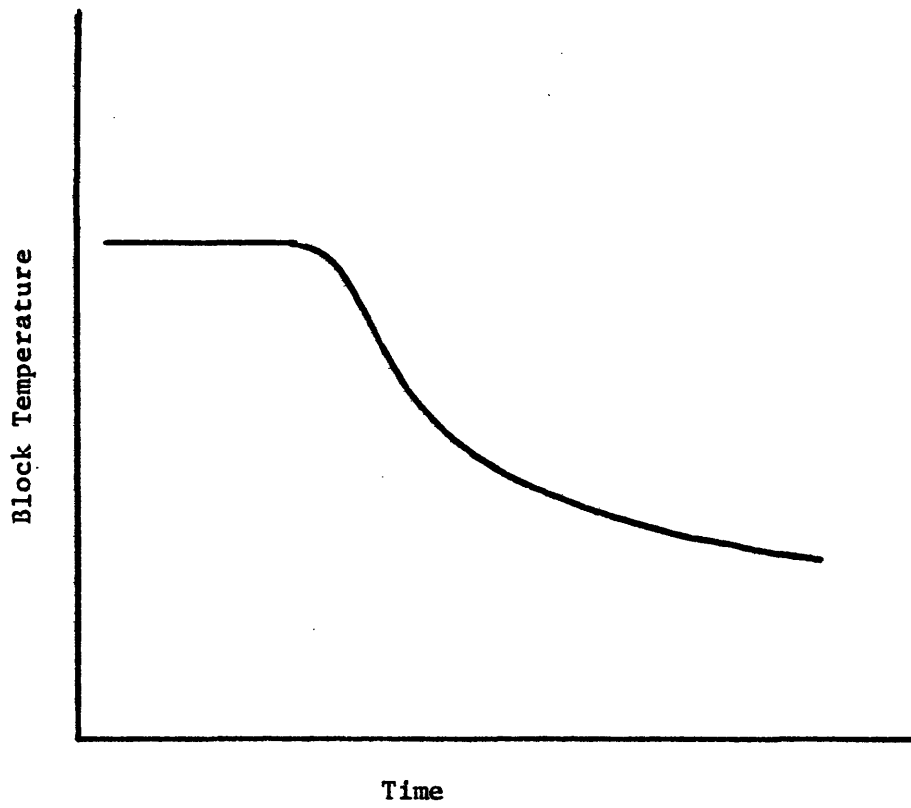
Typical Experimental Results

Figure 6.3

The rounding of the curve as actually observed is probably due primarily to mixing of the hot and cold water at their interface prior to passing the test piece. Small thermal gradients within the test piece could also account for some rounding.

Data was extracted graphically from these graphs, and equation 6.2 used to evaluate the effective film coefficient. Care was taken to avoid the initial regions of the curve where the rounding occurred.

The results are presented in graphical form in Figure 6.4, and tabulated in Table 6.1. From figure 6.4 it can be seen that the experimental results without oil compare favorably with the McAdams relation over all the tested flow velocities. The experimental runs with oil compared reasonably well with the McAdams relation at the higher flow velocities (6.2 ft/sec). At lower velocities, the experimentally measured film coefficients began to deviate from the McAdams relation. At the lowest velocity (3.5 ft/sec), the average measured film coefficient was 19% lower than the McAdams prediction.

Part of this disparity is due to experimental error. Initially, hot water was used solely to heat the test piece, without concern as to whether the oil layer had reached a steady state value. As previously noted, changing to the cold stream, chilling the oil, and thereby increasing the oil's viscosity, will tend to 'freeze' the oil thickness at a value thicker than the steady state value using hot water. Tests conducted with oil layers thicker than steady state values would, of course, yield measured film coefficients lower than the McAdams relation. This effect
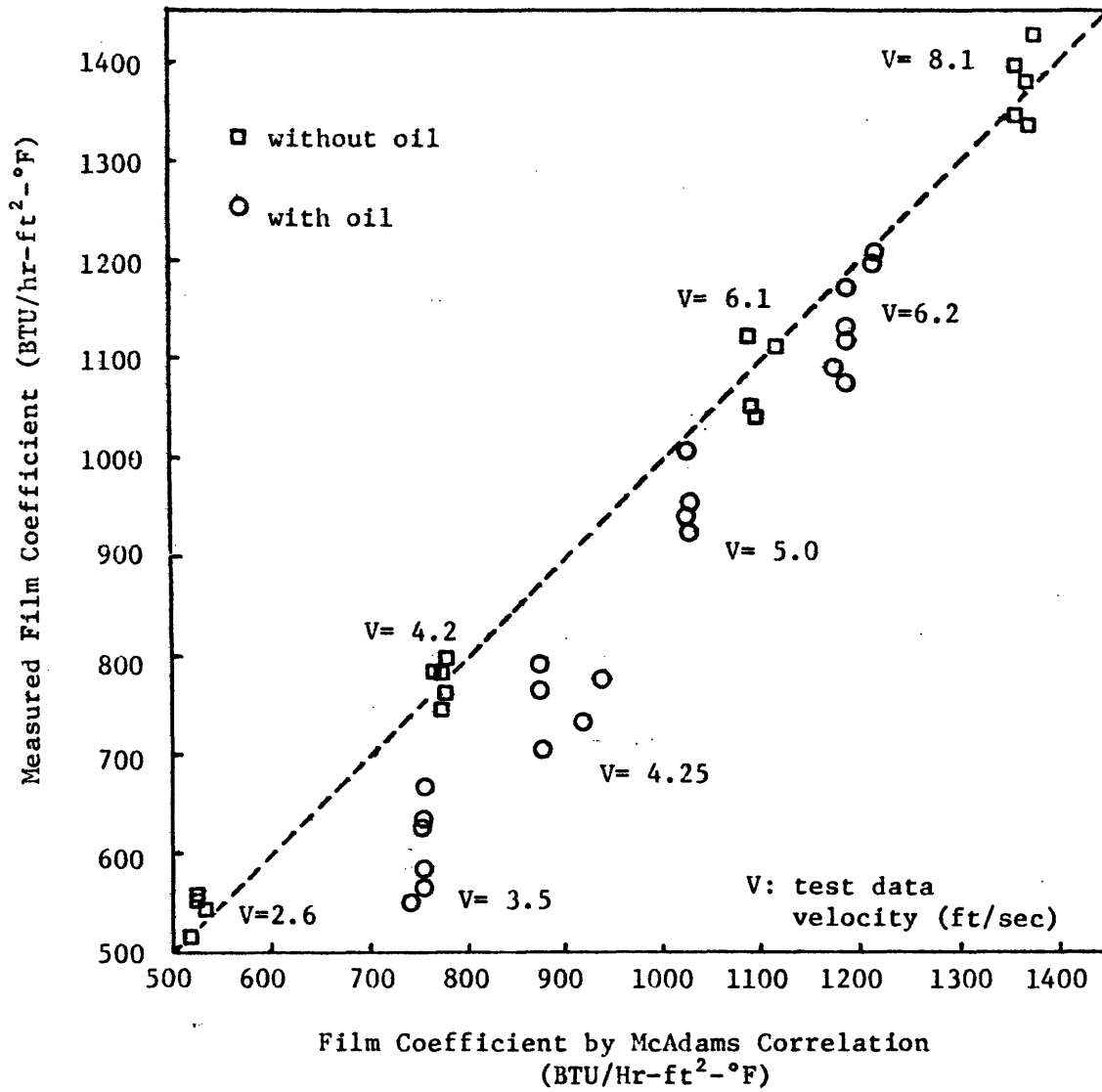
COMPARISON OF EXPERIMENTAL AND PREDICTED
FILM COEFFICIENTS

Figure 6.4

was tested in three runs by flushing the test piece with hot water for 2-4 minutes prior to switching to the cold stream. As can be seen in Figure 6.4, the measured heat transfer coefficient for these three tests compared favorably with the McAdams relation.

7. C-E Air Preheater's periodic Matrix #1

7.1 Introduction

As the experimental and analytical research continued on the PCT, it became apparent that MIT was not properly equipped to fully evaluate the market and production economics of the PCT. This required the involvement of a large scale manufacturer. Discussions held with C-E Air Preheater (APCO) and a licensing agreement signed between MIT and APCO to develop the PCT.

APCO's first effort was to assess methods of matrix fabrication which would minimize material wastage and assembly effort. As noted in section 4.5.3.2, there are inherent advantages to the use of non-solid, or annular discs. APCO, with the principal objective of quickly producing a matrix for testing purposes, fabricated a first-generation annular matrix and shipped it to MIT for testing and evaluation. The following sections describes and discusses the matrix, the performed tests and results.
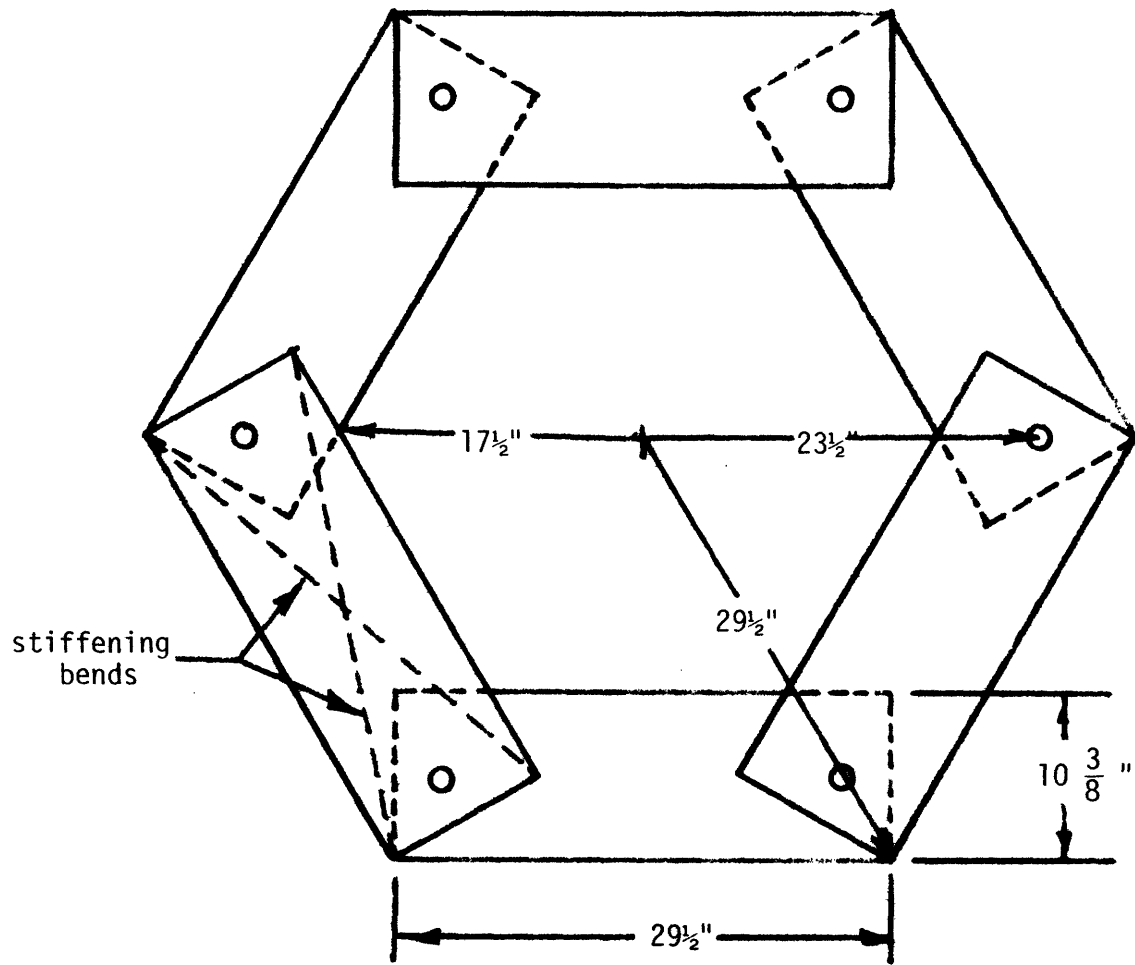
7.2 Matrix Description

Matrix #1 was fabricated of rectangular galvanized steel sheets (29-1/2" x 10-3/8") bolted together to form a hexagonal shaped annulus (see Fig. 7.1). The rigidity of each sheet was increased by bending the sheets slightly on their diagonal (see Fig. 7.1). Twenty-one such annuli were used in the matrix and were separated by 3/8 inch spacers. Structural support was provided by two 1/8 inch thick end plates on each side of the matrix. Large openings were cut into one end plate to allow viewing the matrix interior during operation.

The matrix, by nature of its fabrication is discontinuous. Ideally, in the region of overlap (see Fig. 7.1), the sheets would be flush with one another. However, due to the bending required for stiffness, the regions of overlap were in general making point or line contact rather than plane contact. The distance between a sheet corner and its over-lapping sheet varied from 0 to ∿1/4".

7.3 Full Scale Designs

Prior to the installation of the matrix, the test facility was drained and thoroughly cleaned. The matrix was then installed, new oil and water added to the system, and the system brought up to the operating temperature (∿130-135°F). The water level for the initial test was such that the sheets were totally submerged by 3-4 inches as they passed through the water side. Upon rotation of the matrix, a severe dripping problem was encountered. Severe dripping occurred at three locations (see Fig. 7.2): (1) Oil ran off (as a stream) from the inner sheet corners, when leaving

GEOMETRY OF MATRIX #1

Figure 7.1

A - Interior edges

B - Inner sheet corners
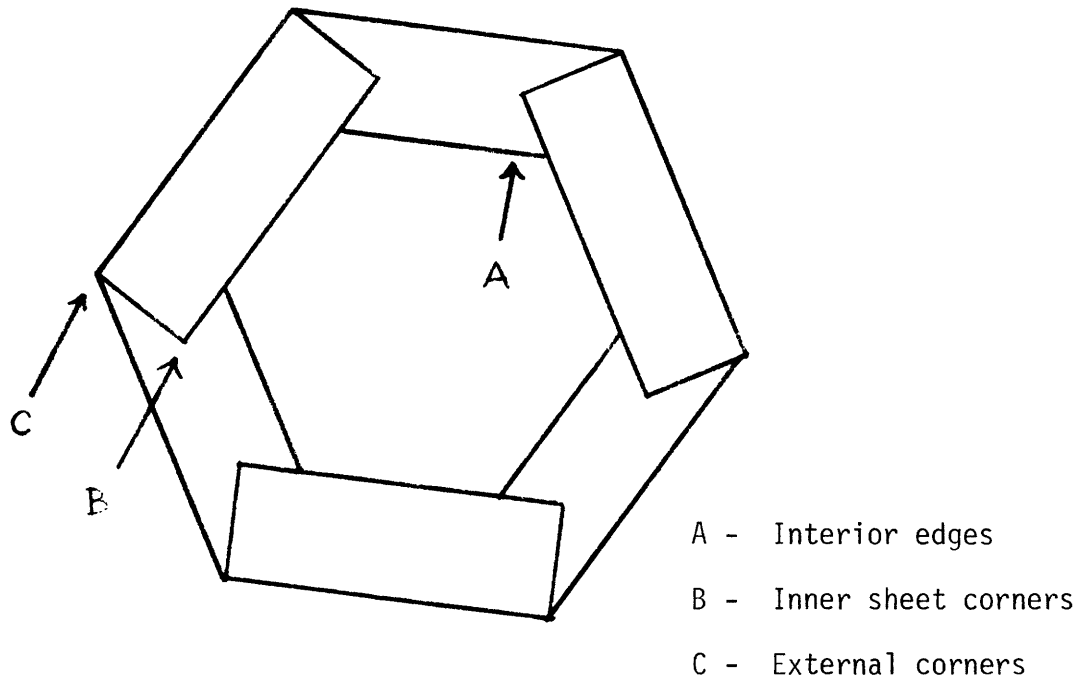
C - External corners

DRIP LOCATIONS

Figure 7.2

Extruded Channel   Slit Tubing
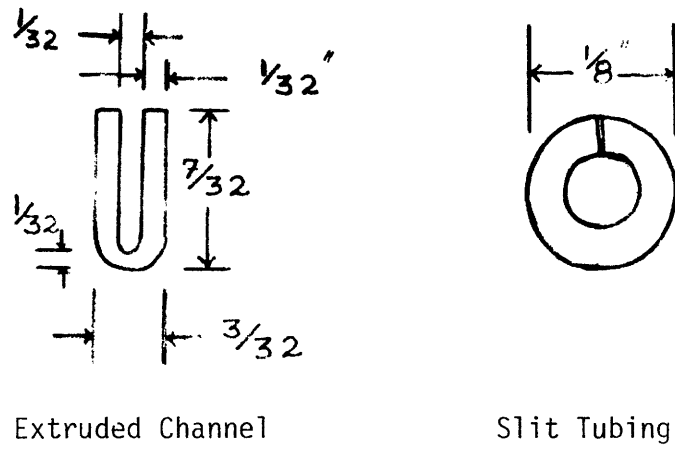
DRIP SHIELDS

Figure 7.3

the oil layer, (2) severe oil dripping occurred at the interior edges of the sheets as the edge passed through the horizontal, and (3) dripping occurred at the external corners of the hex matrix. Dripping was severe enough, and in small enough droplets, such that upon turning on the fan, the flow straighteners downstream of the test section quickly became coated with oil. This condition of excessive dripping existed for all tested rotational speeds (1.5 <RPM <6). Further, no change in drip rate was observed over this range. Drip rate was a stronger function of water level; decreasing slightly with water level.

A significant amount of oil/water mixing was also observed. It is hypothesized that this mixing is induced by three effects: (1) Mixing caused by the spacers which intercept the oil/water interface, as oil could be observed being carried into the water in the wake of the bolts on the end plates, (2) mixing induced by the discontinuities at plate overlaps, and (3) oil bubbles rising from the interior edges of the sheets as the edge passes through the horizontal. This last effect is similar to the dripping in the air side, except that it is driven by buoyancy forces rather than gravity forces. This third effect can be eliminated by lowering the water level to below the height of inner sheet edge.

The thermal performance of the matrix was not experimentally determined because of the severity of dripping. It was felt that (1) the high rate of oil loss by entrainment in the air stream, (2) the high degree of water/oil mixing and (3) the unknown thermal performance of the entrained and/or falling drops would either preclude determining the thermal performance of the matrix itself, or render the matrix unacceptable from

a practical standpoint.

In order to pursue the annular design concept further, it is necess-
ary to determine if the fluid performance problems exhibited by matrix #1
result from problems inherent with the annular concept or with the fabri-
cation and design of matrix #1. If the difficulty lay in the design, it
is desirable to identify improvements, improvements which can hopefully
be made in situ so that matrix 1 can be further tested. To perform these
required tests, and implement design changes rapidly, the small scale test
facility was used.

.4 Small scale testing

The purpose of small scale testing was to be able to rapidly change
designs and test pieces; thereby quickly identifying design problems
and/or solutions. The objective was to first determine the fluid performance
of idealized annuli, and then evaluate modifications of discontinuous de-
signs similar to matrix 1. Tests were performed at water temperatures of
about 130°F.

7.4.1 Idealized Annuli

An idealized annulus was taken to be a continuous surface (i.e. cut
out of one sheet). Two were fabricated; a continuous circular annulus
and a continuous hexagonal annulus identical in proportion to matrix 1.

7 4.1.1 Continuous Circular Annulus

This configuration proved to be the best. Water/oil mixing was at
a minimum and no oil dripping occurred from either exterior or interior
edges so long as the water level was no higher than the inner radius
(0<RPM<20, corresponding to 0<RPM<65 for a 5' diameter rotar).
With higher water levels, dripping occurred from the inner

radius, and was a function of RPM. No external dripping was observed at the higher water levels.

7.4.1.2   Continuous Hexagon

Again, due to the continuous nature of the annulus, oil/water mixing was at minimum. On the external edge, oil dripped from the corners of the hex as the corners left the water. No drips occurred on the interior edge, even at rotational speeds up to 20 RPM, so long as the water level was below the maximum inner radius. At higher water levels, dripping from the interior edge occurred, and increased as water level was further raised. As with the continuous circular annulus, at these high water levels, dripping was also a function of RPM. When the edge is at a slight angle to the horizontal, oil draining from the sheet can flow down the edge rather than drip off. Dripping occurred primarily as the interior edge passed through the horizontal.

If there were a means of temporarily holding the draining oil while the sheet passes through the horizontal, it could be possible to preclude all dripping from the interior edge. A passive system, as a "rain gutter" would accomplish this, but must be small so as to not block the air flow through the matrix or significantly increase the air side pressure drop.

Two drip shields were tried on the continuous hex. One was a "U" shaped extruded rubber channel (Fig. 7.3), and the other was a slit, 1/8 O.D. plastic tubing (Fig. 73). Each was slipped over the inside edge of the annulus. Unfortunately, these drip shields augmented drip rates: drips initiated at lower water levels and lower RPM's than without the shields.

7.4.2   Discontinuous Annuli

The success of the continuous annuli indicates that the fluid problems of matrix 1 lies not with the concept, but with the design or fabrication. Several discontinuous designs were tried to identify the mechanism of dripping and to find solutions.

74.2.1 Flat plates

This is essentially the idealized, discontinuous annulus. Plates overlap, but make continuous contact with the overlapped sheet. Note, there are two patterns for plate overlap (Fig. 7.4); (1) unidirectional overlapping and (2) non-unidirectional lapping (used in matrix 1). The unidirectional overlap performed identical to the continuous hex; the other was very similar in performance, but initiated dripping at lower RPM's.

Drips from the external corners were substantially decreased by cutting the corners to form a dodecagon.

7.4.2.2 Flat plates with spacers between the overlaps.

To model non-continuous contact at the overlaps, spacers were placed between the overlapping sheets. This prevented continuous draining from sheet to sheet, and as expected, caused severe dripping similar to that of matrix 1.

7.4.2.3 Flat plates with "tabs" at overlap

To ensure contact between successive sheets, the ends of each plate were bent (Fig. 7.5). This afforded at least point contact and usually line contact somewhere at a plates edge.

Except for the elimination of flow running off the interior sheet corner, dripping was as severe as in Matrix 1.
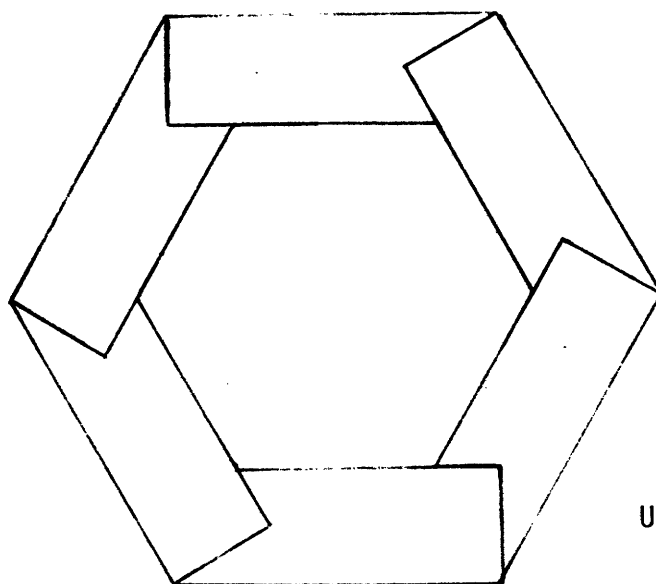
Unidirectional
Overlap
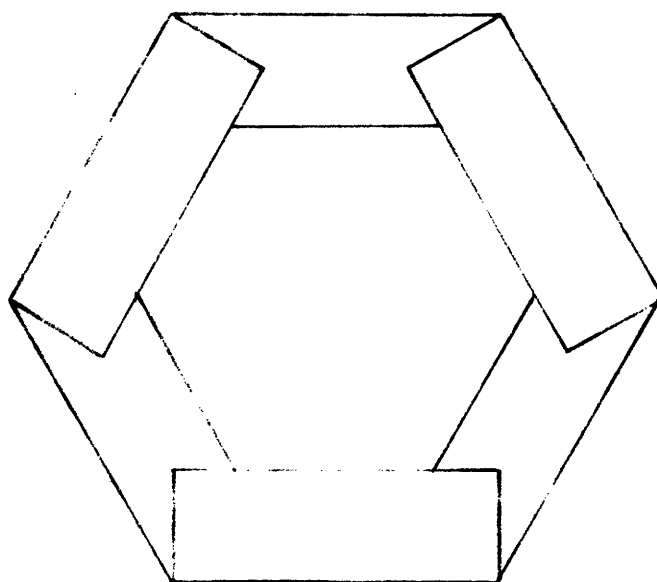
Non-unidirectional
Overlap

OVERLAP PATTERNS

Figure 7.4
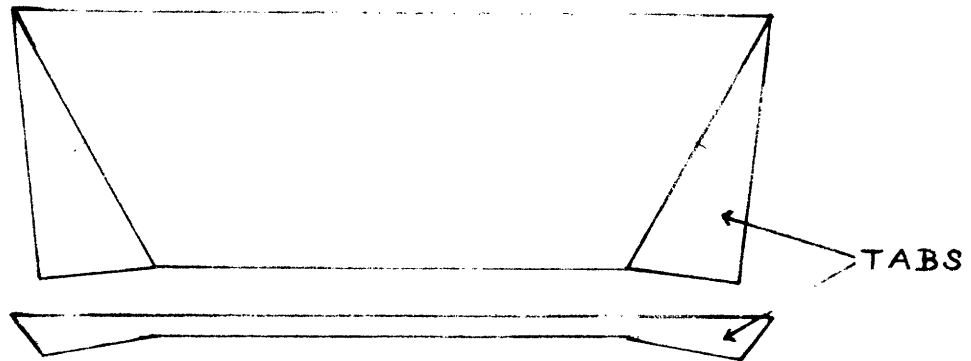
BENT PLATES

Top & Side View
showing tabs

Figure 6.5
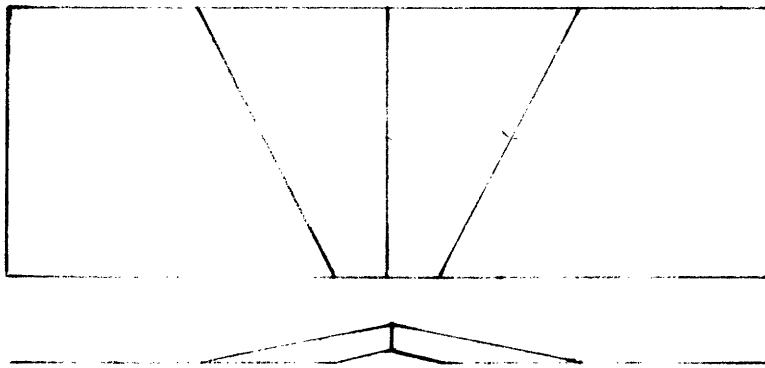
FLAT PLATE

Top & Side View
with center bend

Figure 6.6

7.4.2.4 Plates with diagonal bends

This shape exactly models matrix 1. Performance of the assembled plates was identical to that of matrix 1. The prior small scale tests indicated that to prevent dripping, the plate overlap must provide a continuous path for oil drainage between successive sheets. This was attempted by 2 means: (1) filling the gap between the overlap with a pliable material, and (2) attempting to draw the overlap area together using rivets.

Filling the overlap region with soft foam rubber spacers reduced dripping below 12 RPM. Above 12 RPM, dripping rapidly worsened. Further, the blockage caused by the filler generated considerable oil/water mixing.

Riveting of the overlap area reduced dripping only when sufficient rivets were used to cause continuous contact between plates.

Again, as in the flat plate case, trimming the external corners effectively eliminated external dripping, and the unidirectional overlap had less dripping than the non unidirectional overlap.

Plates were bent in such a way as to leave the overlap regions flat (Fig. 7.6). The bend was fairly large, being a maximum of 1/2 inch out of the plane of the overlap. In general, dripping was reduced to levels similar to the flat, discontinuous, annulus.

Two of the overlap regions were not Co-Planar, resulting in dripping. Due to the magnitude of the bend, there was considerable oil/water mixing.

8. Summary and Conclusions

The following summarizes the work and conclusions to date from each of the six subsections described in detail in the prior sections:

8.1 Full Scale Testing and Modeling

Three separate and distinct operating regimes have been identified: dry, starved, or wet. The PCT can operate in any of these modes, depending upon the quantity of oil in the system (1 gal/disc for dry, 1/3 gal/disc for starved, and no oil for wet operation). Experimental measurements were made to substantiate the existing rotor's performance in each of these modes.

The starved mode is the probable operating regime for an actual PCT. In this starved mode, a tower requires only 1/3 the oil inventory required by a dry mode operation, and experiences about a 15% improvement in performance because of a thinner oil layer on the disc in the water stream, while only incurring small evaporative losses.

The model developed to simulate the performance of the PCT has been compared to the experimental data. Within the range of experimental error for which the data was taken, the model accurately predicts the performance of the PCT in the starved mode. This model will be further used to evaluate tower/system performance.

8.2 OIL STUDIES

The main objectives behind the study of the oil system of the Periodic Cooling Tower were:

1. To determine how the oil system affects the heat transfer performance of the P.C.T.

2. To set guidelines which would help in the selection of an appropriate oil to be used in the P.C.T.

8.2.1 Oil System Influence on the P.C.T. Performance

As described in the preceding sections, the oil system affects the performance of the P.C.T. in two ways. First, the oil film coating the disc surface presents an additional heat transfer resistance. And second, for the oil layer to effectively suppress water evaporation, the angular velocity of the discs must be maintained below some critical value.

In order to calculate the magnitude of the oil film's heat transfer resistance, it was necessary to determine the thickness of the film. This was done analytically and then verified experimentally. In the analysis, the surface of the disc was divided into five sections as shown in Fig. (3.2.4). An expression for the oil film thickness within each region was obtained, except for region III which does not participate in the heat transfer process. The expressions for the film thickness, as well as the equations describing the boundaries between the different regions, are summarized at the end of section (3.2.1.2).

The maximum oil film thickness was found to be a function of the water level, the kinematic viscosity and the tip speed of the disc (ΩR). The maximum film thickness (both on the air and water sides) is proportional to the square root of these three parameters, as indicated in Figs. (3.2.9)

and (3.2.10). From these results it can be concluded that it is desirable to use a low viscosity oil so as to reduce the film heat transfer resistance. The film thickness variation with water level and tip speed should be included in the overall optimization of the P.C.T.

The oil film thickness on the water side was found to be a strong function of the specific gravity of the oil. This indicates the desirability of selecting an oil with a low specific gravity. In addition, it was found that the film thickness on the water side could be substantially reduced by operating the P.C.T. in the starved mode. This reduction in film thickness is very important since the oil film constitutes the largest heat transfer resistance on the water side. In tests made with the full scale model of the P.C.T., J. Dong [17] observed a 15% increase in the total heat transfer in going from dry to starved mode of operation. Another advantage of starved mode operation is that the total volume of oil required is much smaller. This, in turn, implies that the cost of the initial charge of oil is reduced.

Starved mode operation however, has been shown to lead to water beading of the disc surface at high angular velocities. These water beads result in a significant increase in the water evaporation rate, and therefore, this condition should be avoided. To do so, it is necessary that the angular velocity be kept below a certain limit, which is, in general, a function of the type of oil used, the oil layer thickness, the water level and the spacing between the discs. The dependence of the critical angular velocity on these parameters was determined empirically and is shown in Figs. (4.3.1) to (4.3.4).

The effect of the oil properties on the critical angular velocity Ω_c

will be discussed in the following section on the selection of the oil.

There is no clear indication in the experiments performed, as to the optimum oil layer thickness. However, from the data shown in Fig. (4.3.1), it can be seen that most of the increment in Ω_c is obtained at the lower values of D. Since the cost of the initial charge of oil is proportional to the oil layer thickness, it is desirable to keep D small. Therefore, an appropriate value for D would seem to be the point at which the rate of increase of Ω_c with D becomes smaller. Another observation, which reinforces the previous choice of D, is that the rate at which water droplets are entrained in the oil layer increases sharply as D is increased past this point. The water entrainment rate can be reduced by reducing the angular velocity, but then the advantage of increasing D is lost. Therefore, for the oils shown in Fig. (3.3.1) the oil layer thickness should be somewhere between .8 and 1.2 inches.

Again, the effects of the water level and disc spacing on the critical angular velocity, can only be considered in the context of an overall optimization of the P.C.T.

8.2.2 Selection of Oil

The oil properties which have been shown to affect the performance of the oil system are: kinematic viscosity, vapor pressure, specific gravity, surface tension and interfacial tension. All these properties, with the exception of the interfacial tension, show a uniform trend in the way they influence the performance of the oil. In other words, the performance of the oil increases monotonically as the value of these properties decrease. Further modeling of the water beading mechanisms is required in order to determine the relative importance of these parameters. The objective would be to

define some nondimensional combination of these properties, on the basis of which, the relative performance of different oils could be compared. In the meantime, the effect of each of these properties can be qualitatively described, independent of the other properties. In addition, acceptable values of these properties can be suggested, based on the performance of the oils already tested.

Kinematic viscosity: Both the oil film thickness and the critical angular velocity are affected by the viscosity of the oil. A lower viscosity results in a thinner oil film and a higher maximum angular velocity. Furthermore, the lower the viscosity the faster the water droplets entrained in the oil layer coalesce. Therefore, the oil selected should have a low viscosity at the operating temperature.

Vapor pressure: This only affects the rate at which oil evaporates from the P.C.T. The oil evaporation rate should be low, as discussed in section (3.4.1), and thus, the oil must have a low vapor pressure. However, a low vapor pressure implies, in general, a higher viscosity oil, and as mentioned above, this is undesirable. A compromise between these two requirements must therefore be sought.

Specific gravity: A lower specific gravity implies a thinner oil film on the water side, as well as a

higher maximum angular velocity and a faster

breakdown of the water-in-oil dispersion.

Therefore, the specific gravity should be

as low as possible, and certainly less than

one, since the oil must float on top of the

water.

Surface tension: The surface tension affects the spreading

ability of the oil over the water surface.

For a constant interfacial tension, the lower

the surface tension the faster the oil will

spread. This has the advantage of reducing

the water evaporation from the "starved"

side of the water surface, since this side re-

mains covered by a monolayer of oil. In

addition, this monolayer of oil has been ob-

served to increase the maximum angular velocity.

Therefore, a low surface tension is preferable.

Interfacial tension: This property differs from the ones above in

that the oil performs poorly, both for very

high and very low values of interfacial tension.

High interfacial tension reduces the wetting

ability of the oil, and this in turn, causes

water beading on the disc surface. A low inter-

facial tension however, results in a low maximum

angular velocity. Consequently, optimum perfor-

mance must be achieved at some intermediate value.

This optimum value is, in general, different for each oil. It depends on the nature of the surface active agent in the oil. This dependence, however, is not clear, and therefore, the optimum interfacial tension must be determined empirically in each case.

This optimization was carried out for base Texaco oil TL-10150 and a sulfonate additive. The best performance was achieved with an interfacial tension of about 9 dynes/cm. The additive concentration corresponding to this interfacial tension was 345 ppm. The values of the other properties of this oil at 130°F were: kinematic viscosity, 11.06 centistokes; vapor pressure, 1.5×10^{-4} lb/ft^2; specific gravity, 0.85; surface tension, 31 dynes/cm.

This oil has yet to be tested in the full scale model of the P.C.T., but observations done in the 20 inch rig suggest that it is a likely candidate. Therefore, its properties can be considered as representative of acceptable oil properties.

8.3 Augmentation of Disc Performance by Surface Roughening

Heat transfer augmentation has been studied for turbulent flow between parallel plates using repeated-rib roughness. It has been found experimentally that the friction factor and heat transfer coefficient not only depend on the Reynolds number, rib height to hydraulic diameter ratio (e/D_h) and pitch to height ratio (p/e), but also on the rib shape (ϕ) and flow attack angle (α).

Based on the law of the wall similarity which was used by Nikuradse for the sand-grain roughness, and the application of a heat-momentum transfer analogy by Dipprey and Sabersky for the sand-grain roughness, a general friction and heat transfer correlation has been obtained by taking into account the effect of geometrically non-similar parameters (equations 4.4.6 and 4.4.8). The correlations are based on experimental data for air flow with $0.032 \leq e/D_h \leq 0.102$, $5 \leq p/e \leq 20$, $40° \leq \phi \leq 90°$, $20° \leq \alpha \leq 90°$, and $3,000 \leq Re \leq 30,000$.

Friction and heat transfer data of this investigation agree well with Webb, Eckert, and Goldstein's data when the p/e ratio is greater than 10. However, the disagreement between this investigation and Wilkie's data may be up to 50% for $5 \leq p/e \leq 20$, and $20° \leq \alpha \leq 90°$. The discrepancy may be due to Hall's Transformation which was used by Wilkie.

Several performance comparisons show that the repeated-rib roughness with a 45° flow attack angle has the best heat transfer performance when compared with other types of roughness such as the repeated-ribs roughness with 90° flow attack angle, and sand-grain roughness.

A specific application of friction and heat transfer correlations
to the design of the periodic cooling towers for a 1,000 MgW electric power
plant has been performed by using an optimizing computer routine. Under
the same operating conditions the roughnened surface shows significant
economic advantage over the smooth surface in that it is 13.3 % lower
on capital costs and 12.3% lower on incremental costs.

8.4 Improvement of Rotor Performance by Cross-Coupling Rotor System

Studies employing the computer model indicate there are definite gains in heat exchanger effectiveness to be realized by cross coupling rotor systems. The principal gains are due to a specific characteristic of the periodic tower; namely that the water trough is "well mixed" and is essentially at the outlet water temperature. Linking systems in series increases the average temperature differential between the series of trough and the air stream. This effect is especially prominant when operating the tower to achieve a large temperature drop of the water stream.

8.5 Condenser Fouling by Oil Contamination

Degradation of condenser performance was observed as the water velocity was decreased. However, at a water velocity of 6.2 ft/sec., the steady state thickness of oil was sufficiently thin that the measured film coefficients coincided (within experimental accuracy) with the McAdams relation.

Since modern condensers are designed for water velocities of about 8-12 ft/sec, the shear stress between the water and the deposited oil appears to be sufficiently high to reduce the deposited oil to negligible levels.

8.6 Periodic Matrix #1

The primary source of dripping from matrix 1 was due to discontinuities between the overlap regions of the sheets. Discontinuities prevented oil from flowing smoothly from one sheet to another. Rather, oil would accrue at the sheet corners and would drop directly into the air-stream or onto the following sheet. This oil deposited on the second sheet was suffciently close to the inner radius to drip off the second sheet as it passed through

the apex of its motion. Further, all attempted means of "patching" the discontinuties by spacers, bends, rivets, etc. failed to significantly reduce drip rates. The only successful means of preventing interior dripping was to (1) provide sheets whose planes of overlap matched smoothly, or (2) eliminate overlaps. Another prerequisite to eliminate interior dripping is to keep the water level no higher than the maximum inner radius of the annulus. At these low water levels, the annulus could be run at almost any RPM without interior drips forming. At higher water levels there is a critical rotational speed which is itself a function of water level. At rotational speeds greater than this critical speed, interior drops formed. Dripping from the exterior edges could be eliminated by cutting off the corners of the hexagon - i.e., effectively rounding the corners.

The sole successful means of preventing dripping from discontinuous sheets was to ensure good contact between sheets at the overlap. Hence, all future sheets should be made with flat overlap regions. Since the sheets are large enough to require stiffening bends or ribs, it is important that these stiffeners do not disrupt the flat contact areas of the overlap regions.

Finally, from the viewpoint of efficient use of material, it is advantageous to reduce the size of the overlap regions. Also, if the matrix will be run with the water level no higher than the maximum inner radius, the efficient use of material would dictate the use of curved sheet sections.

Appendix 2A

Disc Induced Flow

The rotation of the disc induces flows within the water bath. Flow patterns, as in Figure A2A.1 have been observed in dye studies. This analysis endeavors to predict these observed flows.

Ignoring momentum terms, variations in the Z direction, and shear forces in the Y direction, the local shear force in the X direction is proportional to the relative speed between the disc and the water flow:

$$\tau_x = \mu(V_d - v_x)\, C_d = \mu(\omega y - v_x)\, C_d$$

where v_x is the local water velocity in the x direction and C_d is a constant to allow for the velocity profile between plates. Now, for 'steady-state' operation,

$$F_x = \tau_x - \frac{\partial P}{\partial x}\, S = 0$$

where S is the spacing between plates. Therefore:

$$v_x = \omega y - \frac{S}{C_d \mu}\, \frac{\partial P}{\partial x} \tag{A.2A.1}$$

By continuity, at any fixed x,

$$\int_{y_s}^{y_r} v_x\ dy = \int_{y_s}^{y_r} \omega y - \frac{S}{C_d \mu}\, \frac{\partial P}{\partial x}\ dy = 0$$

assuming that $\frac{\partial P}{\partial x}$ is not a function of y, the above equation yields:

$$\frac{\omega}{2}\, (y_r^2 - y_r^2) - \frac{S}{C_d \mu}\, \frac{\partial P}{\partial x}\, (y_r - y_s) = 0$$

therefore:

$$\frac{S}{C_d \mu}\, \frac{\partial P}{\partial x} = \frac{\omega}{2}\, (y_r + y_s) = \omega y_{avg}$$

this, substituted into equation A.2A.1 yields:

$$v_x = \omega(y - y_{avg})$$

Appendix 2.B

Formulation of Energy and Heat Transfer relations for the simulation

of the rotary heat exchanger

The nomenclature used is defined in Figure 2.5.1a

1. Dilution of inlet stream by induced circulation flows: Applying

an energy balance to inlet and outlet streams yields:

$$\dot{m}_{mix} T_{mix} = \dot{m}_{in} T_{w1} + \dot{m}_{rot} T_{w2}$$

since $\dot{m}_{mix} = \dot{m}_{in} + \dot{m}_{rot}$, where $\dot{m}_{rot}$ can be calculated as indicated in

appendix 2 , and defining the dilution D as $D = \dot{m}_{in}/\dot{m}_{rot}$,

$$T_{wm} = \frac{D T_{w1} + T_{w2}}{D + 1} \tag{A2B.1}$$

This formulation assumes that no energy transfer occurs to the discs during

the mixing process. This is essentially assuming that the inlet and circu-

lating streams mix prior to entering into the heat exchanger.

2. Water side 'hot zone' (region W2, Figure 2.5.1a)

Energy balance equation: Equating energy entering the system to that leaving

yields:

$$c_{pw} \dot{m}_{in} T_{w1} + c_{pw} \dot{m}_{rot} T_{w2} + C_d T_{p3} = C_d T_{p1} + c_{pw} (\dot{m}_{in} + \dot{m}_{rot}) T_{w3}$$

Noting that $c_{pw} \dot{m}_{in} = C_w$, and using the definition of D,

$$T_{w1} = -\frac{1}{D} T_{w2} - \frac{C_d}{C_w} T_{p3} + \frac{C_d}{C_w} T_{p1} + (1 + \frac{1}{D}) T_{w3} \tag{A2B.2}$$

Heat Exchanger relations:

If $C_d > C_w$, $\qquad \varepsilon_{W2} = \dfrac{T_{wm} - T_{w3}}{T_{wm} - T_{p3}}$

using this and equation A2B.1 for T_{wm},

$$T_{w1} = \frac{D + 1}{D} \frac{T_{w3}}{1 - \varepsilon_{W2}} - \frac{D + 1}{D} \frac{\varepsilon_{W2}}{1 - \varepsilon_{W2}} \quad T_{p3} - \frac{1}{D} T_{w2} \tag{A2B.3a}$$

If $C_d < C_w$,

$$\epsilon_{w2} = \frac{T_{p1} - T_{p3}}{T_{wm} - T_{p3}}$$

and again using equ. A2B.1 for T_{wm},

$$T_{w1} = \frac{D+1}{D\epsilon_{w2}} \; T_{p1} + \frac{D+1}{D}(1-\frac{1}{\epsilon_{w2}}) \; T_{p3} - \frac{1}{D} \; T_{w2} \qquad (A2B.3b)$$

3. Primary water side region (region W1, Figure 2.5.1a) energy equation:

$$c_p(\dot{m}_{in} + \dot{m}_{rot}) \; T_{w3} + C_d \; T_{p2} = c_p(\dot{m}_{in} + \dot{m}_{rot}) \; T_{w2} + C_d T_{p3}$$

Again noting that $c_p\dot{m}_{in} = C_w$, and using the definition of D

$$= -C_w(1 - \frac{1}{D}) \; T_{w3} - C_d T_{p2} + C_w(1 + \frac{1}{D}) T_{w2} + C_d \; T_{p3} \qquad (A2B.4)$$

Heat Exchanger relations:

If $C_d > C_w$:

$$\epsilon_{w1} = \frac{T_{w3} - T_{w2}}{T_{w3} - T_{p2}}$$

therefore,

$$0 = (1-\epsilon_{w1})T_{w3} - T_{w2} + \epsilon_{w1} \; T_{p2} \qquad (A2B.5a)$$

If $C_d < C_w$: $\epsilon_{w1} = \frac{T_{p3} - T_{p2}}{T_{w3} - T_{p2}}$

therefore,

$$0 = \epsilon_{w1}T_{w3} + (1-\epsilon_{w1})T_{p2} - T_{p3} \qquad (A2B.5b)$$

4. Air inlet half of air side heat exchanger: (region A2, Fig. 2.5.1a)

Energy Equation:

$$C_d(T_{p4} - T_{p2}) = C_a(T_{a3} - T_{a1})$$

rearranging;

$$T_{a1} = T_{a3} + \frac{C_d}{C_a} \; T_{p2} - \frac{C_d}{C_a} \; T_{p4} \qquad (A2B.6)$$

Heat exchanger relations:

if $C_d > C_a$

$$\varepsilon_{a2} = \frac{T_{a3} - T_{a1}}{T_{p4} - T_{a1}}$$

$$T_{a1} = \frac{1}{1 - \varepsilon_{a2}} T_{a3} - \frac{\varepsilon_{a2}}{1 - \varepsilon_{a2}} T_{p4} \qquad (A2B.7a)$$

if $C_d < C_a$:

$$\varepsilon_{a2} = \frac{T_{p4} - T_{p2}}{T_{p4} - T_{a1}}$$

$$T_{a1} = \frac{1}{\varepsilon_{a2}} T_{p2} - \frac{1 - \varepsilon_{a2}}{\varepsilon_{a2}} T_{p4} \qquad (A2B.7b)$$

5. Air exhaust half of air side heat exchanger (region A1, Fig. 2.5.1a)

Energy equation:

$$C_d(T_{p1} - T_{p4}) = C_a(T_{a2} - T_{a3})$$

$$0 = C_a T_{a2} - C_a T_{a3} - C_d T_{p1} + C_d T_{p4} \qquad (A2B.8)$$

Heat exchanger relations:

if $C_d > C_a$:

$$\varepsilon_{a1} = \frac{T_{a2} - T_{a3}}{T_{p1} - T_{a3}}$$

$$0 = -T_{a2} + (1 - \varepsilon_{a1})T_{a3} + \varepsilon_{a1}T_{p1} \qquad (A2B.9a)$$

if $C_d < C_a$:

$$\varepsilon_{a1} = \frac{T_{p1} - T_{p4}}{T_{p1} - T_{a3}}$$

$$0 = (1 - \varepsilon_{a1})T_{p1} - T_{p4} + \varepsilon_{a1}T_{a3} \qquad (A2B.9b)$$

with ε_{a1}, ε_{a2}, ε_{w1}, ε_{w2}, C_w, C_a, C_d, and D known, equations (A2B.2 thru A2B.9) are eight equations which interrelate the eight remaining unknowns.

Appendix 2C

Heat Exchanger Effectiveness: 1 Side 'well mixed'

A 'well mixed' condition exists when one fluid temperature remains unchanged throughout the heat exchanger. This can be achieved by (1) change of state, or (2) supplying sufficient agitation to one fluid stream so that the inlet stream is effectively diffused throughout the heat exchanger.

Case I: $C_p < C_w$

Refering to Figure A2C.1, effectiveness can be defined as:

$$\varepsilon = \frac{T_{p2} - T_{p1}}{T_{w1} - T_{p1}} \tag{A2C.1}$$

now:

$$q = \frac{U \ A \ [(T_{w2} - T_{p1}) - (T_{w2} - T_{p2})]}{\ln \ \frac{T_{w2} - T_{p1}}{T_{w2} - T_{p2}}} = \frac{U \ A \ (T_{p2} - T_{p1})}{\ln \ \frac{T_{w2} - T_{p1}}{T_{w2} - T_{p2}}} \tag{A2C.2}$$

by the definition of heat capacity,

$$q = C_p \ (T_{p2} - T_{p1})$$

substitution into equation A2C.2 yields:

$$\ln \ \frac{T_{w2} - T_{p1}}{T_{w2} - T_{p2}} = \frac{U \ A}{C_p} = NTU$$

or $\quad (T_{w2} - T_{p2}) = (T_{w2} - T_{p1}) \ \exp \ (-NTU)$

subtracting $(T_{w2} - T_{p1})$ from both sides and multiplying by -1.0 yields:

$$T_{p2} - T_{p1} = (T_{w2} - T_{p1}) \ (1-e^{-NTU})$$

$$= (T_{w1} - T_{p1}) - (T_{w1} - T_{w2}) \ (1-e^{-NTU}) \tag{A2C.3}$$

by an energy balance between the disc and the water:

$$T_{w1} - T_{w2} = \frac{C_p}{C_w} \ (T_{p2} - T_{p1}) \tag{A2C.4}$$

substitution of this into equation A2C.3, manipulation, and equation

A2C.1 yields:

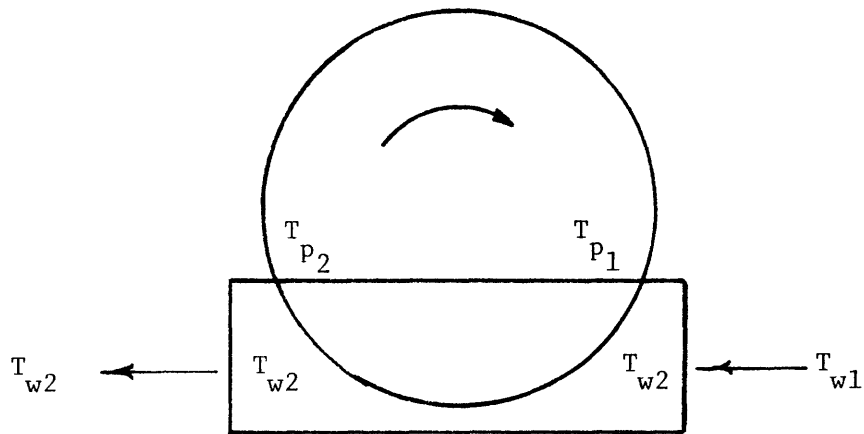$$\varepsilon = \frac{T_{p2} - T_{p1}}{T_{w1} - T_{p1}} = \frac{1 - e^{-NTU}}{1 + \dfrac{C_p}{C_w}(1-e^{-NTU})}$$

Case II: $C_p > C_w$

$$\varepsilon = \frac{T_{w1} - T_{w2}}{T_{w1} - T_{p1}}$$

by equation (A2C.4) $\varepsilon = \dfrac{C_p}{C_w} \dfrac{(T_{p2} - T_{p1})}{(T_{w1} - T_{p1})}$

therefore,

$$\varepsilon = \frac{C_p}{C_w} \frac{1 - e^{-NTU}}{1 + \dfrac{C_p}{C_w}(1-e^{-NTU})}$$

TEMPERATURES IN A PCT

FIG. A2C.1

APPENDIX 3.A

CUBIC EQUATION SOLUTIONS

The relationship between the oil film thickness and the measured oil volume flow rate is given in Eqs. (3.2.43) and (3.2.46) which have the general form:

$$h^3 + ah + b = 0 \qquad\qquad (3.A.1)$$

The form of the solution to this equation depends on the relative magnitudes and signs of the coefficients a and b. In general, there are three solutions to this equation but not all of them are physically possible. This is illustrated in Fig. (3.A). At positions 1 and 3, there is only one value of h corresponding to each value of Q, and the solution to Eq. (3.A.1) has the form [29]:

$$h = -2 \sqrt{a/3} \cot(2\alpha)$$

with

$$tn\alpha = \sqrt[3]{tn(\beta/2)}; \quad |\alpha| \leq 45°$$

and

$$tn\beta = 2/b\sqrt{(a/3)^3}; \quad |\beta| \underset{+}{\leq} 90°$$

At position 3, however, for each value of $Q < Q_{max}$, there are two possible values of h greater than 0. This is due to the fact that at position 3 the oil runs down the disc away from the collector. The oil is pulled down by its own weight, and this force increases as h increases. This implies that increasing h beyond h^* in Fig. (3.A), does not result in further increase in the volume of oil collected. On the contrary Q starts to decrease and eventually becomes negative.
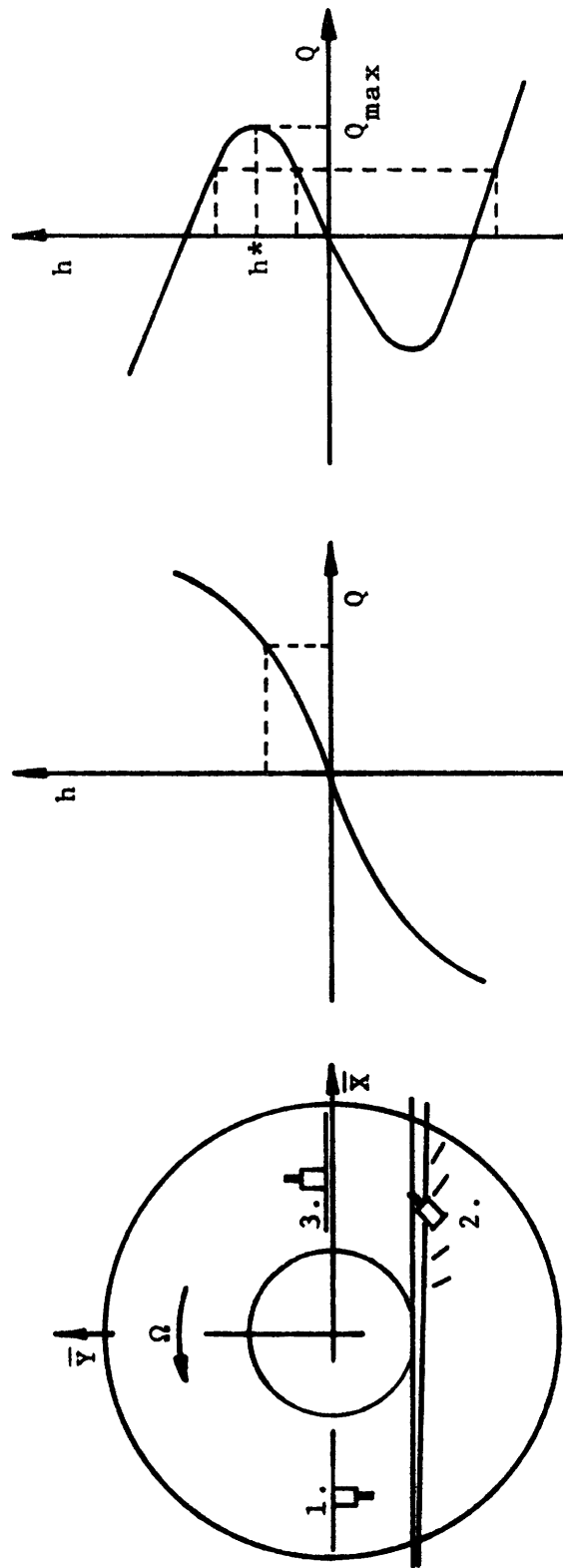
Positions 1. and 2.

Position 3.

RELATIONSHIP BETWEEN THE OIL FILM THICKNESS

AND THE MEASURED OIL VOLUME FLOW RATE

Figure 3.A

To determine which of the two solutions corresponded to the real value of h, the velocity of the oil on the surface of the film was observed. It was found that at all places along the $+ \bar{x}$ axis, with the exception of the oil ridge at $\bar{x} = 1$, this velocity was in the $+ \bar{y}$ direction. It can be shown from Eqs. (3.2.7) and (3.2.41) that for $h = h^*$ the velocity of the oil on the surface of the film is given by:

$$v = \Omega x/2 \qquad > 0$$

The correct solution is, therefore, the smallest one, and has the form:

$$h = -2 \sqrt{-(a/3)} \cos(\frac{\alpha + \pi}{3})$$

with

$$\cos\alpha = - \frac{b}{2\sqrt{-(a/3)^3}}$$

APPENDIX 3B

OIL PROPERTIES

I. Properties at Room Temperature (75°F)

|	Specific Gravity	Kinematic Viscosity (stokes)	Surface Tension (dyn/cm)	*Interfacial Tension (dyn/cm)
ubrex 100	.86	.337	26.9	3.1
A Rubrex 100	.86	.337	26.9	19.3
T1-10150 (T-5000)	.86	.330	31.0	4.9
Synfluid	.81	.249	28.7	19.0
Silicone SF-96	.95	.200	22.3	35.0

II. Properties at Operating Temperature (130°F)

	Specific Gravity	Kinematic Viscosity (stokes)	Surface Tension (dyn/cm)	*Interfacial Tension (dyn/cm)
Rubrex 100	.85	.115	25.5	2.5
A Rubrex 100	.85	.115	25.5	17.1
TL-10150 (T-XXX)	.85	.111	27.7	3.5
Synfluid	.80		27.9	14.4
Silicone SF-96		.109	20.2	34.5

*The interfacial tensions were measured with respect to tap water.

III.   Texaco TL-10150 oil with sulfurate additive.

The variation in the interfacial tension of the oil as a function of additive concentration is shown in Fig. (3.3).
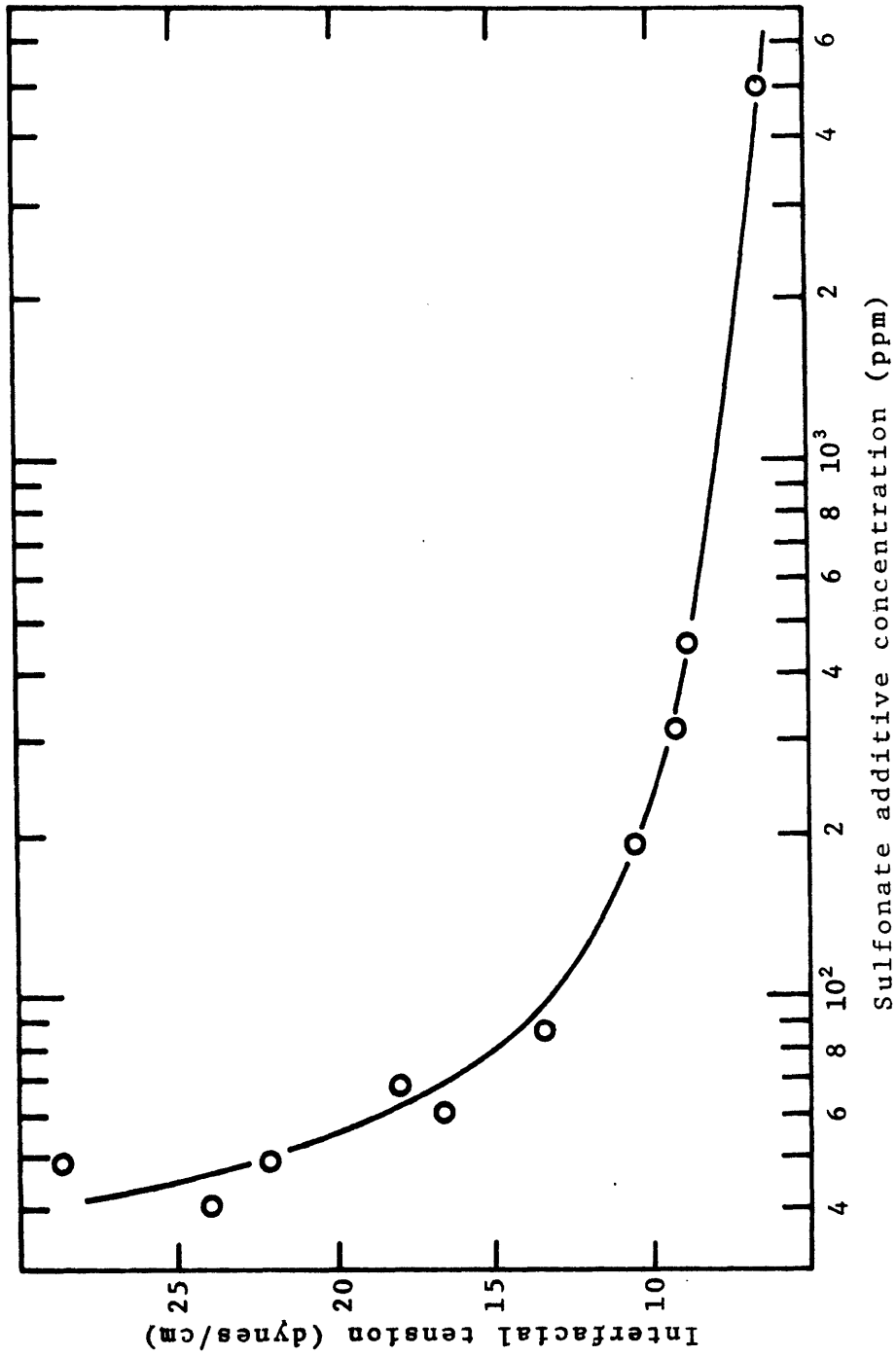
VARIATION OF THE INTERFACIAL TENSION OF TL-10150 OIL
WITH SULFONATE ADDITIVE CONCENTRATION

Figure 3.B

APPENDIX 3C

OIL EVAPORATION FORMULAE

The evaporation rate of an oil surface exposed to a turbulent stream of air can be estimated with existing experimental correlations. These correlations can be found in standard textbooks on mass transfer. The equations used in this section can be found in reference [10].

Mass evaporation rate per unit area is given by

$$\dot{m}/A = h_d(C_{ao} - C_{a*})$$

Assuming that the oil concentration at infinity in the atmosphere is zero, $C_{a*} = 0$. The oil concentration at the oil surface is related to its vapor pressure and temperature by the ideal gas equation:

$$C_{ao} = \frac{P_v}{RT}$$

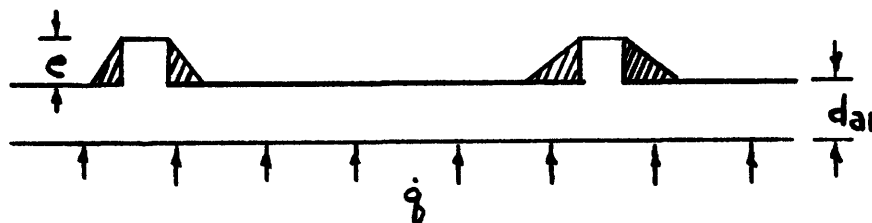The mass transfer coefficient h_d is given by the Gilliland correlation:

$$h_d = 0.023 \frac{d'}{2D} \left(\frac{2DV}{\nu}\right)^{.83} \left(\frac{\mu}{\rho\, d'}\right)^{.44}$$

where the diffusivity d' is given by another Gilliland correlation:

$$d' = 0.0069 \frac{T^{1.5}}{P(V_a^{.33} + V_b^{.33})^2} \left[\frac{1}{M_a} + \frac{1}{M_b}\right]^{1/2}$$

APPENDIX 4A

EFFECT OF CLAY THERMAL RESISTANCE ON HEAT TRANSFER MEASUREMENTS

Thermal conductivity of clay (K_c) = 0.5 Btu/hr-ft-°F

Thermal conductivity of aluminum (K_{al}) = 128 Btu/hr-ft-°F

The overall heat transfer coefficient (U) can be calculated as follows:

$$1/U = 1/h_{air} + 1/h_{clay} + 1/h_{aluminum}$$

$$= 1/h_{air} + d_c/K_c + d_{al}/K_{al}$$

where

$$h_{air} = 10 \ Btu/hr-ft^2-°F$$

$$d_{al} = 0.25 \ inch$$

d_c = average thickness of clay layer

$\quad$ = 0.05 inch for ϕ = 55°

$\quad$ = 0.1 inch for ϕ = 40°.

If ϕ = 55°:

U = 9.23 or about a 7.7% error if one ignores the clay resistance

$\quad$ and uses h_{air}

If $\phi = 40°$:

U = 8.57 or about a 15% error is incurred by ignoring the clay

resistance.

APPENDIX 4B

HEAT TRANSFER AREA REQUIRED AS FUNCTION OF DISC DIAMETER

By the definition of the friction factor,

$$\Delta P = f \; 4L\rho V^2/(2g_c \; D_h), \; or$$

$$\Delta P = P \sim \bar{L} \; V^2 \tag{1}$$

where

L = flow length

$$= K_1 \; D_o \tag{2}$$

since

$$h \sim K_2 \; V^{0.8}$$

$$V^2 \sim K_3 \; h^{2.5}$$

for constant $\dot{Q}$ and ΔT,

$$h \sim 1/A$$

$$V^2 \sim K_4/A^{2.5} \tag{3}$$

For constant ΔP across the rotary heat exchanger, combining equations (1), (2), and (3), one gets

$$A = K_5 \; D_o^{0.4}$$

So, the smaller disc diameter corresponds to the smaller heat transfer area required for the constant ΔP, $\dot{Q}$ and ΔT. Area is directly related to cost.

REFERENCES

1. Jones, W.J., "Natural Draft Cooling Towers", Hamon-Cottell, Inc. 1968.

2. Dickey, J.B., Jr. and R.E. Cates, "Managing Waste Heat with the Water Cooling Tower", The Marley Company, 1970.

3. Glicksman, L.R., "Thermal Discharge from Power Plants", ASME Paper No. 72-WA/Ener-2, 1972.

4. Robertson, M.W., Glicksman, L.R. and Rohsenow, W.M., "Improvement of the Environmental and Economic Characteristics of Cooling Towers, Part II: Periodic Cooling Towers", MIT, Heat Transfer Lab Report Number 80047-82, June 1973.

5. Hon, P.C., Je-Chin Han, Pilger, P., Glicksman, L.R. and Rohsenow, W.M., "Improvement of the Environmental and Economic Characteristics of Cooling Towers Part II of II: The Periodic Cooling Tower - Flow Visualization, Surface Roughening, and Full Scale Model", Energy Lab Report Number MIT-EL 74-008, MIT, June 1974.

6. Hon, P.C. et al, "The Periodic Cooling Tower - Small Scale, Full Scale, and Surface Roughening Tests", Energy Laboratory Report # MIT-EL 75-018, MIT, June 1975.

7. Andeen, B.R. and Glicksman, L.R., "Dry Cooling Towers for Power Plants", EPL Report # DSR 73047-1, Department of Mechanical Engineering, MIT, Cambridge, Mass., 1972.

8. Andeen, B.R. and Glicksman, L.R., "Improvement of the Environmental and Economic Characteristics of Cooling Towers, Part I, Optimized Design Programs, Fluidized Beds, and Non-Metalic Heat Exchangers", Heat Transfer Lab Report # DSR-80047-82, MIT, Cambridge, MA. June 1973.

9. Kays, W.M., Convective Heat and Mass Transfer, McGraw-Hill, New York, 1966.

10. Rohsenow, W.M. and Choi, H.Y., Heat, Mass and Momentum Transfer, Prentice-Hall, New Jersey, 1961.

11. Handbook of Heat Transfer, edited by W.M. Rohsenow and J.P. Hartnett, McGraw-Hill, New York 1973.

12. Eckert, E.R.G. and Drake, R.M., Heat and Mass Transfer, McGraw-Hill, New York, 1959.

13. Bergles, A.E. and Webb, R.L., eds., "Augmentation of Convective Heat and Mass Transfer", ASME, New York 1970.

14. Fink, D.A., "Measurement of the Oil Layer Thickness on a Periodic Heat Exchanger", Backelor of Science Thesis, MIT, Department of Mechanical Engineering, 1975.

15. Schlichting, H., Boundary-Layer Theory, McGraw-Hill, New York, 1968.

16. Levich, V.G., Physiochemical Hydrodynamics, Prentice-Hall, Englewood Cliffs, New Jersey, 1967.

17. Dong, J., S.M. Thesis, "Experimental Performance of the Full Scale Periodic Cooling Tower, Department of Mechanical Engineering, MIT, 1976.

18. Sams, E.W., "Experimental Investigation of Average Heat Transfer and Friction Coefficients for Air Flowing in Circular Pipes Having Square-Thread Type Roughness", NACA RM-E 52D17 (1952).

19. Gargaud, J. and Paumard, G., their data was employed in the paper of "Generalized Heat Transfer and Friction Correlations for Tubes with Repeated-Rib Roughness", by Webb, R.L. et al, Int. J. Heat Mass Transfer, 1971.

20. Molloy, J.,"Rough Tube Friction Factors and Heat Transfer Coefficients in Laminar and Transition Flow," UKAEA AERE-R5415 (1967).

21. Webb, R.L., Eckert, E.R.G. and Goldstein, R.J., "Heat Transfer and Friction in Tubes with Repeated-Rib Roughness", Int. J. Heat Mass Transfer, Vol. 14, pp. 601-617, 1971.

22. Wilkie, D., "Forced Convection Heat Transfer surfaces Roughened by Transverse Ribs", proceed of the 3rd Int. Heat Transfer Conf. Aug. 7-12, 1966. Vol. 1.

23. Sheriff, N. and Gumley, P., "Heat Transfer and Friction Properties of Surfaces with Discrete Roughness", Int. J. Heat Mass Transfer 9, 1297-1320 (1966).

24. Hall, W.B., "Heat Transfer in Channels Having Rough and Smooth Surfaces", J. Mech. Eng. Sci. 4, 287-291 (1962).

25. White, L. and Wilkie, D., "The Heat Transfer and Pressure Loss Characteristics of Some Multi-Start Ribbed Surfaces", paper collected by Bergles, A.E. and Webb, R.L., eds., "Augmentation of Convective Heat and Mass Transfer", ASME, New York 1970.

26. Williams, F., Pirie, M.A.M. and Warburton, C., "Heat Transfer from Surfaces Roughened by Ribs", Paper collected by Bergles, A.E. and Webb. R.L., eds. "Augmentation of Convective Heat and Mass Transfer", ASME, New York 1970.

27. Nikuradse, J., "Laws for Flow in Rough Pipes". NACA TM 1292 (1950).

28. Dipprey, D.F. and Sabersky, R.H., "Heat and Momentum Transfer in Smooth and Rough Tubes at Various Prandtl Numbers", Int. J. Heat Mass Transfer, Vol. 6, pp. 329-353, 1963.

29. Korn, G.A., _Mathematical Handbook for Scientists and Engineers_, McGraw-Hill, N.Y. 1961.